IMPROVEMENT IN TRIBOLOGY AND CORROSION RESISTANCE OF DIAMOND-LIKE CARBON FILM BY TITANIUM DOPING USING THE FILTERED CATHODIC VACUUM ARC TECHNIQUE

Natthaphong Konkhunthot

A Thesis Submitted in Partial Fulfillment of the Requirements for

the Degree of Doctor of Philosophy in Metallurgical Engineering

Suranaree University of Technology

Academic Year 2018

การปรับปรุงสมบัติไทรโบโลยีและความต้านทานการกัดกร่อนของฟิล์มคาร์บอนคล้ายเพชรด้วยการเจือไทเทเนียมโดยใช้เทคนิคฟิลเตอร์แคโธดิกอาร์กในสุญญากาศ

นายณัฐพงศ์ กลขุนทด

วิทยานิพนธ์นี้เป็นส่วนหนึ่งของการศึกษาตามหลักสูตรปริญญาวิศวกรรมศาสตรดุษฎีบัณฑิต
สาขาวิชาวิศวกรรมโลหการ
มหาวิทยาลัยเทคโนโลยีสุรนารี
ปีการศึกษา 2561

IMPROVEMENT IN TRIBOLOGY AND CORROSION RESISTANCE OF DIAMOND-LIKE CARBON FILM BY TITANIUM DOPING USING THE FILTERED CATHODIC VACUUM ARC TECHNIQUE

Suranaree University of Technology has approved this thesis submitted in partial fulfilment of the requirements for the Degree of Doctor of Philosophy

Thesis Examining Committee

_____
(Asst. Prof. Dr. Arthit Chingsoongnern)

Chairperson

_____
(Assoc. Prof. Dr. Pornwasa Wongpanya)

Member (Thesis Advisor)

_____
(Assoc. Prof. Dr. Sirirat Tubsungnoen Rattanachan)

Member

_____
(Asst. Prof. Dr. Tapany Patcharawit)

Member

_____
(Prof. Dr. Santi Maensiri)

Vice Rector for Academic Affairs

and Internationalization
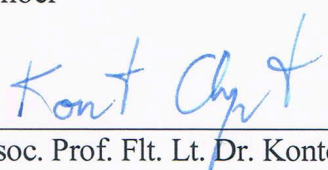
_____
(Assoc. Prof. Flt. Lt. Dr. Kontorn Chamniprasart)

Dean of Institute of Engineering

ณัฐพงศ์ กลขุนทด : การปรับปรุงสมบัติไทรโบโลยีและความต้านทานการกัดกร่อนของ
ฟิล์มคาร์บอนคล้ายเพชรด้วยการเจือไทเทเนียมโดยใช้เทคนิคฟิลเตอร์แคโธดิกอาร์กใน
สุญญากาศ (IMPROVEMENT IN TRIBOLOGY AND CORROSION RESISTANCE OF
DIAMOND-LIKE CARBON FILM BY TITANIUM DOPING USING THE FILTERED
CATHODIC VACUUM ARC TECHNIQUE) อาจารย์ที่ปรึกษา : รองศาสตราจารย์ ดร.
พรวสา วงศ์ปัญญา, 250 หน้า.

งานวิจัยนี้ได้แบ่งการศึกษาออกเป็นสองส่วนคือ (i) การศึกษาเกี่ยวกับการสังเคราะห์และ
การบ่งลักษณะฟิล์มคาร์บอนคล้ายเพชรเพื่อหาเงื่อนไขที่เหมาะสมในการสังเคราะห์ฟิล์มคาร์บอน
คล้ายเพชร และ (ii) การศึกษาเกี่ยวกับการปรับปรุงสมบัติไทรโบโลยีและประสิทธิภาพความ
ต้านทานการกัดกร่อนของฟิล์มคาร์บอนคล้ายเพชรด้วยการเจือไทเทเนียม ในการศึกษาเบื้องต้น
ฟิล์มคาร์บอนคล้ายเพชรได้ถูกสังเคราะห์ขึ้นบนแผ่นซิลิกอนด้วยเทคนิคฟิลเตอร์แคโธดิกอาร์กใน
สุญญากาศซึ่งมีแหล่งกำเนิด 2 ชุด โดยปรับเปลี่ยนแปลงค่าศักย์ไฟฟ้าไบแอสจาก 0.0 ถึง 1.5
กิโลวัตต์ สมบัติทางโครงสร้าง สมบัติทางกล และสมบัติทางแสงของฟิล์มได้ถูกตรวจสอบภายใต้
การเปลี่ยนแปลงค่าศักย์ไฟฟ้าไบแอสระหว่างสังเคราะห์ฟิล์ม ผลจากเทคนิค Raman
spectroscopy แสดงให้เห็นว่าค่าต่ำสุดของ I_D/I_G ratio ที่ศักย์ไฟฟ้าไบแอส 1.0 กิโลวัตต์ เกิดขึ้น
สอดคล้องกับค่าสูงสุดของ sp^3/sp^2 ratio ที่ได้จากเทคนิค XPS การวิเคราะห์ด้วยเทคนิค XRR บ่ง
บอกว่าฟิล์มคาร์บอนคล้ายเพชรมีความหนาแน่นค่อนข้างสูงระหว่าง 2.51 และ 2.79 g/cm^3 อัตรา
การปลูกฟิล์มวัดได้ที่ค่า 3.5 4.8 และ 3.3 nm/min ที่ค่าศักย์ไฟฟ้าไบแอส 0.5 1.0 และ 1.5 กิโลวัตต์
ตามลำดับ ซึ่งเป็นผลของกระบวนการ self-sputtering ของพื้นผิวและกระบวนการ deposition
ความหยาบพื้นผิวของฟิล์มเพิ่มสูงขึ้น เนื่องจากการชนของไอออนที่มีพลังงานสูงภายใต้ค่า
ศักย์ไฟฟ้าไบแอสสูงขึ้น ความแข็งและความยืดหยุ่นมีค่าในช่วง 13–25 GPa และ 114–145 GPa
ตามลำดับ ความเค้นภายในซึ่งเกิดขึ้นระหว่างการสังเคราะห์ฟิล์มภายใต้เงื่อนไขที่ใช้ไบแอสส่งผล
ให้ค่าสมบัติทางกลและความหนาแน่นของฟิล์มคาร์บอนคล้ายเพชรสูงขึ้นซึ่งอธิบายได้ผ่าน
แบบจำลอง subplantation ความสัมพันธ์ระหว่างค่า I_D/I_G ratio และ refractive index ซึ่งได้จาก
เทคนิคที่ง่ายและไม่ทำลายชิ้นงาน ได้แก่ เทคนิค Raman และ spectroscopic ellipsometry เป็น
วิธีที่มีประสิทธิภาพในการอนุมาน sp^3/sp^2 ratio และค่าความแข็งของฟิล์ม ผลจากการศึกษา
เบื้องต้นแสดงให้เห็นว่าเงื่อนไขที่ดีที่สุดที่ทำให้ได้ฟิล์มคาร์บอนคล้ายเพชรที่มีสมบัติทางกลและ
ความหนาแน่นที่ใกล้เคียงกับฟิล์มคาร์บอนคล้ายเพชรที่มีคุณภาพสูง โดยเฉพาะอย่างยิ่งฟิล์ม ta-C
เกิดขึ้นที่ค่าศักย์ไฟฟ้าไบแอส 1.0 กิโลวัตต์ ในส่วนที่สองของการศึกษา ฟิล์มคาร์บอนคล้ายเพชรที่

เจือด้วยไทเทเนียมได้ถูกสังเคราะห์ขึ้นบนเหล็กกล้าไร้สนิม AISI 304 โดยใช้เงื่อนไขการ
สังเคราะห์ที่ได้มาจากการศึกษาเบื้องต้น ในการศึกษานี้ โครงสร้างที่แปรผันกับความร้อน ค่าความ
แข็งแรงการยึดเกาะ สมบัติทางกลและสมบัติไทรโบโลยีในระดับนาโน และความต้านทานการกัด
กร่อนได้ถูกตรวจสอบโดยคำนึงถึงปริมาณของการเจือไทเทเนียม จากการทดลองพบว่า การเพิ่มขึ้น
ของ I_D/I_G ratio และการลดลงของความเค้นภายในเป็นผลมาจากการเพิ่มขึ้นของปริมาณการเจือ
ไทเทเนียม ความมีเสถียรภาพทางความร้อนของฟิล์มคาร์บอนคล้ายเพชรที่เจือด้วยไทเทเนียม
เพิ่มขึ้นอย่างมีนัยสำคัญ เนื่องจากการเกิดขึ้นของเฟส TiC ภายในโครงสร้างของฟิล์ม สมบัติทางกล
และปริมาณ sp^3 ในฟิล์มลดลงเล็กน้อยจากการเจือไทเทเนียม ค่าความแข็งแรงการยึดเกาะถูก
ปรับปรุงอย่างเห็นได้ชัดผ่านการเกิดขึ้นของ atomic intermixing bond ที่รอยต่อของฟิล์ม
คาร์บอนคล้ายเพชรที่เจือด้วยไทเทเนียมและชั้นไทเทเนียมรองพื้น ค่าสัมประสิทธิ์แรงเสียดทาน
เฉลี่ยของเหล็กกล้าไร้สนิมลดลงอย่างสังเกตเห็นได้ เมื่อผ่านการเคลือบด้วยฟิล์มคาร์บอนคล้ายเพชร
ฟิล์ม passivating TiO_2 ที่เกิดขึ้นบนฟิล์มคาร์บอนคล้ายเพชรที่เจือด้วยไทเทเนียมสามารถยับยั้ง
การแพร่ผ่านของสารละลายการกัดกร่อนลงสู่ชั้นวัสดุพื้นด้านล่าง ทำให้ฟิล์มคาร์บอนคล้ายเพชรที่
เจือด้วยไทเทเนียมมีประสิทธิภาพการป้องกันการกัดกร่อนที่สูงขึ้น ในบทสรุปนี้ ฟิล์มคาร์บอน
คล้ายเพชรที่เจือด้วยไทเทเนียมแสดงประสิทธิภาพทางไทรโบโลยีและทางการป้องกันการกัดกร่อน
ที่ดีเยี่ยมซึ่งเหมาะสำหรับการใช้งานทางด้านอุตสาหกรรม

สาขาวิชา <u>วิศวกรรมโลหการ</u>   ลายมือชื่อนักศึกษา <u>Natthaphong Konkhunthot</u>

ปีการศึกษา 2561   ลายมือชื่ออาจารย์ที่ปรึกษา <u>P. Wongpanya.</u>

        ลายมือชื่ออาจารย์ที่ปรึกษาร่วม

NATTHAPHONG KONKHUNTHOT : IMPROVEMENT IN TRIBOLOGY AND CORROSION RESISTANCE OF DIAMOND-LIKE CARBON FILM BY TITANIUM DOPING USING THE FILTERED CATHODIC VACUUM ARC TECHNIQUE. THESIS ADVISOR : ASSOC. PROF. PORNWASA WONGPANYA, Dr.-Ing. 250 PP.

TRIBOLOGY/CORROSION/DIAMOND-LIKE CARBON/FILTERED CATHODIC VACUUM ARC/TITANIUM-DOPED DLC FILM

The thesis is divided into 2 parts: (i) the synthesis and investigation of diamond-like carbon (DLC) films to explore the appropriate condition for DLC films and (ii) the improvement of the tribological properties and corrosion resistance of DLC films with Ti atoms. With regard to (i): the DLC films were synthesized on a Si substrate by pulsed two-filtered cathodic vacuum arc (FCVA) deposition as a function of the substrate negative direct current bias voltage (V_{bias}) from 0.0 to 1.5 kV. The microstructure, mechanical performances, and optical properties of the films have been investigated in respect to the effects of the V_{bias}. The Raman spectroscopy results showed the lowest I_D/I_G ratio at the V_{bias} of 1.0 kV which was consistent with the highest sp^3/sp^2 ratio obtained from the XPS technique. The XRR analysis indicated that the DLC films had a relatively high density between 2.51 and 2.79 g/cm^3. The film growth rate was measured to be 3.5, 4.8, and 3.3 nm/min at the V_{bias} of 0.5, 1.0, and 1.5 kV, respectively, which depended on the self-sputtering of the substrate and the deposition process. The surface roughness of the films increased monotonically due to the bombardment of high-energy ions at a high V_{bias}. The hardness and elastic modulus were measured in a range of 13–25 GPa and 114–145 GPa, respectively. The internal stress during the film growth under the bias condition was found to improve the mechanical properties and

density of the DLC films which could be explained using a subplantation model. The correlation between the I_D/I_G ratio and the refractive index was established here which was an effective method to infer the sp^3/sp^2 ratio and hardness of the film by the simple and non-destructive technique of Raman and spectroscopic ellipsometry. The best deposition condition could be achieved at the V_{bias} of 1.0 kV which provided the DLC films with excellent hardness and density close to high-quality DLC film, especially the tetrahedral amorphous carbon (ta-C) films. As to (ii): Ti-doped DLC films were fabricated on AISI 304 stainless steel under the deposition condition acquired from the preliminary study. The microstructural dependent thermal annealing, adhesion, nano-mechanical and tribological properties, and corrosion resistance were investigated with respect to the effects of the Ti content. As for the results, the increase in the I_D/I_G ratio accompanied by the reduction in the internal stress was observed as the Ti increased. Thermal stability was significantly enhanced due to the formation of the TiC phase. A slight decrease in hardness and the sp^3 content was due to the introduction of the Ti atoms. The adhesion was obviously improved through the atomic intermixing bond at the Ti-doped DLC/Ti layer interface. The average mean coefficient of friction of the bare substrate was greatly decreased by applying the DLC films. The passivating TiO_2 films formed on the Ti-doped DLC films could hinder the diffusion of the corrosive solution into the underlying substrate, thus leading to better corrosion protection performance. In conclusion, the Ti-doped DLC films exhibited excellent tribological and corrosion protection performance suitable for industrial applications.

School of <u>Metallurgical Engineering</u>

Academic Year 2018

Student's Signature Natthaphong Konkhunthot

Advisor's Signature 9. Wongpanya.

Co-Advisor's Signature Pat Photongkam.

ACKNOWLEDGMENTS

for giving me good suggestions, friendly support, and a lot of care and attention during my time in NUT. Heartfelt thanks go to NUT's Thai members for giving me lots of support from the first day I joined the group, with warmth and merriment at the same time, and for taking me on a trip around both Nagaoka city and Japan.

Last but not least, I would like to honestly thank my lovely family: my parents Mr. Amnat Konkhunthot and Mrs. Somsi Konkhunthot, and my brother Mr. Ekkasak Konkhunthot for their endless love and continuous support throughout the writing of this thesis and my life in general. A Ph.D. thesis would not have been completed and possible without the love and compassion of all of those who are beside me.

Natthaphong Konkhunthot

TABLE OF CONTENTS

Page

TABLE OF CONTENTS (Continued)

TABLE OF CONTENTS (Continued)

TABLE OF CONTENTS (Continued)

TABLE OF CONTENTS (Continued)

LIST OF TABLES

LIST OF TABLES (Continued)

LIST OF FIGURES

LIST OF FIGURES (Continued)

LIST OF FIGURES (Continued)

LIST OF FIGURES (Continued)

LIST OF FIGURES (Continued)

LIST OF FIGURES (Continued)

LIST OF FIGURES (Continued)

LIST OF FIGURES (Continued)

LIST OF FIGURES (Continued)

LIST OF FIGURES (Continued)

LIST OF FIGURES (Continued)

LIST OF ABREVIATIONS

%*ER*	=	Elastic recovery
A	=	Area
a-C	=	Amorphous carbon
a-C:H	=	Hydrogenated amorphous carbon
AEY	=	Auger electron yield
Ag	=	Silver
Ag/AgCl	=	Silver/Silver chloride electrode
Al	=	Aluminum
Au	=	gold
AW	=	Anti-wear
BE	=	Binding energy
B-EMA	=	Bruggeman effective medium approximation
BSE	=	Backscattered electrons
C	=	Carbon
C_2H_2	=	Acetylene
CE	=	counter electrode
CH_4	=	Methane
COF	=	Coefficient of friction
Cr	=	Chromium
CR	=	Corrosion rate
Cu	=	Copper

LIST OF ABREVIATIONS (continued)

CVD = Chemical vapor deposition

d = Distance

DC = Direct current

DLC = Diamond-like carbon

DXL = Deep X-ray Lithography

E = Elastic modulus

EBSD = Electron backscattered diffraction

E_{corr} = Corrosion potential

ECR-CVD = Electron cyclotron resonance physical vapor deposition

ECWR = electron cyclotron wave resonance

EDS = energy-dispersive X-ray spectroscopy

EELS = Electron energy-loss spectroscopy

EP = Extreme-pressure

EW = Equivalent weight

EXAFS = Extended X-ray absorption fine structure

F = Fluorine

FCVA = Filtered cathodic vacuum arc

FOV = Field of view

FWHM = Full width at half-maximum

FY = Fluorescence yield

H = Hardness

LIST OF ABREVIATIONS (continued)

H	=	Hydrogen
H/E	=	Plastic index parameter
H_2O	=	Water
HCl	=	Hydrochloric acid
Hf	=	Hafnia
H-free DLC	=	Hydrogen-free diamond-like carbon
HIPIMS	=	High power impulse magnetron sputtering
HOPG	=	Highly oriented pyrolytic graphite
hv	=	Photon
IAD	=	Ion assisted deposition
IBD	=	Ion beam deposition
i_{corr}	=	Corrosion current density
I_{corr}	=	Total anodic current
ICP-MS	=	Inductively coupled plasma mass spectrometry
i_{cruit}	=	Critical current density
I_D/I_G ratio	=	The intensity ratio of the D and G bands
i_p	=	Passive current
IR	=	Infrared rays
k	=	Extinction coefficient
K	=	Wear rate
KCl	=	Potassium chloride

LIST OF ABREVIATIONS (continued)

KE	=	Kinetic energy
kV	=	Kilo voltage
L_a	=	Cluster size of the sp^2 sites
L_c	=	Critical load
LEEM	=	Low-energy electron microscopy
LINAC	=	Linear accelerator
LPR	=	Linear polarization resistance
MAO	=	Microarc oxidation
Me	=	Metal
MeC	=	Metal carbide
Mo	=	Molybdenum
MoDTC	=	Molybdenum dithiocarbamate
MSIBD	=	Mass selected ion beam deposition
N	=	Nitrogen
n	=	Refractive index
NaCl	=	Sodium chloride
Nb	=	Niobium
nc	=	Nano-carbide
NEXAFS	=	Near edge X-ray absorption fine structure
Ni	=	Nickel
NMR	=	Nuclear magnetic resonance

LIST OF ABREVIATIONS (continued)

O_2	=	Oxygen
OCP	=	Open circuit potential
OH^-	=	Hydroxide
P	=	Porosity
PBS	=	Plasma beam source
PECVD	=	Plasma-enhanced chemical vapor deposition
PEY	=	Partial electron yield
PFPE	=	Perfluoropolyethers
P_i	=	Protection efficiency
PSII	=	Plasma source ion implantation
PVD	=	Physical vapor deposition
R	=	Reliability factor
RE	=	Reference electrode
RF	=	Radio frequency
RH	=	Relative humidity
R_p	=	Polarization resistance
SE	=	Spectroscopic ellipsometry
SEM	=	Scanning electron microscopy
Si	=	Silicon
SiC	=	Silicone carbide
SPELEEM	=	Spectroscopic photoemission and low energy electron microscope

LIST OF ABREVIATIONS (continued)

SS	=	Stainless steel
t	=	Thickness
Ta	=	Tantalum
ta-C	=	Tetrahedral amorphous carbon
ta-C:H	=	Tetrahedral hydrogenated amorphous carbon
TEY	=	Total electron yield
Ti	=	Titanium
Ti-DLC	=	Ti-doped DLC
UHV	=	Ultra high vacuum
UMP	=	Unbalanced magnetron sputtering
UV	=	ultraviolet rays
V	=	Vanadium
V_{bias}	=	Negative direct current bias voltage
W	=	Tungsten
WC	=	Tungsten carbide
WE	=	Working electrode
XANES	=	X-ray absorption near-edge structure
X-PEEM	=	X-ray photoemission electron microscopy
XPS	=	X-ray photoelectron spectroscopy
XRR	=	X-ray reflectivity
ZDDP	=	Zinc dithiophosphate

LIST OF ABREVIATIONS (continued)

Δ = Phase difference

θ_c = Critical angle

μ = Absorption coefficient

ρ = Density

σ = Residual internal stress

ϕ = Work function

ψ = Ellipsometric angles
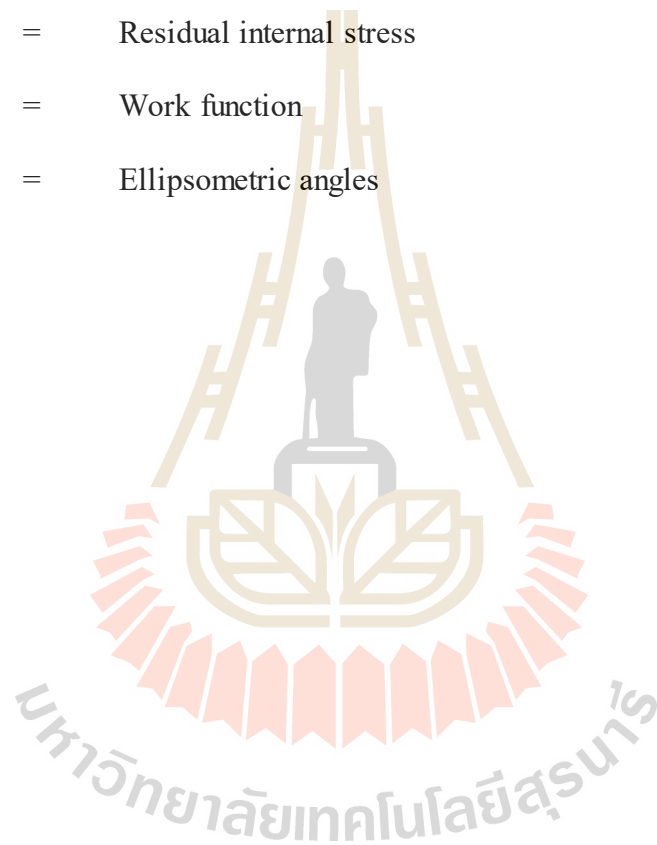
CHAPTER I

INTRODUCTION

1.1   Background and motivation

Diamond-like carbon (DLC) is an amorphous carbon film which consists of a mixture of the sp^2 and sp^3 hybridized carbons. DLC films have been considered as fascinating due to their exceptional properties, such as high hardness and wear resistance, low friction coefficient, chemical inertness, optical transparency, and biocompatibility (Robertson, 1996; Tsai, and Bogy, 1987; Cuomo *et al*., 1991). These properties allow DLC to be a promising coating for a wide range of engineering and industrial applications, e.g., cutting tools, automotive components, magnetic storage disks, electric devices, and solar cells (Robertson, 2002; Lifshitz, 1999; Grill, 1999). It is, however, possible that the DLC films could be damaged while being used in certain circumstances, particularly the combination of an external mechanical shear/normal force and a corrosive environment, with a resultant loss of performance efficiency and an increase in energy consumption. Consequently, it is very necessary to understand the mechanical and tribological performance accompanied by the thermal stability and corrosion behavior of the DLC films for the effect on their long-term performance. It should be noted that several research groups have focused the modification of DLC films to resolve such a problem.

To date, several surface modifications have been shown to be practical for DLC films. One is heat treatment, for example, the carburizing, nitriding, and carbonitriding

processes. Another is the surface coating technology including physical vapor deposition (PVD) and chemical vapor deposition (CVD). When considering the requirement of accuracy and precision in the final dimension of the components, heat treatment should be avoided as it is not a good choice due to the phase transformation and distortion of the complex shape components during the high-temperature process. Therefore, it is obligatory to pursue new technology to overcome the limitations of those processes to obtain the desired properties. In this respect, the surface coating technology is implicated and recognized as a predominant method which performs at a low operating temperature and provides a high-precision dimensional control and high-quality protective coating.

Over the years, a number of research groups have attempted to study the method of improving the material surface with surface coating technology, especially with DLC films. Although DLC films possess many advantages, high residual stress during the films' growth is one of the major problems which results in poor adhesion to the substrate, particularly to a steel substrate (McKenzie *et al*., 1991; Fallon *et al*., 1993; Lossy *et al*., 1995), and thus restricts the films' thickness and their applications. To obtain good adhesion and so a great opportunity to utilize DLC films in advanced applications, the reduction of the internal stress is extremely necessary. Two effective methods were used in the reduction of the internal stress of DLC films: (i) the application of metallic intermediate layers deposited on the steel substrate before DLC deposition and (ii) the incorporation of metallic elements into the amorphous carbon network structure, especially the carbide former, such as Ti, W, Cr, Si, and Mo (Dimigen, and Klages, 1991). In addition, it has been reported that the metal-doped DLC film shows superior tribological properties, corrosion resistance, and adhesion

compared to those of the pure DLC films. For example, the Ti-doped hydrogenated DLC films prepared by radio frequency (RF) discharged plasma and co-sputtering of the Ti targets showed an excellent lubrication and friction performances due to the presence of the transfer layer during measurements (Zhao *et al.*, 2010). Also, the incorporation of the Ti atoms into the DLC matrix produced by magnetron sputtering caused the carbide phase formation in an amorphous carbon structure which resulted in lower residual stress, wear rate, and friction coefficient of the Ti-doped DLC films (Cui *et al.*, 2012). Fu *et al.*, 2005 investigated Mo- and W-doped DLC films deposited by dual metal plasma deposition in an acetylene gas and reported that the doped DLC films exhibited high thermal stability up to annealing temperatures of 500 °C compared to the pure DLC films limited by graphitization just above 350 °C (Akkerman *et al.*, 1996). Another research group indicated that a low Ti doping level into the hydrogenated amorphous carbon films prepared by middle-frequency magnetron sputtering twin targets led to the enhancement of the wear resistance and reduction in the internal stress (Qiang *et al.*, 2013). In an aspect of the corrosion-resistant coatings, Azzi *et al.* (2010) showed that the corrosion barrier properties of the Si-doped DLC films deposited by RF plasma-enhanced chemical vapor deposition (PECVD) were improved through the formation of the passive silicon (Si) oxide surface film. From the above-mentioned examples, the incorporation of metals into the DLC structure, therefore, is a powerful method which provides a promising protective coating for advanced engineering and industrial applications.

At present, a considerable number of methods have been proposed for DLC deposition, for example, magnetron sputtering, high power impulse magnetron sputtering (HIPIMS), ion beam deposition (IBD), ion implantation, PECVD, and the

filtered cathodic vacuum arc (FCVA) technique. Among them, FCVA has been proven as one of the interesting methods capable of producing a fully ionized plasma, and thus it yields high-quality DLC films with a large density and number of C-sp^3 carbon bonds (Robertson, 1996). With the combined adoption of the metallic intermediate layer and the incorporation of the metal into the DLC films, the outstanding properties of the DLC films, such as excellent tribological and mechanical properties, good adhesion, and the corrosion resistance can possibly be tailored.

Since the properties of the DLC films correlate highly with the fraction of the sp^3/sp^2 hybridized carbons, it is very important to emphasize the acquisition of the sp^3/sp^2 ratio to comprehend their properties. To estimate the sp^3/sp^2 ratio in DLC films, near edge X-ray absorption fine structure (NEXAFS) spectroscopy was an attractive and extreme surface-sensitivity analytical tool to be used. The chemically heterogeneous objects in the DLC films, such as local geometrical structure and bonding configurations were simultaneously obtained by this technique. The other surface analytical techniques, such as Raman spectroscopy, X-ray photoelectron spectroscopy (XPS), X-ray photoemission electron microscopy (X-PEEM), X-ray reflectivity (XRR), spectroscopic ellipsometry (SE), and scanning electron microscopy (SEM) which are effective and non-destructive methods for analyzing the microstructure, thermal stability, physical and chemical properties, and surface morphology of the deposited films were performed for the in-depth understanding. Also, supplementary analytical techniques, such as pico- and nano-indentation tests, a nano-scratch test, potentiodynamic polarization test, and inductively coupled plasma mass spectrometry (ICP-MS) were implemented to achieve the nano-mechanical and nano-

tribological properties, e.g., the hardness, elastic modulus, adhesion strength, coefficient of friction, and corrosion performance, respectively, of the DLC films.

In this thesis, pure (undoped) DLC and Ti-doped DLC were fabricated by pulsed two-FCVA deposition. Two strategies, which comprised the use of an adhesive layer of Ti to serve as a Ti bond-coat between the DLC film and the substrate and the incorporation of Ti into the DLC structure were implemented to enhance the adhesion of the DLC films to the steel substrate and to reduce the residual internal stress. A preliminary study associated with manipulating the energy of the carbon ions by means of the substrate negative direct current bias voltage (V_{bias}) was performed to obtain the appropriate deposition conditions for the DLC deposition. It was found that the optimum V_{bias} of 1.0 kV provided the highest sp^3/sp^2 ratio accompanied by excellent physical, mechanical, and optical properties for the DLC films. It, therefore, was the best deposition condition and was chosen for DLC preparation in the subsequent investigation. Subsequently, the possibility of incorporating the Ti atoms into the DLC structure by pulsed two-FCVA deposition was explored. Also, comprehension of the effects of the Ti doping on the tribological properties and corrosion behaviors of the Ti-doped DLC films was systematically conducted. The microstructure and thermal stability of the Ti-doped DLC films as a function of Ti contents were also investigated for a long-term performance. The mechanisms used for describing the phenomenon were discussed in detail. This execution is beneficial for developing a protective DLC coating, which offers to be a good candidate for advanced engineering and tribological applications.

1.2 Objectives of thesis

The objective of this thesis was to fabricate the Ti-doped DLC films on an AISI 304 austenitic stainless steel substrate by pulsed two-FCVA deposition and to find a way to improve the tribological and corrosion performances of the DLC films. The other physical and mechanical properties were supplementarily investigated by a variety of effective analytical techniques to further understand the related mechanisms. The objective was divided into 4 main issues as follows.

1.2.1 To explore the appropriate condition for DLC deposition by the pulsed two FCVA technique.

1.2.2 To study the effect of the V_{bias} on the microstructure and mechanical and optical properties of the DLC films.

1.2.3 To investigate the thermal stability of the Ti-doped DLC films as a function of the annealing temperature in a range of 30–500°C.

1.2.4 To comprehend the mechanisms in the improvement of the adhesion strength, tribological properties, and corrosion performance of the Ti-doped DLC films.

1.3 The scope of the study

1.3.1 The Si (100) wafer and AISI 304 austenitic stainless steel were used as the substrate for the DLC deposition.

1.3.2 The Ti was used as the doping element and served as an adhesive layer.

1.3.3 The developed pulsed two-FCVA deposition with a separate cathodic arc source was used to synthesize the DLC and Ti-doped DLC films.

1.3.4 The important deposition parameters were given by:

- Base vacuum pressure,

- Substrate negative direct current bias voltage,

- Deposition time,

- Arc voltage,

- Pulse repetition rate,

- Duty cycle.

1.3.5 Analytical techniques for identifying the DLC films were:

(a) Microstructure, bonding configuration, and chemical composition by:

- Raman spectroscopy,

- Near edge X-ray absorption fine structure (NEXAFS) spectroscopy,

- X ray photoelectron spectroscopy (XPS).

(b) Surface morphological information by:

- Scanning electron microscopy (SEM) equipped with energy-dispersive X-ray spectroscopy (EDS).

(c) Physical and optical properties by:

- X-ray reflectometry (XRR),

- Spectroscopic ellipsometry (SE).

(d) Mechanical properties by:

- Pico- and nano-indentation test.

(e) Tribological properties by:

- Nano-scratch test.

(f) Electrochemical properties by:

- Potentiostat analyzer using potentiodynamic polarization,

- Inductively coupled plasma mass spectrometry (ICP-MS).

(g) Thermal stability by:

- X-ray photoemission electron microscopy (X-PEEM) in conjunction with the NEXAFS technique.

1.4   The locations of the research

1.4.1   The Center for Scientific and Technological Equipment, Suranaree University of Technology (SUT), Nakhon Ratchasima, Thailand.

1.4.2   Beamline 3.2Ub: PEEM, Research Facility Department, Synchrotron Light Research Institute (SLRI), Nakhon Ratchasima, Thailand.

1.4.3   Building and Utilities Division, Mechanical System Development and Utilities Department, Synchrotron Light Research Institute (SLRI), Nakhon Ratchasima, Thailand.

1.4.4   Electrical and Electronic Division, Technical and Engineering Department, Synchrotron Light Research Institute (SLRI), Nakhon Ratchasima, Thailand.

1.4.5   Opto-electronic Ceramics Laboratory, Department of Chemistry, Nagaoka University of Technology (NUT), Niigata, Japan.

1.5   Anticipated outcomes

1.5.1   Proficiencies and skills in the synthesis and the analysis of DLC and Ti-doped DLC films deposited by simultaneous pulsed two-FCVA deposition.

1.5.2 Understanding of the microstructure, physical and optical properties, bonding configuration, thermal stability, nano-mechanical and nano-tribological properties, and electrochemical corrosion behavior of the DLC depending on the V_{bias} and the Ti doping.

1.5.3 A practical way of improving thermal stability, adhesion strength, and tribological and corrosion performance of the DLC by means of the Ti doping.

1.5.4 International conferences, publication, and overseas experience during the period of being an exchange research student.

1.6 Outline of the thesis

This thesis has been divided into 6 chapters, which are related to the deposition and characterization of the microstructure and properties of the undoped (pure) DLC and Ti-doped DLC films synthesized by the pulsed two-FCVA deposition. The introduction to this thesis has already been described in Chapter I, including the background and motivation, objectives of this thesis, the scope of the study, the locations of the research, and outline of the thesis. The literature reviews in Chapter II provide the basic principle and brief review of the diamond-like carbon (DLC) films, incorporation of the alloying elements in DLC films, deposition methods for DLC films, applications of DLC films, tribological properties of undoped DLC and doped DLC films, tribological properties of DLC films in various contact conditions, friction and wear behavior of DLC films, thermal effects on the tribological behavior of DLC films, electrochemical corrosion, and stainless steel, respectively. In Chapter III, there are the experimental procedures which have been implemented containing the preparation of

the DLC films, the microstructure, bonding configuration, elemental analysis, electrochemical corrosion analysis, and mechanical and tribological performance analysis of the DLC films. Chapter IV contains the detail of the results and discussion of all the works consisting of 2 main topics: (i) the optical and mechanical properties of DLC films, and the correlation between microstructures and deposition conditions and (ii) the enhancement of the thermal stability, adhesion strength, tribological property, and corrosion protection performance of DLC films deposited on stainless steel by Ti incorporation. The conclusions of this thesis are revealed in Chapter V. Finally, suggestions are discussed for the further studies in Chapter VI.
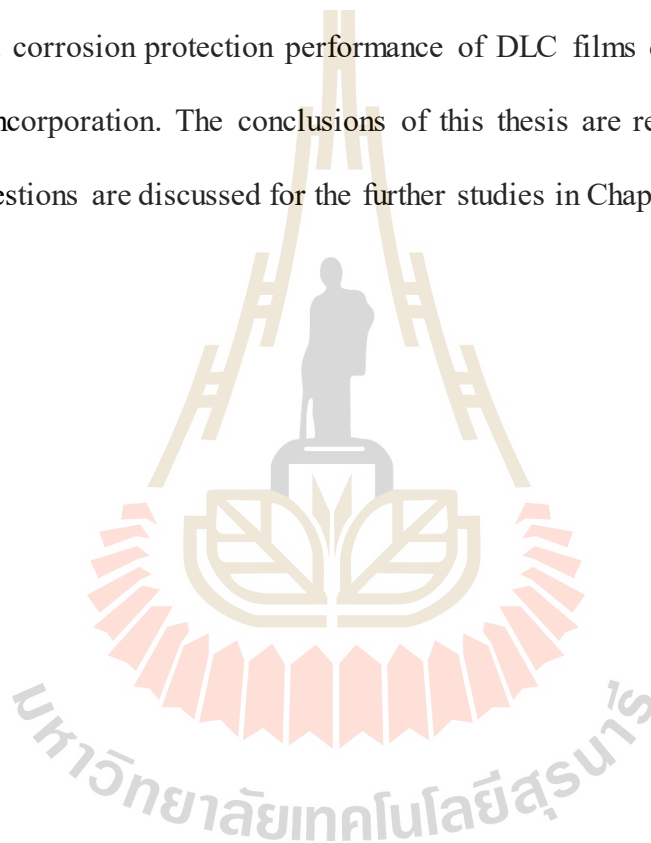
CHAPTER II

LITERATURE REVIEWS

In this chapter, a review is carried out of the theoretical background regarding the deposition and applications of DLC films, and the analytical techniques for characterizing the DLC and metal-doped DLC films. This chapter addresses by the following 10 main issues: (1) the diamond-like carbon (DLC) films, (2) the deposition methods for the DLC films, (3) the applications of the DLC films, (4) the incorporation of metals into the DLC films, (5) the tribology of DLC and metal-doped DLC film, (6) the tribological performance of DLC films in various conditions, (7) the friction and wear performance of the DLC films, (8) the thermal effects on the tribological performance of DLC films, (9) the electrochemical properties, and (10) the AISI 304 austenitic stainless steel.

2.1 Diamond-like carbon (DLC) films

2.1.1 Structure and Categorization of DLC films

As is well-known, carbon is one of the chemical elements existing in many allotropes, for example, short, intermediate, and long range-order configurations. Most of the carbon forms are the crystalline structure, such as graphite (sp^2 hybridizations), diamond (sp^3 hybridizations) and amorphous carbon, such as DLC (Lifshitz, 1999). In the sp^2-hybridized orbitals "graphite structure", 3 of 4 valence electrons of carbon atoms are linked to trigonal planar geometry (120 °) in a layered structure with 3 strong σ bonds in a plane. The fourth valence electron is formed in the

π orbital electron, normal to planar geometry. This π orbital is bonded by weak bonds, called the wan der Waals forces, which allow a graphite layer to easily shear or slide by an external force. In the sp^3-hybridized orbitals "diamond structure", on the other hand, all the fourth valence electrons are occupied to tetrahedral geometry, in which each carbon atom is arranged in the C—C bond with strong σ bonds. This is the reason why diamond has the highest hardness, modulus, and room temperature thermal conductivity, largest atomic density, and the lowest thermal expansion coefficient of any bulk materials in the world (Pierson, 1993). There are, however, still a number of carbon forms found in nature and synthesized carbon in the laboratory in addition to diamond and graphite, for example, fullerene which is also referred to as buckyball, carbon nanotube, carbon nanobud, etc., as shown in Figure 2.1.
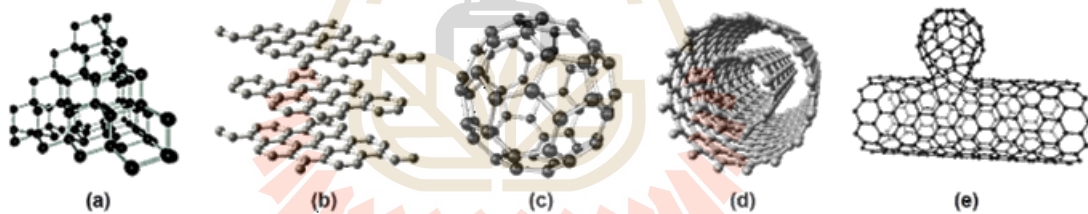
Figure 2.1 The various forms of carbon nanomaterials: (a) diamond, (b) graphite, (c) fullerene, (d) carbon nanotube, and (e) carbon nanobud, respectively.

DLC is one of the amorphous carbon (*a*-C) and/or hydrogenated amorphous carbon (*a*-C:H) films consisting of a mixture of the sp^3 and sp^2 hybridized carbons. The DLC films with highly sp^3 hybridized carbons are typically named as the tetrahedral amorphous carbon (*ta*-C) or tetrahedral hydrogenated amorphous carbon (*ta*-C:H) films if there is a number of hydrogen (H) atoms. DLC films were firstly synthesized using IBD in 1969 (Robertson, 2002; Aisenberg, and Chabot, 1971;

Aisenberg, and Kimock, 1990). Due to the unique combined properties of the high hardness and Young's modulus, low friction coefficient, excellent tribological and wear performance, chemical inertness, optical transparency, optical compatibility, and wide band gap (Robertson, 1996; Santra *et al*., 2010; Song *et al*., 2013; Chaus *et al*., 2014; Silva *et al*., 2014; Wang *et al*., 2011), DLC has attracted interest for a wide range of industrial applications as a protective coating.

Several deposition methods have been widely used to synthesize the DLC films, such as direct IBD, mass selected ion beam deposition (MSIBD), magnetron sputtering, FCVA, laser ablation, PECVD, electron cyclotron resonance physical vapor deposition (ECR-CVD), and ion assisted deposition (IAD). Since the DLC properties, either the physical or the mechanical properties, depend strongly on the sp^3/sp^2 ratio, most of the research was performed in a way to enhance the sp^3 fraction. DLC films can be classified into 4 main types (Reinke *et al*., 1993; Jacop and Möller, 1993; Weiler *et al*., 1994; Ronkainen *et al*., 2008; Zeng *et al*., 2014) depending on the sp^2 and sp^3 hybridizations and the H contents, as seen in Figure 2.2. These 4 types contain the *a*-C, *a*-C:H, *ta*-C, and *ta*-C:H, respectively.

Many deposition methods were used to deposit *a*-C and *ta*-C films, such as MSIBD, magnetron sputtering, FCVA, and laser ablation (Robertson, 2002). The carbon species for DLC deposition are from the carbon source, for example, graphite target and/or rod. To deposit DLC films using the MSIBD method, carbon ions are generated from an ion source by a graphite target and guided by sets of magnetic filters to have the optimum energetic ions before being sent toward the substrate. In magnetron sputtering, the Ar background gas is decomposed into the Ar ion using a direct current (DC) or radio frequency (RF) sputtering power supply placed behind the graphite target.

The bombardment of the Ar ion toward the target results in a glow discharge and vaporization of the carbon plasma, which is the carbon source for the DLC films. The introduction of a reactive gas, such as hydrogen gas into the deposition chamber causes the achievement of the a-C:H films.
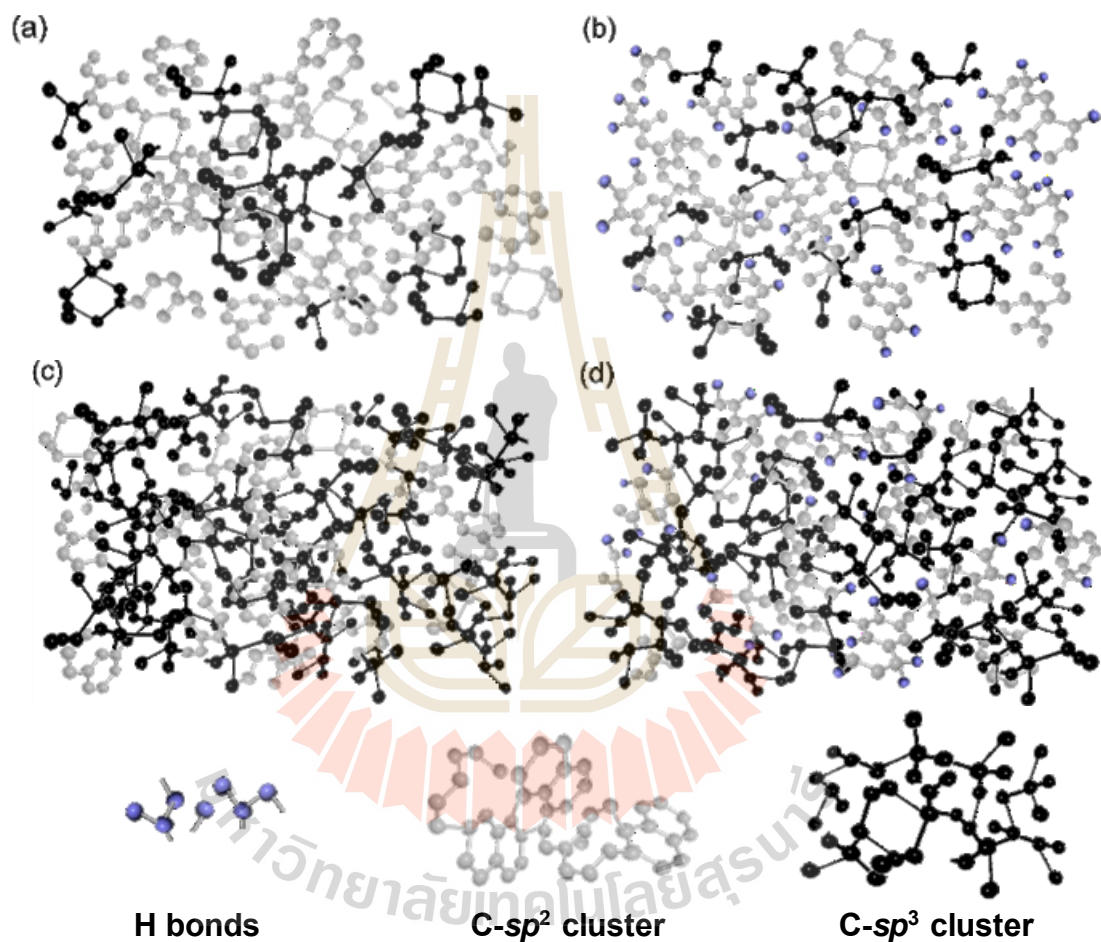
Figure 2.2 Classification of the amorphous carbon films: (a) a-C, (b) a-C:H, (c) ta-C, and (d) ta-C:H film. The H bonds, the C-sp^2 cluster, and the C-sp^3 cluster are also provided, respectively.

In laser ablation, the plasma plume of carbon is generated from the graphite target by a laser source before being emitted toward the substrate. In FCVA,

carbon plasma is obtained from the pure graphite target before passing through a magnetic filter where neutral species and macro-particles are filtered out before arriving at substrate. The FCVA is a fully ionized plasma-based technique among the techniques described above; the energy of the carbon ions, therefore, is effectively controlled using the substrate bias voltage, which determines the structure of the films. Since the *a*-C and *ta*-C films are formed from the pure carbon species without any hydrogen or hydrocarbon gases, they have less than 5% H content and 5−80% the sp^3 contents (Robertson, 2002) for the *a*-C and *ta*-C films, respectively.

Table 2.1 A comparison of the properties of diamond, graphite, and carbon-based

materials.

Types	sp^3 (%)	H (%)	Density (g/cm³)	Gap (eV)	H* (GPa)
Diamond	100	0	3.515	5.5	100
Graphite	0	0	2.267	0	-
Glassy carbon	0	0	1.3−1.55	0.01	3
a-C (evaporated)	0	0	1.9	0.4−0.7	-
a-C (sputtered)	5	0	2.2	0.5	3
ta-C	80−88	0	3.1	2.5	80
a-C:H Hard	40	30−40	1.6−2.2	1.1−1.7	10−20
a-C:H soft	60	40−50	1.2−1.6	1.7−4	<10
ta-C:H	70	30	2.4	2.0−2.5	50

*H is the hardness

On the other hand, the *a*-C:H film is produced by the decomposition of hydrocarbon gas, such as methane (CH_4) and acetylene (C_2H_2) using the conventional method of RF-PECVD, ECR-CVD, and reactive sputtering of the graphite target in a mixture of hydrogen and argon gas. Therefore, the carbon network structure contains

approximately 20−60% H content and 20−70% the sp^3 content for the a-C:H and ta-C:H, respectively (Robertson, 2002). A comparison of the properties of the diamond, graphite, and amorphous carbons is given in Table 2.1 (Reinke *et al*., 1993; Jacop, and Möller, 1993; Weiler *et al*., 1994; Ronkainen *et al*., 2008; Fallon *et al*., 1993; Zeng *et al*., 2014; Robertson, 1986; Koidl *et al*., 1990; Field, 1993).

The amorphous carbon films with a large number of sp^3 hybridized totaling carbons more than 70% (Lifshitz, 1999) are denoted as the ta-C and ta-C:H films; thus they are high-quality DLC films which promotes superior mechanical and tribological properties comparable to those of the a-C and a-C:H films which dominate the sp^2 hybridizations. Figure 2.3 demonstrates the ternary phase diagram of the amorphous carbon films which was first established by Jacob, and Möller, 1993. This diagram gives the relationship of the sp^2 bonding, sp^3 bonding, and H content of the amorphous carbon.

As can be seen in Figure 2.3, the ternary phase diagram contains 3 main regions. The first region in the bottom left corner is hydrogen free a-C. The a-C having the rich sp^2 is typical for glassy carbon or a-C films that are prepared by pyrolysis of hydrocarbon polymers or by an evaporation method, and these are not DLC films. The a-C with the higher sp^3 content without the H content is usually prepared by the sputtering method and are DLC films. Recently, modern technology of sputtering methods, such as unbalanced magnetron sputtering has produced DLC films with a larger number of sp^3 hybridized carbons. The a-C film with the higher sp^3 content is designated as the ta-C film. This high-quality DLC film is specially produced by ion or plasma beams with a high ions flux and narrow ions energy range, which is included in

the MSIBD, FCVA, and pulsed laser ablation deposition techniques at room temperature.
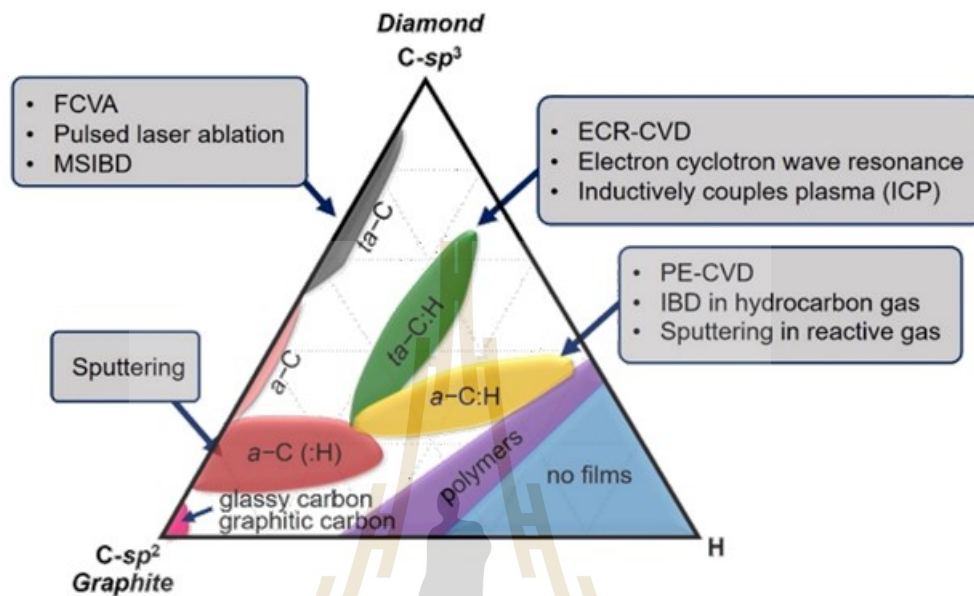
Figure 2.3 A ternary phase diagram of amorphous carbon film containing a mixture of the sp^2 and sp^3 hybridizations, and hydrogen (H) content modified from elsewhere in the literature (Robertson, 2002).

The second region in the bottom right corner of the phase diagram shows the films with a large amount of H content. The carbon atoms do not form a fully connected network, but only gas molecules (Jacob, and Moller, 1993), and thus there is a polymer-like carbon or no film.

The intermediate region of the ternary phase diagram shows the a-C:H films. They are typically generated by PECVD of hydrocarbon molecules, or by reactive sputtering of a graphite target in a mixture of a hydrogen or hydrocarbon gas precursor, or by IBD of a hydrocarbon background gas. At the present time, in modern PECVD method, for example, ECRCVD, Inductively coupled plasma (ICP), the plasma

beam source (PBS) or electron cyclotron wave resonance (ECWR), the plasma density generated from these methods is enhanced to so-called high-density plasma. The operation of low pressure and the application of magnetic fields to provide the long electron path lengths of these methods, they promote high plasma ionization, which yields denser a-C:H films with high sp^3 content designed as the ta-C:H films.

An amorphous carbon film can also be classified into 7 types depending on the H contents and the additional elements by the German Guideline VDI 2840 'Carbon films — Basic knowledge, film types and properties', Beuth-Verlag, 2005. (available as a German/English version) and (Donnet and Erdemir, 2008; Ingenieure, 2005) as follows: (i) a-C hydrogen-free amorphous carbon, (ii) ta-C tetrahedral-bonded hydrogen-free amorphous carbon, (iii) a-C:Me metal-doped hydrogen-free amorphous carbon (Me = W, Ti), (iv) a-C:H hydrogen-containing amorphous carbon, (v) ta-C:H tetrahedral-bonded hydrogen-containing amorphous carbon, (vi) a-C:H:Me metal-doped hydrogen-containing amorphous carbon (Me = W, Ti), and (vii) a-C:X modified hydrogen-containing amorphous carbon (X = Si, O, N, F, B).

2.2 Incorporation of alloying element in DLC films

Although DLCs have excellent mechanical and chemical properties, such as high hardness and wear resistance, low friction coefficient, and chemical inertness, a large intrinsic compressive stress arising during the film growth is the main problem leading to poor adhesion of the DLC films to the substrate, especially a steel substrate. In a case where a thick film is required, the delamination of films with high compressive stress can occur and thus limit the applications of the DLC films in advanced engineering applications. In an attempt to apply DLC films for a wide range of

applications, the elimination of the compressive stress is becoming a key factor and must be primarily considered. A conventional approach to reach a combination of those properties involves an increase in the deposition temperature using the substrate heating or a decrease in carbon energetic ions before arriving at the substrate. These approaches, however, result in the reduction of the sp^3 content in the carbon network structures. Other methods used to reduce the compressive stress in DLC films are the application of an adhesive metallic interlayer between the film and the substrate and the doping of metal atoms into the DLC structure. These methods not only reduce the compressive stress and enhance the film adhesion, but also improve their mechanical and tribological properties, which presents the opportunity to employ the films in more applications.

Besides the improvement of the adhesion and the mechanical and tribological properties of the films, the incorporation of metals into DLC films has an influences on their electrical and optical properties as well as biocompatibility. Therefore, incorporation should be performed carefully and there is a need to comprehend more detailed information in utilizing the doping elements. In general, the structure of the metal-doped DLC films is quite complex and difficult to understand compared to those of the undoped or pure DLC films. When the metal atoms are incorporated into the DLC structure, they are likely to form and/or interact with the carbon atoms as either a pure metal solid solution or metal carbide depending on the nature and concentration of the metals. The metals acting as the metallic carbide former, such as titanium (Ti), tungsten (W), vanadium (V), molybdenum (Mo), tantalum (Ta), and niobium (Nb) (Dimigen and Klages, 1991) and the non-carbide former, such as aluminum (Al), copper (Cu), silver (Ag), gold (Au), and nickel (Ni) (Zhou *et al*., 2012; Wang *et al*., 2012) can embed within the carbon network structure as a nano- or micro-crystalline

structure cluster or can disperse as pure metal. The concentration level of the metals, therefore, is a key factor in determining the properties of developed DLC films. These metal-doped DLC films are beneficial and wide interest in all fields, for instance, biomedical materials, optical devices, electronic and tribological applications, and automobile components.

It should, however, be of concern that the incorporation of a high concentration of metal atoms in an amorphous structure may cause an increase in the sp^2 hybridized carbon and friction. This is because the formation of the metal carbide or metallic nanocluster gives a ceramic-like character; thus, it has a higher coefficient of friction compared to that of diamond- or graphite-like character. Besides as described-above, the other advantages of high metal incorporation are reductions in the films mechanical properties, for example, the hardness and elastic modulus (Bharathy *et al*., 2012) in hard DLC films like the *ta*-C films. In recent decades, various metals have been incorporated in the DLC films, such as Ti, Cr, W, Mo, Ag, and Cu by means of several deposition techniques including the conventional CVD and PVD methods. Advanced deposition technology has been applied, such as the combination of either the CVD and PVD or the PVD and PVD, for example, PECVD and FCVA deposition or unbalanced magnetron sputtering (UMP) of metallic targets in the presence of a gas mixture of hydrocarbon and argon and high power impulse magnetron sputtering (HIPIMS) techniques (Mandal *et al*., 2015).

According to these methods, modified DLC films with a wide range of compositions and structures in the deposition technique and the doping element can be feasible. For example, Ma *et al*. (2012) prepared Ti-doped DLC films on Ti alloy by reactive magnetron sputtering combined with plasma source ion implantation (PSII)

technology. They showed the formation of TiC nanometer grains in the *a*-C:H films. The hardness, wear resistance, and cohesive strength of the Ti-doped DLC films were significantly improved due to the carbide phases and nano-composite structure. The film adhesion was evidently increased by the compositionally graded layers with a large water contact angle compared to that of the unmodified DLC films. Pang *et al*. (2011) also reported the deposition of Ti/Ti-doped DLC and Ti/AlTiN/Ti-doped DLC films on a W18Cr4V high-speed steel substrate by magnetron sputtering. The adhesion was improved with the release of the internal stress in the films. The coefficient of friction (COF) and wear resistance of the steel substrate were also obviously enhanced by the Ti atoms incorporated into the DLC films. Also, similar results were observed by Feng *et al*. (2012). They found that Ti-doped DLC films produced on an AISI 52100 steel substrate using the medium frequency magnetic sputtering process exhibited a lower COF than a perfluoropolyether (PFPE) substrate. In addition to the Ti-doped DLC films, Fu *et al*. (2013) reported an increase in the DLC's toughness due to the formation of tungsten carbide (WC) dispersed in the DLC matrix. They observed a significant improvement in the film's adhesion and wear resistance as the W content increased up to 3.08 at.%. With the application of pure polyalpha olefin (PAO) lubrication, the COF and residual stress of the W-doped DLC films were reduced because of good absorption of the lubricant oil molecules relative to the undoped DLC films. The residual stress was, however, in turn increased as the W content further increased. Other research groups agreed with the adhesive improvement of DLC films by metal doping due to the interfacial adhesion (Gayathri *et al*., 2015) in which the relaxation in the compressive stress can be found by the shifting of the G peak position towards a lower wavenumber in the Raman analysis. One revealed a higher thermal stability of the W- and Mo-doped

DLC films than the pure DLC films. Hydrogen loss and phase transformation was found to decrease with an incorporation of metal atoms (Fu *et al.*, 2005). These investigations showed a good consistency with the results of Tallant *et al.* 1995. For this reason, the incorporation of metals in the DLC films is an effective method used to tailor the DLC's properties. The metal doped into the DLC films provides not only to reduce the residual stress and COF but also to improve the wear resistance and adhesion strength which is beneficial in many industrial applications. The corresponding properties acquired from the incorporation of the metals into the DLC films are summarized, as shown in Figure 2.4.
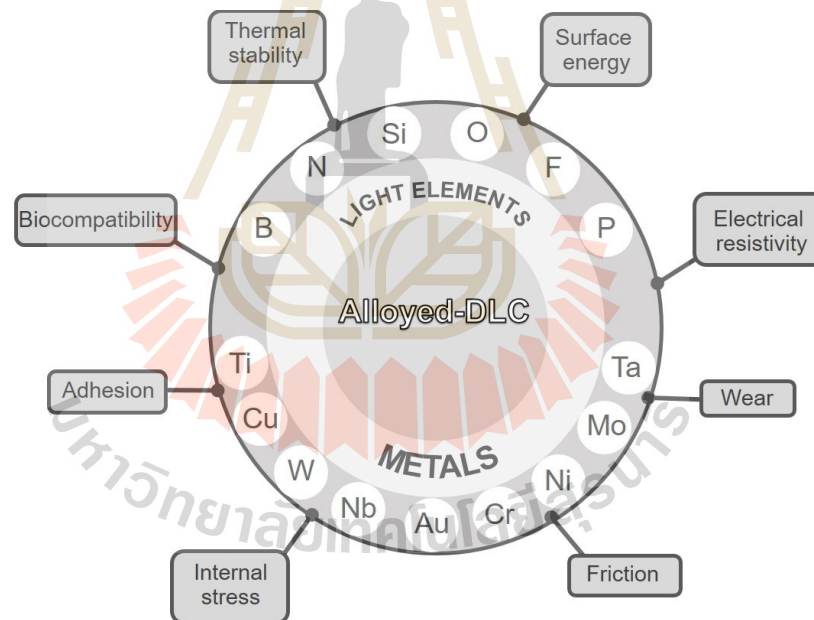
Figure 2.4 A schematic diagram of the incorporation of alloying elements into the DLC films and their corresponding properties adopted from Donnet and Erdemir (2008).

2.3   Deposition methods for DLC films

It is well-known that DLC films can be synthesized by a variety of deposition methods, as shown in Figure 2.5, which includes direct ion beam deposition, arc discharge, filtered cathodic vacuum arc (FCA), pulsed laser deposition, sputtering, ion beam assisted deposition (IBAD), ion assisted deposition (IAD), mass selected ion beam deposition (MSIBD), and plasma enhanced physical vapor deposition (PECVD) (Robertson, 2002; Lifshitz, 1999). Each deposition technique gives different structures and properties of DLC films, which will be described in detail in the following subsections.
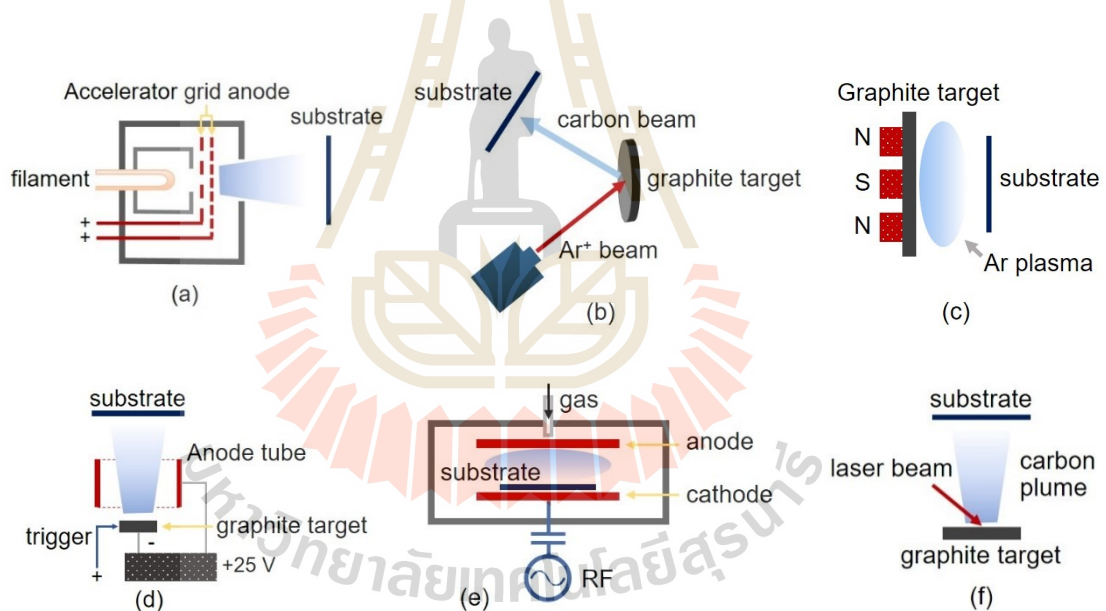
Figure 2.5 The schematic illustrations of various depositions for DLC film: (a) IBAD, (b) IAD, (c) magnetron sputtering, (d) CVA, (e) PECVD, and (f) pulsed laser ablation deposition, respectively, modified from Robertson (2002).

2.3.1 Ion beam assisted deposition (IBAD)

IBD was first explored by Aisenberg and Chabot and used in the synthesis of DLC films (Aisenberg and Chabot, 1971; Aisenberg and Kimock, 1990). The carbon plasma from the IBD method is obtained by sputtering of the graphite target with an ion source. A set of grids electrically connected with high bias voltage is used to accelerate the carbon ions and propel the optimum energetic ions toward the vacuum chamber to form the DLC film on the substrate. Typically, the carbon ions of this method have an intermediate energy of approximately 100 eV which is the optimum energy to produce high-quality DLC films with high density and sp^3 hybridized carbons (Donnet and Erdemir, 2008). Figure 2.6 shows the correlation of the ion energy on the density and sp^3 hybridizations of a-C and a-C:H films. The optimum energy of the carbon ions of 100 eV shows the best deposition condition to give the diamond-like characteristics with the highest sp^3 hybridizations. According to Figure 2.6, the carbon ion energy is a very important factor in determining the properties of DLC films depending strongly on the deposition techniques.
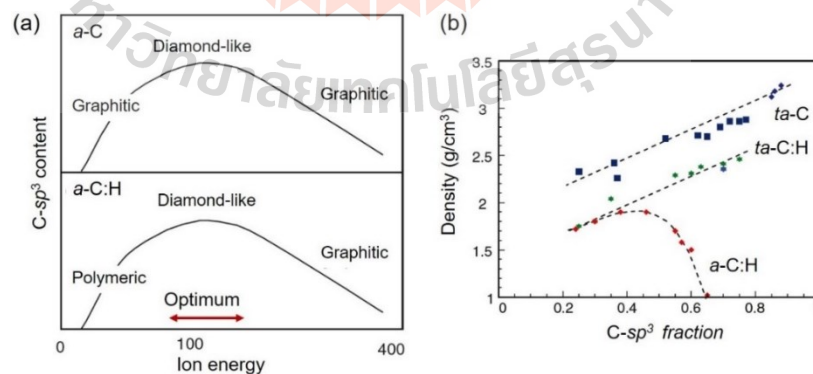
Figure 2.6 A variation of the sp^3 content as a function of (a) ion energy and (b) density adopted from Donnet and Erdemir (2008).

2.3.2 Arc discharge

In arc discharge, carbon ions from pure carbon plasma are generated by an electric discharge between the cathode and anode. In some deposition condition, an initial carbon plasma can be produced by a laser source known as laser-arc deposition. The carbon ions generated in the plasma contain a wide range of species, for example, different charge states and neutral atoms, such as macro-particles or melted droplets. These ions have a broad energy in a range of approximately 30 eV per charge state. The application of the substrate bias voltages, therefore, is required to tune the energy of the ions and to obtain high-quality DLC films (Lifshitz, 1999).

2.3.3 Cathodic vacuum arc (CVA)

The cathodic vacuum arc occurs when a high arc discharge current with an ion current density of approximately up to 10^{13} W/cm^2 is applied to the cathode materials, especially the graphite cathode. With the applied high ion current density, a tiny region on the graphite solid will transform into fully ionized carbon plasma (Jüttner, 1987; Robertson, 2002). An initial carbon plasma that is generated at the local region is referred to as cathode spot which expands through the vacuum chamber rapidly towards the substrate and grounded anode. To obtain good films with a very low oxygen contamination, the base pressure of this method should be approximately 10^{-8} Torr ($\sim 10^{-6}$ Pa). The working pressure is, however, increased to 10^{-5} Torr due to the outgassing of the cathode materials during the deposition process. The ion charge state acquired from the cathodic vacuum arc can vary depending on the arc current (Robertson, 2002) and cathode materials, for example, $\sim$20 eV for light elements and $\sim$200 eV for heavy elements (Sanders and Anders, 2000). With a higher ion charge state relative to the other deposition methods, the cathodic vacuum arc is a potential

technique to produce *ta*-C films with excellent mechanical, chemical, and tribological properties. In the generation of high-quality DLC films, DC, pulsed DC, and RF bias voltage is used to tune the incident ion energy (Fallon *et al*., 1993) from the plasma before arriving at the substrate. One of the disadvantages of such a technique is, however, a droplet of the cathode materials known as a macro-particle. The macro-particle is a drawback for the films used as components in optical and electronic applications which is required a smooth surface. Macro-particles in the form of neutral atoms or uncharged ions can, however, be removed by passing them into a curved magnetic filter where they can escape the coil turn out of the line-of-sight and only the charged ions are guided along the magnetic field toward the substrate. The cathodic vacuum arc with the application of a magnetic filter is called the filter cathodic vacuum arc (FCVA), as shown in Figure 2.7.
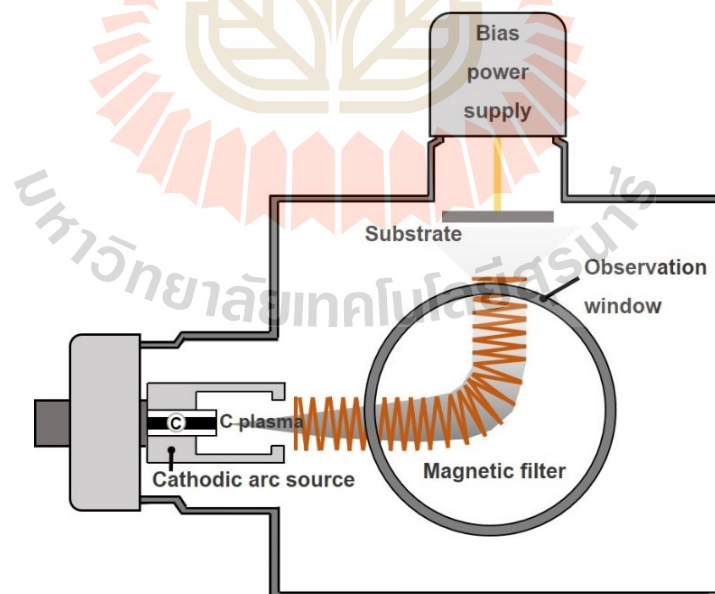
Figure 2.7 A schematic illustration of the typical FCVA system.

2.3.4 Pulsed laser ablation

In the pulsed laser ablation, a short pulse with high energy from a laser source is used to ablate or vaporize the graphite target into an intense carbon plasma plume of energetic ions toward the substrate. A variety of the ion charge states can be obtained depending on the laser's power density. Siegal *et al.* (1998); Merkulov *et al.* (1998) reported the preparation of the *ta*-C film by pulsed laser deposition. They found that the *ta*-C film's properties from the pulsed laser deposition were similar to those from the MSIBD and FCVA techniques.

2.3.5 Sputtering

The sputtering method is widely used in industrial processes due to its usefulness and flexibility. The DC or RF sputtering of a graphite target by Ar^+ plasma is a conventional sputtering in the production of many materials which can be scaled up for a large surface area. Owing to the low sputter yield of a conventional sputtering, a permanent magnetic behind the negative cathode is used to trap electrons; this so-called magnetron sputtering allows the synthesis of the films with a high deposition rate. The DC substrate bias voltage is applied to increase the ion energy and the reactive gas, of hydrogen, nitrogen, hydrocarbon, and oxygen, can be fed during the deposition process to form the *a*-C:H, *a*-C:N films or metallic oxide films, such as TiO_2 and ZnO, and the process is well-known as reactive magnetron sputtering.

2.3.6 Ion assisted deposition (IAD)

In the IAD method, the generation of the carbon species occurs at the carbon target as a result of the bombardment of the energetic ions of the Ar^+ beam (Cuomo *et al.*, 1991). For this reason, the quality of the films depends on the momentum transfer which is attributed to the energy of the carbon ions. The typical momentum

transfer acquired from the IAD method is not sufficient to promote a high energy of the carbon ions. The sp^3 content of the DLC films, therefore, is limited by this method and the substrate bias voltage is required to improve the DLC films (Lifshitz, 1996; Schwan *et al*., 1996).

2.3.7 Mass selected ion beam deposition (MSIBD)

This method is performed under several controlled parameters, such as the selection of only a single ion species, the control of the well-defined energetic ions, the deposition in ultra-high vacuum (UHV) of $10^{-6}-10^{-10}$ Torr, and the incorporation of alloying elements using the dual beam system (Grill, 1999). The ion beam is produced by an ion source from the pure graphite target before being accelerated with a high voltage in the range of 5−40 kV which provides the energy of the carbon ions between 20 and 30 keV. These ions then pass through the magnetic filter where only the carbon ions are selected and diverge at low voltage due to the Coulomb repulsive force; subsequently, they decelerate at the electrostatic lens until the energy is in the range of 5−20 keV before arriving at the substrate. For this reason, it is considered as one of the best methods to provide high-quality DLC films. Due to the high cost and low deposition rate of 0.001 Angstrom/s (Robertson, 2002), the MSIBD method is not popular in general industry.

2.3.8 Plasma enhanced chemical vapor deposition (PECVD)

One of the most used deposition methods in industrial and research applications is the RF-PECVD method. In the RF-PECVD method, there are 2 parallel electrodes which require a capacitive discharge of a 13.56 MHz to generate the surface power density of an order of $100 \, \text{mW/cm}^2$ (Donnet and Erdemir, 2008). The RF power supply is used to produce the carbon ions which involves the decomposition of

hydrocarbon precursors, such as methane (CH_4) and acetylene (C_2H_2) between the 2 electrodes. A DC or pulsed DC substrate bias power supply is frequently employed to increase the energetic carbon ions toward the substrate. A low base pressure is necessary to avoid the collision and interaction of the carbon ions in the plasma with the gas molecules which leads to the reduction of the energetic ions and the existence of contamination in the deposited films.

2.4   Applications of DLC films

The outstanding combined properties, such as high hardness and wear resistance, low friction coefficient, chemical inertness, infrared transparency, biocompatibility, good thermal conductivity, and high electrical resistivity and dielectric strength, make the DLC potentially interesting for a wide range of industrial applications (Lifshitz, 1999) as corrosion and wear-protective coatings for magnetic recording or magnetic storage media, e.g., tape-recording heads, scratch-resistant wear protective coatings, and anti-reflective coating for infrared (IR) optical equipment. In view of the low-temperature process in the deposition of films, DLC films are applied as a wear-protective coating for sunglass lenses which are made of polymers or plastics. Also, they are mostly used in wear resistance applications, such as metal bearings, gears, seals, sliding friction parts in the automotive industry, like precision gages, engine cylinders, and pistons which used self-lubricating properties and to reduce the COF, wear, and the oil consumption. Additionally, they are used as protective coatings for drills and wrought aluminum mills, plastics, copper/copper alloys, and wood. In recent years, one of the important applications of DLC films has focused on the biomedical environment as joints, implants, and artificial heart valves for which the objectives are improving

the potential performance and durability of biomedical components (McHargue *et al.*, 1991). Figure 2.8 illustrates a variety of the applications of DLC films.

(a)

(b)

(c)

Figure 2.8 The applications of the DLC films in various engineering and industrial fields, for example, (a) precision wear resistant and engineered components, (b) automotive and semiconductor components, and (c) biomedical components and goods, respectively.

2.5 Tribological property of the undoped and doped DLC films

Tribology is derived from the Greek word $\tau\rho\iota\beta o\sigma$ (tribos) which means a "rubbing" and the suffix ology meaning "the study of"; thus tribology involves the study of rubbing. In fact, the interaction of the surface in tribological applications is, however, very complicated and requires more knowledge to explain both the theoretical and practical study. Tribology is defined as the science and technology of surface interaction between 2 contact materials. Most tribological study emphasizes the performing conditions which are related to friction, wear, and lubrication. To concentrate on the tribological application, many engineers and scientists have designed and produced mechanical and engine components concerned with minimizing friction and wear rate. For this reason, a detailed understanding of tribological technology is very crucial to obtain the performance efficiency and longer durability of components. DLC is well-known as a wear-protective coating and has become increasingly prevalent in tribological fields due to its excellent properties which provide not only high hardness and wear resistance, but also low COF compared to other soft materials, such as polymer and lamellar solids, e.g., graphite and MoS_2 which have low friction and hardness or low anti-wear coatings. On the other hand, hard ceramics, such as nitrides, carbides, or some oxides have high hardness and wear resistance, but also have a high COF (~0.5) against a steel counterpart compared to those of DLC films with a typical COF of less than 0.2 in normal atmosphere (Donnet and Erdemir, 2008). From the aforementioned description, it seems to be very difficult to combine the desired properties of both high hardness and wear resistance with low friction. The combined properties are feasible by the application of DLC films which are, therefore, an ideal choice for tribological applications. The summary of the COF and wear rates

of various DLC and doped DLC films under different conditions are listed in Table 2.2 (Donnet, 1998; Ronkainen *et al*., 2003; Erdemir, 2004; Field *et al*., 2004; Fontaine *et al*., 2004; Fontaine *et al*., 2004; Gangopadhyay, 1998; Grill, 1997; Grillo and Field, 2003; Harris *et al*., 1997; Hirvonen *et al*., 1990; Klafke *et al*., 2005; Koskinen *et al*., 1994; Miyoshi *et al*., 1992; Park *et al*., 2004; Ronkainen *et al*., 1996; Ronkainen *et al*., 2001; Svahan et *al*., 2003; Tanaka *et al*., 2004; Voevodin and Zabinski, 2000; Zhang *et al*., 2003; Voevodin *et al*., 1996; Donnet and Erdemir, 2008).

Table 2.2 Summarized data of the COF and wear rate of diamond, undoped and doped DLC films tested in a variety of conditions.

Structure	Diamond	H-free DLC	hydrogenated DLC	doped DLC
	CVD diamond	*a*-C *ta*-C	*a*-C:H *ta*-C:H	*a*-C:Me *a*-C:H:Me *a*-C:H:X
Atomic structure	sp^3	sp^2 and sp^3	sp^2 and sp^3	sp^2 and sp^3
H content	−	> 1%	10−50%	
COF in vacuum	0.02−1	0.3−0.8	0.007−0.05	0.03
COF in dry N_2	0.03	0.6−0.7	0.001−0.15	0.007
COF in dry air	0.08−0.1	0.6	0.025−0.22	0.03
15−15% RH COF in humid air	0.05−0.15	0.05−0.23	0.02−0.5	0.03−0.4
15−95% RH COF in water	0.002−0.08	0.07−0.1	0.01−0.7	0.06
COF in oil	−	0.03	0.1	0.1
K in vacuum	1−1000	60−400	0.0001	−
K in dry N_2	0.1−0.2	0.1−0.7	0.00001−0.1	−
K in dry air	1−5	0.3	0.01−0.4	−
15−15% RH K in humid air	0.04−0.06	0.0001−400	0.01−1	0.01−1
15−95% RH K in water	0.0001−1	−	0.002−0.2	0.15
K in oil	−	−	−	0.1

K is wear rate ($\times 10^{-6}$ mm³/Nm) and Me = W, Ti… while X = Si, O, N, F, B…

To apply DLC films as a protective coating, the film's adhesion to the substrate, especially a steel substrate, is extremely necessary to avoid the film's delamination during service conditions. There are 2 approaches used to overcome this problem. The first involves the incorporation of dopants or additional elements, such as Si, fluorine (F), nitrogen (N), Ti, Cr, and W into the cross-linked carbon network structure. The other is the deposition of the metallic intermediate layer, such as Ti, Cr, Si, Al, and W. Especially, it is believed that the carbide-forming elements, e.g., Si, Ti, and W, can improve adhesive strength by the presence of a metallic carbide interface between the film and the substrate. These layers act as a diffusion barrier protecting the diffusion of C atoms from the DLC films into the steel substrate and enhance the bonding strength at the film/substrate interface. One reason is that the metallic layers reduce the compressive stress in the DLC structure. For example, Donnet and Erdemir, (2008); Donnet (1998) reported that a significant improvement in the adhesion of DLC films to the substrate was found to be due to the existence of an intermediate silicide film. The friction-controlling mechanisms of the films during the experiment involved the build-up of the transfer film and led to easy shear at the film/substrate interface. Also, DLC films prepared on aluminum alloy exhibited a good adhesion strength by the presence of the WC interlayer (Utsumi *et al*., 2007). Other research groups showed that the introduction of a Ti functional gradient layer led to the diminishing in the mismatch of the thermal expansion coefficient between the DLC films and the Si substrate and, thus, DLC films with good adhesion and low internal stress were obtained (Wang *et al*., 2007). From these results, it is noticed that various factors determined the tribology behavior of the DLC films, for instance, the compressive stress, the build-up transfer film within the interfacial material, the presence of the O atoms and water vapor in the

system, and the deposition conditions (Donnet, 1998). Among these, the deposition condition is very important because either good adhesion strength or low internal stress can be controlled through the deposition parameters.

In an attempt to reduce the internal stress, incorporation of alloying elements is performed. Little research work has, however, investigated the structure of doped DLC films, which will be thoroughly studied and discussed in this work. The metal atoms into the structure can exist in the form of the nanocrystals or nanoclusters of the pure metal or metal carbide (MeC) depending on the nature and amount of the metals. In the case that the metal content is too high, they will disperse and become incoherent in the cross-linked carbon network. At a very low metal content, on the other hand, metal atoms are in the form of a solid solution of the pure metal. One must, therefore, be careful in the application of the optimum concentration to avoid the formation of nanoclusters of MeC phases that provide ceramic-like properties and thus result in a high COF and wear rate. In general, the objective of the incorporation of the alloying element into the DLC structure is to reduce the internal stress and improve the film's adhesion. For example, Dai and Wang (2011) reported the dispersion and dissolution of very low metal atoms in DLC films. They found that the mechanical and tribological properties of the films were not influenced by the doping in this range, but rather it affected the reduction of the internal stress. Also, they showed that the combination of good properties of low internal stress and relatively high mechanical and wear resistance can be obtained by keeping a very low metal concentration. This was also observed by Kalin *et al*. (2010). They investigated the tribological properties and the reactivity of non-doped and Ti- and WC-doped DLC films with extreme-pressure (EP) oil additives. The XPS data indicated that all the films spontaneously reacted with the

EP oil additives without the direct sliding contact of the steel counter body and confirmed the surface oxidation during the tribological testing. The chemical formations at the worn surface in terms of the phosphorus/sulfur (P/S) ratio in the EP additives, into the boundary-lubrication for the Ti-doped DLC was 25-fold higher than for the WC-doped or non-doped DLC films. This resulted in the lowest wear rate of the Ti-doped DLC films. Another research group suggested the deposition of silver (Ag)-incorporated DLC films as hemocompatible and antibacterial coatings for biomedical applications by the medium frequency unbalanced magnetron sputtering method (Wu *et al*., 2013). The improvement of the adhesion strength due to low internal stress was observed accompanied by a slight decrease in the mechanical properties, such as hardness. The enhanced tribological properties in terms of a low COF and wear rate occurred from the low shear strength of the Ag surface clusters. Also, the wear and anti-corrosion property and bonding strength experienced a major improvement with the Ti and N co-doped DLC/micro-arc oxidation (MAO) coated on an AZ80 Mg alloy substrate. The low COF and corrosion resistance were a beneficial choice as the protective coating on Mg alloy (Yang *et al*., 2013).

According to the research described above, the deposition condition or parameters, which include the application of intermediate layers and the introduction of dopants into DLC structure, are very important factors allowing us the opportunity to modify the DLC films with the combined benefit of excellent mechanical and tribological properties and good biocompatibility for a wide range of engineering and industrial applications.

2.7 Tribological property of DLC films in various contact conditions

The tribological performance of the DLC films depends not only on the deposition conditions as described above, but also the tribological testing parameters, such as the type of lubricants, oil additives, sliding speeds, loads, counterparts, temperature, environment, and tribofilms (Donnet and Erdemir, 2008; Donnet, 1998). Knowledge of the tribological behaviors, therefore, can be explained through such parameters.

Although DLC films have a low COF under dry contact environments, most of the DLC films are still operated with a lubrication, especially a boundary lubrication (Donnet and Erdemir, 2008) by reason of the cooling of the mechanical systems and protecting the interacting surface in relative motion. Also, unlubricated DLC films exhibit inferior tribological properties and are rather sensitive to operation under humid air and atmospheric conditions. Unavoidably, the comprehension of the tribological behavior of DLC films under lubricated conditions should be emphasized to develop new DLC films for machine-component industrial applications. For a detailed understanding of the tribological behaviors under the lubrication, the Stribeck-curve is given in Figure 2.9.
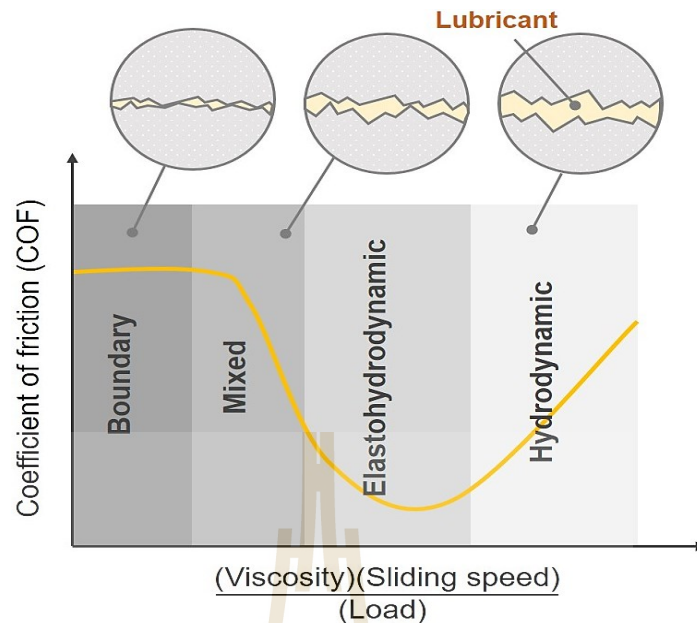
Figure 2.9 The Stribeck-curve consisting of a change in the COF and testing

conditions: $\dfrac{(\textbf{Viscosity})(\textbf{Sliding speed})}{(\textbf{Load})}$ as a function of each regime under

lubrication condition.

As can be seen in Figure 2.9, the boundary lubrication takes place at a high load
and low viscosity and sliding speed. In this regime, the surface contact of DLC films to
the body counter materials is not completely covered by the lubricants which results in
the presence of surface asperities, and thus increases the friction and wear rate during
tribological performance. To apply DLC films in this regime, therefore, the additives
should be involved, and this plays a much greater role in the formation of low friction
tribofilms within the interfacial surface. In the mixed and elastohydrodynamic
lubrication, the surface contact of 2 materials is found to be partially separated by the
lubricant. This regime promotes surface sharps and asperities, but the asperities have
less effect than the boundary lubrication. The friction and wear rate, therefore, are lower

than the boundary lubrication. Taking into account the effect of the viscosity and sliding speed on the tribological behaviors, when the viscosity and sliding speed increase, a steady-state friction and low wear rate are observed. The lowest friction and wear rate are a result of the low shear resistance of the interfacial surface, due to the presence of the fully-lubricated condition. This regime is assigned as hydrodynamic lubrication. Although this regime contributed to the fully lubricating film, there was still a risk of a lack of lubricant due to the increase in the operating temperature during the testing. The tribological parameters, such as the viscosity of lubricant, sliding speed, and applied load, therefore, should be properly controlled to obtain the best conditions for DLC films used in mechanical systems and tribological applications.

The operation of DLC films under the boundary-lubricated sliding conditions is very crucial in the tribological performance. Generally, the COF and wear rate increase rapidly due to the loss of the lubricant. For this case, the base oils, the additives, e.g. anti-wear (AW), such as molybdenum dithiocarbamate (MoDTC) and zinc dithiophosphate (ZDDP), and EP were considered for application during operation. For example, Donnet and Erdemir (2008); Donnet (1998); Liu *et al.* (1996) reported on the formation of a carbon transfer film, which is known as tribochemical film or tribofilms due to the interaction between the additives and the DLC surface during the tribological measurements. They also found that the COF and wear rate of the films were decreased by the presence of tribofilms.

There were other investigations carried out in the case of doped DLC films. For example, the WS_2 or MoS_2 layers of the tribofilms were formed on the W-doped DLC or Mo-doped DLC surface due to the added AW additives in the lubricants. The tribofilms exhibited very easy shear, thus resulting in a dramatic friction reduction of

the surface contacts (Dai *et al*., 2004; Mutafov *et al*., 2014). In addition to the lubrication, the operating temperature and sliding load can influence the friction and wear rate of doped DLC films. The increase in the operating temperature and sliding load during tribological performance leads to the rapid formation of the tribofilms and/or graphitization process at the surface contact. This results in the reduction in the friction and wear rate due to the low-strength atomic carbon interlayer or shear layer compared to normal conditions. With the long duration of testing, the tribofilms are thicker and lead to lower steady-state friction. Importantly, the appropriate deposition conditions and testing parameters should be controlled to acquire a good tribological performance of DLC films in many conditions.

2.8 Friction and wear behavior of DLC films

The study on the friction and wear behavior of DLC films depends on the relationship of the type of DLC structure and the performance environments, such as a vacuum, dry or inert conditions, and humid air, which can be explained by Figure 2.10. The investigation of the friction and wear behaviors which are surrounded by dry air and an inert environment is probably different for the hydrogenated DLC films, such as the *a*-C:H and *ta*-C:H films and H-free DLC films, such as the *a*-C and *ta*-C films. In the case of the hydrogenated DLC films, the COF is quite low in the range of 0.001−0.22 in a vacuum and dry condition, and increases to between 0.01−0.7 in humid air and a water tested environment. The analogous behavior of the friction is observed for the H-free DLC films in humid air. The H-free DLC films have a lower COF and wear rate in oil and humid air environment conditions than those of the hydrogenated DLC films, but exhibit a higher friction in a dry and vacuum condition. The phase

transformation from tetrahedral sp^3 bonding to graphite-like sp^2 bonding, the so-called graphitization process, is one of the mechanisms in the tribological behavior which leads to an increase in the friction and wear rate of the DLC films. The graphitization process is caused by thermal accumulation due to the sliding-induced heat, which results in the release of the sp^3 hybridized bonds in the DLC films. The surface roughness also has an effect on the friction and wear performance of the DLC films, in addition to the testing environment. The DLC films with a rougher substrate reveal a higher friction and wear rate compared to those with a smoother substrate (Andersson *et al*., 2003).

The low friction of the hydrogenated DLC films in a dry and inert environment is derived from the presence of the H-terminated dangling bonds and transfer layer in terms of a weak van der Waals force at the surface contact between the films and body counterparts. It is, however, found to be disturbed by water vapor or oxygen molecules in humid oxygen environments, which results in the removal of the H and the increase in the friction and wear rate. The friction and wear rate of the H-free DLC films, on the other hand, are more stable and lower in humid environments compared to those of the hydrogenated DLC films. The highly sp^3 hybridized bonds exhibit lower friction and wear rate, especially for the *ta*-C films compared to the *a*-C films with a dominant sp^2 content (Ronkainen and Holmberg, 2008; Ronkainen *et al*., 1994). One reason for the reduction in the friction and wear rate for the H-free DLC films is attributed to the presence of the graphitic transfer films and the water-terminated dangling bonds during tribological motion under humid air environments. The friction and wear rate in turn increase in dry and inert environments due to the lack of humidity (Voevodin *et al*., 1996; Gardos, 1994). In summary, the friction performances of the hydrogenated and

H-free DLC films are quite analogous, but in the case where the tribological interaction is subjected to water vapor and gas adsorption in humid environments, the hard H-free DLC films exhibit better anti-wear property, especially the *ta*-C films.
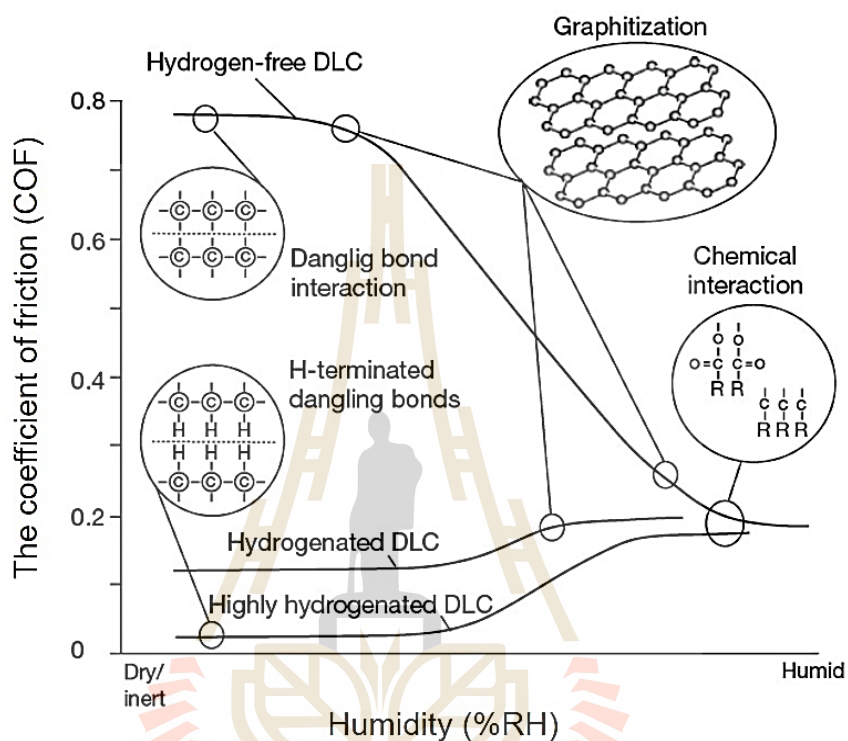
Figure 2.10 A variation of the COF in different humidities of the hydrogenated and H-free DLC films and the mechanisms involved in tribological performance (Ronkainen and Holmberg, 2008).

2.9   Thermal effects on tribological behavior of DLC films

It should be emphasized that the tribological performances of both hydrogenated and H-free DLC films are diminished at elevated temperatures. This is due to the dehydrogenation of the C—H bonds in the hydrogenated DLC structure or desorption of water and the humid environments surrounding H-free DLC films during

the tribological performances. The operating temperature has a direct effect on the stability of the H in the cross-linked carbon network structure, which becomes an important factor in determining a number of the sp^3 configurations in hydrogenated DLC films. Since the presence of the H in the hydrogenated DLC films sustains the sp^3 carbon bonding, the loss of the H at high temperature performance results in deterioration of the properties of the hydrogenated DLC films, particularly the mechanical and tribological properties. The dehydrogenation of the hydrogenated DLC films is found to take place in the temperature range from 300 to 600°C depending on the deposition parameters and the tribological testing conditions. In a similar effect to that of the temperature, the wear rate of the hydrogenated DLC films increases dramatically due to the graphitization process at a higher operating temperature. Conversely, the increased sliding velocity and sliding distance during test conditions enhance the formation of the carbonous transfer layer on the sliding contact which leads to the reduction of the friction (Erdemir *et al*., 1993; Meletis *et al*., 1995; Miyoshi *et al*., 1992). Further Ronkainen *et al*. (1992) observed the enhancement of transfer layer thickness at a high load and sliding speed. The thicker transfer layer reduced the wear rate of the hydrogenated DLC films. Moreover, the formation of the graphitization was observed to reduce the friction of the hydrogenated DLC films (Jahanmir *et al*., 1989). Generally, the graphitization formation is caused by the wear- and friction-induced heating. Also, the strain energy or work hardening accumulated during the tribological testing can also be the reason for this process (Liu *et al*., 1996). However, the graphitization rate reduction was likely to occur at a high humidity level, which has a negative effect on the friction performance. The dramatic increase in wear rate and graphitization at a higher temperature can lead to the rupture of the hydrogenated DLC

films (Erdemir and Fenske, 1996; Liu *et al*., 1999). With the rising temperature, the friction reduction was observed, but the wear resistance of the films was lower. The increased wear rate of the hydrogenated DLC films as a function of the annealing temperature is shown in Figure 2.11.
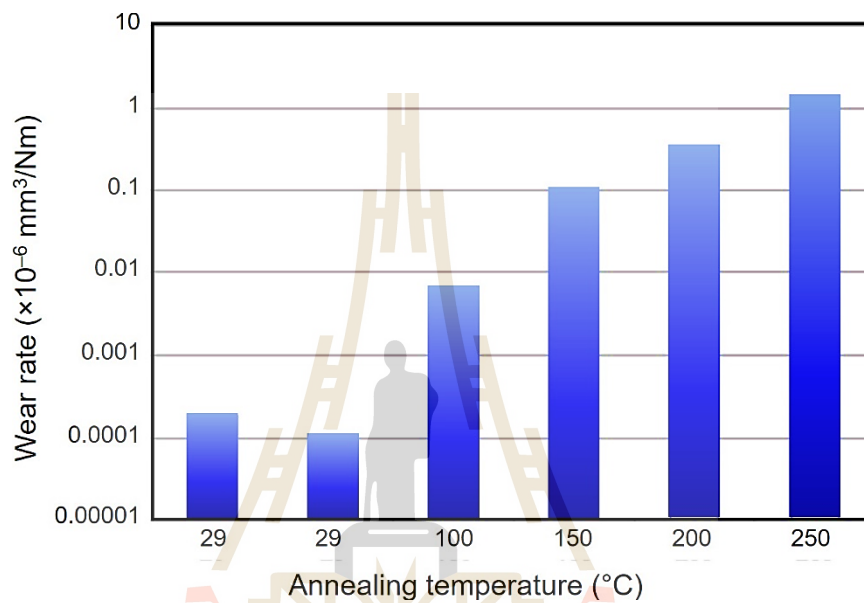
Figure 2.11 The evolution of the wear rate of the hydrogenated DLC films on the annealing temperature modified from Erdemir and Donnet (2005).

Many research groups have attempted to overcome this limitation by incorporating the alloying elements into the hydrogenated DLC films. In this case, the alloying elements which are generally used are Si, F, N, and metals (Ronkainen and Holmberg, 2008). According to Er and So (2014), the Si-doped *a*-C:H films prepared on Si wafer by the reactive sputtering method had a good thermal stability due to the formation of the Si—O and Si—C bonds within the *a*-C:H structure. The COF of the Si-doped DLC films was observed to be lower with the presence of the SiO_2 transfer layer on a worn surface. Further Choi *et al*. (2007) observed that DLC films with high

Si contents showed a slight decrease in hardness compared to the undoped DLC and the DLC with low Si contents after thermal annealing. This was because of the formation of Si oxide on the DLC surface. The DLC films with high Si contents still maintained the sp^3 bonded carbon after thermal annealing. Also, the low COF and wear rate of the annealed Si-doped DLC films were acquired due to the low shear strength of the graphite transfer layer and thick and stable Si oxide layer.

In comparison with the hydrogenated DLC films, the H-free DLC films have a higher oxidation or thermal stability. Especially, for the thermal annealing in a vacuum, it was found by McKenzie *et al*. (1994) that the *ta*-C films deposited by vacuum arc discharge remained a carbon conversion from the sp^3 to sp^2 hybridized carbon up to 727°C. This was attributed to a tiny amount of the H content and high sp^3 hybridized carbon of the *ta*-C films. Similar effects were found by Ronkainen *et al*. (1996). They reported that *ta*-C films prepared by the pulsed laser ablation method had a good thermal resistance in a UHV up to 627°C. The thermal annealing of the H-free DLC films at high temperature in a range of 400–500°C in the air was, however, caused by the increase in the COF and the wear rate. This led to the desorption of the water vapor and humidity level between the films and body counter contact, thus resulting in the reduction of the graphitic transfer films and the water-terminated dangling bonds (Leng *et al*., 2003; Robertson, 2002).

Nonetheless, there are methods used in the improvement of thermal stability of DLC films, for example, the incorporation of metals and/or nanocomposite structure. Abou Gharam *et al*., 2011 observed a reduction in the COF and wear rate at a temperature above 400°C of the W-doped DLC films caused by the formation of the transferred layer of the W-rich oxide on the W-doped DLC surface and 319Al

counterface. Further Zhang *et al.*, 2006 found that the thermal stability and hardness of the nanocomposite nc-TiC/*a*-C(Al) films were stable up to 600°C due to the formation of the TiC nanocrystallites in the matrix, and in the case of pure DLC films, they began to be thermally unstable at an annealing temperature beyond 300°C, as demonstrated by the increase in the I_D/I_G ratio from the Raman analysis. The degradation of the pure DLC films due to the thermal effects was caused by the graphitization, which resulted in a hardness reduction and the loss of film thickness by the oxidation of carbon atoms into the gas phase, for example, the CO_2. The presence of the Ti and Al oxides at high temperatures for the nanocomposite nc-TiC/*a*-C(Al) films was, however, observed to act as a barrier layer to prevent the loss of film thickness.

As described above, the thermal effects on friction and wear performance of the DLC films in tribological performance depend strongly on the surrounding environments, such as the humidity level. The H-free DLC films are sensitive to use in dry and inert environments because they require water molecules or hydrocarbon species to form the water-terminated dangling bonds and graphitic transfer layers. In contrast, the hydrogenated DLC films exhibit better performance in a dry and inert environment, but they are rather sensitive to being used under a humid and elevated temperature because of the dehydration of the hydrogen atoms in the tribocontact. The applications of DLC films in an inappropriate environment, thus, can result in reduced friction and wear performance. A similar friction performance of both the hydrogenated and H-free DLC films was found; however, the *ta*-C films still have the best wear resistance in a normal atmosphere (Ronkainen and Holmberg, 2008).

2.10 Electrochemical corrosion

The corrosion of DLC films is becoming a major issue which occurs generally in a wide range of engineering and industry applications, particularly in mechanical and tribological applications surrounded by aqueous fluids and/or lubrication conditions. The approach to overcome this issue is based on an understanding of the fundamental concepts of corrosion which will be described in detail in the following section.

The corrosion process occurs spontaneously in nature resulting in the deterioration of metals through chemical and/or electrochemical reactions to the surrounding environments. Other physical damage, for example, by friction, wear, erosion, and fretting are not considered as a type of damage in the corrosion process. The corrosion process is, however, likely to involve physical damage, which is assigned by the terms erosion-corrosion, corrosion wear, erosion-corrosion wear, and fretting corrosion. In addition, the term corrosion can be used for nonmetals, for instance, plastics, wood, and concrete, but the rust found during the corrosion process like in iron or iron-base alloys is not to be found for those nonmetals. Three are 3 important reasons to study the corrosion behavior of the materials. The first is about an economic reason which is in agreement with the objective of this study to reduce loss or dissolution of materials from corrosion due to the electrochemical reaction with environments. The second reason involves safety through improvement in the design of suitably functional equipment, e.g., boilers, airplanes, nuclear-power plants, turbine blades, etc. used in corrosive environments for which suggestions are made. The final reason is about conservation. In this case, a reduction in the use of resources and materials is proposed which corresponds to energy and water preservation in production.

The corrosion process of metals depends greatly on the surrounding environment and operating temperatures. Typically, the corrosion process can be classified into 2 main groups, e.g., the oxidation and electrochemical corrosion known as dry or high temperature corrosion and wet corrosion, respectively. In this thesis, the electrochemical corrosion of pure DLC and Ti-doped DLC films will be described in detail, while the high temperature corrosion of the films is investigated through the films' thermal stability; the basic principle of the thermal stability of films is described in section 2.9 on the thermal effects on the tribological behavior of DLC films.

2.10.1 Electrochemical corrosion

The deterioration of metals by electrochemical reaction in aqueous environments is defined as electrochemical corrosion. The mechanisms of electrochemical corrosion are based on the transport reactions of electrons, atoms, and molecules at charged interfaces, which eventually lead to the degradation of conductive substrates (Stansbury and Buchanan, 2000), as schematically illustrated in Figure 2.12 (Fernandez-Solis *et al.*, 2016). According to Figure 2.12, the adsorbed molecules of the solvent and adsorbed species are formed as structured layers near the interface. The group of adsorbed species moving near the interface with the distance (d_1) is called the inner Helmholtz layer. The adsorbed species moving away from the interface with the distance (d_2) is designed as the outer Helmholtz layer. The other distribution of a 3-dimensional form of adsorbed species due to thermal motion is referred as the diffusion layer, which is based on the explanation of the Poisson-Boltzmann equation (Lyklema, 1995). The transportation of adsorbed species in the electrochemical reaction causes the dissolution of the metals in the form of corrosion products or rusts. The rate of the corrosion and related corrosion parameters can be subsequently examined using a

potentiostat analyzer, which will be explained in this thesis. Furthermore, several research groups have been interested in the effects of fluctuation adsorbed species during the electrochemical corrosion processes and have investigated their changes (Okamoto and Onuki, 2011; Dreyer *et al.*, 2014; Lyklema, 2009; Netz and Orland, 2000; Netz, 2001).
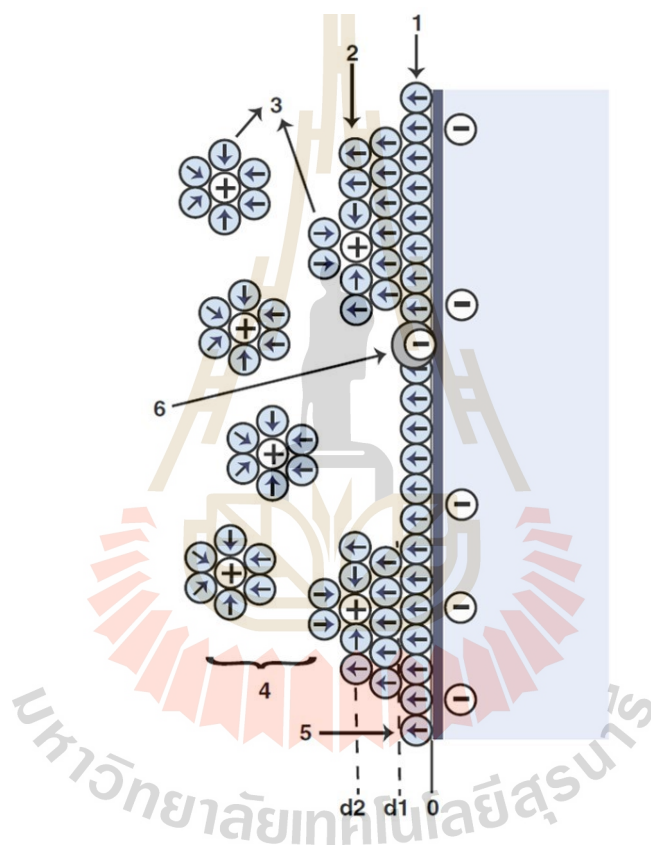
Figure 2.12 A schematic diagram of the structured layers at the solid/solution interface. The numbers 1, 2, 3, 4, 5, and 6 represent the inner Helmholtz layer, outer Helmholtz layer, solvated ions (cations), diffusion layer, electrolyte solvent, and specifically adsorbed ions, respectively, adopted from Fernandez-Solis *et al*. (2016).

2.10.2 Electrochemical analytical techniques

The electrochemical analytical techniques, such as potentiodynamic polarization and electrochemical impedance spectroscopy are widely used at present and allow us to have considerable information on electrochemical corrosion behavior. A concise overview of the potentiodynamic polarization technique is provided and a method of achieving the electrochemical corrosion parameters is proposed. A description of the experimental set-up of the potentiostat analyzer and related electrodes is shown in Figure 2.13. The electrochemical corrosion parameters, such as the corrosion rate (CR), corrosion potential (E_{corr}), corrosion current density (i_{corr}), porosity (P), and protective efficiency (P_i) can be obtained by potentiodynamic polarization measurement based on the current-potential relations. In recent years, the rate of corrosion acquired from the traditional method, such as the weight loss method, has been replaced by this method due to its fast and accurate technique. In the potentiodynamic experiment, as the DC potential is continuously scanned in a potential sweep, the scan potential rate is acquired and the flowing current at the specimen is recorded. The electrochemical process is associated with an anode, a cathode, and electrolyte or electrical conduction path, such as a salt-bridge probe. The electrolyte or ionic conduction path is frequently used to connect the counter and working electrodes, while the salt-bridge probe is employed to link between the polarization and reference cells, as schematically shown in Figure 2.13.
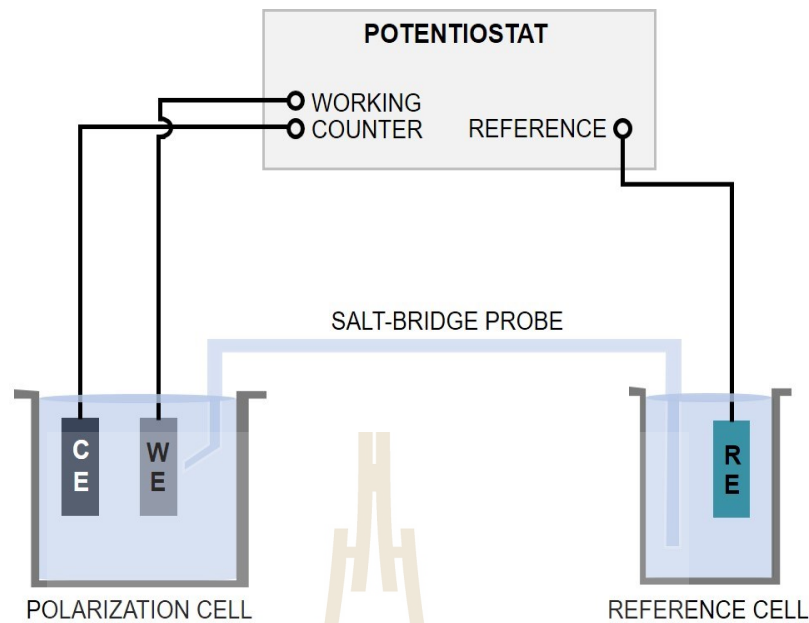
Figure 2.13 A schematic diagram of the potentiostat analyzer and a typical three electrode standard for a potentiodynamic polarization experiment modified from ASTM G5-14.

In the measurement, the degree of the driving force of the electrochemical reactions can be controlled using a potentiostat analyzer (Enos and Scribner, 1997). During the transfer of electrons in the system, electrochemical reactions occur at each electrode. Typically, the anode is designed as a negative electrode, while the positive electrode is obtained from the cathode. The presence of oxidation at the anode, e.g., the metal or specimen can be given by the following reaction:

$$M \rightarrow M^{x+} + xe^-,$$
(2.1)

where M is the pure metal or alloy, M^{x+} is the metal ions, and xe^- is the number of electrons transferred in the system. The other electrochemical reactions take place in addition to the oxidation, for example, oxygen production:

$$2OH^- \rightarrow \tfrac{1}{2}O_2 + H_2O + 2e^-, \tag{2.2}$$

where OH^- is the hydroxide ions. At the cathode surface, the oxide or hydroxide reductions occur possibly in aqueous solutions by this expression:

$$M_x(OH)_y + ye^- \rightarrow xM^+ + yOH^-. \tag{2.3}$$

The water reduction can also be present when the negative potential is high enough, as addressed by:

$$H_2O + e^- \rightarrow H + OH^-. \tag{2.4}$$

For interpretation of the electrochemical data, a semi-log scale of the potential against the logarithmic of the current, typically the current density: the current per unit area exposed to the electrolyte, is plotted, which is well-known as the potentiodynamic polarization curve, as shown in Figure 2.16. This potentiodynamic polarization curve is conducted to achieve the electrochemical corrosion parameters, which provide abundant information on the electrode processes. A standard 3 electrode system used in the potentiodynamic polarization includes: the graphite rod as the counter electrode (CE), the specimen as the working electrode (WE), and the Ag/AgCl electrode as the reference electrode (RE). A schematic diagram of the experimental set-up of the potentiostat analyzer and 3 electrode standard system is shown in Figure 2.13.

Two scan features are used in the potentiodynamic polarization experiments which are the anodic and cathodic potentiodynamic polarization scans (Enos and Scribner, 1997). Figure 2.14 demonstrates the anodic potentiodynamic polarization curve, which is mostly used in the electrochemical measurements. As seen from the figure, the curve starts from point ① and finishes at point ②. When the potential is applied in the positive region toward point A at the open circuit potential (OCP) where the total anodic current and the total cathodic current are equal, the measured current value or the sum of the anodic and cathodic reaction rates is 0. As the potential increases continuously toward point B in the active region, the oxidation reaction of metals is notable, as previously demonstrated in Equation 2.1. As there is a further increase in the applied potential, the current does not increase at the C region, which is attributed to the passivation potential. In the D region, as the potential increases, the current, in turn, decreases due to the formation of passivity called a passive region, as seen in the E region. The current at this region is referred to as the passive current density. As the applied potential increases further toward the positive direction at point F, the current starts to increase greatly in the G region, which is attributable to the breakaway potential or transpassive dissolution. In the G region, some metal exhibits pitting corrosion. Some alloy with a stable protective oxide, for example, cobalt, on the other hand, show the oxygen evolution (Enos and Scribner, 1997).
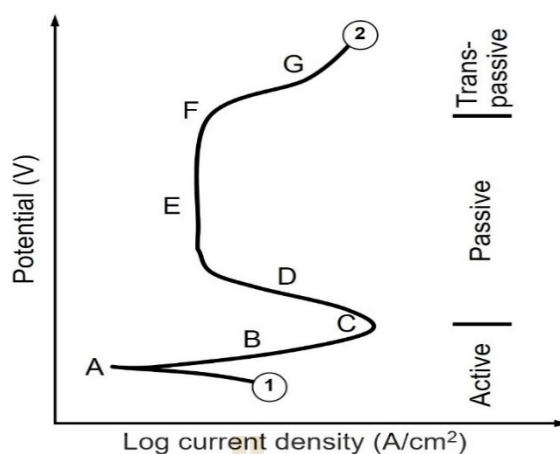
Figure 2.14 An anodic polarization curve modified from Enos and Scribner (1997).

The cathodic potentiodynamic polarization scan is shown in Figure 2.15. The potential is scanned from point ① and decreases in the negative direction toward point ②. The OCP occurs on the point A. As the applied potential decreases toward the B region, the oxygen reduction reaction is dominant. This reaction depends strongly on the pH solution and the concentration of dissolved oxygen. At the potential decreases continuously, the current is limited and does not change in the C region. This limitation is controlled by a charge or mass transport which relates to the concentration and diffusivity of the species in the solution. As the applied potential further decreases, on the other hand, a degree of the driving force, in turn, increases and leads to the occurrence of reactions in the D and E regions, for example, hydrogen evolution or water reduction reaction, as previously described by Equation 2.4.
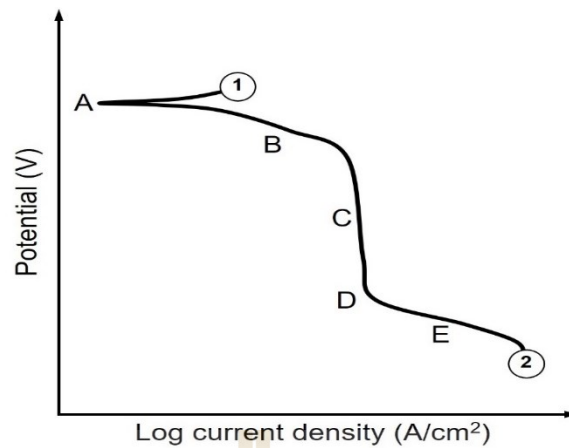
Figure 2.15 A cathodic polarization curve modified from Enos and Scribner (1997).

For in-depth understanding the electrochemical reactions, the potentiodynamic polarization curve with the active-passive type of iron is considered, as revealed in Figure 2.17, modified from Fernandez-Solis *et al.* (2016). There are 6 important reactions that occur in this system from the following equations (Fernandez-Solis *et al.*, 2016):

$$Fe \rightarrow Fe^{2+} + 2e^-, \tag{2.5}$$

$$3Fe + 4H_2O \rightarrow Fe_3O_4 + 8H^+ + 8e^-, \tag{2.6}$$

$$2Fe_3O_4 + H_2O \rightarrow 3Fe_2O_3 + 2H^+ + 2e^-, \tag{2.7}$$

or

$$2Fe^{2+}3H_2O \rightarrow Fe_2O_3 + 6H^+ + 2e^-, \tag{2.8}$$

$$(2-x)Fe_2O_3 + 3xH_2O \rightarrow 2Fe_x^{6+}Fe_{(2-2x)}^{3+} \square_x O_3 + 6xH^+ + 6xe^-, \tag{2.9}$$
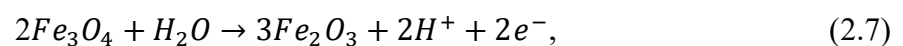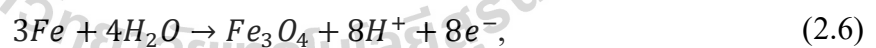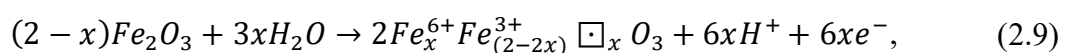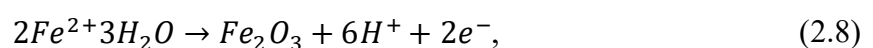
where x is the fraction of the iron lattice sites and $\square$ is the vacancy in the iron lattice sites.

$$Fe_2O_3 + 5H_2O \rightarrow 2FeO_4^{2-} + 10H^+ + 6e^-, \qquad (2.10)$$
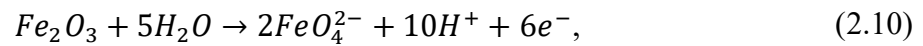
As the applied potential increases progressively, the iron begins to corrode in the A region in the active dissolution, as shown by Equation 2.5. When the potential increases further, the passivity is formed on the iron surface. At this point, the transformation of the active to passive type can be observed at point B, which is attributed to a primary passivation potential (E_{pp}). The measured current at this point is designed as the critical current density (i_{crit}). While the potential increases continuously, the current is found to decrease in the C region. This is due to the formation of the passivity, as illustrated by Equation 2.7. As the potential increases toward the positive direction, no change in the corrosion rate is observed in the D region due to the presence of a stable passivity and the current at this region is assigned as the passive current (i_p). However, at the high potential above the D region, the breakdown of the passivity has taken place accompanied by the rapid increase in the current and corrosion rate. The potential range in the E region is ascribed to the transpassive potential (E_t). In this region, the dissolution of iron into the ions is observed and is presented by Equation 2.8–2.10. Also, the oxygen evolution has taken place at a higher potential range.
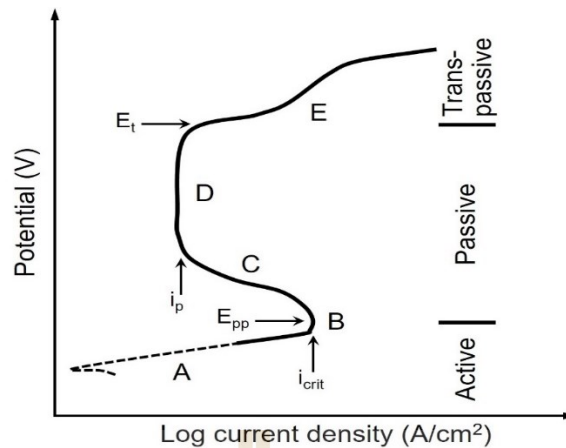
Figure 2.16 Potentiodynamic polarization curve of iron in an aqueous solution of pH = 7.

2.10.3 Interpretation of electrochemical data

The corrosion current density (i_{corr}) and corrosion rate (CR) are very important parameters in the electrochemical corrosion measurement, which can be acquired through 2 significant methods, i.e., the linear polarization resistance and the Tafel slope extrapolation method (ASTM G5–87, 1987; ASTM G59–97, 1994). The measured current achieved from the potentiodynamic experiment is the total anodic current (I_{corr}), which is typically converted into the corrosion current density by this expression:

$$i_{corr} = \frac{I_{corr}}{A}, \tag{2.11}$$

where i_{corr} is the corrosion current density (A/cm^2), I_{corr} is the total anodic current (A), and A is the exposed surface area (cm^2). In the case of alloys or metals with multiple valences, the equivalent weight (EW) is given by:

$$EW = \left(\Sigma \frac{f_i n_i}{W_i} \right)^{-1}, \tag{2.12}$$

where f_i is the mass fraction, n_i is the valence, and W_i is the atomic weight of each component. According to Faraday's law, the CR can be calculated from the relationship of the i_{corr} by the following equation:

$$CR = K \frac{i_{corr}}{\rho} EW, \tag{2.12}$$

where CR is the corrosion rate in units of mm/year, K is the constant value (3.27×10^{-3}), and ρ is the density of the alloys or metals.

The linear polarization resistance (LPR) method is used to assess the CR of alloys or metals in a low potential range of approximately ± 10 mV near the OCP. In the LPR measurement, the potential is scanned in a potential range between ± 5 and ± 25 mV. With a small potential range, the measured current is a relatively linear line, as shown in Figure 2.17.
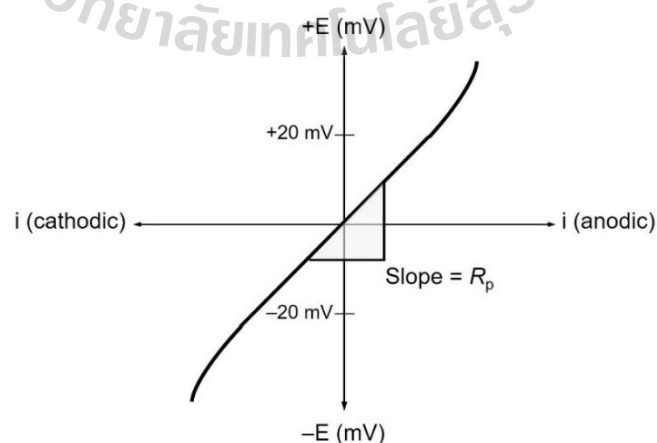
Figure 2.17 Linear polarization resistance curve modified from Enos and Scribner (1997).

The calculated *CR* value acquired from this method is in units of milli-inches per year (mpy) (ASTM G102–89, 1999). The polarization resistance (R_p) of metals based on Ohm's law: potential V = IR is expressed by the ratio of the applied potential (ΔE) to the measured current (Δi). The i_{corr} that relates to such a ratio can be obtained via the following equation:

$$R_p = \frac{\Delta E}{\Delta i} = \frac{\beta_a \beta_c}{2.303 i_{corr}(\beta_a + \beta_c)},$$ (2.13)

where β_a and β_c are the anodic and cathodic Tafel slopes acquired from the Tafel plot (V/decade), respectively.

Rearrangement of Equation 2.13 gives:

$$i_{corr} = \frac{\beta_a \beta_c}{2.303(\beta_a + \beta_c)} \frac{\Delta i}{\Delta E}.$$ (2.14)

The *CR*, therefore, can be calculated by the relationship of the i_{corr} through Equation 2.12. The other method that is extensively used to assess the *CR* is the Tafel slope extrapolation. The reactions in this method are typically controlled through a charge or mass transfer at less than the limiting rate in a potential range of approximately ±300 mV between the anodic region (positive-going potential) and cathodic region (negative-going potential), as illustrated in Figure 2.18.
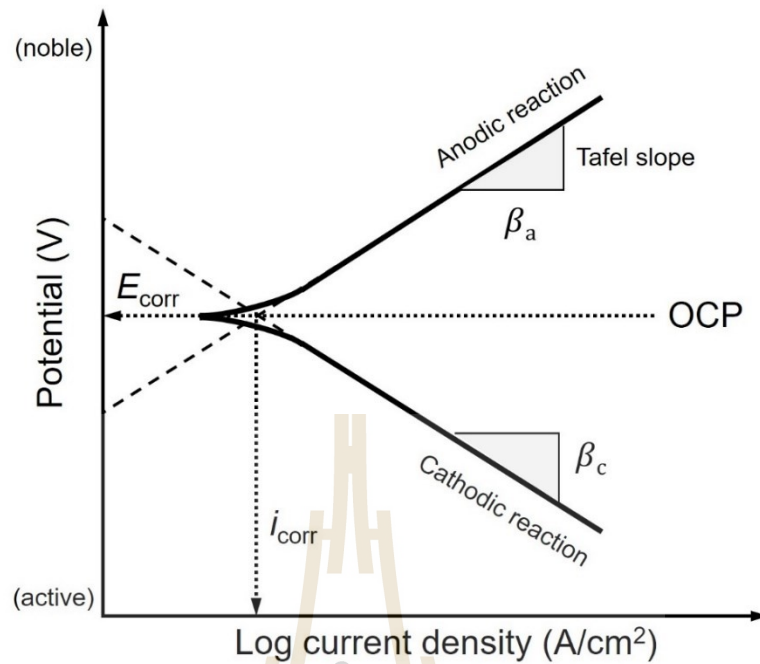
Figure 2.18 Tafel slope extrapolation modified from Enos and Scribner (1997).

The i_{corr} can be achieved through a relationship of the overpotential (η) as follows:

$$\eta = \beta\log\frac{i}{i_o},\qquad(2.15)$$

where β is the Tafel slope, i is the current density, and i_o is the exchange current density.

The Tafel slope extrapolated for the anodic and cathodic reactions at the OCP can be acquired from the linear (dashed line) responses of the polarization curve where the anodic reaction is equal to the cathodic reaction. At this point, the current density is projected to the i_{corr} and the potential is referred to the E_{corr}, as shown in Figure 2.18. The *CR* can be obtained by replacing the i_{corr} into Equation 2.12.

2.11 Stainless steel

Stainless steel is versatile and widely used in engineering and industrial applications due to its anti-corrosion property, high toughness and strength, and mechanical formability (Francisco *et al*., 2015; Marshall, 1984). The requirement of excellent hardness and wear resistance, low COF, and anti-chemical property, especially in chloride ions is, however, very necessary for stainless steel in advanced applications. To overcome these drawbacks, the surface modification technology, for example, DLC films, is considered to be a good choice as a protective coating.

A brief history of stainless steel reveal that it was discovered in 1913 by a metallurgist named Harry Brearley while he was searching for ways to improve the alloy to protect cannon bores. He found that the introduction of approximately 12.8% Cr into the low carbon steel resulted in stain resistance, and this alloy was designed as the first ever stainless steel (Cobb, 2010). The stain resistance is achieved by means of the formation of a transparent and adherent Cr-rich oxide film, which cannot be observed with the unaided eye. This oxide film resists corrosion in many environments, for example, water, atmosphere, food, and alkalis. Further research showed that the oxide film could heal itself instantly when it was surrounded by oxygen. Stainless steel is defined as a steel alloy, which contains a minimum of 10−12 wt.% Cr for protection against the formation of rust. The addition of other elements, such as Ni, manganese (Mn), molybdenum (Mo), Cu, Ti, Si, etc. is performed to enhance particular characteristics, e.g., ductility, scaling and corrosion resistance, and high-temperature strength. Typically, stainless steel can be classified into 5 important families depending on their structures:

(i) Austenitic stainless steel with the austenitic matrix,

(ii)   Ferritic stainless steel with the ferritic matrix,

(iii)   Martensitic stainless steel with the martensitic matrix,

(iv)   Precipitation hardening stainless steel with the addition of Al, Mg, Ni, Ti, etc. to form the precipitate phase in the matrix resulting in the improvement of the yield strength, and

(v)   Duplex stainless steel with a mixture of austenitic and ferritic grains providing attractive properties. Figure 2.19 illustrates the beneficial relationship between the chemical composition and properties of the stainless steel family.
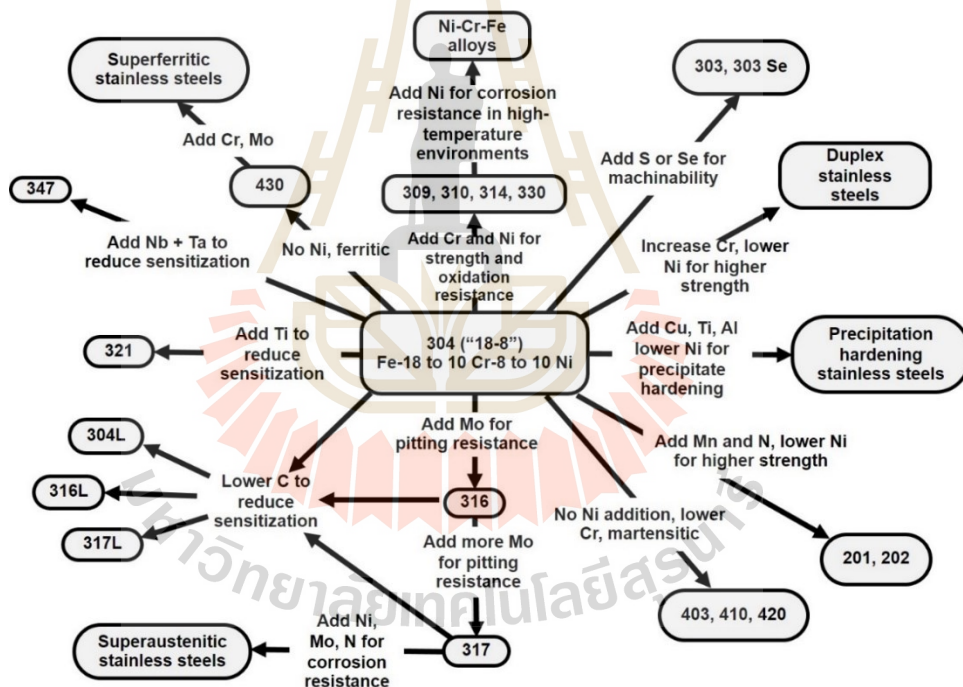
Figure 2.19 Chemical composition and the corresponding properties of stainless steel family modified from Beddoes and Parr (1999).

As seen in Figure 2.19, AISI 304 austenitic stainless steel, as a Fe-Cr-Ni alloy, is generally considered as the most austenitic stainless steel, which is the most versatile

and is typically used in many industrial applications; it accounts for more than 70% of all the stainless steel in the world due to its good formability and weldability, excellent corrosion resistance in many environments, and high yield strength. Cr is the most important element in the stainless steel in developing the passive Cr-oxide film on stainless steel surface. At least 10−12%Cr in the stainless steel can form the protective oxide thin film which is sufficient for the scaling resistance. Ni is a key element that is used to improve the ductility and the corrosion or scaling resistance. In this thesis, type 304 stainless steel was selected to be the substrate before DLC deposition. Table 2.3–2.5 (Beddoes, and Parr, 1999; Long Products Stainless Steel Grade Sheet (North America Stainless, 2010); Stainless Steel 304 1.4301 (ThyssenKrupp Materials, 2017)) show the chemical composition and the mechanical and physical properties of AISI 304 austenitic stainless steel, respectively.

Table 2.3 Chemical composition of AISI 304 austenitic stainless steel.

AISI 304	Chemical composition (wt.%)						
	C	Cr	Ni	Mn	Si	S	P
Min.	−	17.50	8.00	−	−	−	−
Max.	0.07	19.50	10.50	2.00	1.00	0.015	0.045

Table 2.4 Mechanical properties of AISI 304 austenitic stainless steel.

Type	Tensile strength (MPa)	Proof stress (MPa)	Elongation (%)	Reduction of area (%)	Hardness (HRB)
AISI 304	520–720	210 min	45 min	70	81

Table 2.5 Physical properties of AISI 304 austenitic stainless steel.

Density (kg/m^3)		8000
Modulus of elasticity (GPa)		193
Specific heat capacity (J/Kg K)		500
Thermal conductivity at 100°C (W m/K)		16.2
Mean coefficient of thermal expansion (10^{-6}/^{o}C) at	0−100 ^{o}C	17.2
	100−315°C	17.8
	315−538°C	18.4
Electrical resistivity ($\mu\Omega$m)		0.072
Melting point (^{o}C)		1450
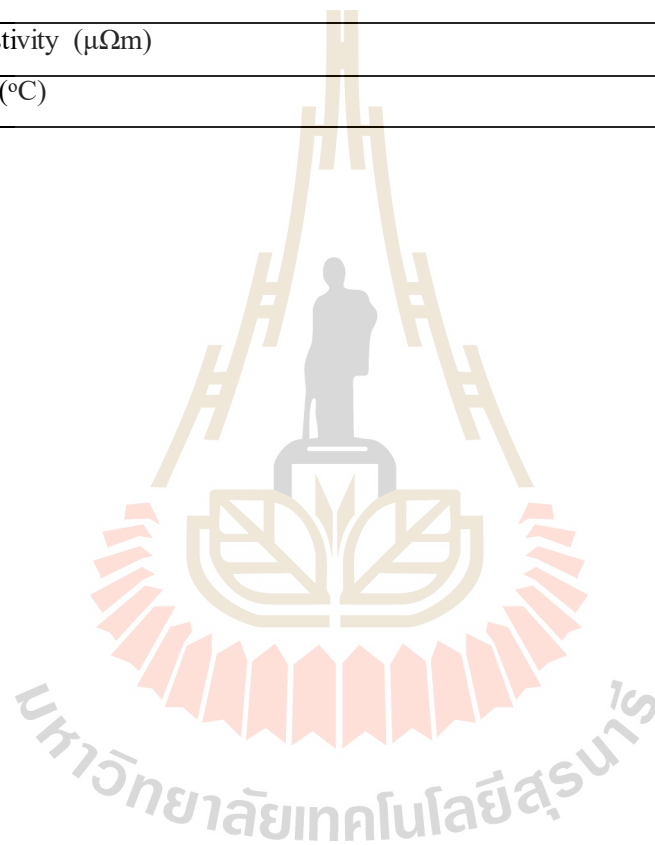
CHAPTER III

EXPERIMENTAL PROCEDURES

The deposition and analysis of the undoped (pure) DLC and Ti-doped DLC films are described in detail. This chapter has been divided into 2 important sections regarding the preparation of the DLC film by the pulsed two-FCVA technique and the characterization of the DLC films by many analytical techniques which can be cataloged into 3 sub-sections. The first sub-section involves the microstructure, bonding configuration, and chemical composition analysis. The second is an investigation in regard to the electrochemical corrosion analysis. The final sub-section involves the mechanical and tribological analysis.

3.1   Preparation of DLC films

In this PhD thesis, pure DLC and Ti-doped films have been successfully synthesized by pulsed two-FCVA deposition. The pulsed two-FCVA system was constructed in the laboratory located at the Synchrotron Light Research Institute, SLRI, Nakhon Ratchasima, Thailand, as demonstrated by Figure 3.1(a) and 3.1(b). The pulsed two-FCVA system has 2 separate cathodic arc sources and its own macro-particle filter, which can be individually or simultaneously controlled by an arc plasma power supply connected to a personal computer-controlled system with the Arduino micro-controller board and open-source Arduino software (IDE). This system allows many potential advantages, for example, the incorporation of alloying elements into the DLC structure and/or the deposition of the multi-layered structures via the controllable deposition

parameters, such as the duty cycle, pulse repetition rate or arc frequency, arc voltage, and arc current.

Two sets of the DLC films were prepared for this Ph.D. thesis. For the first set, all the DLC films were deposited on the Si wafer to avoid the surface roughness effect of the substrate. In this preliminary study, the performance of the pulsed two-FCVA system and the optimum deposition condition were explored through the characterization of the microstructure and mechanical, physical and optical properties as a function of the substrate negative DC bias voltages (V_{bias}). The DLC films deposited at 0.0, 0.5, 1.0, and 1.5 kV were frequently designated as DLC-0, DLC-1, DLC2, and DLC-3, respectively. The second set dealt with the deposition and characterization of the Ti-doped DLC films. The different concentrations of the Ti atoms in the Ti-doped DLC films were controlled by adjusting the applied arc voltages of 0.65 and 0.8 kV connected to a Ti cathode. The samples deposited at different arc voltages were denoted as Ti-DLC1 and Ti-DLC2, respectively. Both the Si wafer and AISI 304 stainless steel were used as the substrate and the films were prepared under the best deposition condition acquired from a preliminary study. The films deposited on the Si substrate were used for the microstructure, bonding configuration, and chemical composition analyses, while the others on the AISI 304 stainless steel substrate were used for the nano-mechanical, nano-tribological, and electrochemical corrosion analyses. The microstructure and properties of the pure DLC films were also investigated in comparison with those of the Ti-doped DLC films.
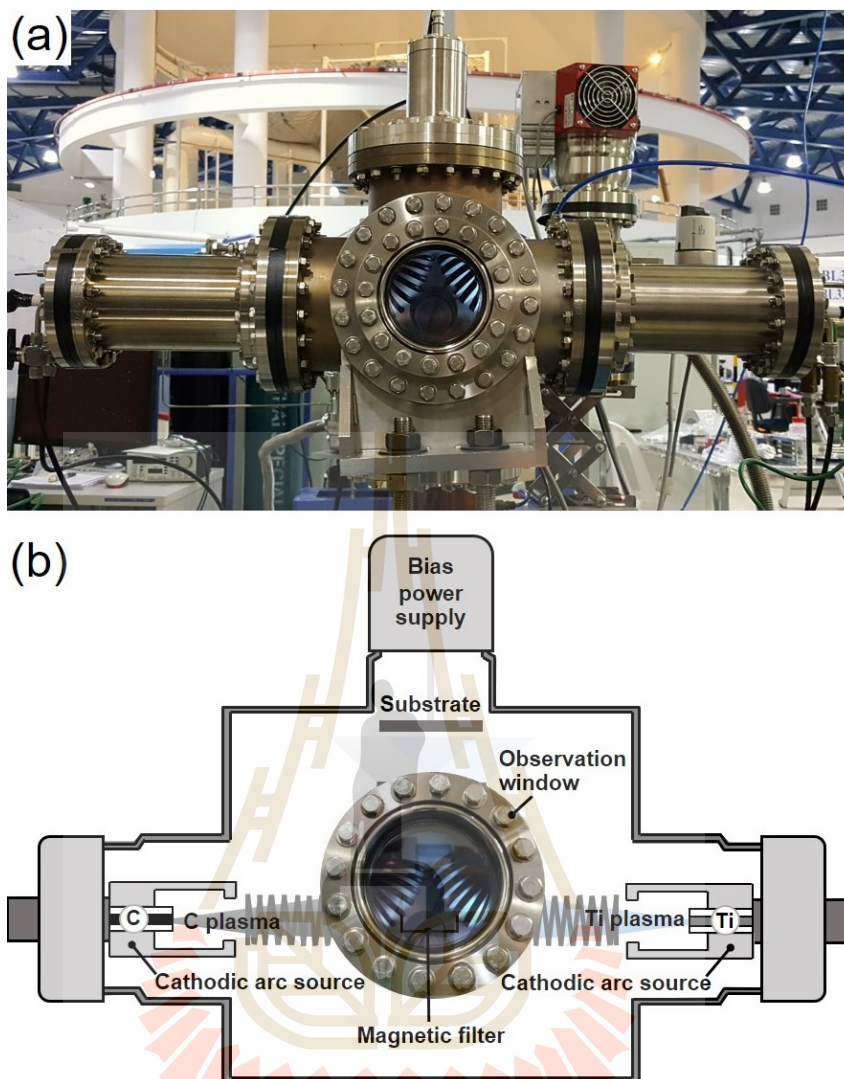
Figure 3.1 A set-up of an in-house developed pulsed two-FCVA system: (a) photograph of the deposition chamber during film growth and (b) corresponding schematic diagram of pulsed two-FCVA deposition used for DLC deposition with the detailed information of all the components inside the deposition chamber.

In the sample preparation, the p-type (100) oriented Si wafers and the AISI 304 stainless steel were cut into rectangular pieces of 10 mm × 10 mm, which is an appropriate size for all the analytical techniques. In the case of the stainless steel

substrates, they were ground and polished with silicon carbide (SiC) sandpapers to achieve a suitable surface profile roughness (R_a) of approximately 30 nm using the surface profilometer, as shown in Figure 3.2. All the substrates were subsequently ultrasonically pre-cleaned with ethanol and acetone for 15 min for each step to remove any surface contamination and afterward dried by nitrogen gas before being introduced into the deposition chamber.
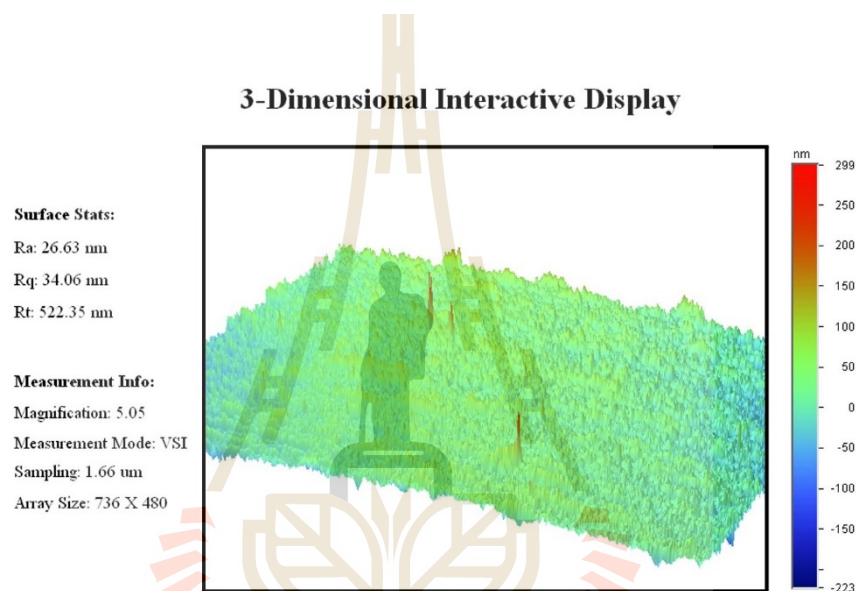
Figure 3.2 The 3-dimension surface profile measurement of AISI 304 austenitic stainless steel substrate using surface profilometer located at the BL6a: Deep X-ray Lithography (DXL), SLRI, Nakhon Ratchasima, Thailand.

In the deposition, the FCVA system is a "triggerless" arc initiation technique and, therefore, a trigger electrode and trigger power supply are not necessary. A graphite rod with a purity of 99.99% (8 mm in diameter) and titanium rod with a purity of 99.50% (8 mm in diameter), surrounded by a ceramic insulator, copper anode cylinder, and cooling system, were inserted into the cathodic arc source acting as the C and Ti source for the pure DLC and Ti-doped DLC films. Due to the small material rod

(8-mm diameter) and no reactive and/or background gas required, the FCVA is an eco-friendly and cost-effective surface modification technique for industrial applications. To generate an initial arc plasma, a conductive path or conductive layer of the cathode materials that are previously deposited on the ceramic insulator surface between the cathode and anode is required to allow the current to cross over to initiate the arc plasma.
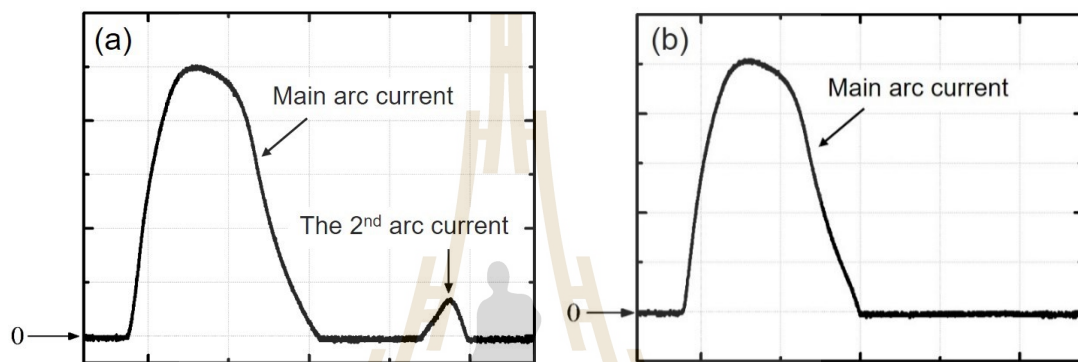
Figure 3.3 The measured arc current by oscilloscope (vertical scale: 100 A/div, horizontal scale: 100 μs/div). (a) Main arc current with the second arc current operated at a pulse repetition rate of 1.0 and 1.25 Hz and duty cycle of 50% and (b) Only the main arc current after pulse repetition rate and duty cycle were changed to 6 Hz and 0.003%.

Prior to the deposition, the chamber was evacuated to a base pressure of 2×10^{-3} Pa by a turbomolecular pump backed up by a diaphragm pump. The V_{bias} in a range of 0 to 1.5 kV was applied to extract the ions and control the energy of the ions from the C^+ and Ti^+ plasma. During the deposition, the working pressure was slightly increased to 3×10^{-2} Pa because of the outgassing of the cathode materials. The arc current was driven at the arc voltage of 0.8 kV. The pulse repetition rate of 6 Hz and a duty cycle of 0.003% were controlled to maintain the cathode consumption and arc

stability. The single arc current or single main arc current (see in Figure 3.3) can be obtained under the above-mentioned conditions. Thus, the arc pulse, is uniform, stable, and countable, which allows accurate control of the film thickness and microstructure.

Any surface oxide films were firstly removed by a bombardment with the energetic ions of Ti$^+$ at the V_{bias} of 1.5 kV for 5 minutes before deposition of the DLC film. This method provided both a freshly cleaned surface and active surface for the subsequent DLC film. To improve the film adhesion and to reduce the delamination during the film growth, a 20 nm thickness of the Ti intermediate layer was pre-coated on the substrate and served as a bond-coat or adhesive layer between the DLC films and the substrate. This approach not only gave a Ti layer as the magnetron sputtering but also promoted the Ti ions into a substrate sublayer, thus resulting in good adhesion of the DLC films to the substrate. The high quality and low macro-particles DLC films can be obtained when the plasma species are passed through an open-architecture, 90°-curved magnetic filter set, which was electrically connected in series with the cathodic arc discharge. The magnetic filter set was made of the copper tube with 20 turns and a 45 mm inner diameter. The distance between the exit of the filter coil and steel substrate was 30 mm. The summarized deposition parameters for the pure DLC and Ti-doped DLC films are listed in Table 3.1.

Table 3.1 The crucial controlled parameters for DLC film deposition.

	Deposition condition parameter
Base pressure (Pa)	2×10^{-3}
Arc voltage (−kV)	0.65 and 0.80
Substrate bias voltage (–kV)	0–2.00
Pulse repetition rate (Hz)	1.0–6.0
Duty cycle (%)	0.003–50
Deposition time (min)	30

3.2   Microstructure, bonding configuration, and elemental analysis

For more understanding of the microstructure, chemical composition, and surface morphology of the pure DLC and Ti-doped DLC films, several analytical techniques including Raman spectroscopy, near edge X-ray absorption fine structure (NEXAFS), X-ray photoelectron spectroscopy (XPS), X-ray photoemission electron microscopy (X-PEEM), and scanning electron microscopy (SEM), energy-dispersive X-ray spectroscopy (EDS), X-ray reflectivity (XRR), and spectroscopic ellipsometry (SE) were performed. The basic principle of their analytical techniques is described by the following sub-sections.

3.2.1   Raman spectroscopy

Raman spectroscopy is the most popular technique and a standard non-destructive analysis for characterizing the microstructure of carbon-based materials (Ferrari and Robertson, 2000, 2001, 2004; Chu and Li, 2006), e.g. crystalline and disordered graphite, amorphous carbon (a-C), and hydrogenated amorphous carbon (a-C:H), and diamond thin films. The basic principle of the Raman method relies on an inelastic scattering or Raman scattering of a monochromatic light beam from a laser source. The interactions of the laser light with the atoms or molecules in the materials lead to the shift of the laser photon (hv), which provides the local structural information about the rotational or vibrational modes of the materials. There are 3 types of light scattering: Rayleigh scattering, Stokes scattering, and anti-Stokes scattering are presented in the Raman spectroscopy, as shown in Figure 3.4. According to Figure 3.4, the Rayleigh scattering originally takes place when the light photon is absorbed and then elastically the scattering goes back to the same frequency and level of an initial excitation light. The Stokes Raman scattering usually has a lower energy level and

frequency due to the interaction between the incident light and atoms or molecules in the materials compared to the initial incident light. The anti-Stokes Raman scattering, on the other hand, has a higher energy and frequency of the emitted photon than the initial incident light. This scattering, however, likely takes place at a high temperature. The inelastic scattering which consists of the Stokes and anti-Stokes Raman scattering, therefore, is commonly used to obtain the Raman information.
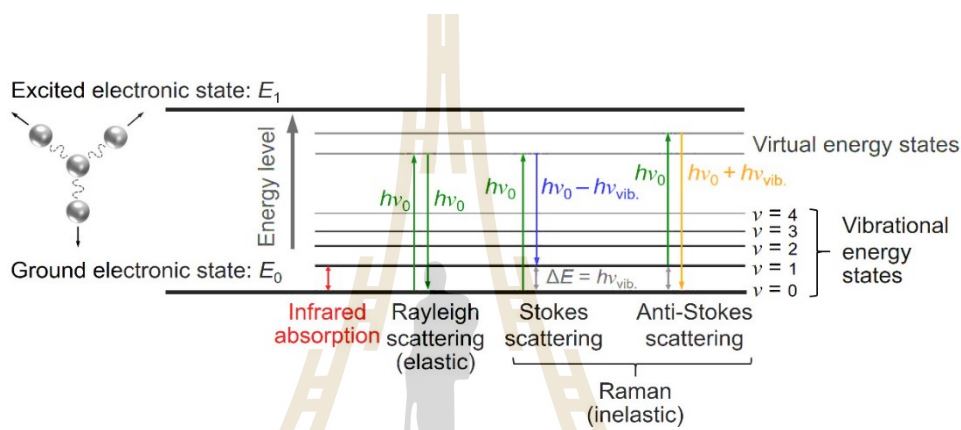
Figure 3.4 A schematic diagram of energy transitions in Rayleigh and Raman scattering edited from Moura *et al.* (2016); Lam *et al.* (2016).

Since the Raman scattering is a very weak signal compared to the intense elastic Rayleigh scattering, the model instruments, such as the notch filter, holographic grating, amplifier, and CCD detector are designed and used to magnify and optimize their signals, as schematically shown in Figure 3.5.
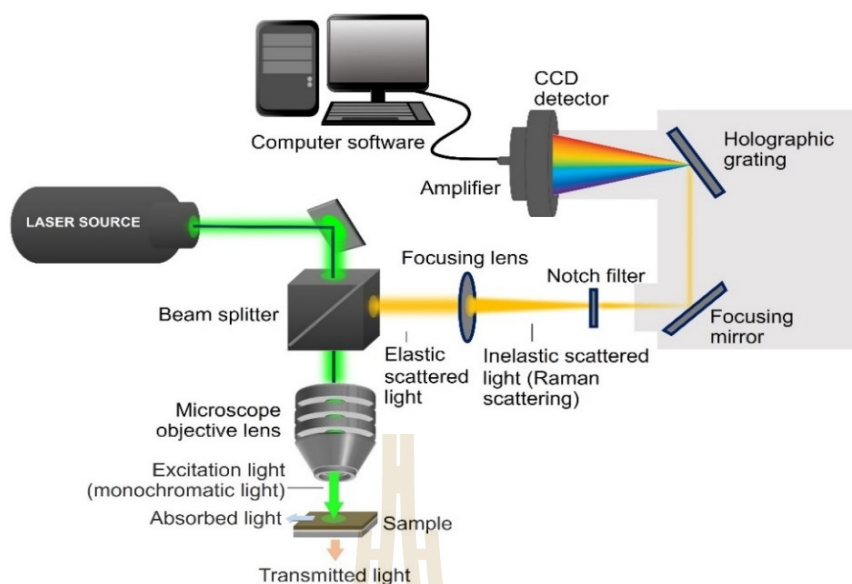
Figure 3.5 A schematic illustration of Raman spectroscope modified from Butler *et al*.
(2016).

The Raman spectrum of diamond with the sp^3 hybridization is located at 1332 cm^{-1} while that of highly oriented pyrolytic graphite (HOPG) with the E_{2g} C—C stretching mode is located at 1582 cm^{-1} and assigned as the G band. The G band is attributed to the stretching mode in all sp^2 sites both in aromatic rings and chains in the graphite. The disordered structure like polycrystalline graphite shows the other sharp peak is located at about 1350 cm^{-1} with the A_{1g} C—C breathing mode. This is associated with the D band which represents the bond-angle disorders of the breathing mode of the sp^2 sites in rings, thus if no ring is present, there is no D band (Irmer and Reisel, 2005; Chu and Li, 2006). Raman spectroscopy in the spectral range between 800 and 2000 cm^{-1} or 1000 and 2000 cm^{-1} (Chu and Li, 2006) is widely studied to identify the microstructural information of carbon-based materials, especially amorphous carbon thin films. The G band is centered at approximately 1580 cm^{-1} and the D band is located

at approximately 1350 cm^{-1}. The Raman parameters, such as the G and D bands positions, the intensity ratio of the D and G bands (I_D/I_G ratio), the full width at half-maximum of the G band (FWHM(G)), and cluster size of the sp^2 sites (L_a) can be obtained from the fitted and deconvoluted well by 2 Gaussian curves on a linear background subtraction. The Raman spectrum of amorphous carbon is dominated by scattering of the sp^2 sites due to the excitation resonances with π states, which is attributed to the G and D bands (Ferrari, and Robertson, 2004).

Although the visible Raman spectrum is not a direct technique for the achievement of the sp^3 content in the DLC films, it is used in a limited range to obtain the relative sp^3/sp^2 ratio which can be compared to the other analytical techniques (Chu and Li, 2006). In addition, the residual stress in the DLC structure can also be calculated by the shift of the G band position, which is associated with the film's mechanical properties. Raman spectroscopy is quite an advantageous technique because it is faster than nuclear magnetic resonance (NMR), near edge X-ray absorption fine structure (NEXAFS), or electron energy-loss spectroscopy (EELS) which are direct methods for the achievement of the sp^3 content, but they all rather suffer a from time-consuming technique.
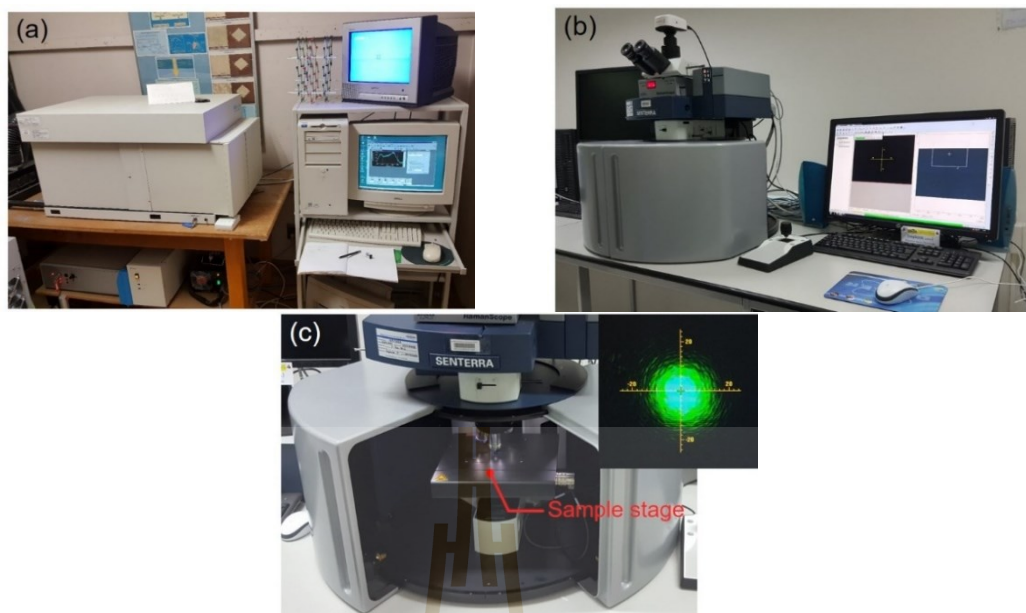
Figure 3.6 Photographs of the Raman spectrometer (a) HORIBA, Jobin-Yvon, LabRAM Infinity, (b) BRUKER RamanScope, SENTERRA, OPUS, and (c) the sample stage and focused the laser beam on the sample inside the SENTERRA.

Two Raman systems were used in this work, as shown in Figure 3.6(a) and 3.6(b). The first system was a laser Raman microscope spectroscopic apparatus (HORIBA, Jobin-Yvon, LabRAM Infinity) located at the Optoelectronic Ceramics Laboratory, NUT, Niigata, Japan. This system was used for the preliminary study operated in the backscattering mode and produced by a 5 mW Ar^+ ion laser with a source wavelength of 514.5 nm. The probe aperture was approximately 10 μm with the wavelength resolution of 1 cm^{-1} and the Raman spectra were performed in a 1000−2000 cm^{-1} spectral range. Another system was a dispersive Raman spectroscopic system (BRUKER RamanScope, SENTERRA, OPUS) located at the SLRI, Nakhon Ratchasima, Thailand. This system was used for the Ti-doped DLC films operated in a

backscattering configuration and produced by a 12.5 mW Ar^+ ion laser as an excitation source at a wavelength of 532.0 nm. The spot size of a laser beam is focused on the sample with approximately 4 μm^2 and the spectral resolution of 3 cm^{-1}. The Raman spectra of the films were carried out in a range of 800–2000 cm^{-1}. The Raman parameters, such as the I_D/I_G ratio, the position of the D and G bands, FWHM, residual stress, and L_a were acquired by fitting the Raman spectrum with 2 Gaussians functions using the OriginPro software. The Raman spectra of the DLC films and standard materials of glassy carbon and HOPG are revealed in Figure 3.7.
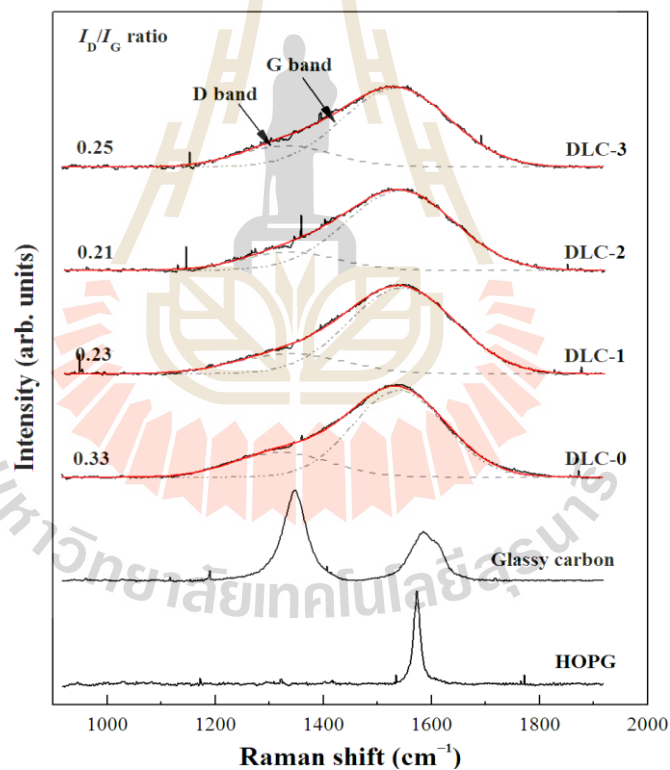
Figure 3.7 Raman spectra of the DLC films at different bias voltage along with the glassy carbon and HOPG standard materials adopted from Natthaphong *et al*. (2018).

3.2.2　Near edge X-ray absorption fine structure (NEXAFS) spectroscopy

NEXAFS spectroscopy is a useful and surface sensitive technique for identifying the electronic structure, chemical functional groups, and molecular orientation of the carbon-based materials, especially the sp^3/sp^2 ratio in the DLC films (Hähner, 2006; Benny *et al*., 2006). NEXAFS is capable of providing the unique information of low atomic number element mean that this is predominantly suited for distinguishing of complex heterogeneous sample because the absorption spectra depend strongly on the local geometric structure of atoms in the sample. NEXAFS spectroscopy is a powerful capabilities for the chemical characterization of DLC forms. It is a synchrotron-based spectroscopic technique in which the synchrotron radiation has a superior radiated intensity than most conventional sources by orders of magnitude, thus high spatial resolution of NEXAFS can be obtained.

To generate the synchrotron radiation (see in Figure 3.8(a)), the electric charges, particularly electrons are produced at a heated cathode of an electron gun before being fed into the booster. The electrons are linearly accelerated using a linear accelerator or LINAC to have the desired velocity of 40 MeV and then transferred into the booster ring or synchrotron. In the booster ring, the electrons are accelerated and forced to move in a circular pattern with a velocity close to the speed of light of 1 GeV before being injected into the storage ring at the final stage where the electron energy can reach up to 1.2 GeV.
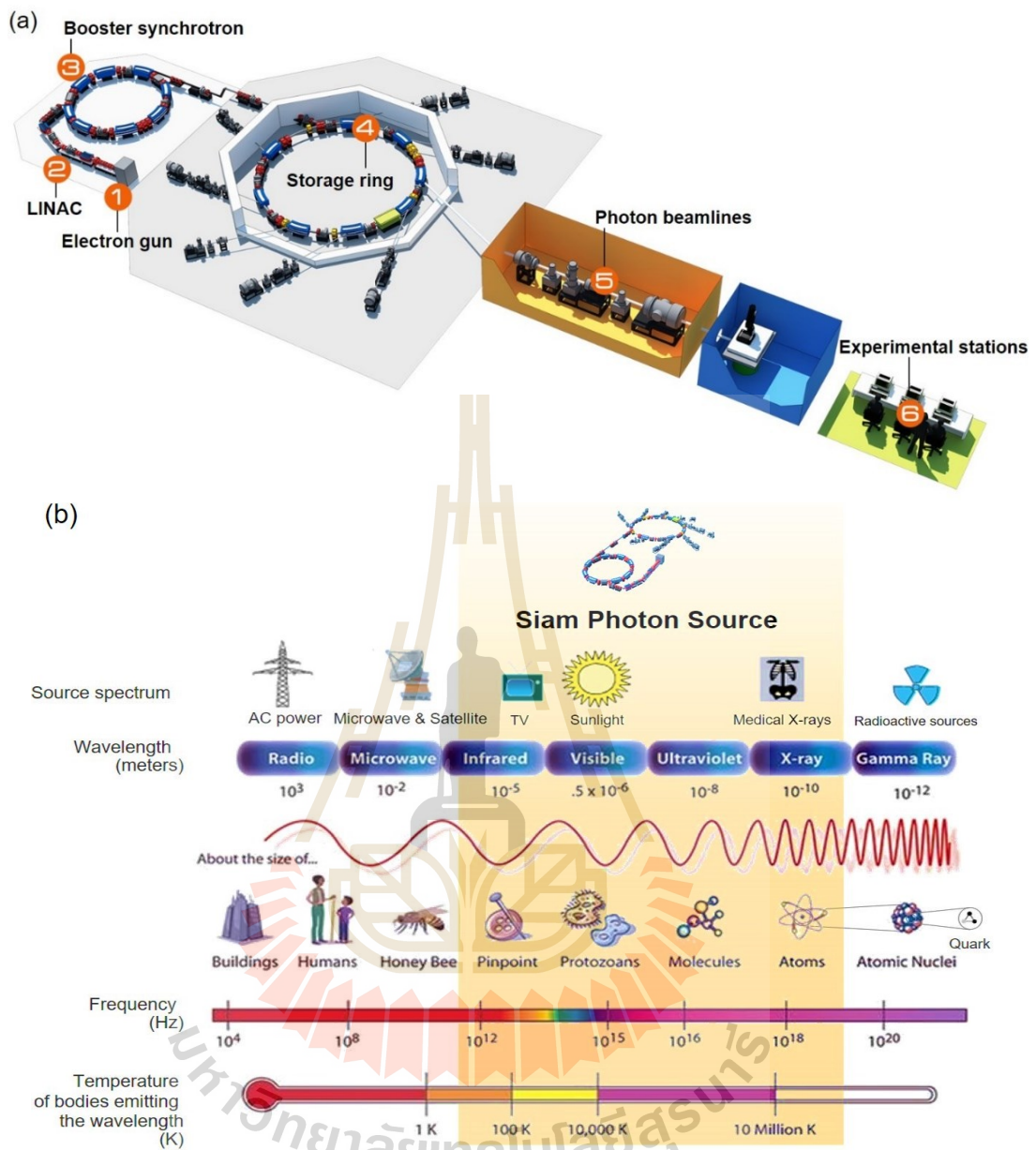
Figure 3.8 Schematic representation: (a) the synchrotron facility at the SLRI, Nakhon

Ratchasima, Thailand and (b) the synchrotron radiation covered a

continuous range of the electromagnetic spectrum (Synchrotron Light

Source and Characteristics of Synchrotron Light, SLRI, 2018–2019).

Then the electrons are forced by the actions of magnetic fields to change

direction making them lose energy and discharge in the form of an electromagnetic

wave or photons the so-called synchrotron radiation, with a wide range of the electromagnetic spectrum covering a continuous range from infrared rays (IR), visible light, ultraviolet rays (UV) and X-rays, as seen in Figure 3.8(b). The synchrotron radiation is then conveyed to experimental stations through photon beamlines in which a single wavelength or appropriate energy, for example, a high brilliance, tunable, monochromatic X-ray source (Hähner, 2006) are selected via a monochromator for matching up to each experiment.

The X-ray absorption experiments deal with an absorption edge structure both in the immediate near-edge jump and above the edge. The near absorption edge region, about the first 50 eV above the absorption edge (<2000 eV) is referred to as X-ray absorption near-edge structure (XANES) standing for near-edge X-ray absorption fine structure (NEXAFS) (Hähner, 2006), while the oscillations extending up to more than 1000 eV are frequently referred to as extended X-ray absorption fine structure (EXAFS), as shown in Figure 3.9. XANES region involves the oxidation or electronic state, bonding characteristics or chemical shift, atomic position of neighbors, bond angle, and geometry of materials, which is dominated by intense and narrow resonances. The EXAFS region is, on the other hand, sensitive to the distribution of electron density, and thus is for quantitative analysis of the bond length and coordination number (Stöhr, 1992; Groot and Kotani, 2008). In recent years, the term EXAFS has been designated for hard X-ray absorption spectra and the term NEXAFS (XANES) is assigned for soft X-ray spectra. NEXAFS and EXAFS are, however, still the most widely used, but NEXAFS spectroscopy is particularly considered as an extremely analytical technique for amorphous carbon thin films through its carbon *K*-edge.
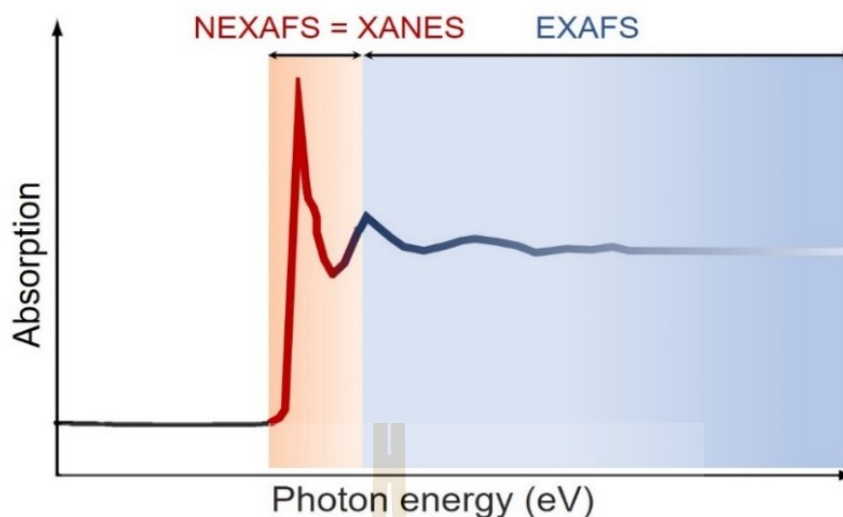
Figure 3.9 A schematic diagram of an X-ray absorption spectrum for the NEXAFS
(XANES) and the EXAFS regions adopted from Stöhr (1992); Penner-
Hahn (2003).

There are 2 modes of measurement of an X-ray absorption spectrum
carried out: (i) transmitted X-ray flux (transmission mode) and (ii) the incident (electron
yield mode). These modes involve the measurement of an absorption coefficient (μ)
behind and in front of the sample based on Beer's law (Hähner, 2006) and is given by
the equation, as shown in Figure 3.10. A transmission mode is a suitable tool for very
thin samples. It, therefore, is limited by an energy of the absorption edge and
concentrated samples, while the electron yield mode referred to as the total electron
yield (TEY) and partial electron yield (PEY) can be used for conventional samples,
especially amorphous carbon thin films.
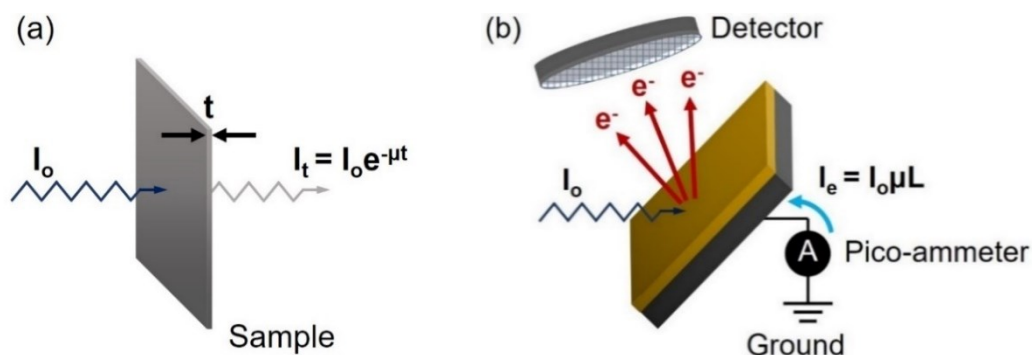
Figure 3.10 A basic principle of XAS geometry setup for the achievement of the μ: (a)
transmission and (b) electron yield modes modified from Stöhr (1992);
Hähner (2006).

In the NEXAFS experiment, the occurrence of photoabsorption
processes is due to the inner-shell excitation process of core electrons; at the photon
energy close to an atomic absorption edge, into unoccupied or empty or continuum
states. This process leads to the following phenomena, as demonstrated in Figure
3.11(a). As monochromatic X-rays with a sufficient energy shines on the sample (step
1), the electrons located at the core level are ejected to the empty states above the
vacuum or Fermi level in a phenomenon known as the photoelectric effect or often also
referred to as photoelectric emission or photoemission, and the emitted electrons are
called photoelectrons (step 2). This phenomenon leaves a core hole in the inner K-shell
or core level in which the created hole is then filled with an electron from the outer shell
(step 3) through the emission of X-rays or a fluorescent photon with the difference in
the energy of the electron between the 2 shells ($L_3 \rightarrow K$), which is characteristic of a
specific atom. The other phenomenon is about Auger decay (step 4), which is prominent
in the soft X-ray regions over the fluorescent photon (Stöhr, 1992; Hähner, 2006; Benny
et al., 2006).
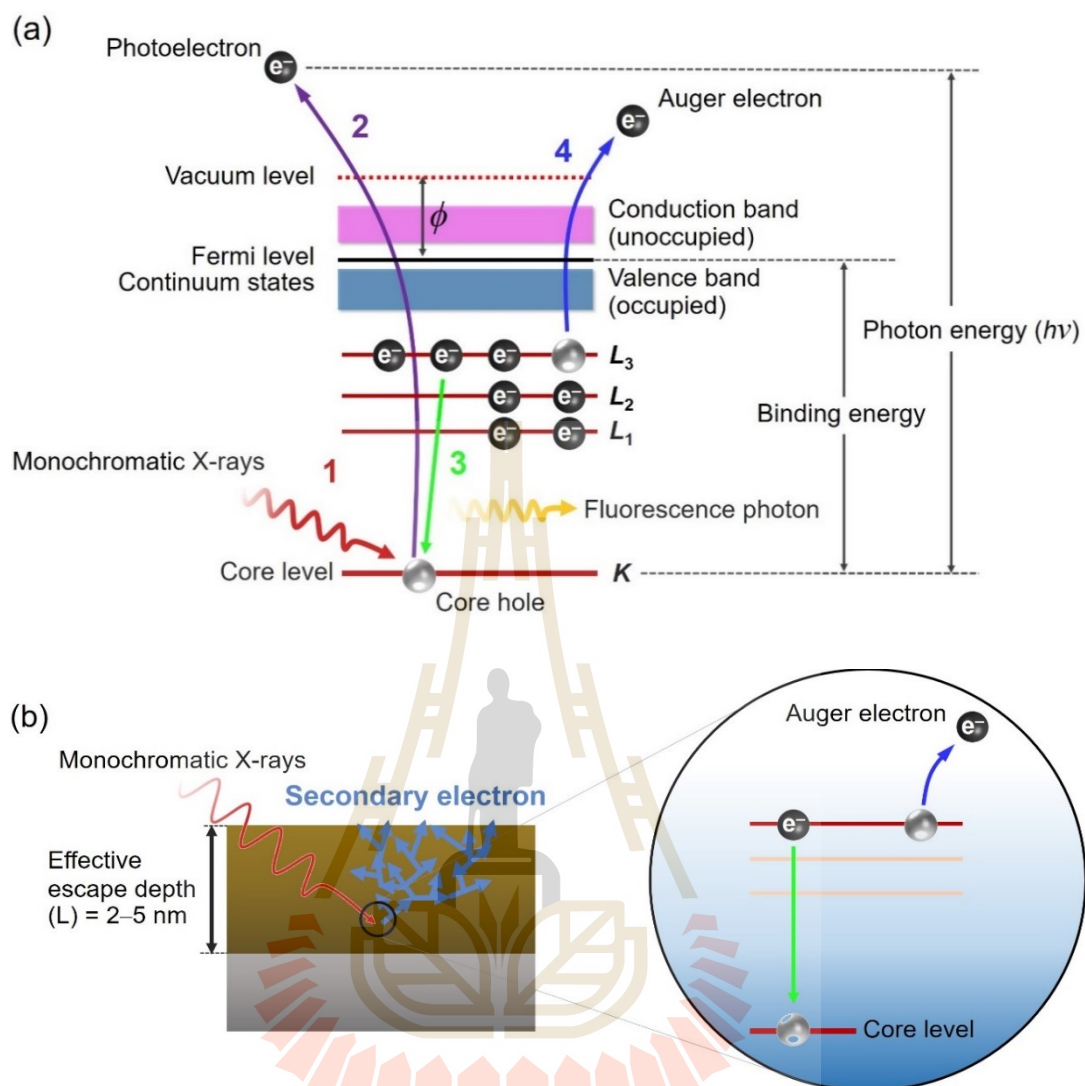
Figure 3.11 A schematic illustration of ionization processes and generations of X-rays edited from Hähner (2006); Benny *et al*. (2006).

Although the photons or monochromatic X-rays will penetrate many microns deep into the sample, all the electrons occurring in the absorption cross-section cannot emerge from the outset surface region, but rather those electrons with a sufficient energy to overcome the work function (ϕ) of the materials. In the NEXAFS, the effective escape depth is measured in a range of approximately 5 nm for metals and

semiconductors, and slightly deeper for insulators in which such electrons, for example, secondary electrons generated from an interaction of the emitted electrons, such as photoelectrons or Auger electrons, can be directly detected via a channeltron and/or an energy analyzer, as illustrated in Figure 3.11(b).

In an attempt to improve the surface sensitivity of the XAS technique, a negative grid detector is inserted before the electrons enter into an electron energy analyzer. This device is used to retard the electrons with a low kinetic energy, thus it allows only the electrons with a sufficient energy to overcome the negative grid potential before they pass through an energy analyzer (approximately 3 nm from the top surface). This technique is referred to as the partial electron yield (PEY) detection. The PEY detection provides a good signal-to-background ratio comparable to the total electron yield (TEY) detection in which all the emitted electrons are recorded in an electron energy analyzer. The other method is the Auger electron yield (AEY) detection in which the specific electron energy analyzer is needed for recording the elastically scattered Auger electrons. One is the fluorescence yield (FY) detection which requires a suitable detector to record an emission of fluorescence photons. The PEY, AEY, and FY detections are adequate signal-to-background ratios for thin films. Because of the limited mean free path of the electrons, the FY detection is suitable for samples in aqueous solution or in a gaseous environment with energy below 1000 eV. In this case, the PEY-NEXAFS technique is the best choice; it provides the surface sensitivity tool and no specific electron energy analyzer is required and so it was selected for identifying the DLC films in this work.

To investigate the bonding configurations and electronic structures of amorphous carbon thin films by the NEXAFS technique, a detailed understanding of

the photoabsorption cross section is a very significant and prerequisite topic. The absorptions or ionization processes involving the excitation of the core electron to unoccupied states or continuum of final states can be described via the transitions into Rydberg states, as shown in Figure 3.12.
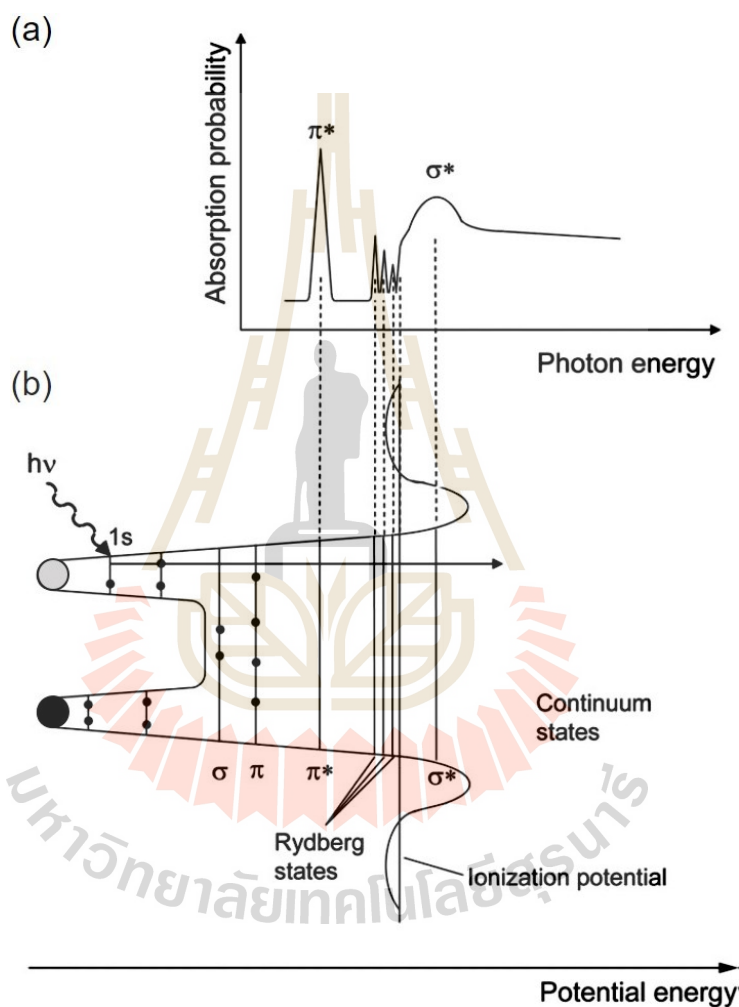
Figure 3.12 A schematic diagram of (a) the corresponding *K*-edge spectrum acquired from (b) the effective potential of a diatomic molecular adopted from Hähner (2006).

According to Figure 3.12, the superimposed resonances in the form of the step-like shape can be observed below the ionization threshold in a range of approximately 50 eV when the energy of incoming X-rays matches up to the difference in energy between the initial state and the unoccupied states. The unfilled (empty) orbitals are assigned to the π^* or σ^* orbitals in which most of them are found above the vacuum level. The $1s \rightarrow \pi^*$ resonance occurs with the π-bonding both in the form of double and triple bonds or aromatic systems, but not in the form of single bonds. A Gaussian line-shape can be used for identifying the resonance width at higher energies. The σ^* resonances are an asymmetric line-shape at higher energies due to the lifetime broadening and molecular vibration along the bond direction. In general, the Rydberg orbitals are located between the π^*-resonance and the ionization potential which can be described as a mixing of the Rydberg orbitals with hydrogen-derived antibonding orbitals, particularly in the C—H bonds. It, therefore, is important and can be typically observed in the case of the hydrogenated DLC or the H-free DLC films with a small amount of the H.

In this thesis, the electronic structures and bonding configurations of carbon atoms in the DLC films were investigated by NEXAFS spectroscopy. The NEXAFS implementation was performed at the BL3.2Ub: PEEM of the SLRI, Nakhon Ratchasima, Thailand. The synchrotron radiation acquired from the storage ring has a beam energy of 1.2 GeV. The photon energy of the beamline covers a range from 40 to 1040 eV with a resolving power of 1000 and total energy resolution of approximately 0.5 eV. The synchrotron radiation was linearly polarized in the plane of the sample surface at any an incident light angle. During the NEXAFS experiment, the samples were irradiated with monochromatic X-rays at an angle of 17°. The typical usage of a

20 kV negative bias voltage on the negative grid detector allows the NEXAFS to perform in the PEY detection in which the absorption spectra can be achieved by normalizing the emitted electron intensity of the DLC films with that of a freshly cleaned Si wafer. The C K-edge NEXAFS spectra of the films and freshly cleaned Si wafer were performed in the same photon energy range and scanning step to obtain the normalized data. To estimate the sp^3/sp^2 ratio, the C K-edge spectra of the films were deconvoluted using the Igor Pro 6.3 software. The C K-edge, O K-edge, Ti $L_{3,2}$-edge, Fe $L_{3,2}$-edge, and Cr $L_{3,2}$-edge NEXAFS spectra were carried out in the photon energy range of 275−335, 525−555, 450−475, 700–730, and 565–595 eV, respectively, with a scanning step size of 0.1 eV to investigate the changes in the bonding configuration of the films after the electrochemical corrosion tests.

3.3.3 X-ray Photoemission electron microscopy (X-PEEM)

Photoemission electron microscopy (PEEM) has been proved as a powerful tool providing microscopic images of thin film materials, surface physics and chemistry, and surface biomaterials. PEEM is also referred to as photoelectron microscopy (PEM) which is nearly related to low-energy electron microscopy (LEEM). In the operation of PEEM, the samples should be well-cleaned and should have ultrahigh vacuum (UHV) compatibility, electrically conductive materials, and flat and smooth surfaces to avoid the effects of surface electron charging and arc discharge during the increasing –20 kV biased voltage between the sample and the objective lens. This is one of the major drawbacks which leads to damage on the surface of a sample. For the non-conductive materials, a thin conductive layer, for example, platinum, copper or gold is pre-deposited on the sample surface to solve the electron charging. In recent years, PEEM has been improved to achieve enhanced resolution in an order of

magnitude. The UHV PEEM was developed to obtain a spatial resolution of 10 nm and more beautiful micrographs. LEEM and PEEM can be simultaneously utilized to obtain a specific surface imaging by changing the excitation source from the UV light to an electron. The images in LEEM mode take place due to the reflection of low energy electrons at a sample surface. In addition, selected-area low-energy electron diffraction (LEED) can also be conducted for the achievement of domain structures in single-crystal and polycrystalline materials (Euaruksakul *et al*., 2013). Instead of the low-energy electron by the X-ray source, a high resolution of a magnetic domain can be achieved, which is referred to as X-ray photoemission electron microscopy (X-PEEM).

Different image contrast mechanisms commonly occur in X-PEEM analysis (Stöhr, 1992; Hähner, 2006; Tonner *et al*., 1996) which consists of surface topology, work function, and elemental and chemical composition contrasts, as shown in Figure 3.13. The topographic contrasts take place on the rough samples due to the distortion or curvature of the accelerating electric field or the electron trajectories at the surface topographic features. This contrast is caused by the presence in the spatial resolution and local focusing of a sample surface. The work function contrasts are dominant, as the excitation source with energy close to or more than the local work function of materials is radiated. The difference in the work function results in the different micrographics of each region. In the case in which an excitation source has higher energy than the work function of the materials, that region appears as a brighter surface comparable to that with a lower energy than the work function. The elemental and chemical composition contrasts are known as some of the most substantial mechanisms in distinguishing each region of the materials. The region with a strong absorption of species appears brighter in the X-PEEM image. The chemical contrast is

also related to the oxidation states and electric band structures, such as bonds and molecular orbitals. The region with a predominant oxidation state and electric band structures, therefore, appears brighter.
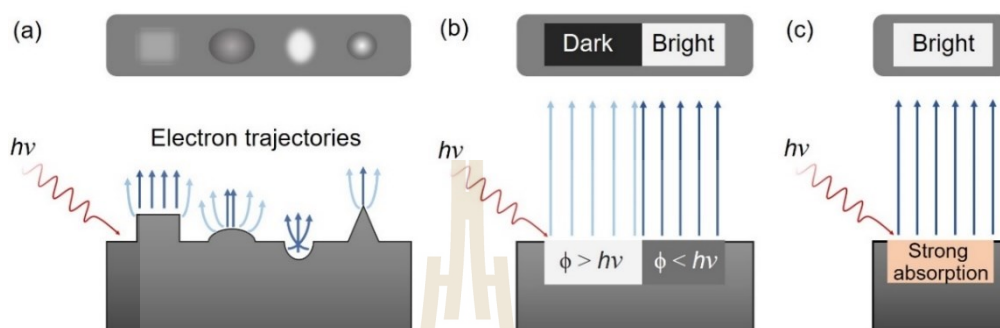
Figure 3.13 A schematic representation of the image contrast mechanisms: (a) surface topographic, (b) work function, and (c) elemental or chemical composition contrasts.

In the X-PEEM experiments, an appropriate spot size with a 75 µm field of view (FOV) on the MCP screen can be obtained by focusing monochromatic soft X-rays with a much higher intensity and solution from the varied line-spacing plan-grating monochromator on the sample, as revealed in Figure 3.14(a). With the potential difference of –20 kV between the sample and the objective lens, the emitted electrons near a minimum of the secondary electron mean a free path generated by photoemission and photoabsorption processes is accelerated into the microscope where the resolution and transmission of electrons or digital signals are determined by the combination of the objective lens and contrast aperture. The digital signals are then collected and magnified onto a microchannel plate intensifier or a phosphor screen by the intermediate lens and the projective lens. The digital signals on the phosphor screen are

88

subsequently converted into the visible image and captured by a Sensicam QE couple-charged device (CCD) camera connected to a personal computer. This is a relatively fast technique due to the parallel image-acquisition and, hence, a series of images or image sequences accompanied by the photoabsorption spectra at different energies can be obtained known as a stack. In this case, a video record can be made by accumulating the series of a stack, enabling a study of the alteration of the process in real-time.
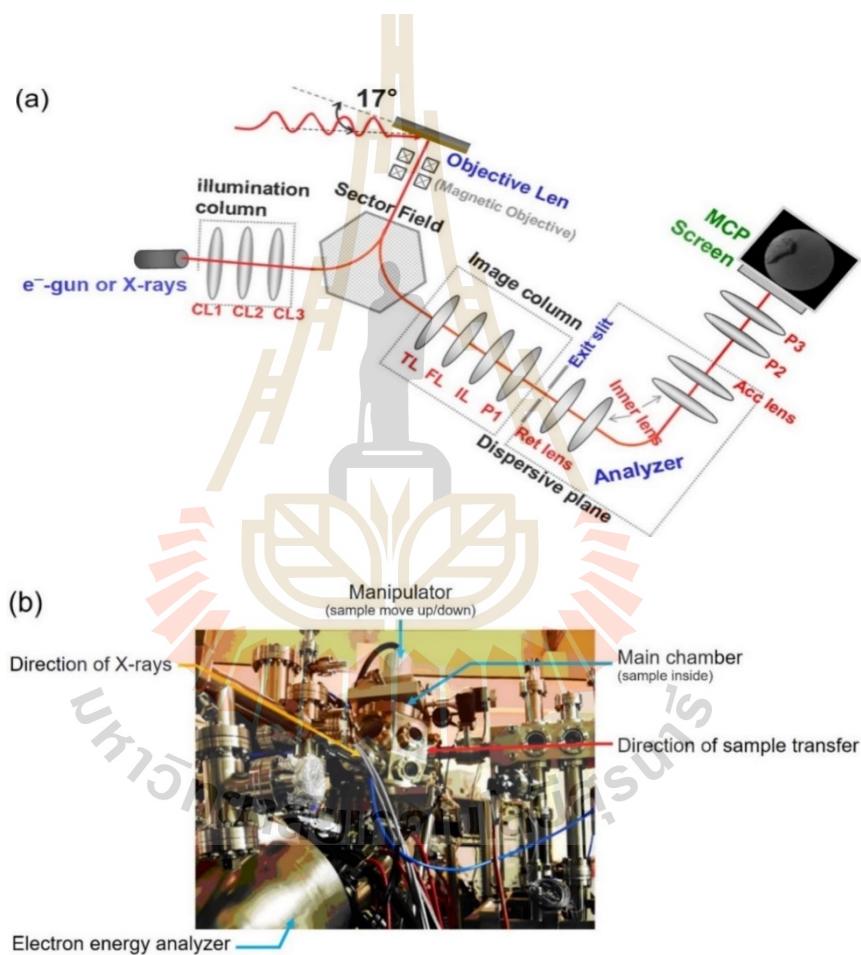
Figure 3.14 (a) Schematic diagram of X-PEEM and (b) a photograph of the X-PEEM apparatus (Schematic diagram and Photograph of X-PEEM system, SLRI, 2018).

In this thesis, the local bonding configuration of the deposited DLC films before and after the thermal annealing and the electrochemical corrosion measurements were thoroughly determined using the NEXAFS spectroscopy in connection with the X-PEEM technique, the so-called spectroscopic photoemission and low energy electron microscope (SPELEEM), located at the beamline (BL) 3.2Ub: PEEM of the SLRI, Nakhon Ratchasima, Thailand. X-PEEM is a very effective probe for inspection of the chemically distinct surface and interface phenomena which yield the combined analysis of the images and spectral features, the so-called spectromicroscopy technique. To attain the high spatial resolution of approximately 1 nm, a hemispherical electron energy analyzer (ELMITEC Elektronenmikroskopie GmbH, Germany) equipped with LEEM III at the end-station of the BL3.2Ub: PEEM was employed. This device acts as a low pass energy filter of a few eV bandwidths near the threshold of the photoelectrons and is used for collecting and selecting the energy of the photoelectrons that are readily emitted at particular photon energies. For the qualitative analysis, the X-PEEM technique operated under a UHV of $\sim 3 \times 10^{-10}$ Pa with a photon energy range of 40–1040 eV and the image resolution of 30 nm and was performed to approach the C $1s$, O $1s$, Ti $2p$, Fe $2p$, and Cr $2p$ X-PEEM images of particular areas. The stack acquired from a series of images at different energies was collected using the ImageJ software. The corresponding C K-edge, O K-edge, Ti L-edge, Fe L-edge, and Cr L-edge NEXAFS spectra obtained from the X-PEEM images were performed to analyze the local bonding structure of carbon coordination in the DLC films before and after the electrochemical corrosion tests.

For the thermal stability analysis, the vacuum heating system in conjunction with the X-PEEM chamber was applied which enables the annealing

temperature over the temperature range from approximately 30 to 1200°C. The change in the local bonding structure as a function of the thermal annealing was also measured in the real-time analysis. A freshly flashed Si wafer was employed for normalizing the out-coming emitted electron absorption signals from the DLC films corresponding to the same photon energy range. The HOPG standard material with a highly pure sp^2 bonding was employed as the reference for energy calibration and quantitatively estimating the absolute $sp^2/(sp^2 + sp^3)$ fraction of the pure DLC and Ti-doped DLC films. The C K-edge, O K-edge, and Ti $L_{3,2}$-edge NEXAFS spectra were investigated in the photon energy range of 270–350 eV, 525–555 eV, and 450–475 eV, respectively, at the scanning step size of 0.1 eV. The heatable substrate holder used in the thermal stability analysis and the unheatable (normal) substrate holder are shown in Figure 3.15.

Figure 3.15 Photographs of (a) the unheatable substrate holder, (b) heatable substrate holder, and (c) heatable substrate holder during annealing in X-PEEM main chamber.

3.3.4 X-ray photoelectron spectroscopy (XPS)

XPS is known as the standard electron spectroscopy for chemical analysis (ESCA) technique. XPS is extensively used as a surface sensitive tool in a wide range of materials, such as metals, semiconductors, ceramics, and biocomponents

which provides both qualitative and quantitative surface chemical information. Since the average escape depth is estimated at approximately 5−10 nm, XPS is a good choice for surface characterization of an ultra-thin film in various industrial and research applications. The basic principle of XPS relies on the photoelectric effect, as shown schematically in Figure 3.16.
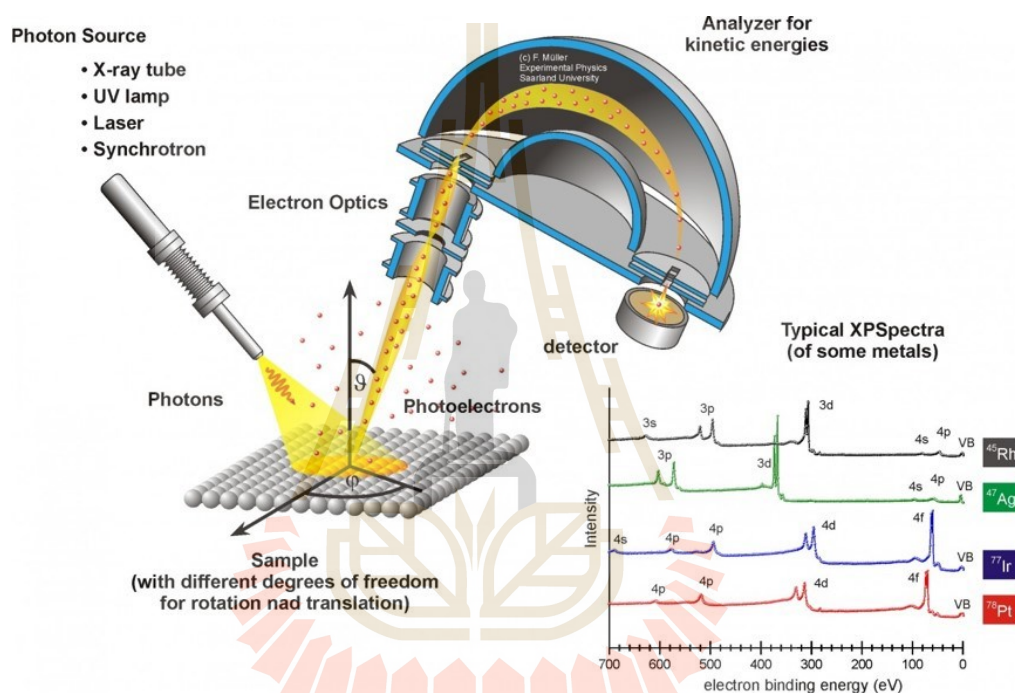
Figure 3.16 A schematic illustration of the basic principle of XPS technique (Schematic of a typical XPS setup, 2019).

The photoelectric effect occurs as the sample is irradiated by a monochromatic X-ray source with sufficient photon energy, rather higher than the binding energy of the materials. The photoelectric effect emits the electrons the so-called photoelectrons before being detected by an electron energy analyzer. The photoelectrons of each element have their own characteristics with different kinetic

energies. The XPS technique, therefore, is used to identify the elemental composition and oxidation state of the DLC films in this thesis. The kinetic energy of electrons is measured by an electron energy analyzer that is converted into the binding energy by the following equation:

$$KE = h\nu - BE - e\phi, \qquad (3.1)$$

where $h\nu$ is the photon energy of the monochromatic X-ray source, BE is the binding energy of the materials, and $e\phi$ is the work function of the electron energy analyzer.

In this thesis, 2 types of XPS system were used. The first was the XPS (JEOL, JPS-9010TR) located at the Department of Materials Science and Technology, NUT, Niigata, Japan. It was employed to characterize the chemical composition and structural information in terms of the sp^3/sp^2 ratio of the pure DLC films in the preliminary study. A monochromatic Mg K_α X-ray source was used as an excitation source. The emitted photoelectrons from the sample were collected using a hemispherical electron energy analyzer at the pass energy of 20 eV with a step size of 0.1 eV and a dwell time of 10 s. The C 1s and O 1s XPS spectra were carried out under a UHV condition of approximately 10^{-6} Pa. The bombardment with Ar$^+$ ions at a kinetic energy of 1 kV was performed for 1 min before the measurements to remove any native oxide surface. Another system was the XPS: PHI5000 Versaprobe ULVAC-PHI, Japan located at the BL 5.3 SUT-NANOTEC-SLRI XPS of the SLRI, Nakhon Ratchasima, Thailand. It was used to obtain the chemical composition of the pure DLC and Ti-doped DLC films. A monochromatic Al K_α radiation with the photon energy of 1486.6 eV was employed as an excitation source. A hemispherical electron energy analyzer was

employed to detect the emitted photoelectrons that were recorded in the C 1*s*, O 1*s*, and Ti 2*p* regions with a spot size on the sample of 100 μm, a depth of 10 nm, a pass energy of 46.95 eV, a step size of 0.1 eV, and a dwell time of 100 eV. The XPS experiment was performed at a UHV of approximately 10^{-7} Pa. The bombardment with the Ar^+ ions at a kinetic energy of 2 kV was performed for 12 s to remove any surface oxides and residual contamination. For the quantitative analysis, MultiPak Spectrum: ESCA software equipped with the XPS apparatus was employed to achieve the elemental composition of the films.

3.3.5 Scanning electron microscopy (SEM) and Energy-dispersive X-ray spectroscopy (EDS)
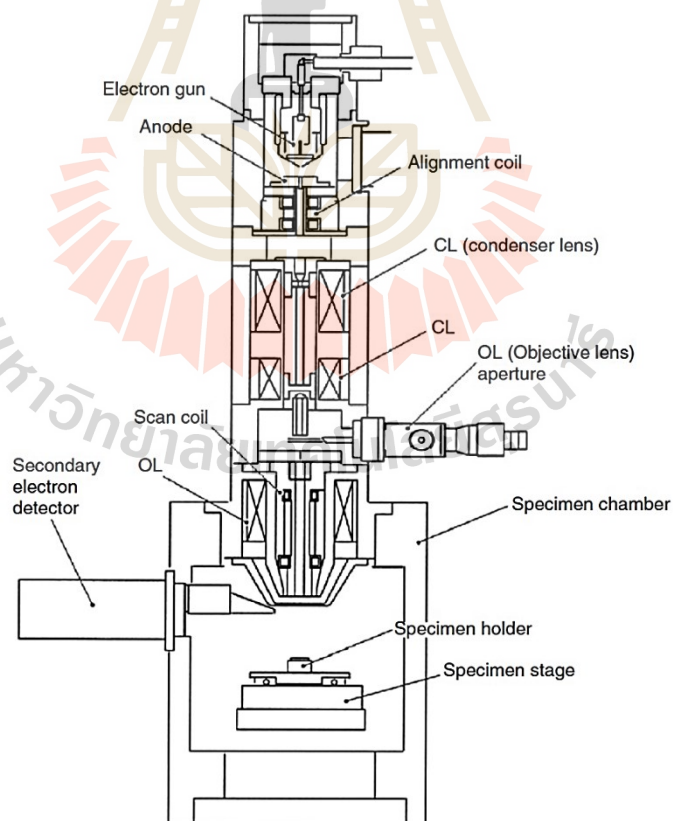
Figure 3.17 A schematic diagram of SEM (Zhou *et al*., 2007).

SEM is undertaken with an electron microscope with a superior performance compared to light optical microscopy due to its high-resolution surface imaging and spatial resolution. SEM using an elemental composition detector has been routinely performed in many applications of nanomaterials sciences to provide information on the surface topographical and elemental composition (Reichelt, 2007). The schematic representation of the principle of conventional SEM is demonstrated in Figure 3.17.

In the standard electron microscope, a tungsten filament cathode at the top of the column is electrically heated using a thermionic electron gun to generate electrons. The emitted electrons with a typical range energy of 0.1 to 30 keV are then accelerated down and focused in an electron beam of approximately 5–10 nm by a series of condenser lenses and apertures before hitting the sample mounted on a stage inside the chamber which is evacuated by pre-vacuum and high vacuum pumps. With a low pressure, typically in an order of 10^{-4} Pa, the electron beam travels toward the sample without much interaction with residual gas molecules. The position of the incident electron beams on the sample is controlled by scan coils located below the objective lens. This device allows us to scan the electron beam to the desired regions. As the emitted electron beam penetrates into the sample's surface, it interacts with the localized atoms of the sample which leads to their scattering and adsorption. These processes occur within a teardrop shape known as the sample-interaction volume caused by the energy loss of the penetrated electrons through elastic and inelastic interactions, as illustrated in Figure 3.18(b). The width and depth of the interaction volume depend on the sample's average atomic number and the accelerating voltage.
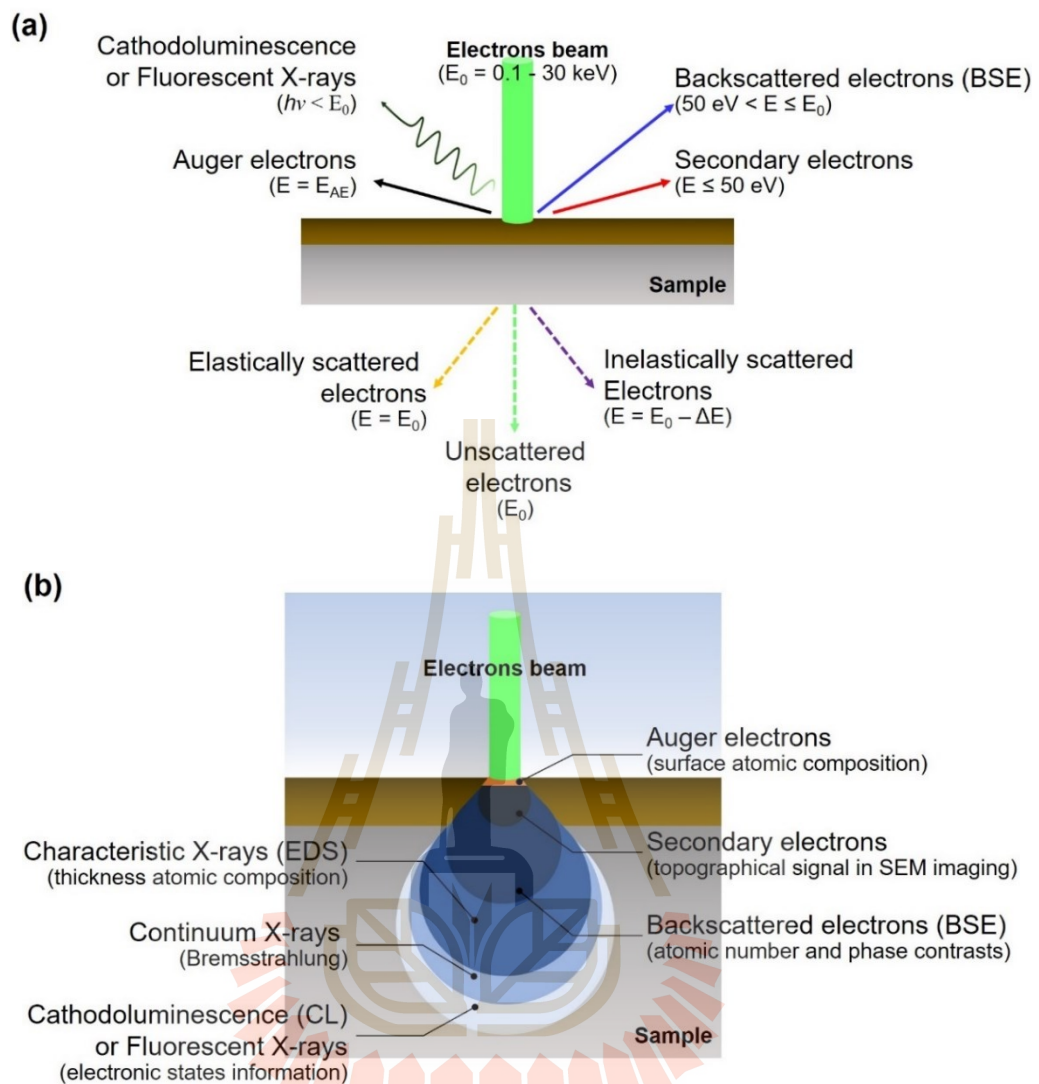
Figure 3.18 A schematic demonstration of (a) the interaction of electron beam with the localized atomic nucleus and (b) the sample-interaction volume with detectable signals.

In the elastic scattering, the interaction of the electron beam with the atomic nucleus or outer shell electrons is caused by the scatters and changes in their trajectory at a similar kinetic energy and velocity which is known as elastic scattering or electron backscattering. Electron backscattering at more than 90° is usually referred

to as the backscattered electrons (BSE) which provides a useful information of the surface morphology in the SEM technique. In the case that the incident electrons pass through the sample completely in the same direction after interacting with the localized atomic nucleus, this process is called the unscattered or transmitted electrons in which no additional electrons are generated. The electron energy of the BSE and transmitted electrons is in a range of 50 eV up to the accelerating voltage (E_0).

The inelastic scattering involves the interaction of the electron beams with the orbitals electrons in the localized atomic nucleus in the sample with loss of the electron energy. The process provides phenomena, such as secondary electrons, phonon excitation (heating), characteristic X-rays, plasmon production from secondary electrons, Auger electrons (AE) acquired from the outer shells, continuum or Bremsstrahlung (breaking) X-rays, and cathodoluminescence or visible light fluorescence, as schematically shown in Figure 3.18(b). Typically, the secondary electron is acquired from the ejection of the loosely bound outer shell in the valence or conduction band into the vacuum level. It, thus, is generated near the surface and carries energy of ≤ 50 eV which is a useful information for surface topography and morphology in SEM imaging. Small electrons ejected from the inner shells are detected and result in ionization of the atoms in the sample which leads to the formation of characteristic X-rays, with a higher energy than SE, as shown in Figure 3.18(a). Since the characteristic X-rays provides the chemical information for the sample, it is widely used in the microstructural analysis technique in SEM. The presence of the characteristic X-rays is due to the interaction of a decelerating high-energy electron with the electron cloud and localized atomic nucleus in the sample results in the formation of a continuous background followed by the generation of the Bremsstrahlung or continuum

X-rays. The AE is also generated from ionization of the atoms by the incident electron and has the characteristic electron energy. It carries low energy because of the emission from very near the surface and thus gives chemical information from only a few nanometer depths of the outer surface. Cathodoluminescence is a process of energy stabilization generated by the collision of the incident electron beams after filling the holes with electrons from the outer shells. In some materials, excess energy will be released in a form of photons, such as infrared, visible light fluorescence, or ultraviolet wavelengths which can be detected via a photomultiplier in the same way as the SE detector acquired from approximately 50 nm of the outer surface.

In a conventional SEM, the microscope is typically equipped with energy-dispersive X-ray spectroscopy (EDS or EDX) and electron backscattered diffraction (EBSD) for the quantitative analysis. EDS is an analytical technique which is widely used to identify the regions of small interest or contaminating spots. It provides the elemental or chemical composition of the samples which can be scanned and imaged in the SEM measurement. The basic principle of the EDS technique relies on the photoelectric effects which emit a characteristic X-ray due to the bombardment of a high energy beam of electrons or X-rays. The energy and count of an emitted X-ray photon from the sample are characteristic of the element that generated it which are collected and identified by an energy dispersive spectrometer. In addition to scanning the electron beam over the sample, the elemental distribution images known as maps or lines scanning can also be performed which is important information for the microanalytical method in SEM.

The diffraction of electrons is an optional technique in SEM occurring from the interactions of the accelerated electron beam with the crystalline or

polycrystalline materials which are obtained using electron backscattered diffraction (EBSD). The EBSD pattern of each diffraction is characteristic of the crystalline structure and orientation of the materials, the so-called Kikuchi bands. The obtained electron diffracted pattern, therefore, is very useful for identifying the crystalline structure, orientation, and phase of the materials. As described above, SEM equipped with an EDS or EBSD device is a very powerful technique for studying the surface topology, morphology, elemental and chemical information, crystalline structure, and orientation of the materials. In this thesis, SEM through FEI QUANTA 450 equipped with an Oxford Instrument electron energy dispersive spectroscopy (EDS), as shown in Figure 3.19 was employed to achieve the surface topologies, morphologies, and elemental composition of the pure DLC and Ti-doped DLC films both before and after the electrochemical measurements.

Figure 3.19 A photograph of SEM (FEI QUANTA 450) equipped with EDS device located at SLRI, Nakhon Ratchasima, Thailand.

3.2.6 X-ray reflectometry (XRR)

XRR is a non-destructive and surface-sensitive analytical tool for determining the thickness, true density, and interface roughness for the multilayered thin film structure of amorphous and crystalline structures. The fundamental principle of the XRR technique involves the interaction of a beam of monochromatic X-rays with the samples. As the X-rays interact with the structure of the samples, they will reflect and provide the intensity of the X-rays in a form of the interference fringe in relation to the change in the layer thickness, surface and interface roughness, and surface and layer density of thin films or multilayered structures. The deviations of the specular reflected intensity of the X-rays, as illustrated by the interference fringe, are determined to obtain the sample's thickness, density, and roughness based on the Fresnel reflectivity (Lengeler, 1990; Parrat, 1954; Wormington et al., 1996; Sinha et al., 1988). The analysis in XRR experiments can be performed using a reflectometry pattern known as the whole-pattern fitting of Parratt's theory (Parratt, 1954; Sakurai et al., 2008). A typical XRR profile is plotted on a semi-logarithmic scale in which a particular stacking structure model is required for the simulated XRR profile of each sample. The best stacking model matches up to the sample structure results in reliably fitting and precise data. An example of the stacking structure models used for determining the density and thickness of the hafnia (Hf) oxide film was simulated, as schematically shown in Figure 3.20. The minimal value of the reliability factor (R) of 0.0197 was obtained for the model D which provides the density and thickness of the HfO_2 film of 8.72 g/cm^3 and 11.5 nm. In this case, the four-layer model that had the SiO_2 and HfSiO layers as intermediate layers were considered the best model.
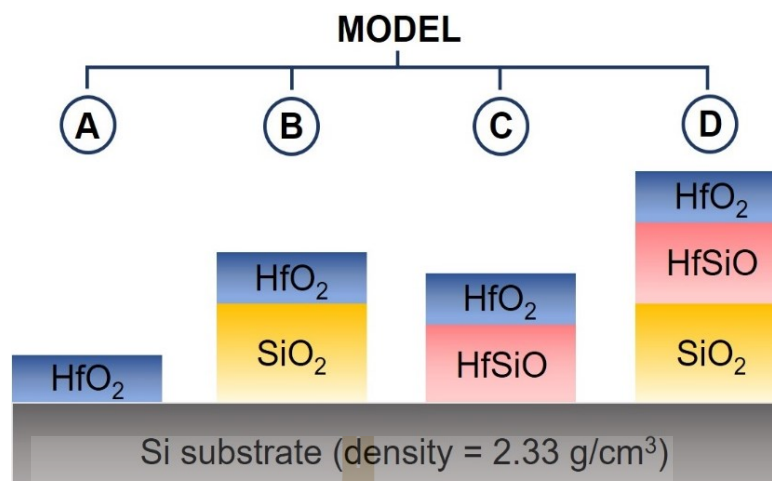
Figure 3.20 The stacking structure model A, B, C, and D of a hafnia oxide film on the Si substrate for simulated XRR fitting adopted from Kishimoto *et al*. (2008).

The XRR profile obtained by the fitting consists of the valuable parameters including a critical angle (θ_c) whose period is correlated to the average electron density which provides the true density, the interference fringes whose period is assigned to the total thickness, and the slope which is related to the roughness, as illustrated in Figure 3.21. In this work, the reflection intensity for the XRR analysis was performed through an X-ray diffractometer (M03XHFMXP3, MacScience), as shown in Figure 3.22. A rotating anode Cu K_α radiation operated at 40 kV and 15 mA with a wavelength of 1.54 Å in the $\theta/2\theta$ configuration was employed. The XRR spectrum was scanned in a range of 0.2–2.5° with a step size of 0.004°. The incident X-ray beam was monochromatized using a curved graphite monochromator. The incident and reflected X-rays were collimated with a receiving slit of 0.05 mm to obtain a parallel and small angle. The film density, thickness, and roughness were evaluated by fitting the simulated reflectivity profile to the experimental reflectivity profile. The best-fit solution is derived by the least squares fitting method with a minimal R factor using a

commercial analyzing package (GXRR software, Rigaku) based on Parratt's theory (Parratt, 1954).
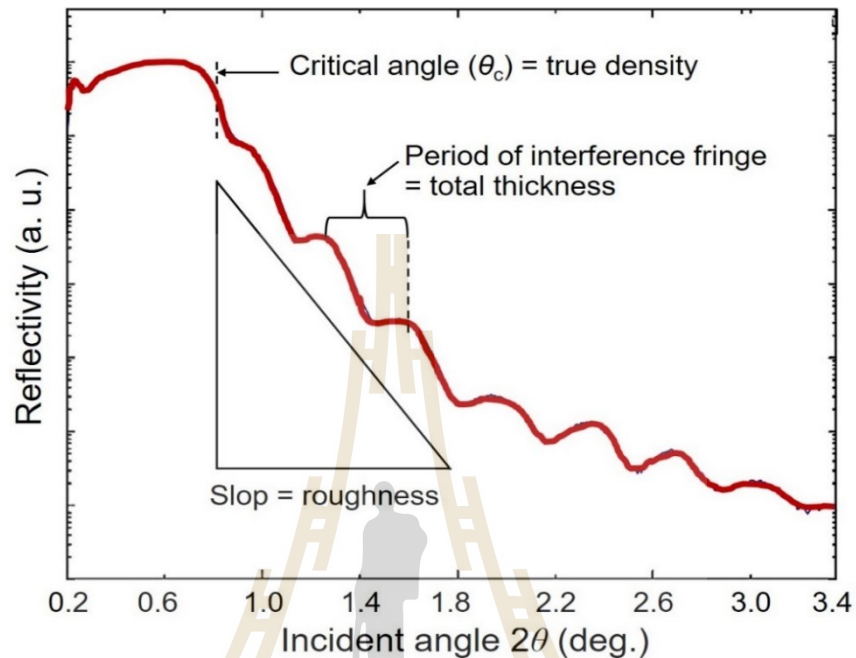
Figure 3.21 A typical XRR profile of thin film which consists of the important parameters, such as critical angle and period of an interference fringe.

Figure 3.22 A photograph of XXR apparatus located at the Department of Materials Science and Technology, NUT, Niigata, Japan used for determining the film's density, thickness, and roughness.

3.2.7 Spectroscopic ellipsometry (SE)

SE is a surface-sensitive and non-destructive optical technique used with many different materials, such as semiconductors, microelectronics, optoelectronics, photovoltaics, optical coatings, surface chemistry, metallurgy, and biomedical components to obtain the thickness and optical constants, such as the refractive index (n) and extinction coefficient (k) of thin films, graded layers, anisotropic layers, and multilayer film structures (Tompkins and Gahan, 1999). The basic principle of SE relies on the reflection and/or transmission of the polarized incident light with the materials (Caurel et al., 2013). The changes in the polarized incident light by interaction with the structure of materials are detected by the amplitude ratio of the ellipsometric angles (ψ) and phase difference (Δ). Since the SE experiments are based on a model-dependent method by numerical inversion, a specific model is required to achieve the best fit. With a minimum mean square error, meaning the matching up between the created model and the real state of the sample, the measured data is reliable and accurate.

The standard and fitting models used for simulating the thickness and optical constant of the pure DLC films are schematically shown in Figure 3.23. The standard model represented a single DLC film on an adhesive layer of Ti. A single DLC film was, however, not a good fit with the real state of the samples with a higher mean square error. In this case, a new model was designed. Taking the surface roughness or void layers into account, the fitting model was considered as the best candidate that provided a lower mean square error. Therefore, it was the most appropriate model with reasonable accuracy. In this work, the SE system (HORIBA, Jobin-Yvon, UVISEL-23301010I) (Aspnes, 1982) with a Xenon arc lamp operated at a power of 75 W was used to generate the light beam with a spot size of 500 μm^2. A wide wavelength range

of 300–1000 nm was conducted to obtain the *n* and *k* of the DLC films. Two independent monochromators at a reflection angle of 70° were employed to reflect the polarized incident light beam onto a sample surface and detect the reflected light beam under an operating temperature of 20°C, as shown in Figure 3.24. The optical constants of the films were calculated using the void volume of 50% by the Bruggeman effective medium approximation (B-EMA) (Aspnes, 1982; Mori *et al*., 1995).
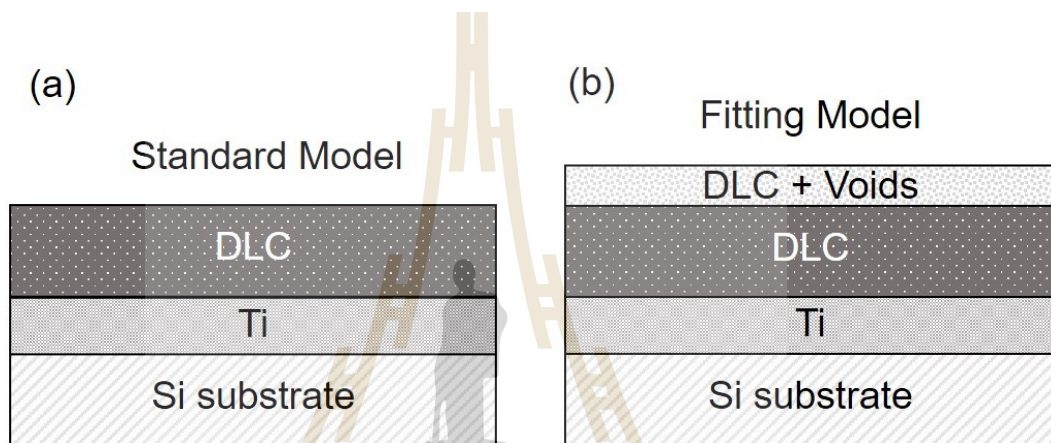
Figure 3.23 The schematic diagrams of (a) the standard and (b) fitting models used for simulating the optical constants of the DLC films adopted from Konkhunthot *et al*. (2018).
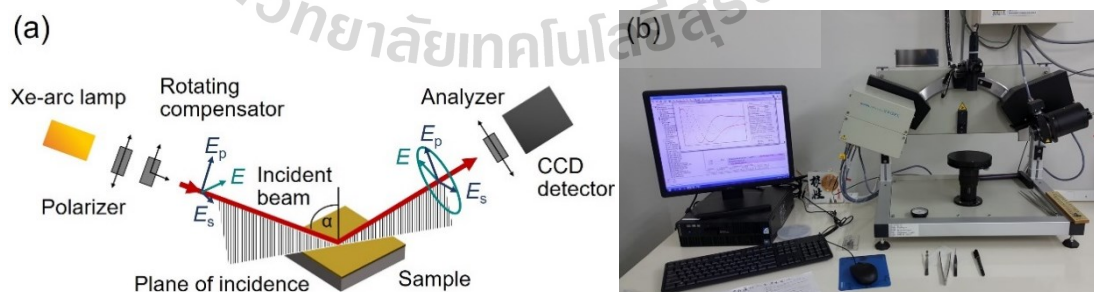
Figure 3.24 (a) Schematic diagram and (b) photograph of SE system located at the Department of Materials Science and Technology, NUT, Niigata, Japan used for measuring the optical constants of the films.

3.3 Electrochemical corrosion analysis

3.3.1 Potentiodynamic polarization technique

A potentiodynamic polarization measurement is routinely performed to obtain the electrical current-potential relationship of the metals surrounded by an aqueous solution. This technique provides important information which is used to assess the electrochemical corrosion behaviors. The mechanisms of the corrosions are associated with the electrochemical reactions of the atomic, ionic, or molecule transportations at a sample interface surrounded by an aqueous solution or electrolyte which results in the dissolution of the metals known as the corrosion process. In this thesis, the corrosion behaviors of the pure DLC and Ti-doped DLC films were explored using potentiodynamic polarization measurement by Autolab potentiostat PGSTAT 128N (Metrohm AG, Switzerland) in an aerated 3.5 wt.% sodium chloride (NaCl) solution consisting of 3.5 g/l NaCl and distilled water (pH $\approx$ 6.6) balanced. The operating temperature was kept at $27 \pm 0.5°C$ during the electrochemical corrosion experiments. Due to the nature of the chemical stability and solvent resistance of the DLC film, the pH of the solution in this work was tuned with 1 M hydrochloric acid (HCl) to 2.0 (an acidic solution) to accelerate the corrosion reactions and to observe the corrosion resistance of the DLC films in a relatively short period of time. From this point, the samples will encounter various active species dissolved in an aqueous solution of pH 2, for example, Cl^-, H^+, and OH^-. These active species, therefore, are a major factor in determining the corrosion rate of the films and might cause more aggressive damage in these experiments..
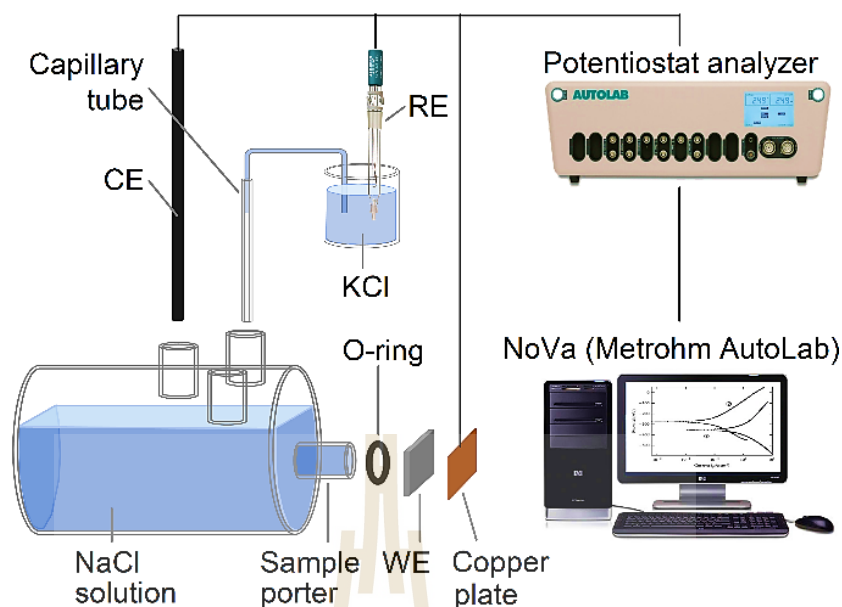
Figure 3.25 A schematic diagram of an electrochemical cell consisting of a standard three-electrode system. The potentiostat analyzer and personal computer with a NoVa (Metrohm Autolab) software used for performing the electrochemical corrosion data are shown adopted from Konkhunthot *et al.* (2019).

For the experimental details, the electrochemical cell of a conventional three-electrode system was constructed which contains the saturated silver to silver chloride (Ag/AgCl) with 3 M potassium chloride (KCl) as a reference electrode (RE), a 99.99% purity graphite rod as a counter electrode (CE), and the samples as a working electrode (WE). The schematic diagram of the electrochemical cell set-up is shown in Figure 3.25. In an attempt to reduce the ohmic drop or iR drop effect during measurements, a capillary glass tube joined to the RE at the end of which the capillary tube was extended very close to the WE surface. The samples were tightly mounted between an O-ring and a copper plate for the electrical connection. An exposed area of the samples was limited by the 6 mm inner diameter of the O-ring which gives the

exposed area inside the O-ring of 0.28 cm². Prior to the corrosion measurements, the samples were exposed to an aqueous solution for 30 min to stabilize the open circuit potential (E_{OCP}) or steady state potential and to stimulate the passivation, if it was present. In the potentiodynamic polarization conditions, a scan rate was set at 0.167 mV/s according to ASTM F 2129; Kociubczyk *et al*. (2015) with a potential range from –500 mN below the E_{OCP} within a cathodic region to +500 mV above the E_{OCP} within an anodic region. The important corrosion parameters, such as the corrosion potential (E_{corr}) and the corrosion density (i_{corr}) were achieved using the Tafel extrapolation technique as a commercial analyzing package. Moreover, the corrosion rate (CR) in millimeters per year (mm/year) can also be calculated by Faraday's law (ASTM standard G102 -89):

$$CR = \frac{K \times i_{corr} \times EW}{\rho}, \tag{3.2}$$

where K is the constant value ($K = 0.13$) and determines the unit of the CR to be mm/year and EW is the equivalent weight which is given by:

$$EW = \frac{1}{N_{EQ}}, \tag{3.3}$$

where $N_{EQ} = \Sigma \left(\frac{f_i n_i}{W_i}\right)$, f_i is the mole fraction of the alloying elements, n_i is the number of electrons transferred during the corrosion, and W_i is the atomic weight of the alloying elements. The ρ in Equation 3.2 can be precisely evaluated to be 2.79, 2.68, and 2.49 g/cm³ for the pure DLC, Ti-DLC1, and Ti-DLC2, respectively, by the XRR method and the detailed measurements in XRR technique can be found elsewhere (Konkhunthot *et*

al., 2018). The porosity (P) of the films is determined using the following expression (Matthes et al., 1991):

$$P = \frac{R_{\mathrm{p}}^0}{R_{\mathrm{p}}} \times 10^{-\left|\Delta E_{\mathrm{corr}}/\beta_{\mathrm{a}}\right|}, \tag{3.4}$$

where R_{p}^0 and R_{p} are the polarization resistance of the substrate and the film, respectively. ΔE_{corr} is the corrosion potential difference between the substrate and the film. β_{a} is the anodic Tafel slope of the substrate. In addition, the protective efficiency (P_{i}) is one of the crucial parameters and can be estimated by this equation (Yu et al., 2003):

$$P_{\mathrm{i}} = 100 \left(1 - \frac{i_{\mathrm{corr}}}{i_{\mathrm{corr}}^0} \right), \tag{3.5}$$

where i_{corr}^0 and i_{corr} are the corrosion current density of the substrate and the films, respectively.

3.3.2 Inductively coupled plasma mass spectrometry (ICP-MS)

The basic principle of the ICP-MS technique is associated with the generation of the ions from liquid solution by an Ar^+ plasma solid-state RF generator at a high temperature between 6000 and 9000°C toward a mass spectrometer where the ions are subsequently separated and analyzed by an ICP-MS detector. Prior to the experiment, the samples of approximately 8 mL acquired from electrochemical corrosion tests were collected into the sample vial and were introduced by a peristaltic pump into a nebulizer where were mixed with Ar gas to form an aerosol. Large aerosols were dropped and eliminated as they touched the wall of the Peltier-cooled spray

chamber. Fine aerosols were, on the other hand, collected into the plasma channel where they were then dried, decomposed, atomized, and ionized as positively charged ions when they passed through the ICP torch. After that, the positive ions were focused by a shield torch before they passed through an orifice and then a skimmer cone into a high vacuum region. The positively charged ions and neutral species were separated by an electrostatic lens into the reactive cell where the octopole reaction system (ORS) with an octopole ion guide was employed for removal of polyatomic spectral interferences as the ions interact and collide with helium gas inside a pressurized reaction cell of the ORS into the true hyperbolic quadrupole. The true hyperbolic quadrupole is a mass filtering used to improve the sensitivity of the spectrum. The spectral peak was then separated based on the mass to charge (m/Z) ratio. Finally, the abundance ions entered through the advanced detection system of an electron multiplier detector where the electronic signals were processed and collected in a multi-channel scaler generating a mass spectrum. Subsequently, the intensity at a given mass of the spectrum was proportional to the concentration of the isotope.

In this thesis, the ICP-MS (Agilent 7500ce, USA) technique, as shown in Figure 3.26, was performed for the ultra-trace determination over a wide concentration range of elements, particularly the released metallic ions after the electrochemical corrosion measurements against the obtained potentiodynamic polarization results. For the qualitative analysis of the type and concentrations of the released metallic ions, the standard solutions with an exact concentration of Ti, Cr, Mn, Fe, Ni, and Mo were prepared from a 1000 ppm commercial solution to have the following concentrations: 0.001, 0.03, 0.05, 0.07, and 0.1 mg/L, respectively. In ICP-MS experiments, the solutions acquired from the individual samples and standard

solution were collected into the sample vial and then loaded onto a tray before being analyzed. The helium collision mode, the ORS and hyperbolic quadrupole technology, and internal standard solution were used to optimize the data acquisition. The intensity of the standard spectra was conducted for the calibration curves. Four samples of each condition were performed to achieve the average statistical data.
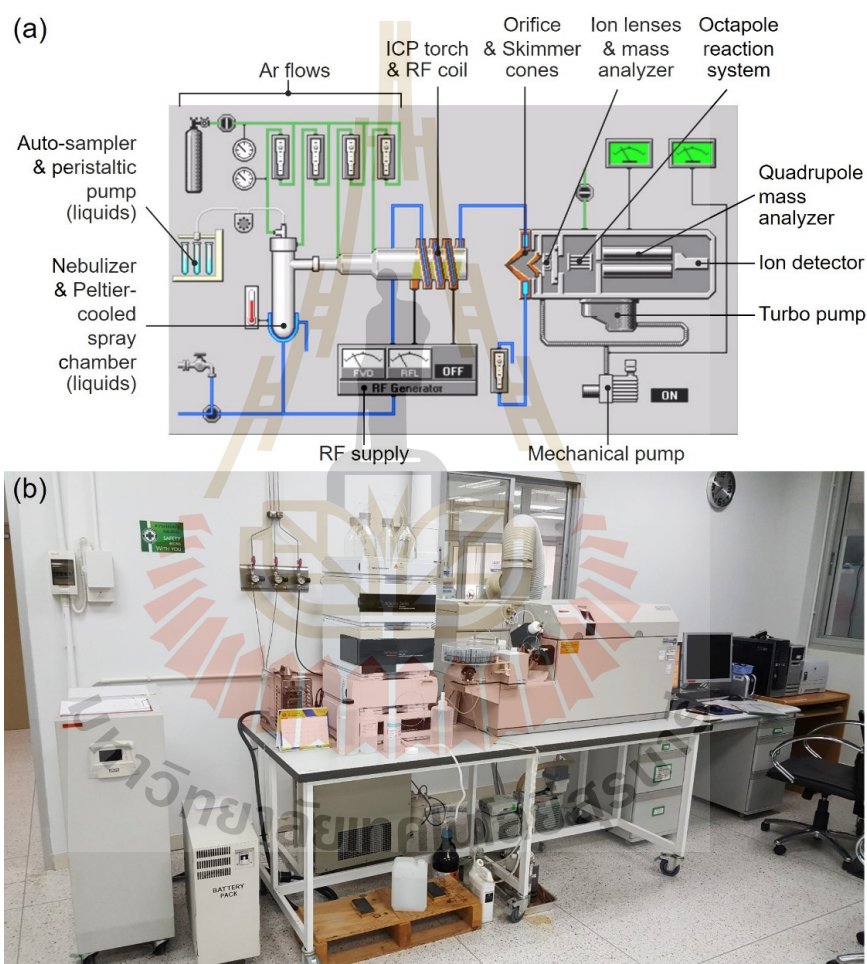
Figure 3.26 (a) Schematic diagram and (b) photograph of the ICP-MS device located at the Center for Scientific and Technological Equipment, SUT, Nakhon Ratchasima, Thailand.

3.4 Mechanical and Tribological performance analysis

3.4.1 Pico- and Nano-indentation tests

Data acquisitions of the instrumented indentation method are based on calculation by the power law fitting through the cycle of the loading and unloading process (Oliver and Pharr, 1992, 2003). In a typical indentation test, both a diamond Berkovich-triangular pyramidal and Vickers indenter can be used. The measured penetration depth is compared to the calibrated diamond indenter to evaluate the H and E of the films, as schematically shown in Figure 3.27. The important parameters which include the maximum indentation load (P_{max}), indenter displacement at maximum load (h_{max}), and the contact stiffness ($S = dP/dh$) can be obtained from the load-indentation displacement curve and subsequently are used in the calculation of the H and E values. Taking into account all the 3 parameters, the H can be calculated by the ratio of the P_{max} and the contact area (A) under load which is given by:

$$H = \frac{P_{max}}{A},$$

(3.6)

where A is the kh_c, in which k is the proportionality constant depending on the bluntness of the indenter; $k = 24.5$ for the Berkovich or Vickers indenter, and h_c is the contact depth which is defined as:

$$h_c = h_{max} - h_s.$$

(3.7)

The elastic deflection (h_s) is the $\epsilon(P_{max}/S)$, in which ϵ is the constant relating to the geometry of the indenter. The reduced elastic modulus (E_r) can be estimated by the following equation:

$$\frac{1}{E_r} = \left[\left(\frac{1-v_s^2}{E_s}\right)\right] + \left(\frac{1-v_i^2}{E_i}\right), \tag{3.8}$$

where E_s and E_i are the Young's moduli for the sample and indenter, respectively, and v_s and v_i are the Poisson ratio for the sample and indenter, respectively.
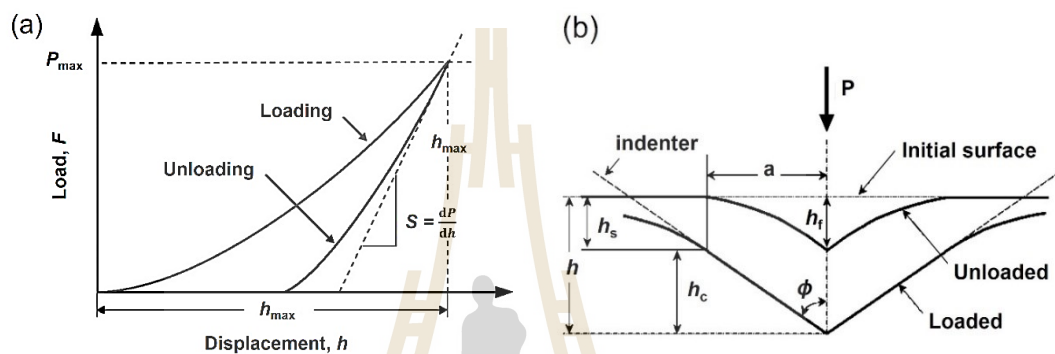
Figure 3.27 The schematic representations of (a) the indentation load versus indentation displacement curve and (b) the loading-unloading process with the important parameters modified from Oliver and Pharr (1992, 2003).

Two analytical techniques used in the measurement of the mechanical properties, such as the hardness (H) and Young's modulus (E) of the pure DLC and Ti-doped DLC films are the pico- and nano-indentation tests, as shown in Figure 3.28(a) and (b). In the preliminary study, the mechanical properties of the pure DLC films deposited on the Si substrates by pulsed two-FCVA deposition at a different V_{bias} were measured by pico-indentation (FISCHER H-100) system located at the Department of Materials Science and Technology, NUT, Niigata, Japan. In each sample, 6 repeated indentations were carried out to achieve satisfactory statistical reliability and average values. Prior to the measurement, a fused SiO_2 standard was first conducted to ensure

that the pico-indentation system was calibrated. An applied ultra load of 0.1mN at the maximum indentation depth of less than 10% of the total film thickness was performed to reduce the Si substrate effects. A diamond Vickers indenter was constantly moved at a speed of 0.1 m/s with the loading and unloading rates of 0.001 mN/s. At the maximum load, the indenter was paused and held for 10 s. The measured values from the loading and indentation depth curve are calculated based on the Oliver and Pharr method [Oliver and Pharr, 1992, 2003, 2004).

In the study of the Ti-doped DLC films, the mechanical properties were measured by nano-indentation measurement through the NanoTest (Micro Materials, UK) located at the Center for Scientific and Technological Equipment, SUT, Thailand. The nano-indentation technique is a modular system which is designed for nano-indentation, nano-scratch, and nano-impact tests. Since it is based on the pendulum-based depth-sensing method, the most reliable information about the nano-mechanical behavior of an amorphous carbon thin film can be obtained (Beake *et al*., 2006; Hassan *et al*., 2015). In this experiment, the sample was vertically placed on the platform while the normal load was electromagnetically applied with respect to the sample surface normal. Meanwhile, the flowing current in the conductive coil drives the pendulum to rotate and induces a diamond tip to penetrate the sample. A simultaneous measurement of the displacement was performed through a parallel capacitor plate, which gives the resolution in the nanometer scale. Six indentations were also conducted for each sample with a Berkovich-type diamond indenter to attain the statistical reliability value. A fused SiO_2 standard was also used to calibrate the system before the measurement. The maximum penetration depth of an indenter into a sample surface was maintained to be less than 20 nm to avoid the effect from the underlying substrate (Modabberasl *et al*.,

2015; Ishpal *et al.*, 2012; Liu *et al.*, 2003; Trava-Airoldi *et al.*, 2007) which is approximately 15% of the total film thickness from a previous study of the literature (Konkhunthot *et al.*, 2018). The nano-indentation load versus indentation displacement curve was carried out with a loading rate of 0.1 mN/s and a holding time of 10 s at a maximum load before unloading. The nano-mechanical properties of the Ti-doped DLC films in comparison with the pure DLC films can be obtained using the Oliver-Pharr method (Oliver and Pharr, 1992, 2003, 2004) effective for determining mechanical values, for instance, the contact hardness (Zhang *et al.*, 2005).
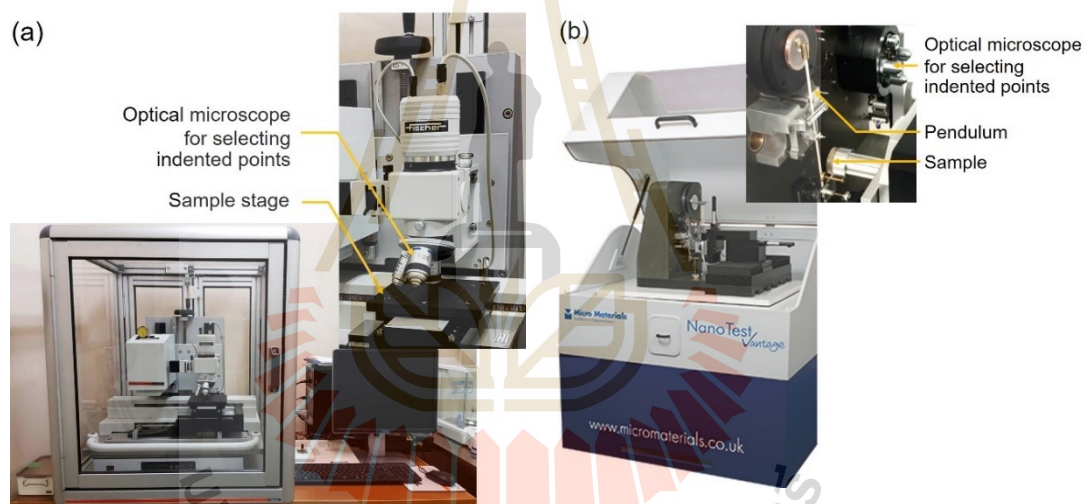
Figure 3.28 Photographs of (a) pico-indentation and (b) nano-indentation apparatus used for mechanical property measurement.

3.4.2 Nano-scratch tests

Adhesion strength is one of the major properties for the films used in tribological applications which can be directly evaluated by the nano-scratch method, especially DLC films on steels, and can be obtained through nano-scratch testing. In the nano-scratch experiment, the applied load and sliding distance of the indenter on a

sample's surface can be precisely controlled, as the samples mounted on the platform or stage are vertically moved against the indenter and the friction force and acoustic emission are continuously monitored.
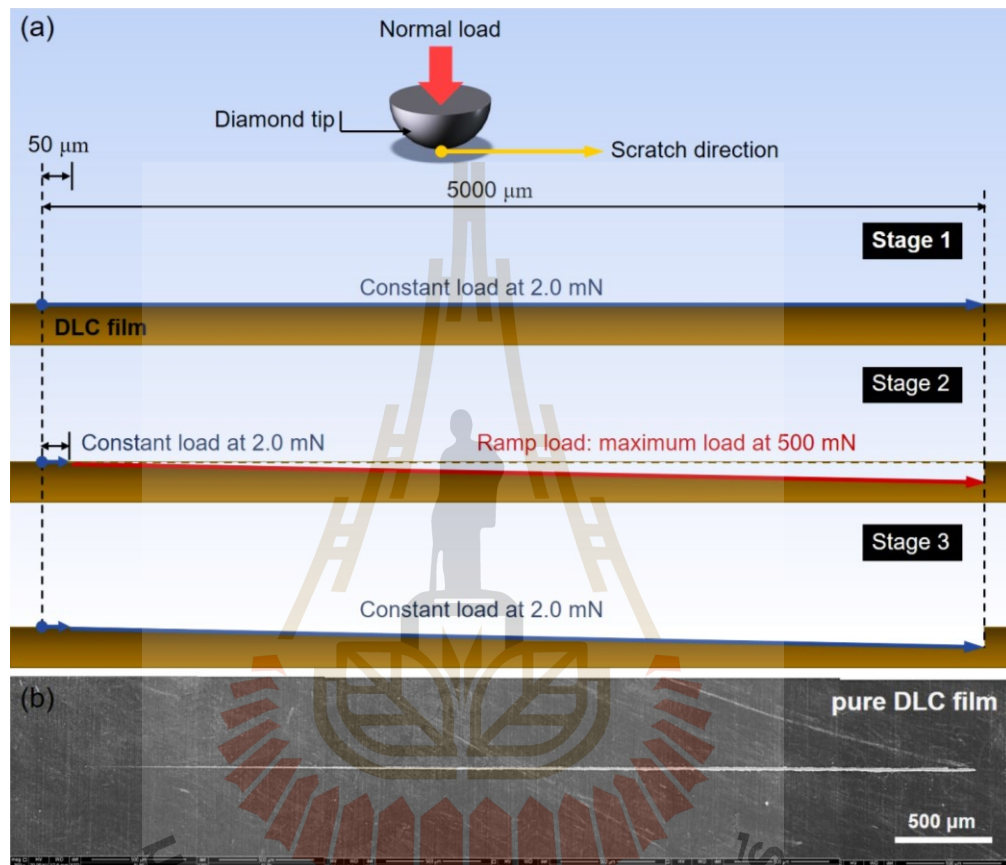
Figure 3.29 A schematic illustration of (a) nano-scratch procedures with three sequential stages and (b) SEM micrograph of residual scratched track of the pure DLC film.

For typical nano-scratch measurements, 3 scratch tracks were conducted for an individual sample using a 90° conospherical diamond tip with a 5 μm nominal radius, as given in Figure 3.29. A pre-scratching procedure was regularly performed to remove any surface roughness, topography, slope, and instrument bending effects

(Beake *et al*., 2006; Hassan *et al*., 2015). The nano-scratch procedures in a multipass wear test mode involved 3 sequential scans at a velocity of 50 μm/s over a scan length of 5000 μm by the following stages: (1) a preliminary topography scan at a constant load of 2.0 mN, (2) a scratch scan where the constant load was conducted over the first 50 μm and then ramped at 3.0 mN/s to a maximum load of 500 mN, and (3) a final topography scan at a 2.00 mN constant load over the scratched track. Three scratches were carried out at a new location and along a 5000 μm straight line, as can be seen in Figure 3.29(a). A very low speed of 50 μm/s was maintained during the scratch tests to reduce the graphitization of the DLC films due to the thermal effect. The SEM and a digital capture system were employed to observe the residual scratched tracks and define the scratch parameters, such as the critical load (L_c), as can be seen in Figure 3.29(b). The COF of the films as a function of scratch distance is calculated by the ratio of the lateral friction force (F) to the applied normal load (L) which provides the failure mechanisms and tribological properties of the films. The nano-indentation and scratch tests in this thesis were performed under humidity and temperature conditions of approximately 50% and 27 ± 0.5°C, respectively.

CHAPTER IV

RESULTS AND DISCUSSION

Chapter IV is associated with the results and discussion of this thesis which is divided into 2 main parts. The first part or a preliminary study entitled "*The optical and mechanical properties of DLC films: Correlation between microstructures and deposition conditions*" was performed to search for the appropriate deposition conditions for depositing the DLC films. This part dealt with the deposition of the DLC films by the pulsed two-FCVA technique at different V_{bias}. A variation of the V_{bias} in a range of 0.0–1.5 kV was conducted to manipulate the energy of the ions in the plasma before arriving at the substrate. These energetic ions directly affected the microstructure and properties of the DLC films. In these experiments, a film's microstructure and compressive internal stress were measured using the Raman spectroscopy. The chemical bonding structure in terms of the sp^3/sp^2 ratio and the physical properties, e.g., density (ρ), thickness (t), and roughness, were accurately determined through the XPS and XRR techniques. The mechanical properties, for example, hardness and elastic modulus of the DLC films were evaluated by means of the pico-indentation test. A film's optical properties, such as the refractive index and extinction coefficient were measured with the SE method. The influences of the V_{bias} during a film's growth on the microstructure and the properties of the DLC films were analyzed and discussed in the first part.

Another part with the title "*Enhancement of thermal stability, adhesion strength, tribological property, and corrosion protection performance of DLC films on stainless steels by Ti incorporation*" is mainly concerned with the incorporation or doping of the Ti atoms into the DLC films, typically called the Ti-doped DLC films, and the characterization of the deposited films. The best deposition condition acquired from a preliminary study was selected for depositing the undoped (pure) DLC and Ti-doped DLC films in this part. The microstructures and a variety of properties including thermal stability, adhesion strength, mechanical and tribological properties, and corrosion protection performance of the Ti-doped DLC films were thoroughly investigated relative to the pure DLC films. The conversion of the sp^3/sp^2 ratio due to thermal annealing in the aspect of thermal stability of the films was investigated by the NEXAFS technique. The internal stress of the pure DLC and Ti-doped DLC films was studied using the Raman spectroscopy. The mechanical properties and adhesion strength were assessed through the nano-indentation and nano-scratch tests. The corrosion protection performance of the deposited films was measured by means of the potentiodynamic polarization technique. The surface morphologies after the electrochemical corrosion tests and the corrosion-induced structural transformation were interpreted via the SEM and NEXAFS equipped with the X-PEEM methods. The roles of the Ti concentration levels in the DLC films on the microstructure, the sp^3/sp^2 ratio, thermal stability, adhesion strength, mechanical and tribological properties, and corrosion behavior were investigated and described in detail.

4.1 The optical and mechanical properties of DLC films: Correlation between microstructures and deposition conditions

4.1.1 Microstructure analysis

In a preliminary study, the microstructure of the DLC films was investigated by Raman spectroscopy over a range of 900–1900 cm^{-1}. To obtain the qualitative results, i.e., the Raman parameters, the Raman spectrum of the DLC films was deconvoluted into 2 typical Gaussian functions, the D band located at approximately 1350 cm^{-1} and the G band located at approximately 1540 cm^{-1}. The position of these 2 bands showed a good consistency with the results reported by others (Lung *et al*., 2001). The breathing mode of the graphitic sp^2 sites due to the disordered structure within the sixfold aromatic rings was known as the D band and the stretching mode in both the rings and chains of the sp^2 sites was associated with the G band (Ferrari and Robertson, 2000; Casiraghi *et al*., 2005). Figure 4.1 demonstrates the Raman spectra of all the deposited films prepared at the different V_{bias} of 0.0, 0.5, 1.0, and 1.5 kV, respectively. The black and red lines illustrated the experimental and fitted curves. The deconvolution of the D and G bands is shown in the bright green lines. The standard materials of glassy carbon and highly ordered pyrolytic graphite (HOPG) were also plotted here for comparison. In these experimental details, the DLC films deposited at the V_{bias} of 0.0, 0.5, 1.0, and 1.5 kV were frequently denoted as the DLC-0, DLC-1, DLC-2, and DLC-3, respectively.
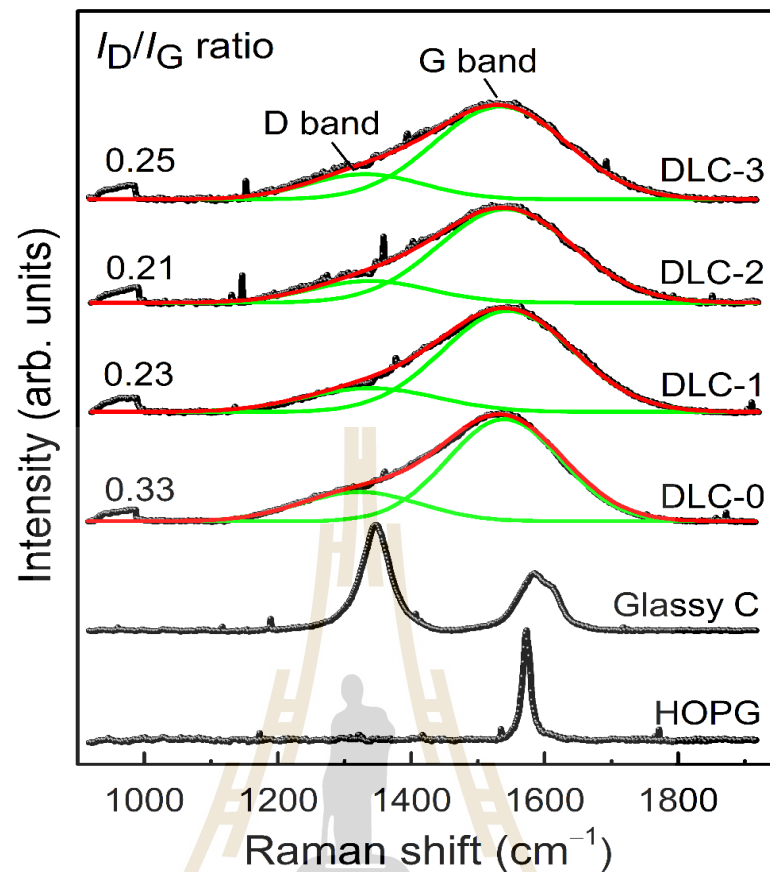
Figure 4.1 The Raman spectra of the DLC films deposited at V_{bias} against the standard materials of glassy carbon and HOPG modified from Konkhunthot *et al.* (2018).

As can be seen in Figure 4.1, the peak located at approximately 950 cm^{-1} was attributed to a second-order phonon scattering of the underlying Si substrates (Prawer *et al.*, 1996). The peak intensity of this spectrum was suggestive of the optical transparency of the films depending on the sp^3 hybridizations in the DLC structure. The Raman parameters, such as the D and G band positions, FWHM(D) and (G), intensity ration of the D and G bands (I_D/I_G ratio), cluster size of the sp^2 sites (L_a), and internal stress (σ) are listed in Table 4.1.

Table 4.1 The detailed Raman parameters of the DLC films deposited at different V_{bias}.

Sample	V_{bias}	D band		G band		I_D/I_G ratio	L_a	σ
	(kV)	Position	FWHM	Position	FWHM		(nm)	(GPa)
		(cm^{-1})	(cm^{-1})	(cm^{-1})	(cm^{-1})			
DLC-0	0.0	1347.4	239.3	1531.4	207.6	0.33	7.7	0
DLC-1	0.5	1331.1	214.2	1543.2	235.5	0.23	6.5	2.0
DLC-2	1.0	1321.1	209.6	1545.7	238.5	0.21	6.1	2.4
DLC-3	1.5	1321.2	226.3	1540.4	232.2	0.25	6.7	1.5

The alteration in the I_D/I_G ratio and σ were calculated and plotted as shown in Figure 4.2. The inset in Figure 4.2 shows the correlation between the position of the G band and the FWHM(G). As can be seen in Figure 4.2, the I_D/I_G ratio abruptly decreased from 0.33 to 0.21 as the V_{bias} increased from 0.0 to 1.0 kV and slightly increased from 0.21 to 0.25 with the further increase to 1.5 kV of V_{bias}. The variation in the I_D/I_G ratio due to the V_{bias} was associated with the change in the carbon network structure in the DLC film. Based on a three-stage model proposed by Ferrari and Robertson (2004) it was found that the decrease in the I_D/I_G ratio and the increase in the G band position were related to the conversion of the ordered graphitic C-sp^2 (graphite-like carbon) to C-sp^3 (diamond-like carbon) bonds and the changes in the sp^2 hybridizations from rings to chains. The minimum I_D/I_G ratio at the V_{bias} of 1.0 kV, therefore, was accompanied by the maximum sp^3 content which was consistent with the mechanical values.
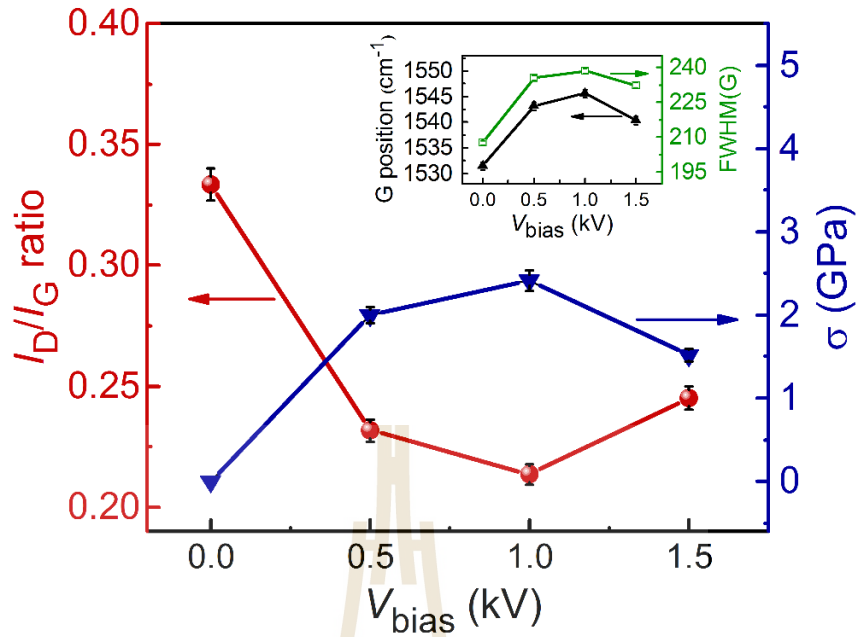
Figure 4.2 The relationship of the I_D/I_G ratio and the **σ** as a function of the V_{bias}. The inset shows the G band position versus the FWHM(G) at different V_{bias} modified from Konkhunthot *et al.* (2018).

The positions of the G band were 1531.42, 154.19, 1545.64, and 1540.34 cm^{-1} for DLC-0, DLC-1, DLC-2, and DLC-3, respectively, as also listed in Table 4.1. It is well-known that the shift in the position of the G band was related to the stress condition in the DLC film which could be calculated using the following equation (Narayan, 2005; Lubwama *et al.*, 2013; Miki *et al.*, 2015; Nakamatsu *et al.*, 2005):

$$\sigma = 2G \left[\frac{1+\nu}{1-\nu}\right]\left[\frac{\Delta w}{w_0}\right], \tag{4.1}$$

where G is the shear modulus (Lifshitz *et al.*, 1989) ($G = 70$ GPa), ν is the Poison's ratio of approximately 0.3 (Lifshitz *et al.*, 1989), Δw is the shift in the Raman wavenumber of the G band, and w_0 is the Raman wavenumber of reference.

By choosing the position of the G band of the DLC-0 as the reference Raman wavenumber in Equation 4.1, the relative compressive σ in the DLC films at the different V_{bias} could be calculated to be 1.99 ± 0.10, 2.41 ± 0.12, and 1.33 ± 0.08 GPa for DLC-1, DLC-2, and DLC-3, respectively. The shift of the G band position upward to a higher Raman wavenumber was due to the changes in the carbon network structure during the film's growth (Miki *et al*., 2015) which was indicative of the larger σ in the DLC films. Figure 4.2 shows the relationship of the I_D/I_G ratio and the σ as a function of the V_{bias} along with the G band position and FWHM(G) in the inset. As seen in Figure 4.2, the opposite trend between the I_D/I_G ratio and the σ was observed as the V_{bias} increased from 0.0 to 1.0 kV. This indicated the formation of the sp^3 content with the increase in the σ. The existence of the σ was related to the interatomic force constant and interatomic separation which could be explained through the atomic vibrational frequency (Narayan, 2005; Lubwama *et al*., 2013). As the DLC films were subjected to mechanical compression, the bond lengths within the DLC structure decreased, and the force constants and the vibrational frequencies increased (Narayan, 2005; Lubwama *et al*., 2013). Hence, the interatomic distance became shorter which led to the increase in the compressive σ and the density of the DLC structure, as confirmed by the XRR analysis. The occurrence of the compressive σ in the DLC films also involved the impingement of the ions during the film growth which could be describe this phenomenon using the subplantation model (Lifshitz *et al*., 1989; Lifshitz *et al*., 1990). Regarding this model, as the incident ion in the plasma impacted the substrates, the atomic packing density increased. The density of the atomic packing structure generated the intrinsic stress condition within the films which was the preferred formation of the C-sp^3 sites in the DLC structure. However, as the V_{bias} further increased,

the compressive stress was likely to decrease due to the release of the residual stress and the bombardment with high energetic ions at a high V_{bias}.

The inset in Figure 4.2 reveals the similar feature of the G band position and the FHWM(G) as a function of the V_{bias}. The variations in the FWHM(G) corresponded to the disordered structure and the L_a of the sp^2 sites in the DLC films. In this work, the L_a of the sp^2 sites in the DLC films was estimated by the following equation:

$$\frac{I_D}{I_G} = C'(\lambda) L_a^2, \tag{4.2}$$

where $C'(514 \text{ nm})$ is the constant value (~ 0.0055) (Ferrari and Robertson, 2000).

The L_a of the DLC-0, DLC-1, DLC-2, and DLC-3 was measured to be 7.8, 6.2, 6.0, and 6.6 nm, respectively. This result elucidated the role of the V_{bias} on the L_a of the sp^2 sites. The decrease in the L_a of the sp^2 sites was correlated to the decrease in the I_D/I_G ratio and the increase in the FWHM(G) which was consistent with the other reports in the literature (Ferrari $et\ al.$, 2003). It, therefore, should be noticed that the DLC films with the higher sp^3 content provided a lower value of L_a.

The XPS was employed to measure the elemental chemical composition and the sp^3/sp^2 ratio of the DLC films. Figure 4.3(a) and (b) illustrated the C 1s and O 1s XPS spectra of the DLC films deposited at the different V_{bias}, such as the DLC-0, DLC-1, DLC-2, and DLC-3, respectively. The C 1s XPS spectra showed the multiple bonding states of the carbon atoms as can be observed in Figure 4.3(a). The C 1s XPS spectra were deconvoluted into 3 Gaussian peaks to estimate the sp^3/sp^2 ratio in the DLC films through the XPS technique. The first peak located at approximately 284.3

eV and the second peak located at around 285.3 eV were assigned to the C═C bonds (C-sp^2 hybridizations) and the C—C bonds (C-sp^3 hybridizations), respectively. The other higher binding energy range of 286.0–287.0 eV corresponded to the C—OH bonds and C—O and/or O—C═O bonds which were attributed to the atmosphere or gas exposure of the dangling bonds (Chen *et al*., 2001; Ahmed *et al*., 2013; Rüdiger *et al*., 2012; Phase and Sathe, 2004). In addition to the C 1s XPS spectra, the O 1s XPS spectra of the DLC films were concerned as shown in Figure 4.3(b). A broad peak located between 531.3 and 532.9 eV was due to the C—O and C—OH bonds which was the nature of the oxides on the DLC surface (Chen *et al*., 2001; Ahmed *et al*., 2013; Rüdiger *et al*., 2012; Phase and Sathe, 2004; Milošev *et al*., 2000).
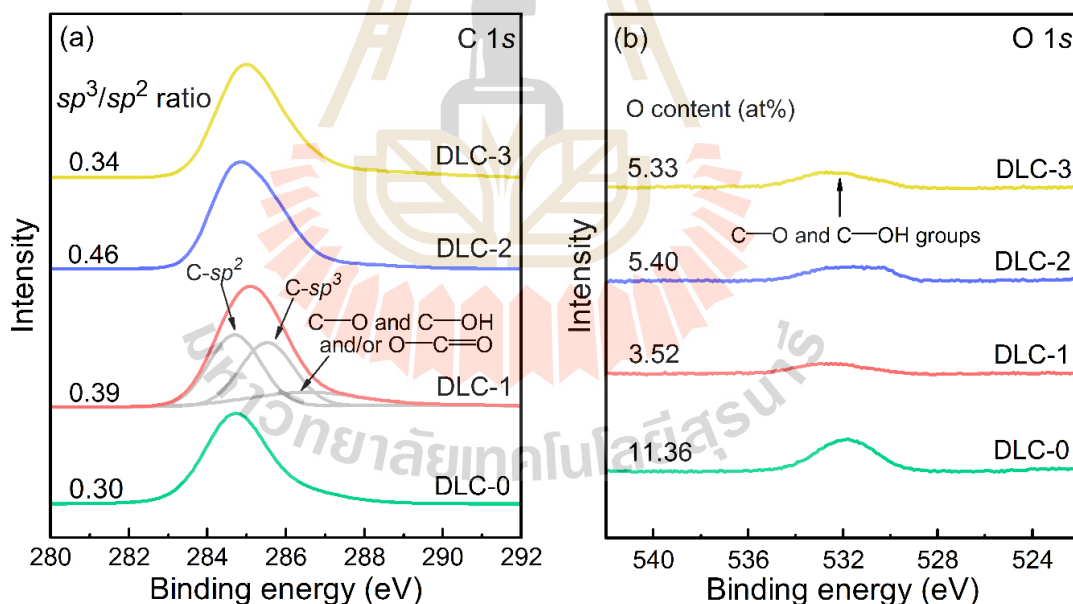
Figure 4.3 (a) The C 1s (a) and (b) the O 1s XPS spectra of DLC-0, DLC-1, DLC-2, and DLC-3, respectively, modified from Konkhunthot *et al*. (2018).

The sp^3/sp^2 ratio of all the DLC films could be acquired by dividing the area of each peak to the total area. The estimated sp^3/sp^2 ratio and the O atomic percentage of the DLC films are listed in Table 4.2. As can be seen in Table 4.2, the amount of the O content greatly decreased from 11.36 to 3.52 as the V_{bias} increased from 0.0 to 0.5 kV. This was indicative of a large decrease in the O percentage in the DLC films during the increasing V_{bias} which was consistent with the results as reported elsewhere in the literature (Damasceno and Camargo, 2008). As there was a further increase in the V_{bias} from 0.5 to 1.5 kV, the amount of the O percentage revealed a slight change between 3.52 and 5.40 at.% which was not significant in the O content at the higher V_{bias}. The results of the XPS analysis, however, confirmed the enhancement of the sp^3 content in the DLC films under biasing conditions and the decrease in the O content.

According to the Raman and XPS analysis, it was found that the sp^3/sp^2 ratio in the DLC films was observed to be effectively controlled by adjusting the V_{bias}. The mechanism used for describing the formation of the C-sp^3 bonding in the DLC films was based on the subplantation process depending on the energy of the incident ions. In the DLC deposition without the biasing condition, the incident ions with not enough energy cannot penetrate into a surface and are thus just stuck on a sample's surface in the form of the C-sp^2 graphite-like phase. As the V_{bias} was higher, the incident ions of higher energy were capable of penetrating the surface into the subsurface interstitial site. This process generated the local density and local compressive internal stress within the DLC structure, which was a suitable condition to form the C-sp^3 diamond-like phase. However, as the V_{bias} further increased, the higher energy of the incident ions penetrated deeper into the sublayer and resulted in the displacement of the

atoms. This process led to an accumulation of the phonons or the energy in the form of heat. The generation of heat within the film structure, in turn, relaxed an excess of local density and the compressive stress in the DLC structure and was caused by the reduction in the C-sp^3 diamond-like character, as demonstrated by the increase in the I_D/I_G ratio at the V_{bias} of 1.5 kV (Robertson, 1993, 2002; Ferrari *et al.*, 2002).

Table 4.2 The ρ, *t*, roughness, sp^3/sp^2 ratio, and O content of the DLC films acquired from XRR and XPS.

Sample	V_{bias} (kV)	ρ (g/cm^3)	*t* (nm)	roughness (nm)	sp^3/sp^2 ratio	O content (at.%)
DLC-0	0.0	–	–	–	0.30	11.36
DLC-1	0.5	2.73	105.04	3.77	0.39	3.52
DLC-2	1.0	2.79	143.66	4.17	0.46	5.40
DLC-3	1.5	2.51	98.66	5.11	0.34	5.33

4.1.2 Physical property analysis

The physical properties, such as density, thickness, and roughness of the DLC films could be obtained using the XRR technique, which was an appropriate and precise tool used for the multi-layer thin films. Figure 4.4 demonstrates the XRR profiles of the deposited DLC films at the different V_{bias} over an incident angle range of 0.2–2.5°. The black and red lines represented the experimental and simulated XRR profiles. The accurate values of the density (ρ), thickness (*t*), and surface roughness of the deposited films could be acquired with a minimum reliability factor of 0.02–0.05 which confirmed that the simulation was reasonable for a measured sample. The reflectivity profiles consisted of a critical angle and interference fringe, which provided information about the average electron density and the total thickness, respectively.
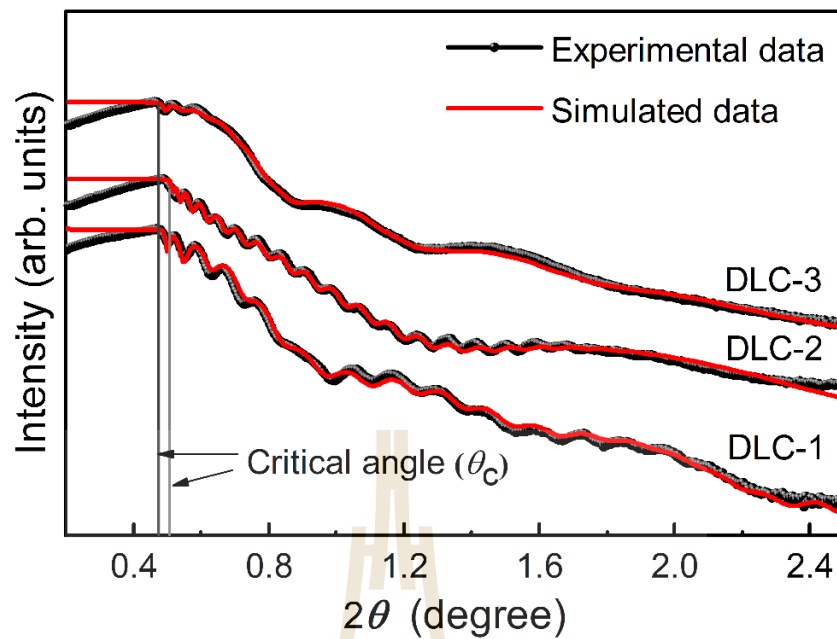
Figure 4.4 The XRR profiles of the DLC films deposited at different V_{bias} of 0.0, 0.5,

1.0, and 1.5 kV, respectively, adopted from Konkhunthot *et al*. (2018).

The ρ of the deposited films could be obtained by simulating the critical

angle at a low angle with the following equation (Ferrari *et al*., 2000; Chu and Li, 2006;

Zhang *et al*., 1998; Liu *et al*., 2016; Kishimoto *et al*., 2008):

$$\rho = \left[\frac{\pi \theta_c^2}{N_A r_e \lambda^2} \right] \left[\frac{X_C(M_C - M_H) + M_H}{X_C(Z_C - Z_H) + Z_H} \right], \tag{4.3}$$

where θ_c is the critical angle in radian, r_e is the classical electron radius, N_A is

Avogadro's number, λ is the wavelength used by the instrument, X_C and X_H are the

relative atomic fraction of C and H (in this case the atomic fraction of X_H is a form of

1–X_C), respectively, Z_C and Z_H are the atomic numbers of C and H, respectively, and

M_C and M_H are the molar mass of C and H, respectively. In addition, the correlation

between the density and thickness of the films was estimated as follows (Kishimoto *et al.*, 2018):

$$\rho = \frac{\Sigma\rho_i t_i}{\Sigma t_i}, \tag{4.4}$$

where ρ_i and t_i are the density and thickness of each layer, respectively. The thickness of the DLC films could be obtained by replacing the density from Equation 4.3 into Equation 4.4.

To obtain the exact values of the ρ, t, and roughness of the films from the XRR method, the deposited film should have a smooth surface without any film delamination. However, it was found that the DLC film deposited without the V_{bias} (DLC-0) had some spalling. The DLC-0, therefore, was not in a good condition for measurement by the XRR method and the values of this sample are not shown in Figure 4.4. The simulated data acquired from the XRR profile are also listed in Table 4.2. As seen in this table, the ρ of the films was 2.73, 2.79, and 2.51 for DLC-1, DLC-2, and DLC-3, respectively, which showed a significant change by adjusting the V_{bias}. The interference fringes could be observed for all the reflectivity profiles which confirmed that the deposited films by the pulsed two-FCVA deposition contained more than a single layer, the so-called multilayered films (Ferrari *et al.*, 2000; Van der Lee *et al.*, 2001). It was noticed that the ρ of the films was increased as the V_{bias} increased. The maximum value of the ρ was measured for DLC-2 (2.79 g/cm^3) associated with the V_{bias} of 1.0 kV. The XRR profile of DLC-3 revealed a different feature which corresponded to the reduction in the ρ and t as demonstrated by a smaller number and larger period compared to the other films. The ρ of DLC-3 (2.51 g/cm^3) decreased and showed a

lower value than that of DLC-1 (2.73 g/cm^3) which indicated that a longer development of the ρ did not occur as the V_{bias} increased further to 1.5 kV. The reduction in the ρ of the deposited films at a higher V_{bias} was caused by the relaxation of the excess internal compressive stress and local density within the amorphous carbon structure. The bombardment of the high energetic ions at a high V_{bias} resulted in the increase in the substrate temperature which led to the transition of the sp^3 diamond-like to sp^2 graphite-like carbon known as the graphitization process (Sugimoto *et al*., 2013). The correlation of the ρ and the sp^3/sp^2 ratio of the DLC films had a similar effect to the variation in the V_{bias}. In addition, it was noticed that the DLC films with a lower I_D/I_G ratio exhibited a higher ρ and the sp^3/sp^2 ratio as confirmed by the XPS and Raman results.

The t of the deposited films was simulated to be 105.0, 143.6, and 98.7 nm for DLC-1, DLC-2, and DLC-3, respectively. The t of the films was initially increased with the increase in V_{bias} from 0.0 to 1.0 kV, but decreased with the further increase in the V_{bias} up to 1.5 kV. A lesser predominance of the deposition process than the self-sputtering process of the substrate materials under higher energetic ions resulted in the reduction in the t of the deposited films. The effect of the sputtering yields, therefore, must be less than the deposition process to obtain the film growth (Lifshitz, *et al*., 1989). The diffusion layer between the DLC film and an adhesive layer of Ti was also estimated to be approximately 2.70 ± 0.9 nm in thickness. The diffusion layer was almost unchanged during film growth with a density of 4.37 ± 0.8 g/cm^3. The diffusion layer was a mixture of the carbon ion impingements into the surface of a Ti intermediate layer. The impingement of a high energy of the ions generated at a high V_{bias} on a Ti intermediate layer was the main reason for the monotonic increase in the

surface roughness of 3.77, 4.17, and 5.11 nm for DLC-1, DLC-2, and DLC-3, respectively.

4.1.3 Mechanical property analysis

The hardness and elastic modulus could be acquired from the pico-indentation load and indentation depth curves based on the Oliver and Pharr method (Oliver and Pharr, 1992, 2004). The pico-indentation load and indentation depth curves of the DLC films at the different V_{bias} of 0.0, 0.5, 1.0, and 1.5 kV, respectively, are illustrated in Figure 4.5.
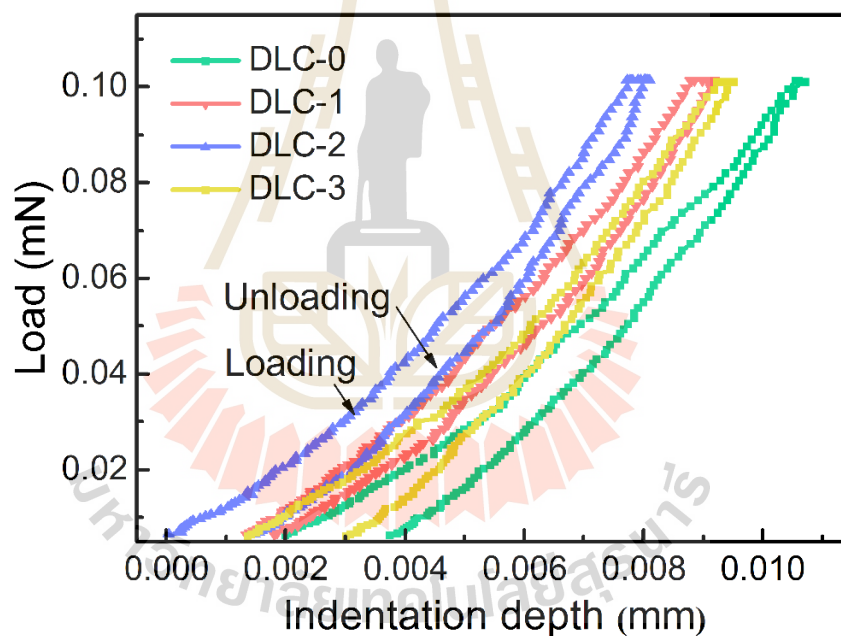
Figure 4.5 Pico-indentation load versus indentation depth of the DLC films deposited at different V_{bias} modified from Konkhunthot *et al.* (2018).

In pico-indentation experiments, the ultra-low applied load of 0.1 mN was employed to control the indentation depth in a range of 8–11 nm which was less than 10% of the total film thickness. The effect of the Si substrate, therefore, could be

reasonably neglected during a pico-indentation measurement (Fischer-Cripps, 2006; Andriollo *et al*., 2017; Liang *et al*., 2015; Mirkarimi *et al*., 1997; Guo *et al*., 2015). As can be observed in Figure 4.5, it was found that the indentation depth of the deposited films was first decreased from 10.8 to 8.0 nm as the V_{bias} increased from 0.0 to 1.0 kV and then slightly increased from 8.0 to 9.5 nm with the further increases up to 1.5 kV. The hardness of DLC-1 and the DLC-2 experienced a significant improvement compared to DLC-0 as demonstrated by the reduction in the indentation depth by applying the V_{bias}. This revealed that the V_{bias} was an effective method for adjusting the mechanical properties of the DLC films deposited by the FCVA deposition.
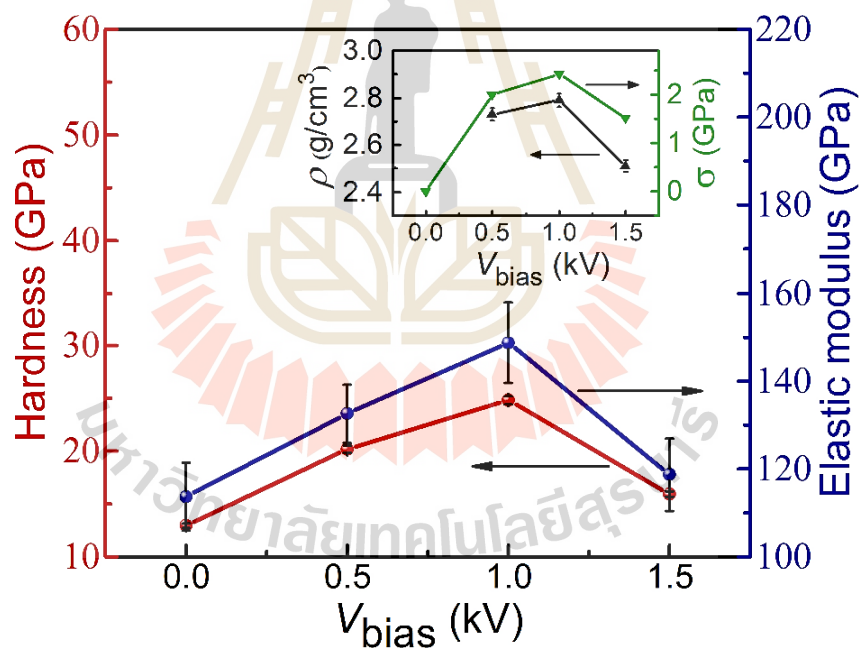
Figure 4.6 The hardness and elastic modulus of the DLC films deposited at different V_{bias} along with the correlation between the ρ and the σ as a function of V_{bias} (see inset) modified from Konkhunthot *et al*. (2018).

Figure 4.6 shows a typical plot between the hardness and elastic modulus of the DLC films prepared at the various V_{bias}. The inset in Figure 4.6 illustrates the relationship of the ρ and internal stress in the DLC films as a function of the V_{bias}. The summarized results of the hardness and elastic modulus of the DLC films are also listed in Table 4.3.

Table 4.3 The hardness and elastic modulus of the DLC films deposited at different V_{bias}.

Sample	V_{bias} (kV)	Hardness (GPa)	Elastic modulus (GPa)
DLC-0	0.0	12.93 ± 0.95	113.64 ± 7.66
DLC-1	0.5	20.18 ± 1.23	132.57 ± 6.62
DLC-2	1.0	24.83 ± 2.10	148.66 ± 9.20
DLC-3	1.5	15.94 ± 1.41	118.68 ± 8.22

As seen in Figure 4.6, the hardness and elastic modulus of the deposited films showed the maximum value of 24.83 and 148.66 GPa as the V_{bias} increased to 1.0 kV. The hardness and elastic modulus decreased as the V_{bias} was less than or more than 1.0 kV which was indicative of a significant change in the carbon network structure during the increasing V_{bias} in this range. An ion subplantation model was employed to describe this phenomenon (Robertson, 2002; Lifshitz *et al*., 1989; Robertson, 1993; Ferrari *et al*., 2002) which was contained in the following 3 stages: (i) the energetic ions collision at the surface, (ii) the thermalization, and (iii) the relaxation of the excess local density and loss of the sp^3 phase. According to a subplantation model, the enhancement of the mechanical properties was associated with the increase in the ρ and internal compressive σ in the DLC films which was between the collision of the ions and the thermalization process. This enhancement was consistent with the other

researchers (Guo *et al*., 2015; Lin *et al*., 2017; Tai *et al*., 2006; Guo *et al*., 2017; Robertson, 1992; Zhang, Lau, Sheeja, and Tay, 2005; Gou *et al*., 2007; Chowdhury *et al*., 2004; Singh *et al*., 2009).

It was observed from the pico-indentation result that the hardness of the DLC films had a relatively low value compared to the other DLC films deposited by FCVA deposition which was in a range of 20–80 GPa (Guo *et al*., 2015; Robertson, 2003; Kamiya *et al*., 2008; Zou *et al*., 2011). This result was related to the presence of oxygen in the DLC films. The XPS analysis showed that a relatively high oxygen content in the DLC films during the films' growth at high base pressure was a result of a lower value of the hardness. The roles of the base pressure or residual gas pressure during the films' growth were related to the observed reduction in the mechanical properties which had also been investigated in the other literature (Wu *et al*., 2007; Dwivedi *et al*., 2013). They reported that as the residual gas pressure was increased, the energy of the ions decreased. This was due to the collisional phenomenon between the atoms and molecules and/or ions in the gas background and the plasma. With a low energy of the ions, the highly graphitic phase was formed and thus led to the reduction in the hardness of the deposited films. The other investigations showed that large oxygen-incorporated DLC films might be trapped on the interfacial regions which resulted further in breaking the bonding between the deposited films and the substrate and had a comparatively lower hardness. It could, however, be noticed that the best conditions for the film deposition with the highest hardness of approximately 25 GPa associated with a density of 2.79 g/cm^3 were nearly comparable for the *ta*-C films with a hardness of more than 20 GPa and density close to 3 g/cm^3 (Robertson, 2002; Luo *et al*., 2007; Grill, 1997). From the above-mentioned results, the deposition of the DLC

films at the V_{bias} of 1.0 kV would be the best condition in a preliminary study which provided high-quality *ta*-C films. For a detailed understanding, the mechanical properties of the DLC films, a fine step of the V_{bias} should be applied during the film deposition.

4.1.4 Optical property analysis

The optical properties, such as the reflective index and extinction coefficient of the DLC films deposited at various V_{bias} of 0.0, 0.5, 1.0, and 1.5 kV, respectively, were investigated by the SE technique. Figure 4.7(a) and (b) illustrates the plot between the reflective index and extinction coefficient against the wavelength of the DLC films at the different V_{bias}. It can be observed from Figure 4.7 that the reflective index of the DLC films deposited under the bias condition increased with the rise in the wavelength and started to become saturated when the wavelength increased up to 750 nm. The DLC-0, on the other hand, displayed different features with the decrease in the reflective index as the wavelength increased from 300 to 1000 nm. The extinction coefficient of the DLC films deposited under the biasing showed a small change and was found to decrease gradually with the increase in the wavelength. This indicated that the biased DLC films became transparent at higher wavelengths, typically beyond 800 nm, while the DLC film deposited without the biasing showed different features with a slight rise as the wavelength increased to more than 500 nm. The reflective index and extinction coefficient of the DLC films measured at the wavelength of 550 nm are also listed in Table 4.4.
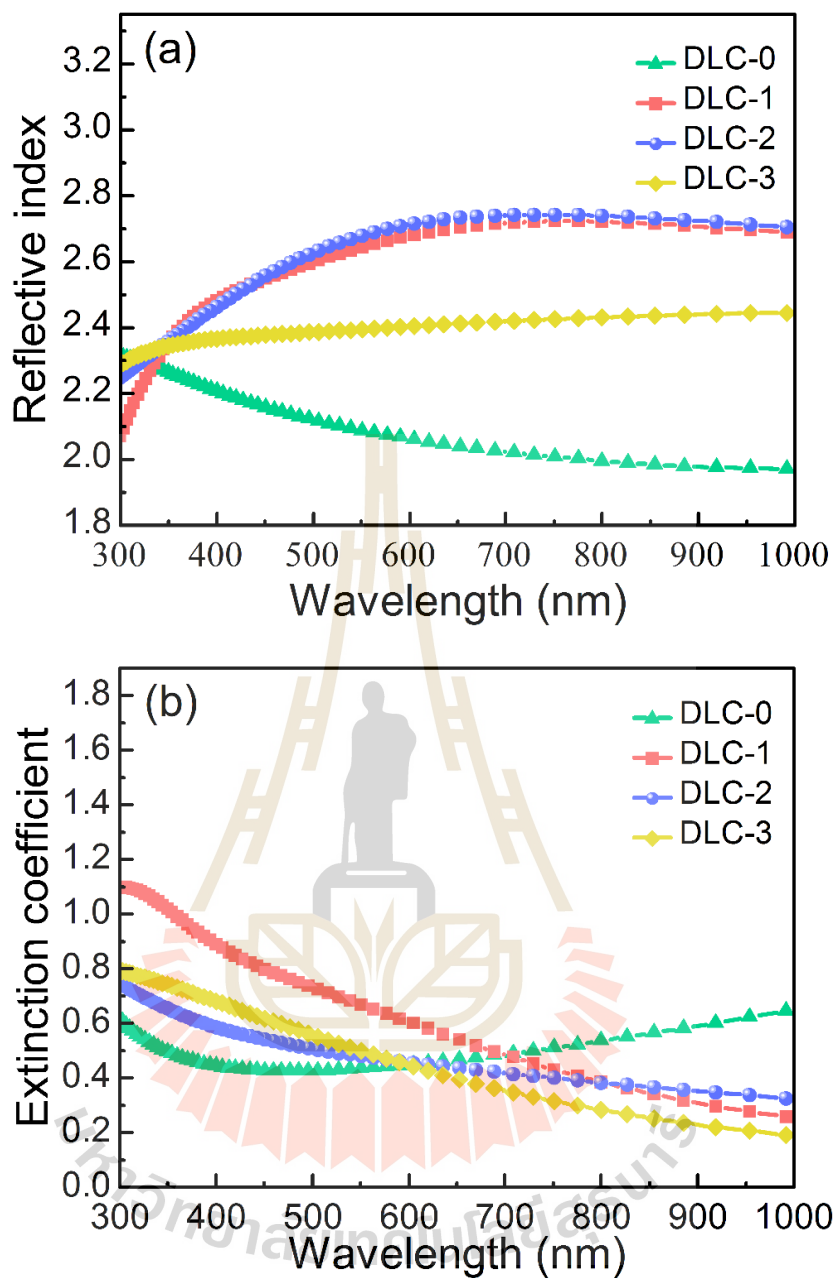
Figure 4.7 The optical constants, such as reflective index (a) and extinction coefficient
(b) of the DLC films deposited at different V_{bias} over a range of 300–1000
nm wavelength modified from Konkhunthot *et al.* (2018).

Table 4.4 The summarized reflective index and extinction coefficient of the films

deposited at different V_{bias}.

Sample	V_{bias}	Reflective index	Extinction coefficient
	(kV)	(wavelength, $\lambda = 550$ nm)	
DLC-0	0.0	2.10	0.43
DLC-1	0.5	2.64	0.61
DLC-2	1.0	2.68	0.53
DLC-3	1.5	2.58	0.49

As can be seen in Table 4.4, the reflective index and the extinction coefficient of the DLC films were observed to be in the range of 2.10–2.68 and 0.43–0.61, respectively. Previous research groups have reported that the increase in the reflective index and the decrease in the extinction coefficient of the DLC films were correlated with the increase in the film transparency and the sp^3 content, respectively (Lee, Collins *et al*., 1998; Hiratsuka *et al*., 2013). From the results, it was obvious that the extinction coefficient of all the DLC films had almost no change from applying the V_{bias}. It remained at an approximately constant value at 0.52 ± 0.09 which was indicative of the minor impact of the V_{bias} on the film transparency. The relatively constant value of the extinction coefficient might be caused by a Ti intermediate layer effect which was a naturally non-transparent material (Axelevitch *et al*,, 2012). Only the relationship between the refractive index and the DLC properties, therefore, was considered. In this work, the reflective index was directly related to the sp^3 content in the DLC films as confirmed by the XPS analysis. It was seen that a lower value of the reflective index was measured as the V_{bias} increased above or decreased below 1.0 kV.

As previously described, the reflective index and the I_D/I_G ratio were the important parameters related to the sp^3 content and the mechanical properties of the DLC films. However, the relationship of the reflective index and I_D/I_G ratio has not been systematically investigated. This relationship, therefore, would be further studied and discussed as shown in Figure 4.8.
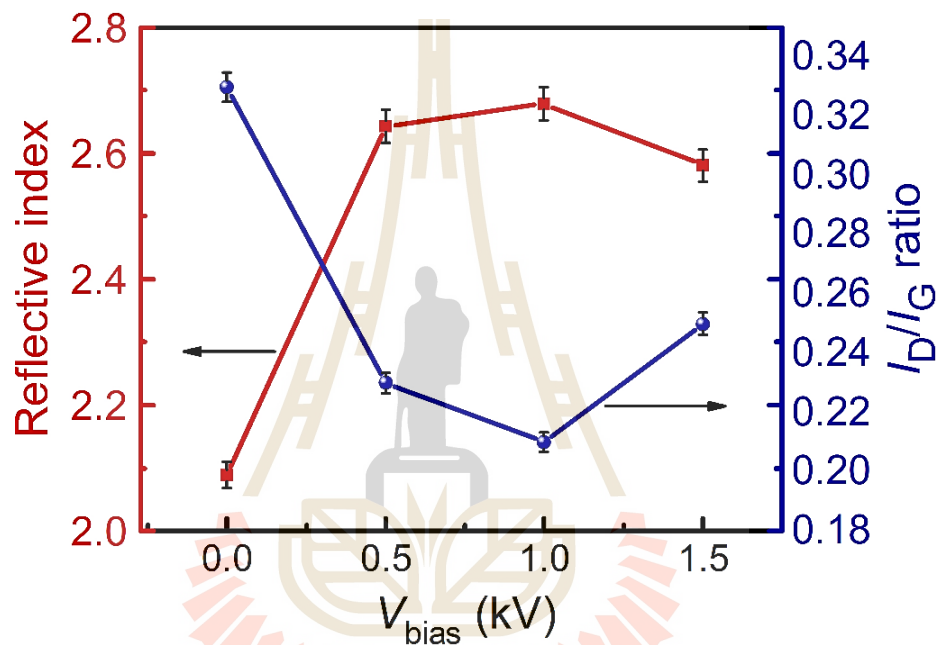
Figure 4.8 The established correlation between the reflective index and the I_D/I_G ratio of the DLC films deposited at various V_{bias} modified from Konkhunthot *et al*. (2018).

As seen in Figure 4.8, the opposite trend between the reflective index and I_D/I_G ratio was observed. The reflective index increased as the I_D/I_G ratio decreased depending on the V_{bias}. The maximum value of the reflective index (= 2.68) and the minimum value of the I_D/I_G ratio (= 0.21) were measured at the same condition, the V_{bias} of 1.0 kV. The further increase of the V_{bias} up to 1.5 kV resulted in the decrease in the reflective index

and the increase in the I_D/I_G ratio. It was found that the reflective index and the I_D/I_G ratio were well correlated with the microstructural, physical, and mechanical properties of the DLC films depending on the deposition parameters, especially the V_{bias}. For this case, the established correlation between the reflective index and the I_D/I_G ratio should be emphasized since it could be used for inferring the microstructure in terms of the sp^3/sp^2 ratio, ρ, and hardness of the DLC films which was the most important parameters in determining the properties of the DLC films. To acquire these important values through the established correlation, the method used was either the reflective index or the I_D/I_G ratio acquired from a comparatively simple and non-destructive analytical technique from the SE and Raman techniques (Ferrari and Robertson, 2004). Using the established correlation, the number of samples for the experiment could be reduced which is a cost-effective method for industrial applications.
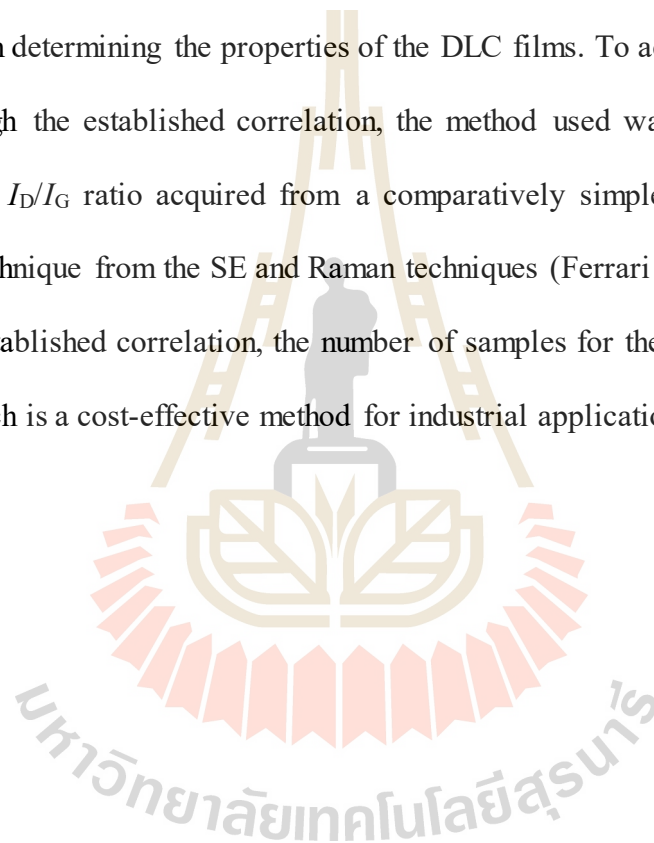
4.2 Enhancement of thermal stability, adhesion strength, tribological property, and corrosion protection performance of DLC films deposited on stainless steels by Ti incorporation

4.2.1 Surface morphology and chemical composition analysis

By coupling the SEM/EDS and XPS techniques, the surface morphologies and chemical compositions of the pure DLC and Ti-doped DLC films were explored. In these experiments, 2 concentration levels of Ti in the DLC films were controlled by adjusting the applied arc voltages of 0.65 and 0.80 kV connected to a Ti cathode as revealed in Table 4.5. These samples were subsequently designed as Ti-DLC1 and Ti-DLC2. Figure 4.9 demonstrates the surface morphologies and the peak intensity acquired from the SEM and EDS of the pure DLC, Ti-DLC1, and Ti-DLC2, respectively. From the SEM micrographs, a very smooth surface and uniform density were observed for all the films. There was no film delamination found which indicated that an adhesive layer of Ti was beneficial to considerably improve the film adhesion strength to the substrate. The columnar structures and grains were not observed over the film surface which was due to an amorphous carbon structure of the DLC films. Although the magnetic filtering had been employed, some macro-particles were captured over the film surface which was a typical characteristic of cathodic arc deposition.
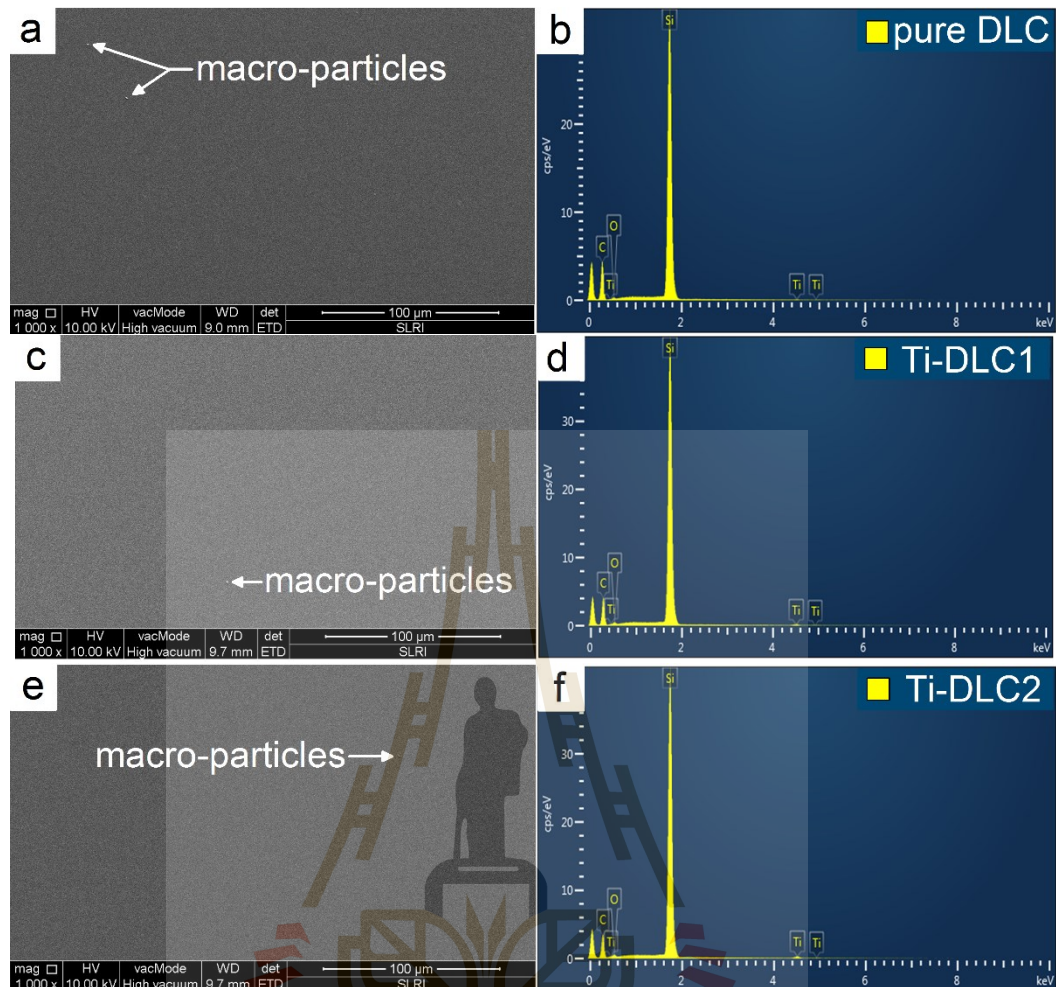
Figure 4.9 SEM micrographs of (a) pure DLC, (c) Ti-DLC1, and (e) Ti-DLC2, and the EDS spectra of (b) pure DLC, (d) Ti-DLC1, (f) Ti-DLC2, respectively. The macro-particles are indicated by an arrow modified form Konkhunthot *et al.* (2019).

The existence of the small amount of microparticles had been considered as a minor point in certain mechanical and tribological applications. It might, however, be the major problem in corrosive environments when it acts as an initial point for the localized corrosion. SEM equipped with the EDS technique was used to provide information about the chemical characterization in terms of the elemental composition analysis of the deposited films, particularly the Ti atoms in the Ti-doped DLC films. A

spot size of the incident beam of around 3 mm × 3 mm on the sample covered the distribution of Ti over the sample surface. The EDS spectra of the pure DLC film mainly demonstrated the Si and C peaks which originated from an underlying Si substrate and the DLC film, respectively. The O and Ti peaks were also observed, and they had a rather weak intensity due to the limitation of this technique. It was, however, confirmation of the incorporation of the Ti atoms into the DLC films. In addition to the EDS, the elemental concentration of the DLC films was accurately analyzed by the XPS technique. Table 4.5 illustrates a variation in the chemical elemental composition of all the deposited films. From the XPS analysis, the concentration levels of the C atoms decreased from 97.8 to 92.6 at.% with the increase in the concentration levels of the Ti atoms from 0.0 to 2.1 at.%. The O percentage also increased together with the increasing Ti percentage which was attributed to the formation of the oxide film once the Ti-doped DLC surface was exposed to oxygen in the air. This was represented as an absorbed O atom on the Ti-doped DLC surface (Francz *et al.*, 1999). The oxide layer formed on the Ti-doped DLC surface was, however, believed to prevent the diffusion of the active species or water molecules into the underlying substrate. It, hence, inhibited the damages from the active species which will be described later in the Electrochemical corrosion behavior analysis section.

Table 4.5 The elementary composition of the pure DLC, Ti-DLC1, and Ti-DLC2, respectively, acquired from the XPS analysis.

Sample	Arc voltage (−V)		Concentration level (at.%)		
	C cathode	Ti cathode	C	O	Ti
pure DLC	800	–	97.8	2.2	0.0
Ti-DLC1	800	650	95.8	3.4	0.8
Ti-DLC2	800	800	92.6	5.3	2.1

4.2.2 Raman spectroscopy analysis

Raman spectroscopy was routinely performed to obtain microstructural information on the pure DLC and Ti-doped DLC films. In this experiment, the Raman spectra of the pure DLC, Ti-DLC1, and Ti-DLC2, respectively, in a range of 800–2000 cm^{-1} were recorded as shown in Figure 4.10. The black and red lines represent the experimental and fitted curves. The deconvolution of the D and G bands is presented in the bright green lines.
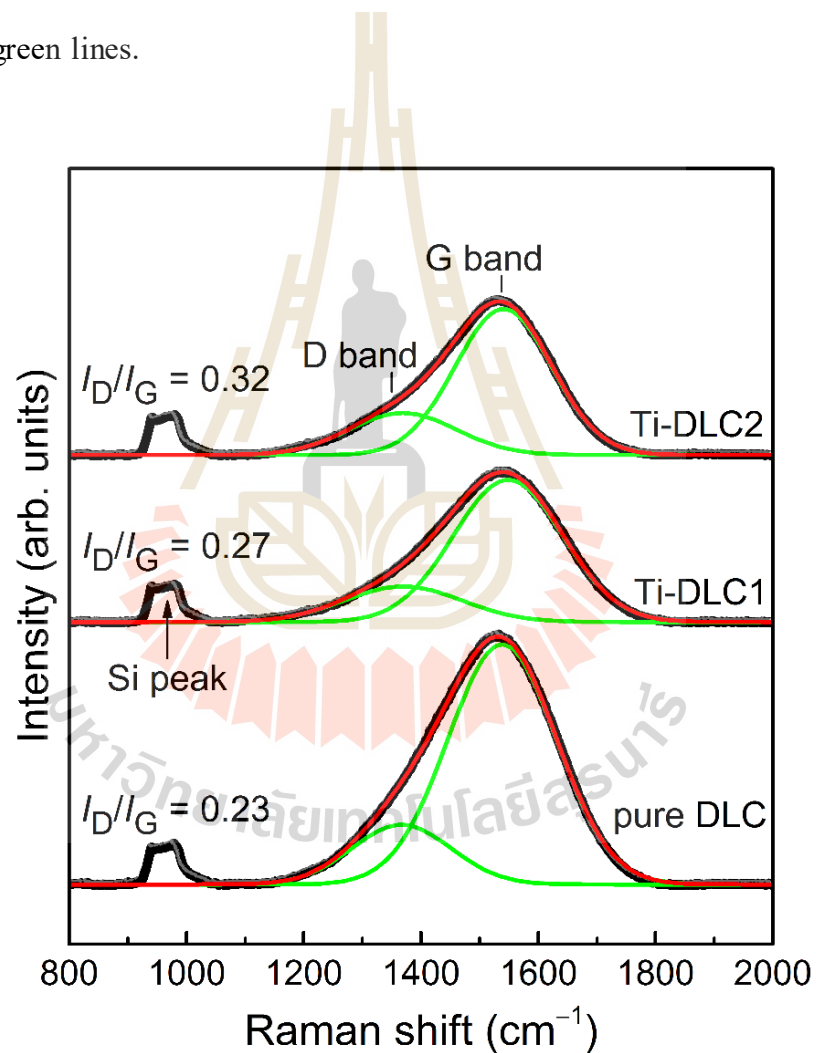
Figure 4.10 Raman spectra of the pure DLC, Ti-DLC1, and Ti-DLC2, respectively, adopted from Konkhunthot *et al*. (2019).

The DLC films were deconvoluted in their Raman spectra region into 2 Gaussian functions located at approximately 1545 and 1355 cm^{-1}, respectively. The first band, G, was for the zone center phonons due to the symmetric E_{2g} stretching mode of all the sp^2 sites in both rings and chains (Ferrari and Robertson, 2000; Chu and Li, 2006). Another band, D, was for the zone-edge K-point phonons due to the symmetric A_{1g} breathing mode of the sp^2 sites in aromatic rings as a result of the bond angle's disordered structure (Ferrari and Robertson, 2000; Chu and Li, 2006). The square feature observed at approximately 950 cm^{-1} was attributable to the second-order spectral region of the underlying Si substrate. This feature indicated the optical transparency of the measured films (Zhang et al., 2005). The Raman parameters, such as the G band position, full width at half maximum of the G band (FWHM(G)), and I_D/I_G ratio of the pure DLC and Ti-doped DLC films acquired by the fitting the Raman spectra are listed in Table 4.6.

Table 4.6 The summarized Raman parameters of the pure DLC and Ti-doped DLC films acquired from the Raman analysis.

Sample	G band position (cm^{-1})	FWHM(G)	I_D/I_G ratio
Pure DLC	1546.5	220.9	0.23
Ti-DLC1	1545.4	218.5	0.27
Ti-DLC2	1540.7	194.8	0.32

From the Raman spectra, the position of the G band shifted toward the lower wavenumber with the increasing amount of the Ti atoms. The shift of the G band position involved the fluctuation in the cluster size of the graphite and the cumulative stress in the deposited films (Ferrari, and Robertson, 2001). This observation was also

found as a function of the V_{bias} as shown in the previous description (Konkhunthot *et al*., 2018). The investigation showed that the shift of the G band position toward the lower wavenumber was caused by a large amount of the cumulative stress developed by the subplantation process. In addition to the increased internal stress, the density and the sp^3 content in the DLC films were observed to increase.

In a comparison to the results from Konkhunthot *et al*. (2018) shift of the G band toward the lower wavenumber with the increasing Ti doping level led to the reduction in the internal stress of the Ti-doped DLC films. There were 3 factors used to describe this situation: (i) the addition of the Ti atoms into the DLC structure led to the decrease in the sp^3 content and resulted in the reduction in the internal stress; (ii) The existence of the adatom mobility due to the bombardment with the Ti$^+$ ions generated a new degree of freedom causing the relaxation in the local density and intense sp^3 hybridized bonds and thus, the reduction in the internal stress; (iii) the introduction of the Ti atoms was as a result of the distortion of the atomic bond-angle disorder within the DLC structure and led to the reduction in the internal stress (Qiang *et al*., 2013; Lifshitz *et al*., 1989). Although the density and sp^3 content were lower with the reduction in the internal stress, the adhesion of the films was in turn better. This advantage will be further described later in the Adhesion analysis section. Furthermore, the low and high values of the FWHM(G) and I_D/I_G ratio of the Ti-doped DLC films could be indicative of the increase in the sp^2 hybridized bonds in both numbers and sizes (Ferrari and Robertson, 2001) which was consistent with the NEXAFS results and mechanical properties as further described in detail here.

4.2.3   Local bonding structure and thermal stability analysis

NEXAFS spectroscopy was carried out to elucidate local bonding information of the pure DLC and Ti-doped DLC films as a function of thermal annealing over the range from RT to 500°C. Figure 4.11(a)–(c) demonstrates the C K-edge NEXAFS spectra of the pure DLC, Ti-DLC1, and Ti-DLC2, respectively, annealed within the UHV at various annealing temperature ranges from RT to 500°C, respectively. As seen in Figure 4.11, these spectra showed different features in the local bonding configuration as a function of thermal annealing. The pre-edge peak at the photon energy of approximately 285.4 eV was due to the transition of the C 1s core-level electrons to the unoccupied π^* symmetry orbitals mainly generated from the sp^2 (C=C) and the sp (C≡C) sites if presented. The broad region from approximately 288 to 335 eV was attributable to the overlapping C 1s to the unoccupied σ^* transition at the sp, sp^2, and sp^3 sites.

It was noticed that the Ti-doped DLC films showed a small area of the broad region of the C K-edge NEXAFS spectra compared to the pure DLC film. The intensity ratio of the pre-edge peak and broad region of the pure DLC films tended to increase with the Ti doping level which inferred the transformation of the sp^3 into sp^2 hybridized carbon the so-called graphitization process. The spectral features of the Ti-doped DLC films were not much different to those of the pure DLC films which indicated that the carbon network structure almost did not change with a small doping concentration level of the Ti atoms. Additionally, the observed results confirmed that the intensity ratio of the annealed films was larger with the increased annealing temperature. This indicated the occurrence of the graphitization process of the films under thermal annealing.
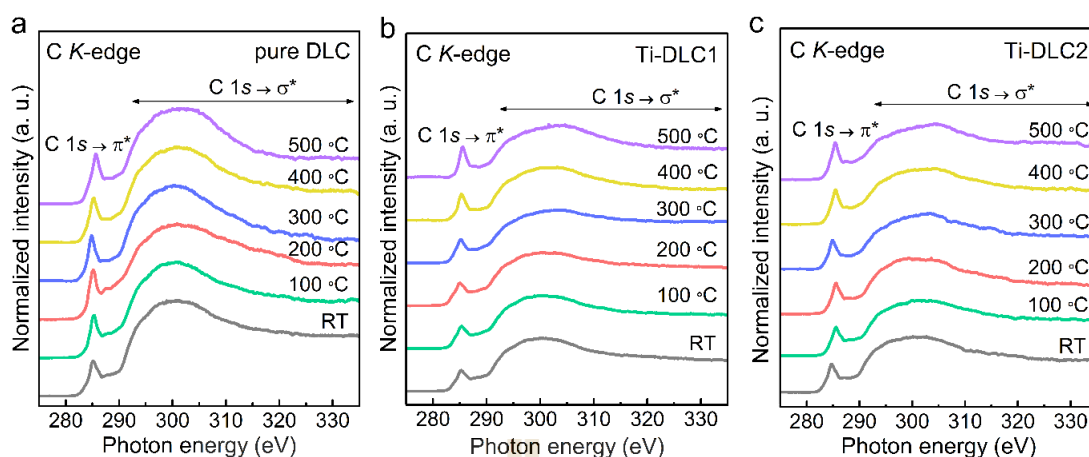
Figure 4.11 The C *K*-edge NEXAFS spectra of (a) pure DLC, (b) Ti-DLC1, and (c) Ti-DLC2 as a function of thermal annealing in the range from RT to 500°C modified from Konkhunthot *et al.* (2019).

The Ti *L*-edge NEXAFS spectra of the pure DLC, Ti-DLC1, and Ti-DLC2, respectively, as a function of the thermal annealing are shown in Figure 4.12(a)–(c). It can be seen that the Ti atoms were effectively introduced into the DLC structure by the pulsed two-FCVA system as demonstrated by the presence of the intensity of the Ti $L_{3,2}$-edge NEXAFS spectra in both Ti-DLC1 and Ti-DLC2 compared to that of the pure DLC film without the Ti peak intensity. The spectral features of the Ti-doped DLC films showed 4 dominant peaks when the annealing temperature increased to 400°C. The first 2 peaks located at approximately 458 and 460 eV were due to the excitations of the L_3-edge core level from the Ti $2p_{3/2}$ to the unoccupied Ti $3d_{5/2}$ electronic states. The other peaks located at approximately 464 and 465 eV corresponded to the L_2-edge core level from the Ti $2p_{1/2}$ to empty Ti $3d_{3/2}$ electronic states. These spectral features and positions showed similarity to the TiC power (Kanda *et al.*, 2014). The results indicated that the Ti incorporated into an amorphous structure in the range of 0.62–2.80

at.% Ti doping could exist in a form of the Ti—C bonds and/or the amorphous TiC phases which was consistent with other research groups (Pandiyaraj *et al*., 2012; Wang *et al*., 2012; Bharathy *et al*., 2010; Jo *et al*., 2018). The Ti atoms, on the other hand, were likely to form as a solid solution (Wang *et al*., 2012) within the DLC matrix when the concentration level was less than 0.42 at.% Ti (Qiang *et al*., 2013). This was because the Ti atoms cannot bond with the C atoms. In the present work, it was found that the decrease in the metal-stable sp^3 hybridized carbon contributed to the formation of the TiC phases in the DLC films. This occurrence could be explained in terms of the replacement of the C–C bonds by the Ti–C bonds as demonstrated by the decrease in the sp^3/sp^2 ratio using the NEXAFS measurement. The oxidation of the Ti as the TiO_2 surface could thermodynamically have taken place on the Ti-doped DLC surface when it was exposed to the atmosphere. The presence of the TiO_2 was detected as demonstrated in the O *K*-edge spectra in Figure 4.13. Therefore, it was realized that the removal of the residual O contamination on the Ti-doped DLC surface was not probable because it could be immediately formed after expose to the air. However, the results confirmed that the TiC was a dominant phase in the DLC structure when the Ti concentration was maintained in the range of 0.8–2.1 at.%.

Considering the effects of thermal annealing on the local bonding structure, it was noticed that the spectral features of the Ti-doped DLC films exhibited a difference at the annealing temperature beyond 300°C. The change in the spectral features was observed by the disappearance of the double-peak structure, L_3 and L_2-edge. This was by reason of the reduction in the carbonate surface contamination (Martinez *et al*., 2009; Lippitz *et al*., 1996) which was attributable to the chemisorbed O process at the Ti-doped DLC surface as CO and/or CO_2. The loss of the surface

carbonation could be observed by the formation of the Ti oxide behind, specifically the monoxide (TiO) phase without the $L_{3,2}$-edge doubled-structures (Stoyanov *et al.*, 2007). It was, however, reported that the occurrence of the TiO phase led to the reduction in oxidation resistance (Martinez *et al.*, 2009).
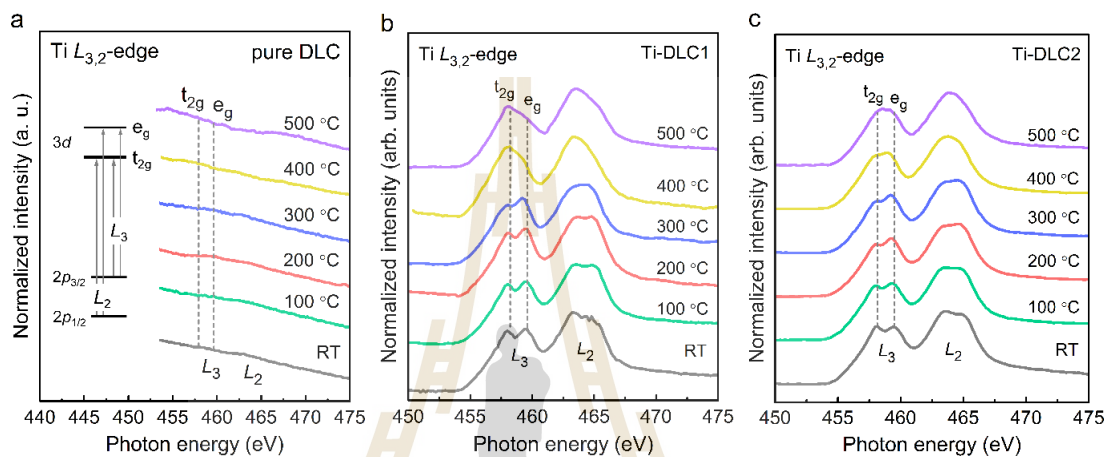
Figure 4.12 The Ti $L_{3,2}$-edge NEXAFS spectra of (a) pure DLC, (b) Ti-DLC1, and (c) Ti-DLC2 as a function of thermal annealing in the range from RT to 500°C modified from Konkhunthot *et al.* (2019).

Figure 4.13(a)–(c) shows the O K-edge NEXAFS spectra of the pure DLC, Ti-DLC1, and Ti-DLC2, respectively, as a function of the annealing temperature in the range of RT–500°C. The observed spectral features of the pure DLC films exhibited natural oxidation on the film surface which was assigned to the O surface contamination from the environment. The O K-edge NEXAFS spectra of the pure DLC films could be divided into 2 regions: the first region located at approximately 528 eV corresponded to the O $1s \rightarrow \pi^*$ (C=O) transitions principally originated from the carbonyl and carboxyl groups. The other region between 533 and 550 eV was due to

the O $1s \rightarrow \pi^*$ (C—O—C), and the O $1s \rightarrow \sigma^*$ (—OH) transitions. In the case of the Ti-doped DLC films, there was a noticeable difference in the O K-edge NEXAFS spectra. The first spectral region between 531 and 534 eV was due to the transitions from the O $2p$ states with the empty Ti $3d$ states split into t_{2g} and e_g electron orbitals (Hiratoko *et al.*, 2013). The second spectral region between 537 and 550 eV was attributed to the O $2p$ states coupled to the Ti $4s$ and $4p$ states.
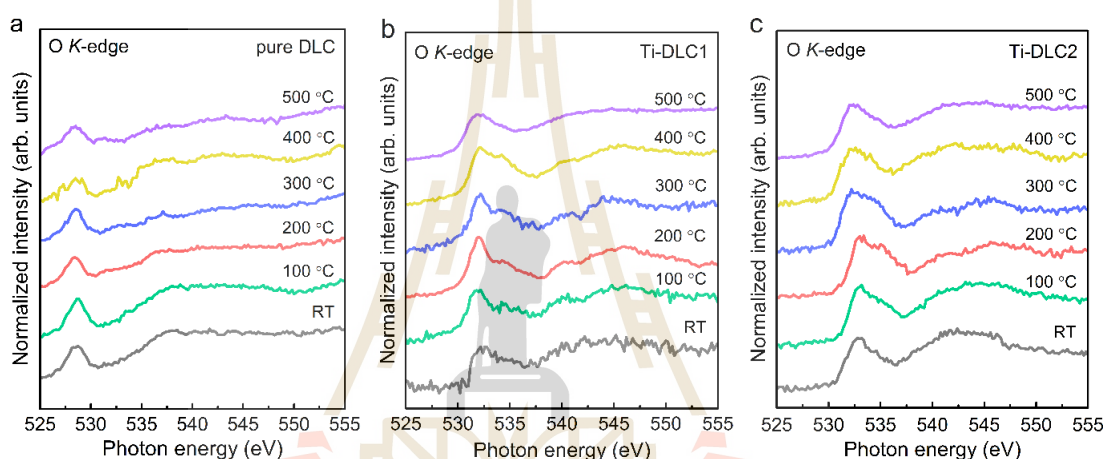
Figure 4.13 The O K-edge NEXAFS spectra of (a) pure DLC, (b) Ti-DLC1, and (c) Ti-DLC2 as a function of thermal annealing in the range from RT to 500°C modified from Konkhunthot *et al.* (2019).

From the NEXAFS analysis, it was found that the spectral features of the Ti-doped DLC films were similar to those of the residual TiO_2 (Velasco-Velez *et al.*, 2016). However, no significant difference was observed between the spectral features of the pure DLC and Ti-doped DLC films which indicated that the local bonding structure of the Ti-doped DLC films did not change much due to the addition of the Ti atoms in this study range. In addition, it was seen that the O K-edge NEXAFS spectra of the Ti-doped DLC films annealed at an elevated temperature had transformed

to the former ones as demonstrated by the drop of the first and second spectral region. This phenomenon confirmed the disappearance of the carbonate surface contamination at a higher temperature.

The sp^2/sp^3 ratio obtained through the NEXAFS technique is one of the most important parameters in determining the properties of DLC films. Evaluation of the relative sp^2 fraction in the DLC films was performed by normalizing the area under the pre-edge peak located at ~285.4 eV which contributed to the C $1s \rightarrow$ unoccupied π^* transitions at the sp^2 sites with the area under the broad region over the range of 288–335 eV which was attributed to the C $1s \rightarrow$ the unoccupied σ^* transition at the sp, sp^2, and sp^3 sites. All the C K-edge spectra were deconvoluted to obtain the area of each peak with the IGOR Pro 6.3 software. Figure 4.14 shows an example of the evaluation of the sp^2 ratio of the pure DLC film before thermal annealing. The application of the error function step as demonstrated in the blue line was to fit an edge jumping at the ionization potential.
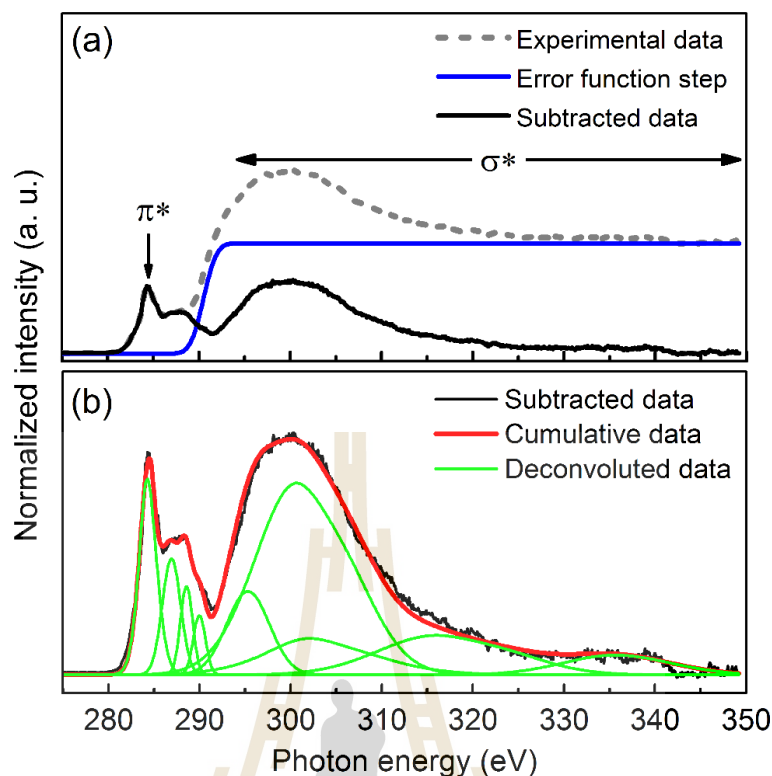
Figure 4.14 (a) The C *K*-edge NEXAFS spectrum of the pure DLC films before and after subtraction by the error function step. (b) The deconvoluted the C *K*-edge NEXAFS spectrum into the multiple-Gaussian peaks with the IGOR Pro 6.3 Software adopted from Konkhunthot *et al.* (2019).

According to Figure 4.14, the multiple-peaks between the pre-edge peak and the broad region were fitted at approximately 286.7, 288.0, and 289.4 eV which were attributed to the σ* (C—H), π* (C=O) and/or π* (C≡C), and σ* (C—C) states, respectively. The high photon energy range of the spectra was dominated at approximately 296.2 and 302.3 eV which was due to the σ* (C=C) and σ* (C≡C) (Jimenez *et al.*, 2001; Ray *et al.*, 2004), respectively. Since the pulsed two-FCVA system in this work did not require any reactive or background gas during the film deposition, the presence of the σ* (C—H) states was considered as the surface carbon

dangling bonds from the hydrogen saturation (Soin *et al*., 2012) and as the residual C oxides for the π^* (C═O) states which could spontaneously occur on the DLC surface surrounded by the water molecules or O functional group (Jimenez *et al*., 2001). To obtain the absolute value of the $sp^2/(sp^2 + sp^3)$ ratio, the C *K*-edge NEXAFS spectra of the films were compared to those of HOPG standard material by the following equation:

$$f_{sp^2} = \frac{I_{\text{sam}}^{\pi^*} \, I_{\text{ref}} \, (\Delta E)}{I_{\text{ref}}^{\pi^*} \, I_{\text{sam}} \, (\Delta E)}, \tag{4.5}$$

where $I_{\text{sam}}^{\pi^*}$ and $I_{\text{ref}}^{\pi^*}$ are the areas of the π^*(C═C) resonance of the films and the HOPG standard material, respectively. $I_{\text{sam}} \, (\Delta E)$ and $I_{\text{ref}} \, (\Delta E)$ are the areas of the remaining resonances between 288 and 335 eV of the films and the HOPG standard material, respectively (Lenardi *et al*., 1999; Outka and Stöhr, 1988; Mangolini *et al*., 2014).

Figure 4.15 demonstrates the $sp^2/(sp^2 + sp^3)$ ratio of the pure DLC, Ti-DLC1, and Ti-DLC2, respectively, as a function of thermal annealing in the range of RT–500°C. It was obvious that the $sp^2/(sp^2 + sp^3)$ ratio of all the deposited films increased continuously as the annealing temperature increased. However, the $sp^2/(sp^2 + sp^3)$ ratio observed between the pure DLC and Ti-doped DLC films was a significant difference. Before thermal annealing, it was found that the pure DLC film had a lower $sp^2/(sp^2 + sp^3)$ ratio than the Ti-doped DLC films. The $sp^2/(sp^2 + sp^3)$ ratio of the pure DLC films started to increase steadily from 0.33 to 0.35 with the increase in the annealing temperature from RT to 200°C. With the further increase in the annealing temperature from 200 to 500°C, the $sp^2/(sp^2 + sp^3)$ ratio of the pure DLC film increased dramatically from 0.35 to 0.58. A sharp increase in such a ratio implied the degradation

of the properties of the films, especially the mechanical properties. In contrast, the $sp^2/(sp^2 + sp^3)$ ratio of the Ti-doped DLC films increased gradually as the annealing temperature rose from RT to 500°C. These results indicated that the graphitization process in the Ti-doped DLC films had taken place at a slower rate and with a higher annealing temperature compared to the pure DLC film. The enhanced thermal stability of the Ti-doped DLC films might be attributed to the formation of the TiC phases as confirmed by the NEXAFS analysis. It was recognized that the TiC phase exhibited natural stability at high temperature up to 600°C (Lin *et al*., 2009). Therefore, the formation of the TiC phases in the Ti-doped DLC films could impede the graphitization process and maintain the sp^3 hybridized carbon (Er and So, 2010; Ma *et al*., 2012).
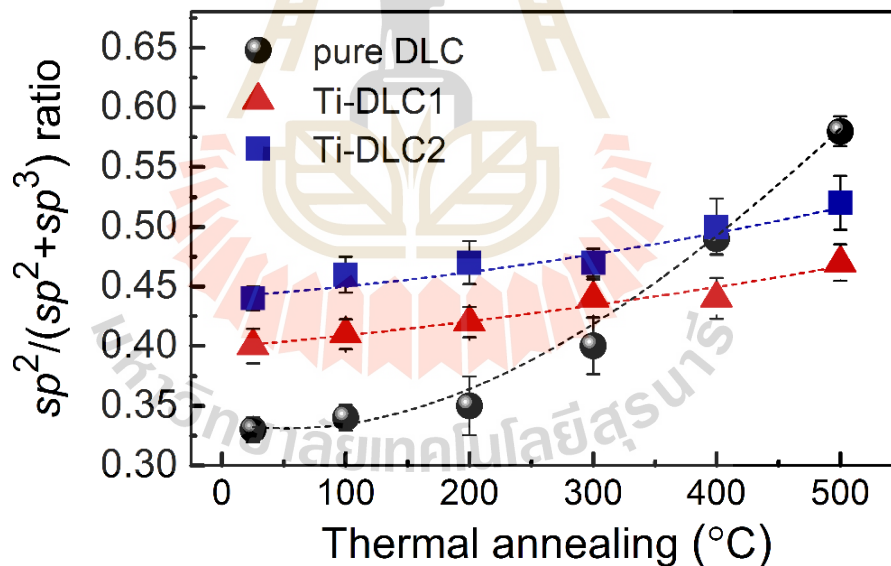
Figure 4.15 Thermal annealing versus the $sp^2/(sp^2 + sp^3)$ ratio of the pure DLC, Ti-DLC1, and Ti-DLC2, respectively, adopted from Konkhunthot *et al*. (2019).

4.2.5 Mechanical property analysis

The nano-indentation measurement was regularly performed to obtain the nano-mechanical properties, such as hardness (H), reduced Young's modulus (E), plastic index parameter (H/E), and elastic recovery (%ER) of the pure DLC and Ti-doped DLC films based on the standard Oliver and Pharr method (Oliver and Pharr, 1992). The nano-indentation load and indentation displacement curves acquired from the nano-indentation test were plotted as shown in Figure 4.16. The estimated nano-mechanical parameters are also summarized in Table 4.7. It was apparent from Figure 4.16 that the bare substrate with a larger area under a curve than those that of the deposited films exhibited a high plastic deformation which is a typical characteristic of most metals (Mirkarimi et al., 1997). The degree of the plastic deformation could be observed from the displacement difference between the maximum and residual displacement after load removal which was clearly seen in the bare substrate. On the other hand, a notable elastic recovery could be observed in all the deposited films. The high elastic recovery was caused by the relief of the elastic strain within the amorphous carbon-network structure which referred to a typical character of the hard and adherent coatings (Ankit et al., 2017; Coll and Chhowalla, 1996). It was found that a film's elastic recovery depends on the number of the sp^3/sp^2 ratio. In this case, the Ti-doped DLC films with a lower sp^3 content would exhibit a lower elastic recovery. To attain the same depth, a higher applied load, therefore, was needed as demonstrated by the maximum applied load and minimum residual displacement of the pure DLC film.
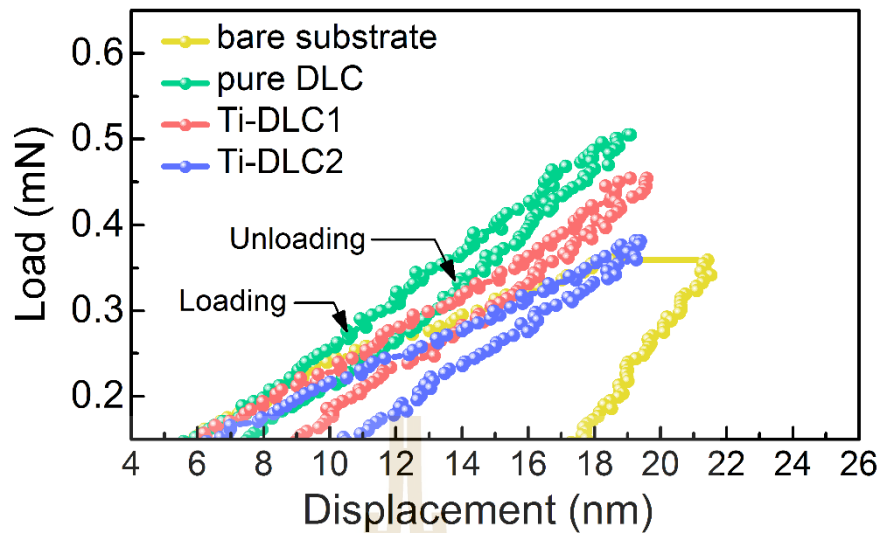
Figure 4.16 Nano-indentation load versus indentation displacement curves of bare SS

substrate, pure DLC, Ti-DLC1, and Ti-DLC2, respectively modified from

Konkhunthot *et al.* (2019).

As can be observed in Table 4.7, it was obvious that the mechanical properties of the bare AISI 304 stainless steel substrate sustained a great improvement by applying either the pure DLC or Ti-doped DLC films. For example, the *H* value of the bare substrate increased more than 5 times from 5.6 GPa to 32.8 GPa by applying the pure DLC film. In the results, the maximum *H* and *E* values of the deposited films can be acquired from the pure DLC film and with slightly decreased values but still at an acceptable level with the Ti doping. The nano-mechanical properties of the deposited films showed a consistent result with the sp^3 content in the DLC films as confirmed by the NEXAFS results. It was, however, seen that the *H* values of the deposited films were in the range comparable to those of the *ta*-C films (Grill, 1997; Robertson, 2002; Luo *et al.*, 2007) and hence there could be a wide variety of hard scratch- and wear-resistant coatings (Ankit *et al.*, 2017).

The *H/E* was a vital parameter in the mechanical properties which could be obtained by estimation from the nano-mechanical results. This parameter was used to explain the elastic-plastic behavior and wear resistance of the deposited films (Ishpal *et al.*, 2012). Thus, high wear resistance could be expected when the films had a high *H/E*. As seen in Table 4.7, the bare substrate had the highest *H/E* value compared to the deposited films which was indicative of the lowest wear resistance. The bare substrate would be mainly damaged with a large strain in the plastic deformation. The *H/E* was observed to be the maximum value for the pure DLC film and slightly decreased with the increase in the Ti doping. However, the *H/E* values were not much different and remained an almost constant value at 0.135 ± 0.004 which indicated a slight change in the wear resistance as long as the Ti doping was kept between 0.8 and 2.1 at.%.

The elastic recovery (%*ER*) was calculated here due to its being beneficial for assessing the film's tribological performance. The %*ER* could be obtained by the following equation:

$$\%ER = \left(\frac{d_{\max} - d_{\text{res}}}{d_{\max}}\right) \times 100, \tag{4.2.6}$$

where $d_{\max}$ and d_{res} are the displacements at the maximum load and residual displacement after the load removal, respectively.

The variation in the %*ER* of all the samples are also listed in Table 4.7. It was seen that the %*ER* exhibited the same tendency as the *H*, *E*, and *H/E* values. The pure DLC film had the highest value and flow by the Ti-DLC1, Ti-DLC2, and bare substrate, respectively. The %*ER* of the bare substrate was actually a low value compared to that

of the deposited films which indicated that the tribological performance of the bare substrate had been considerably improved by applying the DLC films. The other important parameters to be further investigated to evaluate the films' tribological properties were the adhesion strength and corrosion resistance which will be described in the next section.

Table 4.7 Mechanical parameters obtained from the nano-indentation test of all the samples.

Sample	H, (GPa)	E, (GPa)	H/E	ER, (%)
bare substrate	5.6 ± 1.60	254.0 ± 5.41	0.022	17
pure DLC	32.8 ± 2.19	234.7 ± 7.08	0.139	60
Ti-DLC1	28.8 ± 1.01	215.0 ± 6.54	0.134	54
Ti-DLC2	27.6 ± 1.48	213.0 ± 5.84	0.130	46

4.2.6 Nano-tribological behaviors

(i.) Adhesion strength analysis

The nano-tribological behaviors in terms of the adhesion strength and friction mechanisms were studied with a nano-scratching experiment in correlation to the surface morphologies. Extreme adhesion strength was required for high-quality DLC film used in engineering and tribological applications. Obviously the adhesion did not depend on the mechanical properties (Ding *et al*., 2002); therefore, the relevance of the adhesion strength with respect to the effects of Ti incorporation were analyzed by comparing the surface morphologies and their microstructure. The main problem that was found when a hard DLC film was subjected under the external normal or shear force was premature delamination. This was due to poor adhesion of the films to the

underlying substrate, particularly on a steel substrate. Therefore, it was very important to study the adhesion of the films for long-term performance. The L_c was well-known as the major parameter correlated to the tribological performance (Oliver and Pharr, 2004; Donnet, 1998) and could be obtained from a point at which the friction force sharply increased and/or the adhesion coating failure had taken place.
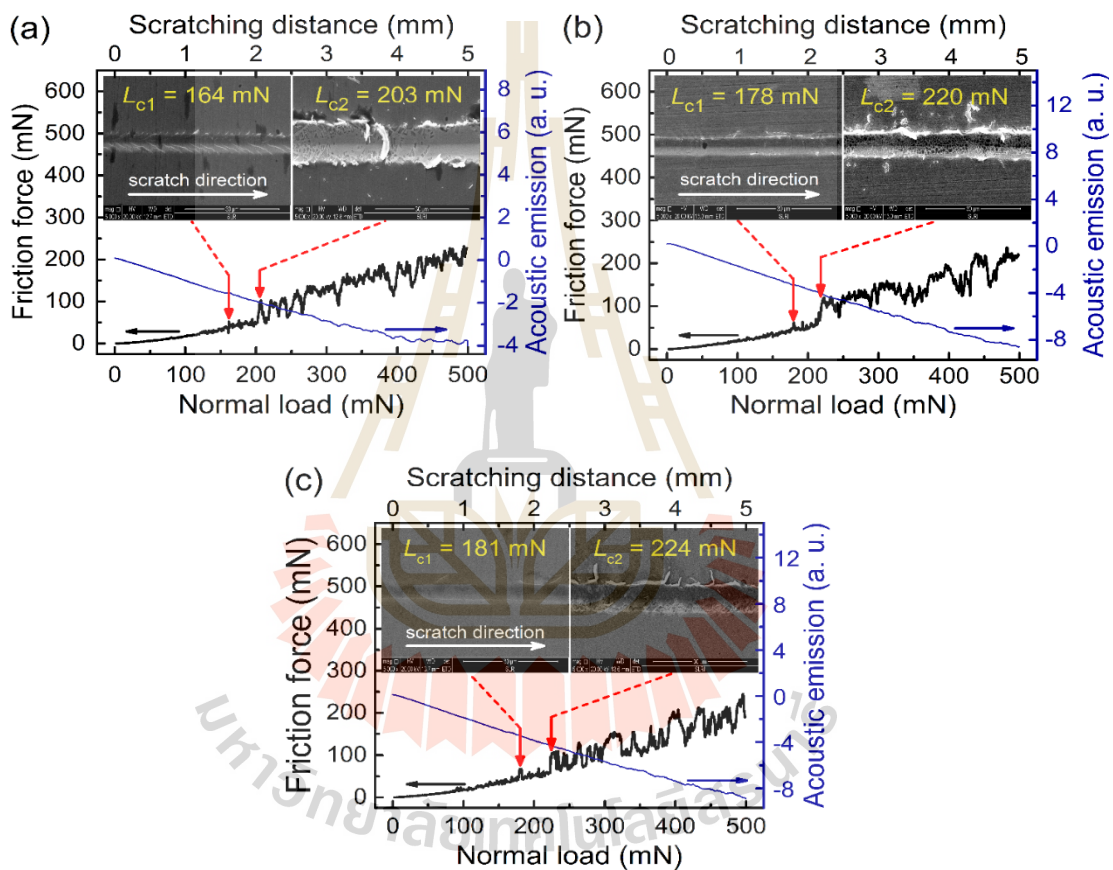
Figure 4.17 Typical scratch curves of (a) pure DLC, (b) Ti-DLC1, and (c) Ti-DLC2, respectively. Inset demonstrates the SEM micrographs of the corresponding scratch tracks at a point of the L_{c1} and L_{c2}, respectively, obtained from Konkhunthot $et\ al.$ (2019).

Figure 4.17(a)–(c) illustrated the typical scratch curves of the pure DLC, Ti-DLC1, and Ti-DLC2, respectively. The acoustic emission curves of each film were also plotted to compare to the scratch curves and to determine the adhesion failure at the interface consistent with the L_c. The scratch curves were plotted in correlation to SEM micrographs to inspect the L_c which were comprised of the L_{c1} and L_{c2}, respectively as demonstrated in the inset in Figure 4.17. The L_{c1} occurred when the friction force started to fluctuate and the first cohesive failure occurred. This included the plastic deformation, parallel cracks, and fine cracks along the scratch edge. The L_{c2} appeared when the friction force rose rapidly and the coating adhesion failed which comprised external transverse cracks and delamination. The L_{c1} and L_{c2} values were measured at 164, 178, and 181 mN, and at 203, 220, and 224 mN for the pure DLC, Ti-DLC1 and Ti-DLC2, respectively. It was obvious that the L_{c1} and L_{c2} of the pure DLC film had been significantly improved by the Ti addition. The improvement in the adhesion strength of the deposited films was influenced from the reduction in the compressive internal stress and the formation of the atomic intermixing interface rather than from mechanical properties. These behaviors were correlated to the elastic stored energy within the DLC structure during the film growth. In the case where the film adhesive energy was less than the elastic stored energy, film delamination would occur (Hassan *et al*., 2015; Zhang *et al*., 2007). The reason that the Ti-doped DLC films had a lower internal stress than the pure DLC film contributed to the increase in the sp^2 (C=C) sites. Since the bond length of the sp^2 (C=C) sites was shorter than those of the sp^3 (C—C) sites, the increase in the sp^2 (C=C) sites could lead to a reduction in the strain within the film and thus increased the L_c (Bootkul *et al*., 2014). Another reason might be due to the atomic intermixing interface which occurred during the

impingement of the high energy of the C ions on an adhesive Ti layer. Because the Ti atoms could react easily with the C atoms to form the TiC phase, it was reasonable that a mixing compound generated between the Ti-doped DLC film and a Ti layer had a stronger bond than that between the pure DLC film and a Ti layer. For this reason, the film adhesion in terms of the L_c of the Ti-doped DLC films was higher compared to the pure DLC film.

The inset in Figure 4.17(a)–(c) shows the SEM micrographs of the L_{c1} and L_{c2} regions of the pure DLC, Ti-DLC1, and Ti-DLC2, respectively, and the corresponding nano-scratch tracks. It was apparent that the initial strain failures which consisted of edge and fine cracks at the L_{c1} region were observed for the pure DLC film. The failures were, however, found to decrease and the scratch track seemed to be smoother with a slight edge and fine cracks for the Ti-DLC1 and Ti-DLC2, respectively. The Ti-DLC2 especially showed a shallower scratch track without the edge and fine cracks. At the L_{c2} region, the first adhesion coating failure had occurred accompanied by the deformation cracks and exfoliations. In addition, the films were severely damaged deep into the underlying substrate. The delamination of the films could be observed at the localized scratch track with the explosion of an underlying substrate. It was evident that the pure DLC film exhibited brittle fractures as shown by the segment cracks and splits along both sides of the scratch track, while these features seemed to be lower for the Ti-DLC1. Only splits and exfoliations at the upper edge of the scratch track without the brittle fractures could be observed for the Ti-DLC2 with the inference that the adhesion strength of the DLC films had been significantly enhanced through Ti incorporation. The enhancement of the film adhesion might be attributed to the residual stress and mechanical parameter, such as the %ER as previously described. It was

noticed that the pure DLC films with high residual stress and %*ER* were likely to be fractured in a brittle behavior, while the films with the lower stress and %*ER*, such as the Ti-DLC1 and Ti-DLC2 tended to be damaged without the brittle fracture, but rather had ductile deformation. In the nano-scratching experiments, it was confirmed that the adhesion strength and/or toughness of the DLC films were effectively improved by Ti doping without much sacrifice to the mechanical properties.

(ii.) Coefficient of friction analysis

The nano-scratching experiment was also used to assess the quantitative analysis in terms of the failure mechanisms, such as elastic/plastic deformation, surface crack formation, delamination, and nano-tribological characteristics, especially the coefficient of friction (COF) of the pure DLC and Ti-doped DLC films. Figure 4.18(a)–(d) shows the COF of the bare substrate, pure DLC, Ti-DLC1, and Ti-DLC2, respectively, as a function of the scratching distance over 5 mm. It was apparent that the COF of the bare substrate had an abrupt increase from 0.17 to 0.50 and maintained a constant value of 0.50 which was attributed to the average mean COF for the bare substrate. The COF of the deposited films was different. A lower COF at the initial ramping load might be attributed to the COF of the oxide surface formed on the bare substrate. The COF of the deposited films could be divided into 3 stages as illustrated in Figure 4.19. The first stage referred to the fully elastic recovery with high elasticity. This stage contained a smooth, shallow scratch trace, and almost no obvious scratch was observed. The second stage where the first crack had occurred referred to the elasto-plastic behavior with the elasticity of approximately 60%. This included the tiny cracks and edge cracks along the trace known as a fishbone-like scratch. The final stage was where the COF had suddenly increased. This stage

exhibited plastic deformation and delamination of the films which was associated with the L_{c2}. The portion of the fracture occurred due to plowing which was followed by a large number of brittle fractures as demonstrated by the inset in Figure 4.17. All the stages of the failure mechanisms are given in Figure 4.19 by ①, ②, and ③, respectively, which corresponded to the COF curves in Figure 4.18.
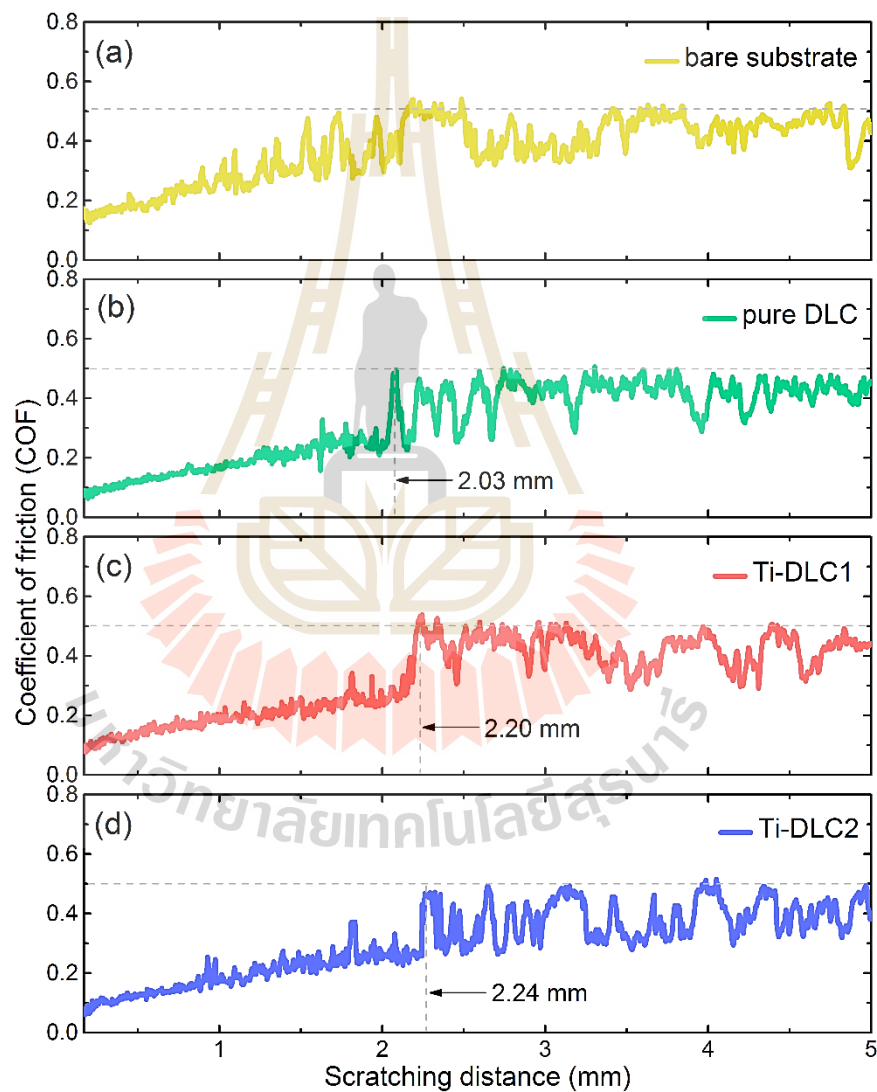
Figure 4.18 The COF of (a) the bare substrate, (b) pure DLC, (c) Ti-DLC1, and (d) Ti-DLC2, respectively.

As seen in Figure 4.18(b)–(d), the COFs of all the films increased gradually from 0.07 to 0.50 at the scratching distance range of 2.03, 2.20, and 2.24 mm for the pure DLC, Ti-DLC1, and Ti-DLC2, respectively. The constant value of the COF at 0.50 corresponded to the COF of the bare substrate. An abrupt change in the COF implied the delamination of the films and the penetration of the indenter into the bare substrate. The COF of the deposited films was determined by taking the mean values in the sliding distance before the film's delamination. The average mean COF of 0.17, 0.19, and 0.20 were obtained for the pure DLC, Ti-DLC1, and Ti-DLC2, respectively. It could be concluded from the results that the COF of the DLC films in correlation to the effect of Ti incorporation was not much changed as long as the Ti concentration level was low. Additionally, the COF showed an inverse relationship to the film adhesion, but it was the dominant mechanical property, especially the H. On this point, the films with lower H exhibited a decrease in load carrying capacity which resulted in the increased COF.
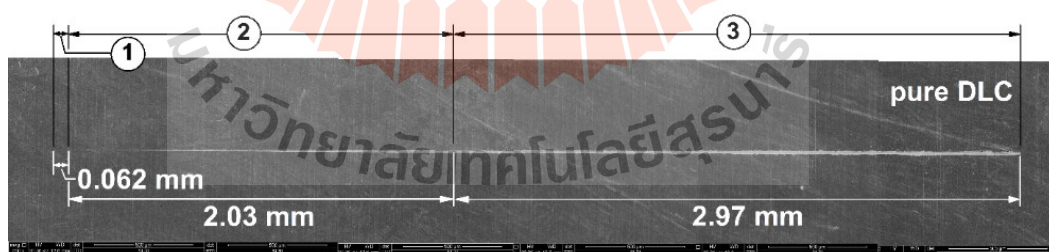
Figure 4. 19 SEM micrograph of scratch trace over the entire sliding distance of the
pure DLC film.

4.2.8 Electrochemical corrosion analysis

The corrosion protection performance of the bare substrate and DLC films was investigated using the potentiodynamic polarization test. Figure 4.20 demonstrates the polarization curves of the bare substrate, pure DLC, Ti-DLC1, and Ti-DLC2, respectively, tested in an aerated 3.5 wt.% NaCl solution of pH 2. The corrosion parameters achieved from the Tafel extrapolation method consisted of the E_{corr}, i_{corr}, β_a, β_c, R_p, and CR, respectively, as listed in Table 4.8.
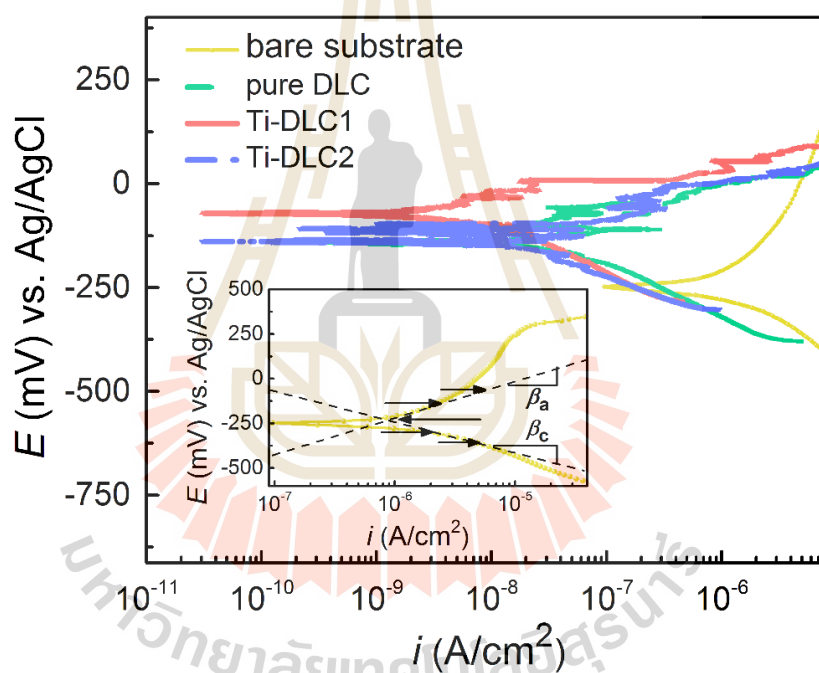
Figure 4.20 The potentiodynamic polarization curves of bare SS substrate, pure DLC, Ti-DLC1, and Ti-DLC2, respectively, in an aerated 3.5 wt.% NaCl solution of pH 2.0 operated at 27 ± 2°C. The example of the Tafel extrapolation method of the bare substrate used to acquire the simulated parameters (see inset) modified from Konkhunthot *et al*. (2019).

It was clear that the corrosion resistance of the bare substrate had greatly improved by applying the DLC films as demonstrated by the shift of the E_{corr} toward a more positive region and the orders of the magnitude decreased in the i_{corr}. Comparing between the pure DLC and Ti-doped DLC films, it was found that the E_{corr} and i_{corr} of the pure DLC film were –146.02 mV and 14.15 nA/cm^2, respectively, and those of the Ti-DLC1 and Ti-DLC2 were –70.70 mV and 3.25 nA/cm^2, and –138.95 mV and 5.20 nA/cm^2, respectively. From the results, the Ti-doped DLC films had higher E_{corr} and lower i_{corr} than that of the pure DLC film. It should be pointed out that the corrosion resistance of the DLC film could be effectively improved by Ti doping, particularly the Ti-DLC1 in which the E_{corr} increased 2 times and the i_{corr} decreased fivefold compared to the pure DLC film. The improvement of the corrosion resistance of the Ti-doped DLC films was due to the formation of the TiO_2 and/or the TiC enriched on the Ti-doped DLC surface which acted as the primary diffusion barrier against the attacks of the active ions, water molecules, and oxygen into the underlying substrate. Consequently, it improved the corrosion resistance of the Ti-doped DLC films.

Table 4.8 The corrosion parameters consisting of the E_{corr}, i_{corr}, β_a, β_c, R_p, and CR, respectively, of all the samples obtained from the potentiodynamic polarization measurement.

Samples	E_{corr}	i_{corr}	β_a	β_c	R_p	CR
	(– mV)	(nA/cm^2)	(V/decade)	(V/decade)	($\times 10^3$ Ω cm^2)	($\times 10^{-2}$ mm/y)
bare SS	163.400	507.870	119.960	259.430	19.412	1.886
pure DLC	146.020	14.150	15.046	9.208	175.336	0.021
Ti-DLC1	70.695	3.252	25.507	11.988	1089.300	0.005
Ti-DLC2	138.950	5.203	7.882	7.988	331.212	0.010

The porosity and protective efficiency of the pure DLC, Ti-DLC1, and Ti-DLC2, respectively, were qualitatively analyzed as shown in Figure 4.21. It was noticed that a large amount of the porosity was accompanied with a low value of the polarization resistance (R_p), and it had a strong impact on the film's resistivity and durability. The fact is that the porosity acted as the diffusion path which was caused by the penetration of active ions and water into the underlying substrate. Therefore, it was easy for the aggressive ions to penetrate the path toward the steel substrate which led to localized corrosion and the eventual release of the metallic ions. The released metallic ions had been inspected by the ICP-MS method which will be described later in the Metallic ion analysis section. In Figure 4.21, the porosity in the pure DLC film was found to have the maximum value and was followed by the Ti-DLC2 and Ti-DLC1, respectively. These results were consistent with the electrochemical parameters and the SEM surface morphology (Figure 4.22). Accordingly, the DLC films with less porosity would have a better corrosion protection performance. On the other hand, the protective efficiency showed the opposite trend to the porosity. In this work, the Ti-DLC1 had the lowest porosity and highest protective efficiency and, therefore, it was a potential candidate for corrosion protection from acidic and saline solutions.
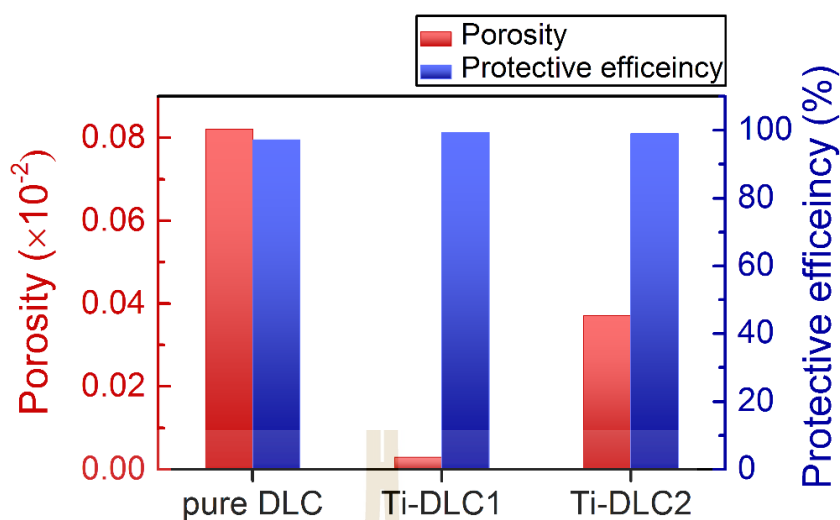
Figure 4.21 The porosity and protective efficiency of the pure DLC, Ti-DLC1, and Ti-DLC2, respectively, obtained from the potentiodynamic polarization tests.

4.2.9 Metallic ion analysis

The ICP-MS method was performed to obtain the concentration of the released metallic ions in the solution after the electrochemical corrosion tests. However, since the results of the electrochemical corrosion analysis revealed a massive improvement in the corrosion resistance of the bare substrate by the application of the DLC films, it was not necessary to investigate the released metallic ions of the bare substrate; only those of the deposited films would be analyzed with the ICP-MS. For the qualitative analysis of the ICP-MS, a solution of 8 mL of each sample was collected before being put onto a tray. The results demonstrated that the pure DLC film had released the highest amount of metallic ions with Fe: 0.5559 mg/L, Cr: 0.0805 mg/L, Ni: 0.0323 mg/L, Mn: 0.0093 mg/L, and Ti: 0.0029 mg/L, respectively, and was followed by the Ti-DLC2 and Ti-DLC1, respectively, as listed in Table 4.9. The concentration of the released metallic ions was proportional to a number of elements in

an AISI 304 stainless steel substrate which consisted of Fe balanced, Cr 18–20, Ni 8–10, and Mn 2 wt.%, respectively.

Two crucial parameters were used to describe the mechanisms of the released metallic ions: (i) an electrochemical potential (E) and (ii) the pH of the solution. In electrochemistry, a Pourbaix diagram known as the E-pH diagram illustrates the regions of possibility and the stability of the forms and/or phases and even the chemical species of an aqueous electrochemical system. Regarding the available thermodynamic data of the Pourbaix diagram at pH 2 in a potential range of 0–300 mV of the main elements, such as Fe (Beverskog, and Puigdomenech, 1996), Cr (Beverskog and Puigdomenech, 1997), Ni (Beverskog and Puigdomenech, 1997), Mn (Najafpou *et al*., 2017), and Ti (Oliveira *et al*., 2017), it was found that most of the elements were in a form of aqueous species, for example, Fe^{2+}, Cr^{3+}, Ni^{2+}, and Mn^{2+}, except for Ti, which could probably be formed as the TiO_2 film in the passivity region. This would be the reason why the Ti-doped DLC films had better corrosion resistance than the pure DLC film.

Observation of the SEM surface morphologies in Figure 4.22 might be used to clarify these behaviors. It was noticeable from Figure 4.22 that the pure DLC film had more and larger localized corrosion than those of the Ti-doped DLC films. The Ti-DLC1 especially showed a smoother surface with few signs of the localized corrosion. According to the above-mentioned results, the Ti incorporation into the DLC films was considered to be a potential method for improving the corrosion protection performance.

Table 4.9 The concentration level of the released metallic ions obtained after the

potentiodynamic polarization tests.

Sample	Concentration level of the released metallic ions (mg/L)				
	Fe	Cr	Ni	Mn	Ti
Pure DLC	0.5559	0.0805	0.0323	0.0093	0.0029
Ti-DLC1	0.1350	0.0160	0.0048	0.0029	0.0021
Ti-DLC2	0.4897	0.0587	0.0168	0.0084	0.0026

4.2.10 Surface morphology analysis after electrochemical corrosion tests

Figure 4.22(a)–(d) illustrates the SEM surface morphologies of the bare

substrate, pure DLC, Ti-DLC1, and Ti-DLC2, respectively, after the potentiodynamic

polarization test. It was evident that the bare substrate showed severe corrosion as

demonstrated by the distribution of localized corrosion, such as pitting corrosion over

a sample surface. Pitting corrosion often takes place in stainless steels immersed in

acidic solutions with active species, for example, chlorine ions (Cl^-). The morphologies

of the pits a included pit mouth as a center hole surrounded by flask shapes and lacy

metal covers. The rate of the pitting corrosion could be very high and, therefore, serious

damages could be observed for the bare substrate as confirmed by the potentiodynamic

polarization test. The surface morphologies of the pure DLC and Ti-doped DLC films

exhibited different features. There was no pitting corrosion as found in the bare

substrate, but localized corrosion could be found which might have mainly originated

from the film defects, such as porosities or pinholes during the films' growth. The

aggressive species, such as Cl^-, H^+, and OH^- dissolved in an aqueous solution would

be the main factors that penetrated and damaged the films' surfaces. It was also found

that the number and size of the corroded traces were directly correlated with the

porosity of the films. A high level of porosity in the pure DLC films led to the formation of a large number and size of the corroded traces. In addition, it was found that the sp^2 content ratio in the DLC films could have an effect on the corrosion resistance. As the sp^2 content increased, the transfers or exchanges of electrons or charged ions at the solution/film interface could occur easily which was followed by a high rate of metal dissolution. Therefore, the Ti-DLC1 with a small amount of porosity and low sp^2 content would be the best anti-corrosion coating in terms of the chemical inertness in this work.
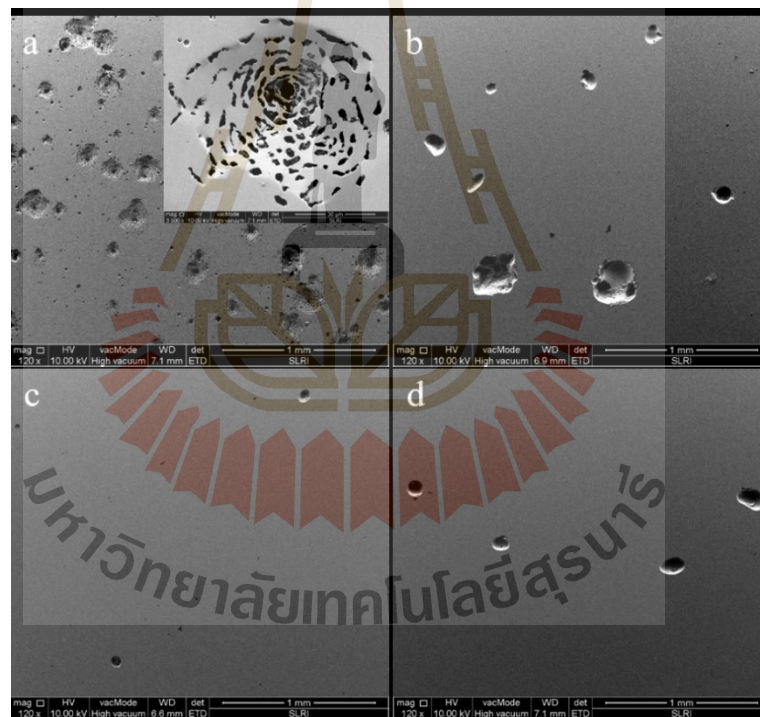
Figure 4.22 SEM surface morphologies of (a) the bare substrate, (b) pure DLC, (c) Ti-DLC1, and (d) Ti-DLC2, respectively. The inset in Figure 4.22(a) shows high magnification of SEM micrograph of the bare substrate obtained from Konkhunthot *et al.* (2019).

4.2.11 Local bonding configuration analysis after electrochemical tests

The local bonding structural-dependent corrosion resistance of the deposited DLC films after the potentiodynamic polarization tests was investigated by X-PEEM connected with the NEXAFS technique. The combined imaging and spectroscopic techniques of X-PEEM and NEXAFS provided much surface sensibility and there were particular advantages in a non-destructive probe of nanoscale materials. Figure 4.23(a)–(c) reveals the stacks of the C K-edge X-PEEM images of the pure DLC, Ti-DLC1, Ti-DLC2 taken at photon energies of 285.4, 288.0, 289.4, 296.2, and 302.3 eV, respectively. The photon energies were taken on the strong C $1s$ absorption peaks which corresponded to the deconvoluted peaks of the π^* (C=C), π^* (C=O) and/or π^* (C≡C), σ^* (C—C), σ^* (C=C), and σ^* (C≡C) states as demonstrated in Figure 4.14.
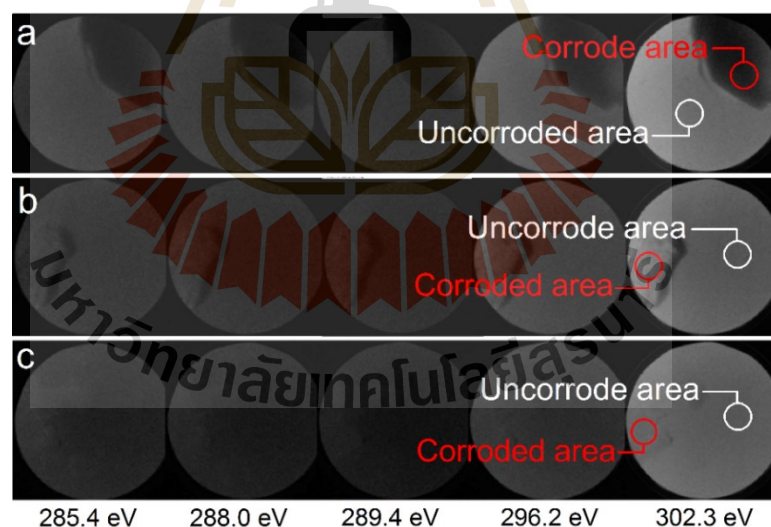
Figure 4.23 A stack of the C K-edge X-PEEM image of (a) pure DLC, (b) Ti-DLC1, and (c) Ti-DLC2 at different photon energies of 285.4, 288.0, 289.4, 294.6, and 302.5 eV, respectively. The field of view of each image = 75 μm adopted from Konkhunthot *et al.* (2019).

As seen in Figure 4.23, the dark and bright regions were determined by the image contrast mechanisms which consisted of topography, work function, and elemental and chemical contrasts. The elemental and chemical contrasts were the most important mechanisms in distinguishing each region related to the electric band structure, such as bonds and molecular orbitals. The area with the predominant elements or bonds, therefore, appeared as a bright region. By scanning the photon energy, the C K-edge X-PEEM images would vary which corresponded to the changes in the C absorption peak intensity as demonstrated by the different regions. The results indicated that the corroded areas appeared darker which was consistent with the area with a slight absorption of the C species, while the uncorroded areas appeared brighter which corresponded to the area with a strong absorption of the C species. The bright regions were due to the overlapping C $1s \rightarrow$ the σ^* transitions at the sp^2 and sp^3 sites.

For an in-depth understanding of corrosion-induced structural transformation in terms of the sp^3/sp^2 ratio, the NEXAFS equipped with the X-PEEM technique was performed. Figure 4.24(a)–(c) illustrates the corresponding C K-edge NEXAFS spectra obtained from the C K-edge X-PEEM images of the pure DLC, Ti-DLC1, and Ti-DLC2, respectively. It was seen that the C K-edge X-PEEM images of the pure DLC film sustained dramatic corrosion until the steel substrate was exposed as shown by the dark region due to the low C absorption signal. This was very consistent with the SEM results. The corresponding C K-edge NEXAFS spectra had different features compared to those before the electrochemical corrosion tests (Figure 4.11). A sharp increase in the pre-edge π^* (C═C) peak together with a great decrease in the broad section (the sp, sp^2, and sp^3 sites) was visibly found in the pure DLC film. The $sp^2/(sp^2 + sp^3)$ ratio after the corrosion tests was calculated to be 0.89 and 0.88 for the

corroded and uncorroded areas, respectively, by Equation 4.5. This confirmed a major conversion from the sp^3 to sp^2-bonded carbon atoms in the DLC structure. There was no main difference observed in both spectra which indicated that most of the metastable C-sp^3 bonding was completely transformed to the C-sp^2 bonding after being induced by the active species in the acidic solution (Robertson, 2008). In this work, it was seen that the observed spectra of the pure DLC films resembled that of the graphite oxide (De Jesus *et al*., 2013; Gandhiraman *et al*., 2014). As described above, in the DLC films with a larger sp^2 content, the rate of the dissolution of the metal was higher which was in good agreement with the corrosion results. Consequently, the increased sp^2 content during the electrochemical corrosion test was probably the key point in determining the corrosion resistance of the DLC films which could be explained through the combined X-PEEM and NEXAFS techniques.

In the case of the Ti-doped DLC films, the different behaviors were due to the formation of the TiO_2 surface layer or passive film. No significant difference in the spectra before and after the corrosion tests were observed. This indicated that the addition of Ti atoms in the DLC films was an effective method for improving the corrosion resistance in acidic solution as noticed from a slight increase and decrease in the pre-edge π^* (C=C) peak and the broad section, respectively. The other peaks could be observed in the spectra located at between 288 and 290 eV. These peaks corresponded to the σ (C—H) and the π^* (C=O) sites that might probably be the corrosion products and/or surface oxide on the Ti-doped films. The $sp^2/(sp^2 + sp^3)$ ratios of the Ti-DLC1 and Ti-DLC2 were also calculated to be 0.73 and 0.60 and 0.77 and 0.72 in the corroded and uncorroded areas, respectively, although the Ti-doped DLC films had an excellent corrosion resistance compared to the pure DLC film. However,

since there had been the active ions, such as Cl^-, H^+, and OH^- added into the solution at pH 2, the aggressive attacks of those ions might be the main reason for the significant change in the sp^3/sp^2 ratio of the deposited films in this work.
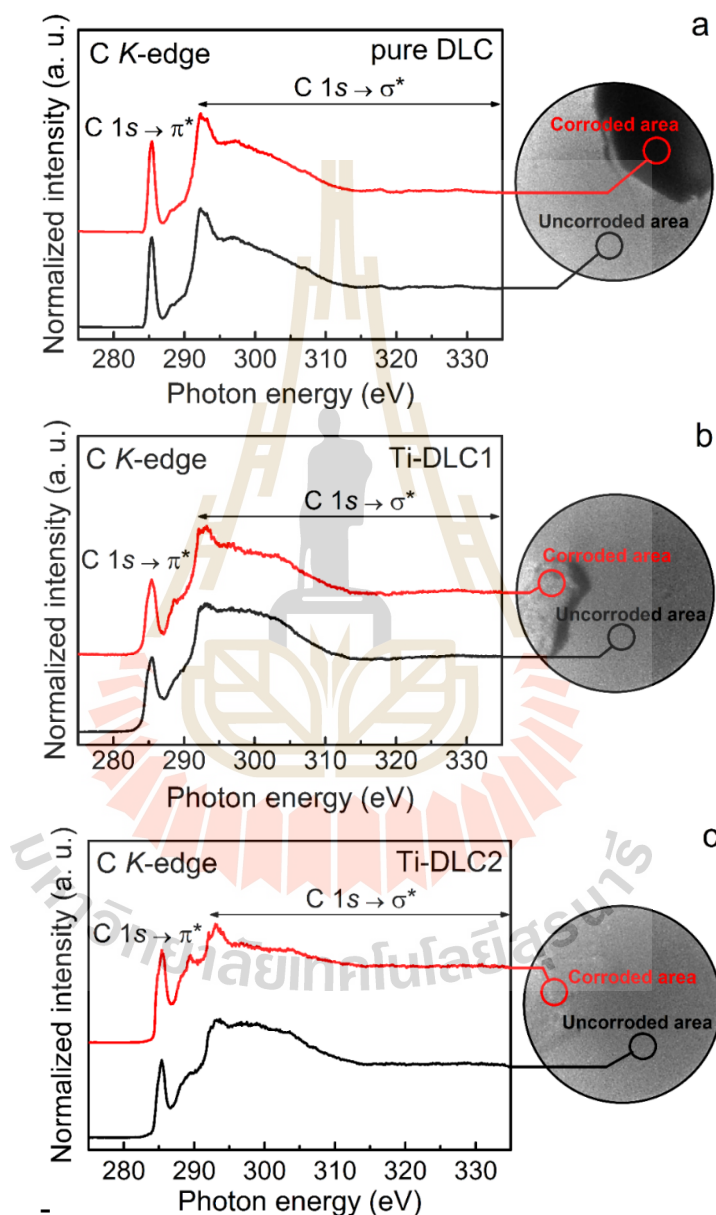
Figure 4.24 The corresponding C K-edge spectra acquired from the C K-edge X-PEEM images of (a) pure DLC, (b) Ti-DLC1, and (c) Ti-DLC2, respectively, adopted from Konkhunthot *et al.* (2019).

To further investigate the corrosion-induced microstructural transformation of the pure DLC and Ti-doped DLC films after the corrosion tests, the corresponding Ti $L_{3,2}$-edge NEXAFS spectra obtained from the Ti $L_{3,2}$-edge X-PEEM images were implemented as shown in Figure 4.25.
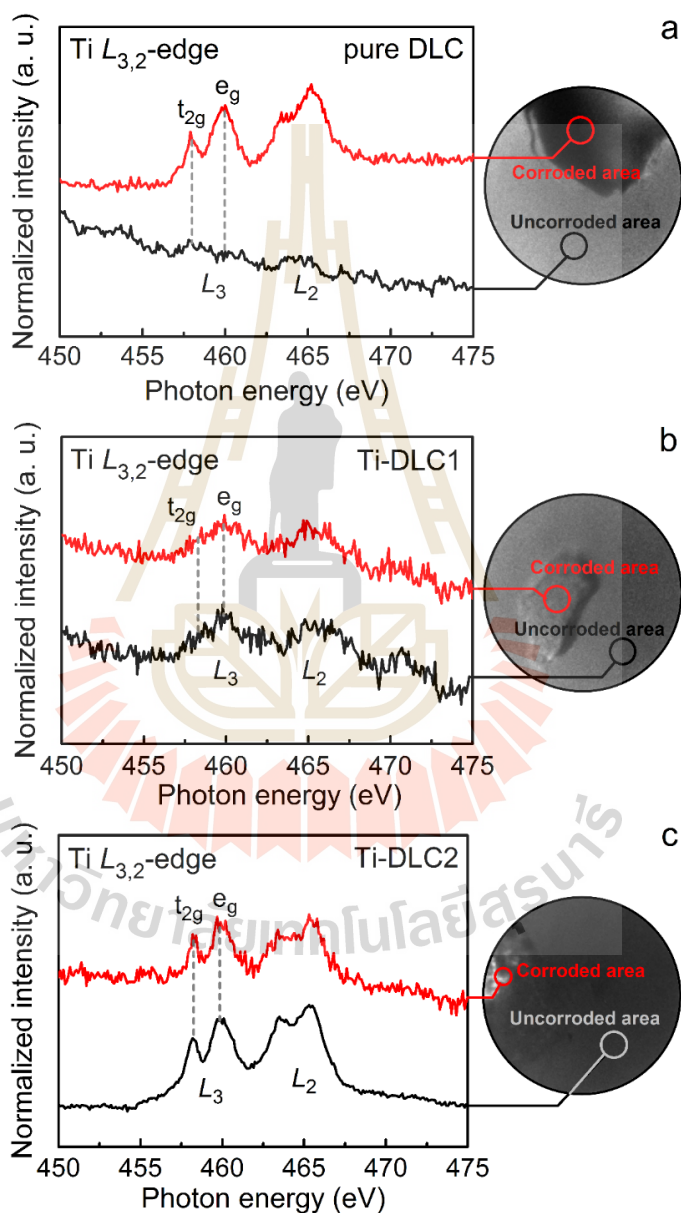
Figure 4.25 The corresponding Ti $L_{3,2}$-edge spectra acquired from the Ti $L_{3,2}$-edge X-PEEM images of (a) pure DLC, (b) Ti-DLC1, and (c) Ti-DLC2, respectively, adopted from Konkhunthot *et al.* (2019).

It was obvious that the pure DLC film showed different spectral features in 2 areas. The corroded area as demonstrated by the dark region revealed a sign of the Ti $2p$ peak intensity which indicated the delamination of the top of the DLC film until the Ti intermediate layer was exposed. In contrast, there was no intensity of the Ti $2p$ peak observed in the uncorroded area as illustrated by the bright region which confirmed that the top of the DLC film did not peel off, but the complete transformation in the carbon network structure had occurred as previously described. In the case of the Ti-doped DLC films, the Ti $2p$ peak intensity was detected. These spectra would probably be the interactions of Ti–O bonds, particularly the TiO_2 film based on the Pourbaix diagram which naturally occurred on the Ti-doped DLC surface (Velasco-Velez et al., 2016). A different intensity was observed for the Ti-doped DLC films due to the amount of the Ti content in the Ti-DLC1 and Ti-DLC2. Due to higher Ti content (2.1 at.%) in the Ti-DLC2, the Ti peaks appeared at a stronger intensity in the double-peak structure L_3 and L_2-edge than that of the Ti-DLC1 with a lower Ti content (0.8 at.%). The improvement in the corrosion resistance of the Ti-doped DLC films was found be to due to the stable form of the TiO_2 passive films as demonstrated in the Pourbaix diagram (Oliveira et al., 2017). In this case, the passivation would act as a diffusion barrier that hindered the damage from the active ions, water molecules, and other species in the substrate (Viswanathan et al., 2017), and thus retarded the conversion from the sp^3 bonding to the sp^2 bonding. Although the formation of the TiO_2 film resulted in better corrosion resistance of the Ti-doped DLC films, the Ti-DLC2 had almost the same corrosion behavior as the pure DLC film in terms of the E_{corr} and i_{corr}. In addition to the effect of the TiO_2 surface film on the corrosion resistance, another effect involved the sp^3/sp^2 ratio in the DLC films. As the Ti atoms further increased,

the sp^2 content in the DLC films was found to increase together with an increase in the degree of discontinuity in the carbon network structure. This formation generated defects and/or vacancies within the DLC structure, for example, porosity or pinholes which eventually led to localized corrosion as shown in Figure 4.22, even if the passive TiO_2 films still remained.

In an attempt to further assess the corrosion behaviors and the corrosion products of the DLC films, the corresponding Fe $L_{3,2}$-edge NEXAFS spectra obtained from the Fe $L_{3,2}$-edge X-PEEM images of the pure DLC, Ti-DLC1, and Ti-DLC2, respectively, were implemented as illustrated in Figure 4.26. It was obvious that the pure DLC film showed a big difference in the spectral features in both areas. The Fe peak intensity was found in the corroded area which indicated that the film in this area was severely damaged, while the uncorroded area showed no sign of the Fe peak. The spectral feature of the Fe in the corroded area was found to be similar to those of the AISI 304 stainless steel (Bastidas *et al*., 1998). This observation confirmed that the top DLC film and Ti intermediate layer deposited on the steel substrate had been fractured and peeled off during the corrosion tests. The same feature as in the pure DLC film could be seen for Ti-DLC2, but it showed some difference because the Fe spectral feature was found to resemble the Fe_2O_3 or Fe_3O_4 spectrum (Soriano *et al*., 1993) which principally originated from the corrosion products over the pit mouth. However, no such feature was observed in Ti-DLC1 in both areas which confirmed that it had an excellent corrosion protection performance without serious damages and exhibited much stability in an acidic chloride solution compared to the other films.
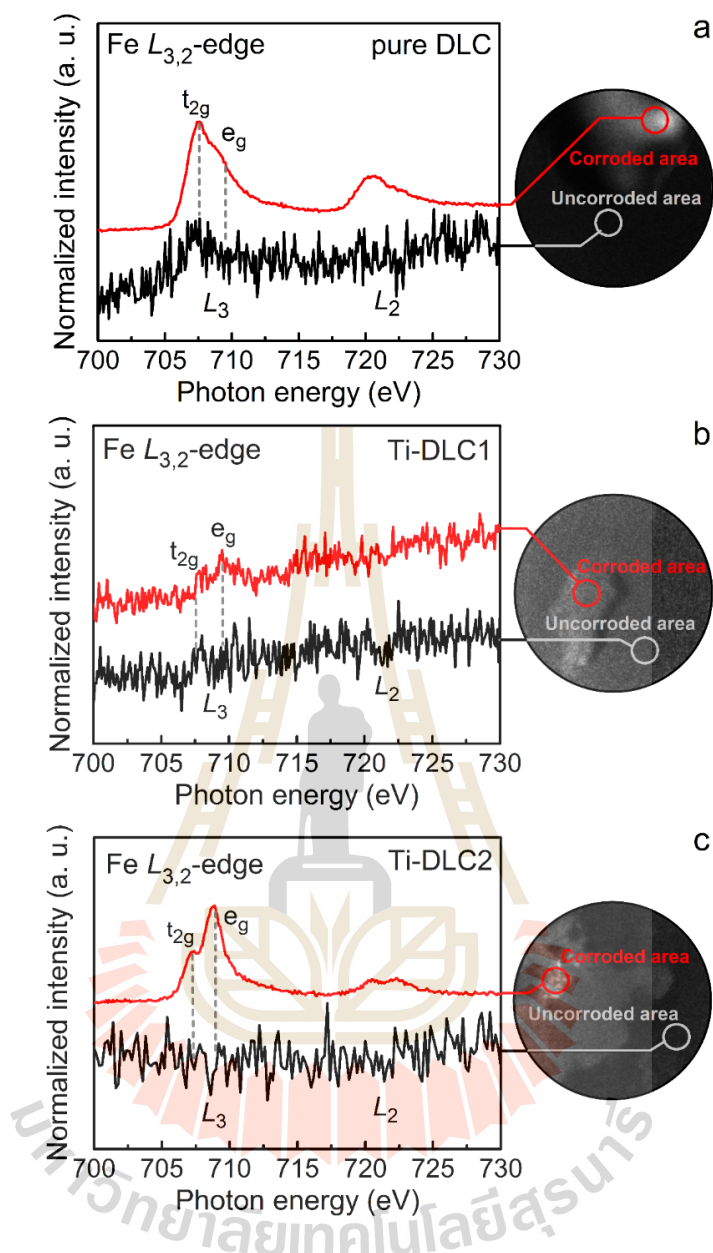
Figure 4.26 The corresponding Fe $L_{3,2}$-edge spectra acquired from the Fe $L_{3,2}$-edge X-
PEEM images of (a) pure DLC, (b) Ti-DLC1, and (c) Ti-DLC2,
respectively, adopted from Konkhunthot *et al*. (2019).

The Cr $L_{3,2}$-edge NEXAFS spectra had also been implemented as shown
in Figure 4.27, to analyze the oxide form on the film surface. The results of the Cr $L_{3,2}$-
edge NEXAFS spectra showed the same trend as the Fe $L_{3,2}$-edge NEXAFS spectra.

For this case, the spectral shape of the Cr peak intensity for the pure DLC and Ti-DLC2 resembled those of the Cr oxides formed on an AISI 304 stainless steel (Bastidas *et al*., 1998), particularly the Cr_2O_3 oxides (Soriano *et al*., 1993) which was the most stable form of the Cr oxide on the stainless steel and was difficult to eliminate.
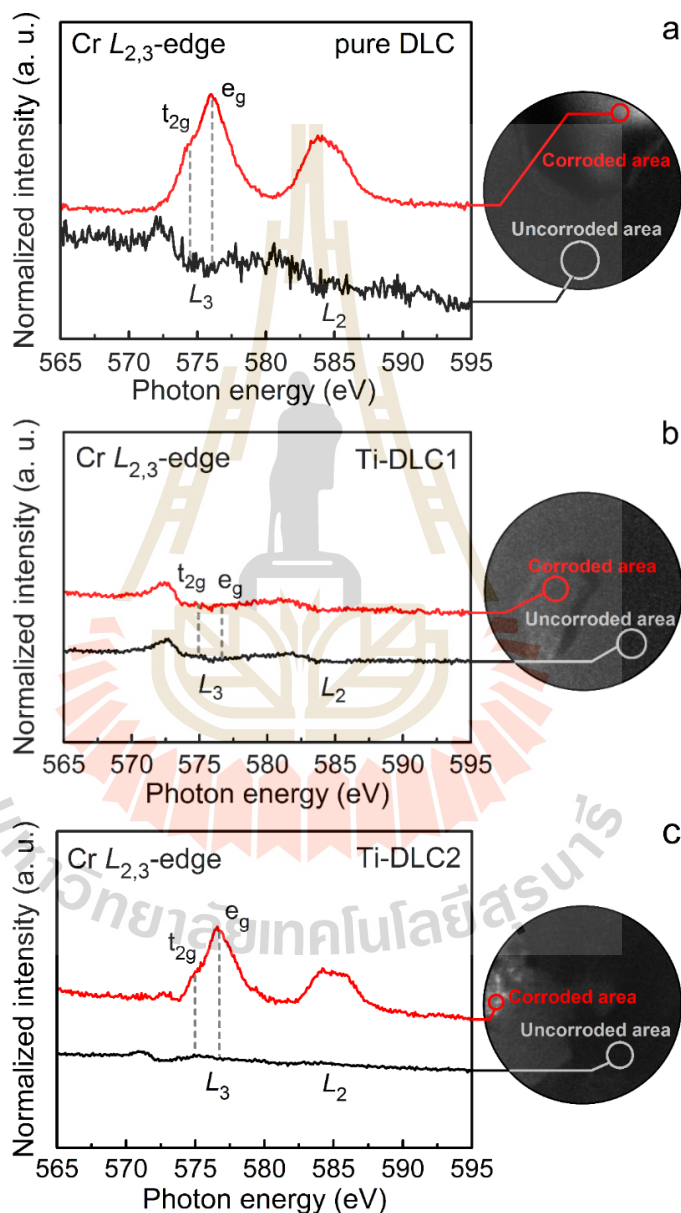
Figure 4.27 The corresponding Cr $L_{3,2}$-edge spectra acquired from the Cr $L_{3,2}$-edge X-PEEM images of (a) pure DLC, (b) Ti-DLC1, and (c) Ti-DLC2, respectively, adopted from Konkhunthot *et al*. (2019).

From the above-mentioned descriptions, the X-PEEM and NEXAFS results provided good consistency with the SEM and electrochemical corrosion characterizations. Interestingly, the Ti-doped DLC films provided the combined exceptional properties not only by exhibiting excellent mechanical property, enhanced thermal stability, and good corrosion protection performance but also by offering improved adhesion strength and tribological characteristic when being incorporated with only 0.8 at.% Ti. These properties make the Ti-doped DLC films ideal as the protective coatings in many engineering and industrial applications. In addition to the valuable properties, the pulsed two-FCVA system used for the DLC deposition in this thesis was a comparatively eco-friendly and cost-effective methods useful in developing new DLC films in the future.
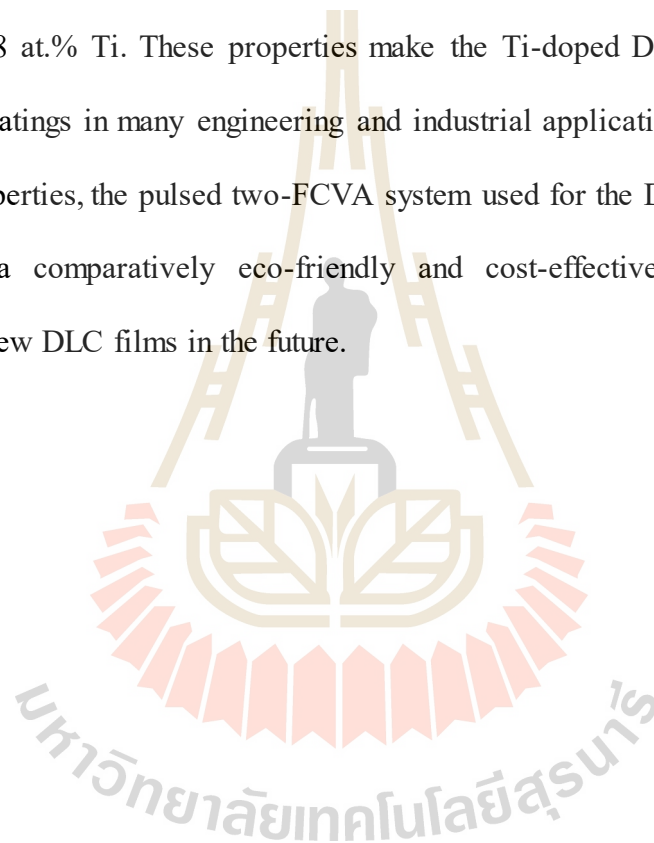
CHAPTER V

CONCLUSIONS

The important conclusion in this PhD thesis has been divided into 2 main parts. First an investigation was performed to explore the appropriate deposition conditions for DLC films. In the preliminary studies, DLC films were deposited on a Si (100) wafer substrate by pulsed two-FCVA deposition as a function of the V_{bias} in correlation with the microstructure and mechanical and optical properties. An intermediate layer of Ti was firstly deposited on the substrate to serve as an adhesive coating. A wide range of the V_{bias} from 0.0 to 1.5 kV was conducted to investigate the growth rate, microstructure, and several properties of the DLC films. The results of the XRR analysis revealed that the DLC films had a relatively high density between 2.51 and 2.79 g/m^3 which indicated the good quality of the DLC films. The growth rate of the DLC films was evaluated to be 3.5, 4.8, and 3.3 nm/min at the V_{bias} of 0.5, 1.0, and 1.5 kV, respectively which depended strongly on the self-sputtering of the substrate material and the deposition process. The films' surface roughness increased monotonically due to the impingement of the high energy of the ions during the increasing the V_{bias}. A low surface roughness could be obtained during the film growth under the optimum bias condition. The Raman analysis showed the lowest I_D/I_G ratio at V_{bias} of 1.0 kV which corresponded to the highest sp^3/sp^2 ratio acquired from the XPS analysis.

In addition to the sp^3/sp^2 ratio, the XPS results showed that the unbiased DLC film contained a large O content of 11.36 at.%. However, the O content of the deposited films decreased greatly in a range of 3.52–5.33 at.% as the V_{bias} increased from 0.5 to 1.5 kV. The hardness and elastic modulus of the DLC films were in a range of 13–25 GPa and 114–145 GPa, respectively. The mechanical properties were rather low compared to those of the ta-C films due to a high base pressure condition during the film deposition. A high value of the hardness and elastic modulus was associated with a large degree of internal stress during the film deposition which could be evidently elucidated through the subplantation model. The established correlation between the refractive index and the I_D/I_G ratio showed a good consistency with the mechanical and physical properties. This correlation could be applied to infer the sp^3/sp^2 ratio, hardness, and density of the films using either the refractive index or the I_D/I_G ratio acquired from the spectroscopic ellipsometry and Raman techniques, as simple, non-destructive, and reliable analytical methods. By using the established correlation, the number of samples was reduced. Therefore, it was an effective method for identifying the valuable properties of the DLC films which could be used for quality control and development in engineering and industrial applications. From the preliminary experiments, it could be concluded that the best deposition condition which provided high-quality DLC films with hardness and density of 25 GPa and 2.79 g/cm^3, respectively, close to the ta-C films was achieved at the V_{bias} of 1.0 kV. The mechanical and optical properties of the DLC films could be effectively tailored by regulating the V_{bias} which was corresponded to the microstructural transformation.

The further examination was associated with the deposition of the Ti-doped DLC films through the best deposition condition obtained from the preliminary study

in correlation with the pure DLC film. The microstructure in terms of the sp^3/sp^2 ratio and the several properties, such as thermal stability, adhesion strength, mechanical and tribological properties, and corrosion protection performance of the pure DLC and Ti-doped DLC films were thoroughly investigated in respect to the effects of Ti incorporation. The samples, in this experiment, were divided into 2 sets. One set was the films that were deposited on an AISI 304 stainless steel substrate and those were prepared for nano-mechanical, nano-scratch, nano-tribological, and electrochemical corrosion tests. The other set was the films that were deposited on the Si wafer substrate and those were used for elementary composition, microstructure, bonding configuration, and thermal stability analysis. Prior to the DLC deposition, an adhesive layer of Ti was also prepared on both substrates representing a bond coat. From the results, the SEM micrographs showed that the surface morphologies of all the films were very smooth and dense without delamination. The XPS analysis confirmed the existence of Ti atoms in the DLC films deposited by the pulsed two-FCVA technique. The application of the arc voltage was a potential method to introduce Ti atoms into the DLC films with an exact concentration level. A notable reduction in the residual internal stress and the increase in the I_D/I_G ratio of the DLC films as the Ti content increased was analyzed by the Raman analysis which showed good consistency with the NEXAFS results. The thermal stability of the Ti-doped DLC films experienced an enhancement due to the presence of the TiC phase as confirmed by the NEXAFS spectra. The nano-mechanical properties of the Ti-doped DLC films did not decrease much with the addition of a 0.8% (at.) Ti, but the adhesion strength was notably enhanced due to the reduction in the internal stress and the formation of the strong atomic intermixing bond at the Ti-doped DLC/Ti layer interface. The nano-tribological performance in terms of the COF of AISI

304 stainless (~0.50) steel exhibited a large improvement with the application of the DLC films (~0.19). The COF was, however, found to increase slightly for the softer DLC films. The NEXAFS in conjunction with X-PEEM techniques confirmed the formation of the passivating TiO_2 film on the Ti-doped DLC films. The passivation of the Ti-doped DLC surface led to a significant improvement in the corrosion protection performance as demonstrated by the E_{corr} shifting toward a positive region and the orders of magnitude decreasing in the i_{corr}, as seen in the potentiodynamic polarization curves. It was, however, noticed that the DLC films with a higher sp^3 content exhibited better corrosion resistance than those with a dominant sp^2 hybridized carbon, even if the TiO_2 film was included. This behavior could be attributed to the dense atomic packing and chemical inertness of the sp^3 hybridized carbons. In addition to the effect of the sp^3/sp^2 ratio in the film, the discontinuity of the cross-linked carbon network of the films, for example, the incoherent phases or porosities within the DLC films of high Ti content could have a negative effect on the corrosion performance. As described above, the DLC film with 0.8 at.% Ti doping provided high thermal stability, excellent mechanical property, good adhesion, enhanced tribological characteristics, and corrosion protection performance and was the potential candidate for mechanical and tribological applications.

CHAPTER VI

SUGGESTIONS AND FURTHER STUDIES

For the future prospects of carbon based-materials, especially DLC films, this PhD thesis has proposed a variety of investigations relating to DLC films which it is very much hoped will play an important part in increasing knowledge and providing a good foundation for further research and development in related areas. The incorporation of Ti in DLC has been proved to be a promising method in developing new materials with exceptional properties in engineering and industrial applications. A specific analytical technique is, however, essential to clearly explain certain phenomena. Furthermore, the improvement of the pulsed two-FCVA system is required to achieve a better performance. Further studies, therefore, should be conducted into the following items:

(i.) Investigation of the nanostructure of the Ti-doped DLC films using cross-sectional transmission electron microscopy (TEM) could be performed to ensure the existence of Ti in the DLC structure either in a form of nano-carbides or a solid solution of pure metals.

(ii.) Measurement of tribological performance under dry and lubrication conditions at elevated temperatures is required to monitor the films in real service conditions.

(iii.) The electrochemical impedance spectroscopy technique could be carried out to perfect the resistance of each layer.

(iv.) A higher arc burning voltage and greater energy input of the arc plasma power supply are required for ionization of metals with a large cohesive energy and boiling point, e.g., tungsten.

(v.) The application of a trigger electrode and trigger power supply are essential to stabilize the arc voltage and to maintain the cathode material consumption.

(vi.) The gaseous reactive species, such as nitrogen, oxygen, etc., could be introduced into the system to produce oxides, nitrides, compounds (carbides and carbonitrides), and alloys in the reactive FCVA deposition process.

(vii.) A pulsed bias voltage is required to yield high-quality DLC films without the electrical charge-up of any positively charged ions when the films are deposited on insulator substrates, such as polymers and glass.
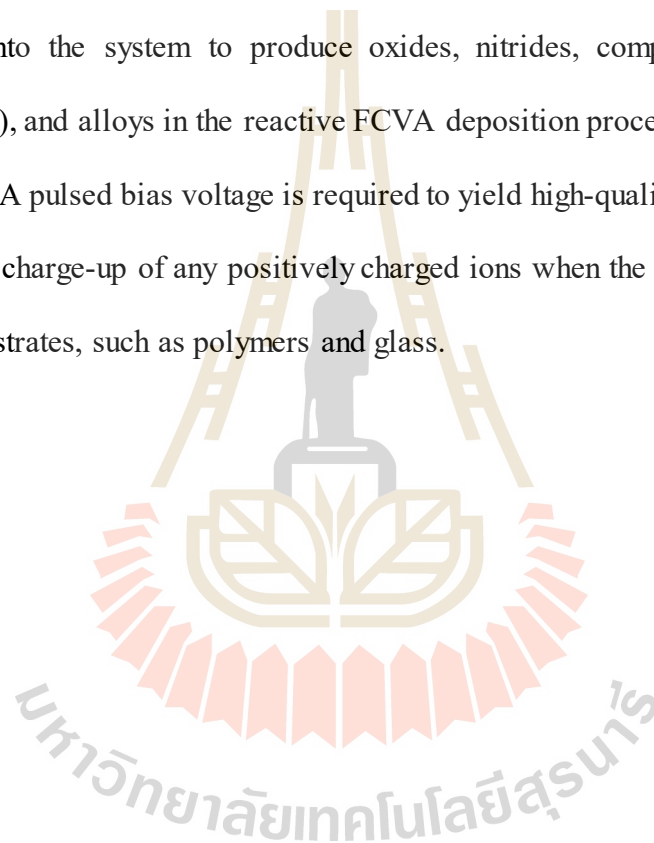
REFERENCES

Ahmed, M.H., Byrne, J.A., McLaughlin, J., and Ahmed, W. (2013). Study of human serum albumin adsorption and conformational change on DLC and silicon doped DLC using XPS and FTIR spectroscopy. **Journal of Biomedical Nanotechnology**. 4: 194–203.

Aisenberg, S., and Chabot, R. (1971). Ion-beam deposition of thin films of diamondlike carbon. **Journal of Applied Physics**. 42: 2953–2958.

Aisenberg, S., and Kimock, F.M. (1990). **In: Properties and Characterization of Amorphous Carbon Films: Materials Science Forum** (Pouch, J.J., and Alterovitz, S.A. (Eds.)), Zürich: Trans Tech. Publication, 52–53: 1–40.

Akkerman, Z.L., Efstathiadis, H., and Smith, F.W. (1996). Thermal stability of diamondlike carbon films. **Journal of Applied Physics**. 5: 3068–3075.

Andersson, J., Erck, R.A., and Erdemir, A. (2003). Friction behavior of diamond-like carbon films in vacuum and under varying water vapor pressure. **Surface and Coating Technology**. 163–164: 535–540.

Andersson, J., Erck, R.A., and Erdemir, A. (2003). Friction of diamond-like carbon films in different atmospheres. **Wear**. 254: 1070–1075.

Andriollo, T., Thorborg, J., and Hattel, J. (2017). Analysis of the equivalent indenter concept used to extract Young's modulus from a nano-indentation test: Some new insights into the Oliver-Pharr method. **Modelling and Simulation in Materials Science and Engineering**. 25: 1–22.

Ankit, K., Varade, A., Reddy, N., Dhan, S., Chellamalai, M., Balashanmugam, N., Krishna, P. (2017). Synthesis of high hardness IR optical coating using diamond-like carbon by PECVD at room temperature. **Diamond and Related Materials**. 78: 39–43.

Aspnes, D.E. (1982). Optical properties of thin films. **Thin Solid Films.** 89: 249–262.

ASTM G102-89. (1999). **Standard Practice for Calculation of Corrosion Rates and Related Information from Electrochemical Measurements**. West Conshohocken: ASTM International.

ASTM G5-14. (2016). **Standard reference test method for making potentiodynamic anodic polarization measurements**. West Conshohocken: ASTM International.

ASTM G5-87. (1987). **Practice for Standard Reference Method for Making Potentiostatic and Potentiodynamic Anodic Polarization Measurements**. West Conshohocken: ASTM International.

ASTM G59-97. (1994). **Standard Test Method for Conducting Potentiodynamic Polarization Resistance Measurement**. West Conshohocken: ASTM International.

Axelevitch, A., Gorenstein, B., and Golan, G. (2012). Investigation of optical transmission in thin metal films. **Physics Procedia**. 32: 1–13.

Azzi, M., Amirault, P., Paquette, M., Klemberg-Sapieha, J.E., and Martinu, L. (2010). Corrosion performance and mechanical stability of 316L/DLC coating system: Role of interlayers. **Surface and Coating Technology**. 204: 3986–3994.

Bastidas, J.M., Lopez, M.F., Gutierrez, A., and Torres, C.L. (1998). Chemical analysis of passive films on type AISI 304 stainless steel using soft X-ray absorption spectroscopy. **Corrosion Science**. 40: 431–438.

Beake, B., Vishnyakov, V., R. Valizadeh, R., and Colligon, J. (2006). Influence of mechanical properties on the nanoscratch behaviour of hard nanocomposite TiN/Si3N4 coatings on Si. **Journal of Physics D: Applied Physics**. 39: 1392–1397.

Beddoes J., and Parr, J.G. (1999). **Introduction to Stainless Steels, 3 edition**. US: ASM International.

Benny, T.H., Banerjee, S., Sambasivan, S., Balasubramanian, M., Fischer, D.A., Eres, G., Puretzky, A.A., Geohegan, D.B., Lowndes, D.H., Han, W.Q., Misewich, J.A., and Wong, S.S. (2006). Near-Edge X-ray Absorption Fine Structure Spectroscopy as a Tool for Investigating Nanomaterials. **Small**. 2: 26 – 35.

Beverskog, B., and Puigdomenech, I. (1996). Revised Pourbaix diagrams for iron at 25–300°C. **Corrosion Science**. 38: 2121–2135.

Beverskog, B., and Puigdomenech, I. (1997). Revised Pourbaix diagrams for chromium at 25–300°C. **Corrosion Science**. 39: 43–57.

Beverskog, B., and Puigdomenech, I. (1997). Revised Pourbaix diagrams for nickel at 25–300°C. **Corrosion Science**. 38: 969–980.

Bharathy, P.V., Nataraja, D., Chu, P.K., Wang, H.V., Yang, Q., Kiran, M.S.R.N., Albero, J.S., Mangalarai, D. (2010). Effect of titanium incorporation on the structural, mechanical and biocompatible properties of DLC thin films prepared by reactive-biased target ion beam deposition method. **Applied Surface Science**. 257: 143–150.

Bharathy, P.V., Yang, Q., Kiran M.S.R.N, Rha, J.J., Nataraj, D., and Mangalaraj, D. (2012). Reactive biased target ion beam deposited W–DLC nanocomposite thin films – microstructure and its mechanical properties. **Diamond and Related Materials**. 23: 34–43.

Bootkul, D., Supsermpol, B., Saenphinit, N., Aramwit, C., and Intarasiri, S. (2014). Nitrogen doping for adhesion improvement of DLC film deposited on Si substrate by filtered cathodic vacuum arc (FCVA) technique. **Applied Surface Science**. 310: 284–292.

Butler, H.J., Ashton, L., Bird, B., Cinque, G., Curtis, K., Dorney, J., Esmonde-White, K., Fullwood, N.J., Gardner, B., Martin-Hirsch, P.L., Walsh, M.J., McAinsh, M.R., Stone, N., and Martin, F.L., (2016). Using Raman spectroscopy to characterize biological materials **Nature Protocols**. 11: 664-687.

Casiraghi, C., Ferrari, A.C., and Robertson, J. (2005). Raman spectroscopy of hydrogenated amorphous carbon. **Physical Review B**. 72: 1–14.

Casiraghi, C., Piazza, F., Ferrari, A.C., Grambole, D., and Robertson, J. (2005). Bonding in hydrogenated diamond-like carbon by Raman spectroscopy. **Diamond and Related Materials**. 14: 1098–1102.

Characteristics of Synchrotron Light, digital image of Synchrotron Light Research Institute (SLRI), Nakhon Ratchasima, Thailand. Available from: (https://www.slri.or.th/en/what-is-synchrotron-light.html). Assessed date: December 13, 2018.

Chaus, A.S., Fedosenko, T.N., Rogachev, A.V., and Čaplovič, L. (2014). Surface, microstructure, and optical properties of copper-doped diamond-like carbon

coating deposited in pulsed cathodic arc plasma. **Diamond and Related Materials**. 42: 64–70.

Chen, J.S., Lau, S.P., Sun, Z., Tay, B.K., Yu, G.Q., Zhu, F.Y., Zhu, D.Z., and Xu, H.J. (2001). Structural and mechanical properties of nitrogen ion implanted ultra high molecular weight polyethylene. **Surface and Coatings Technology**. 138: 33–38.

Choi, J., Nakao, S., Miyagawa, S., Ikeyama, M., and Miyagawa, Y. (2007). The effects of Si incorporation on the thermal and tribological properties of DLC films deposited by PBII&D with bipolar pulses. **Surface and Coating Technology**. 201: 8357–8361.

Chowdhury, S., Laugier, M.T., and Rahman, I.Z. (2004). Effect of target self-bias voltage on the mechanical properties of diamond-like carbon films deposited by RF magnetron sputtering. **Thin Solid Films**. 468: 149–154.

Chu, P.K., and Li, L. (2006). Characterization of amorphous and nanocrystalline carbon films. **Materials Chemistry and Physics**. 96: 253–277.

Cobb, H.M. (2010). **History of stainless steel**. Ohio: ASM International.

Coll, B.F., and Chhowalla, M. (1996). Amorphous diamond film by enhanced arc deposition. **Surface and Coatings Technology**. 79: 76–86.

Cui, J., L. Qiang, L., Zhang, B., Ling, X., Yang, T., and Zhang, J. (2012). Mechanical and tribological properties of Ti-DLC films with different Ti content by magnetron sputtering technique. **Applied Surface Science**. 258: 5025–5030.

Cuomo, J.J., Doyle, J.P., Bruley, J., and Liu, J.C. (1991). Sputter deposition of dense diamondlike carbon films at low temperature. **Applied Physics Letters**. 58: 466–468.

Cuomo, J.J., Pappas, D.L., Bruley, J., Doyle, J.P., and Saenger, K.L. (1991). Vapor deposition processes for amorphous carbon films with sp^3 fractions approaching diamond. **Journal of Applied Physics**. 70: 1706–1711.

Dai, M.J., Zhou, K.S., Lin, S.S., Hou, H.J., Zhu, X.G., Li, H.W., and Niu, S.C. (2007). A Study on Metal-Doped Diamond-Like Carbon Film Synthesized by Ion Source and Sputtering Technique. **Plasma Process Polymer**. 4: 215–219.

Dai, W. (2011). Synthesis, characterization and properties of the DLC films with low Cr concentration doping by a hybrid linear ion beam system. **Surface and Coating Technology**. 205: 2882–2886.

Damasceno, J.C., and Camargo Jr., S.S. (2008). Plasma deposition and characterization of silicon oxide-containing diamond-like carbon films obtained from CH_4:SiH_4:O_2 gas mixtures. **Thin Solid Films**. 516: 1890–1897.

De Groot, F., and Kotani, A. (2008). **Core Level Spectroscopy of Solids**. Florida: Taylor & Francis Group.

De Jesus, L.R., Dennis, R.V., Depner, S.W., Jaye, C., Fischer, D.A., and Banerjee, S. (2013). Inside and outside: X-ray absorption spectroscopy mapping of chemical domains in graphene oxide. **The Journal of Physical Chemistry Letters**. 4: 3144–3151.

Dimigen, H., and Klages, C.P. (1991). Microstructure and wear behavior of metal-containing diamond-like coatings, **Surface and Coating Technology**. 49: 543–547.

Ding, X.Z., Taya, B.K., Lau, S.P., Zhang, P., and Zeng, X.T. (2002). Structural and mechanical properties of Ti-containing diamond-like carbon films deposited by filtered cathodic vacuum arc. **Thin Solid Films**. 408: 183–187.

Donnet, C. (1998). Recent progress on the tribology of doped diamond-like and carbon alloy coatings: A review. **Surface and Coatings Technology**. 100–101: 180–186.

Donnet, C., and Erdemir, A. (2008). **Tribology of Diamond-Like Carbon Films: Fundamentals and Applications**. New York: Springer. pp. 15,22,156−157,416,521.

Dreyer, W., Guhlke, C., and Landstorfer, M. (2014). A mixture theory of electrolytes containing solvation effects. **Electrochemistry Communications**. 43: 75–78.

Dwivedi, N., Kumar, S. and Malik, H.K. (2013). Role of base pressure on the structural and nanomechanical properties of metal/diamond-like carbon bilayers. **Applied Surface Science**. 274: 282–287.

Enos, D.G., and Scribner, L.L. (1987). **The Potentiodynamic Polarization Scan** (1–14). Hampshire: Solartron Instruments.

Er, K.H., and So, M.G. (2014). Effects of Si incorporation on thermal stability and tribological properties of DLC films. **Journal of Ceramic Processing Research**. 15: 141–145.

Er, K.H., and So, M.G. (2010). Thermal annealing behavior of Si-doped diamond like-carbon films deposited by reactive sputtering. **Journal of Ceramic Processing Research**. 11: 760–764.

Erdemir, A. (2004). Genesis of superlow friction and wear in diamondlike carbon films. **Tribology International**. 37: 1005–1012.

Erdemir, A., and Fenske, G.R. (1996). Tribological performance of diamond and diamondlike carbon films at elevated temperatures. **Tribology Transactions**. 39(4): 787–794.

Erdemir, A., and Donnet, C. (2005). Tribology of Diamond and Diamond-Like Carbon Films: An overview. **In: Wear – Materials, Mechanisms and Practice** (Stachowiak, G. (Eds.)), New York: John Wiley & Sons.

Erdemir, A., Nichols, F.A., Pan, X.Z., Wei, R., and Wilbur, P. (1993). Friction and wear performance of ion-beam-deposited diamond-like carbon films on steel substrates. **Diamond and Related Materials**. 3: 119–125.

Euaruksakul, C., Jearanaikoon, N., Bussayaporn, W., Kamonsutthipaijit, N., Photongkam, P., Tunmee, S., and Songsiriritthigul, P. (2013). Photoemission electron microscopy beamline at the Synchrotron Light Research Institute. **Journal of Physics: Conference Series**. 425: 182011-1–182011-4.

Fallon, P.J., Veerasamy, V.S., Davis, C.A., Robertson, J., Amaratunga, G.A.J., Milne, W.I., and Koskinen, J. (1993). Properties of filtered-ion-beam-deposited diamondlike carbon as a function of ion energy. **Physical Review B**. 48: 4777–4782.

Feng, X., and Xia, Y. (2012). Tribological properties of Ti-doped DLC coatings under ionic liquids lubricated conditions. **Applied Surface Science**. 258: 2433–2438.

Fernández-Solis, C.D., Vimalanandan, A., Altin, A., Mondragón-Ochoa, J.S., Kreth, K., Keil, P., and Erbe, A. (2016). Fundamentals of Electrochemistry, Corrosion and Corrosion Protection. **In: Soft Matter at Aqueous Interfaces** (Lang, P.R., and Liu, Y. (Eds.)), Cham: Springer.

Ferrari, A.C., and Robertson, J. (2000). Interpretation of Raman spectra of disordered and amorphous carbon. **Physical Review B**. 61: 14095–14107.

Ferrari, A.C., and Robertson, J. (2001). Resonant Raman spectroscopy of disordered, amorphous, and diamondlike carbon. **Physical Review B**. 64: 075413-1–075414-13.

Ferrari, A.C., and Robertson, J. (2004). Raman spectroscopy of amorphous, nanostructured, diamond-like carbon, and nanodiamond. **Philosophical Transactions of Royal Society of London A**. 362: 2477–2512.

Ferrari, A.C., LiBassi, A., Tanner, B.K., Stolojan, V., Yuan, J., Brown, L.M., Rodil, S.E., Kleinsorge, B., and Robertson, J. (2000). Density, sp^3 fraction, and cross-sectional structure of amorphous carbon films determined by X-ray reflectivity and electron energy-loss spectroscopy. **Physical Review B**. 62: 89–103.

Ferrari, A.C., Rodil, S.E., and Robertson, J. (2003). Interpretation of infrared and Raman spectra of amorphous carbon nitrides, **Physical Review B**. 67: 1–20.

Ferrari, A.C., Rodil, S.E., Robertson, J., and Milne, W.I. (2002). Is stress necessary to stabilise sp^3 bonding in diamond-like carbon? **Diamond and Related Materials**. 11: 994–999.

Field, J.E. (1993). **Properties of Natural and Synthetic Diamond**. London: Academic Press.

Field, S.K., Jarratt, M., and Teer, D.G. (2004). Tribological properties of graphite-like and diamond-like carbon coatings. **Tribology International**. 37: 949–956.

Fischer-Cripps, A.C. (2006). Critical review of analysis and interpretation of nanoindentation test data. **Surface and Coatings Technology**. 200: 4153–4165.

Fontaine, J., Belin, M., Mogne, T.L., and Grill, A. (2004). How to restore superlow friction of DLC: the healing effect of hydrogen gas. **Tribology International**. 37: 869–877.

Fontaine, J., Loubet, J.L., Mogne, T.L, Grill, A. (2004). Superlow friction of diamond-like carbon films: a relation to viscoplastic properties. **Tribology Letters**. 17: 709–714.

Francisco, J.B.L, Cynthia, D.G.E., Ramon, C.H., Susana, P.A.R., Manuel, J.P.C., Jose, E.L.S., Roberto, M.S., and Jose, M.H.R. (2015). Influence of size on the microstructure and mechanical properties of an AISI 304L stainless steel: A comparison between bulk and fibers. **Materials**. 8: 451–461.

Francz, G., Schroeder, A., Hauert, R. (1999). Surface Analysis and Bioreactions of Ti- and V-containing *a*-C: H. **Surface and Interface Analysis**. 28: 3–7.

Fu, R.K.Y., Mei, Y.F., Fu, M.Y., Liu, X.Y., and Chu, P.K. (2005). Thermal stability of metal-doped diamond-like carbon fabricated by dual plasma deposition. **Diamond and Related Materials**. 14: 1489–1493.

Fu, R.K.Y., Mei, Y.F., Fu, M.Y., Liu, X.Y., and Chu, P.K. (2005). Thermal stability of metal-doped diamond-like carbon fabricated by dual plasma deposition. **Diamond and Related Materials**. 14: 1489–1493.

Fu, Z.Q., Wang, C.B., Zhang, W., Wang, W., Yue, W., Yu, X., Peng, Z.J., Lin, S.S., and Dai, M.J. (2013). Influence of W content on tribological performance of W-doped diamond-like carbon coatings under dry friction and polyalpha olefin lubrication conditions. **Material and Design**. 51: 775–779.

Gandhiraman, R.P., Nordlund, D., Javier, C., Koehne, J.E., Chen, B., and Meyyappan. M. (2014). X-ray absorption study of graphene oxide and transition metal oxide nanocomposites. **The Journal of Physical Chemistry C**. 118: 18706−18712.

Gangopadhyay, A., (1998). Mechanical and tribological properties of amorphous carbon films. **Tribology Letters**. 5: 25–39.

Garcia-Caurel, E., De Martino, A., Gaston, J.P., and Yan, L. (2013). Application of Spectroscopic Ellipsometry and Mueller Ellipsometry to Optical Characterization. **Applied Spectroscopy**. 67: 1−21.

Gardos, M.N. (1994). Tribology and wear behaviour of diamond. **In: Synthetic Diamond: Emerging CVD Science and Technology** (Spear, K.E., and Dismuke, J.P. (Eds.)), New York: Wiley, 419–502.

Gayathri, S., Kumar, N., Krishnan, R., Ravindran, T.R., Amirthapandian, S., Dash, S., Tyagi, A.K., and Sridharan, M. (2015). Influence of transition metal doping on the tribological properties of pulsed laser deposited DLC films. **Ceramics International**. 41: 1797–1805.

Gharam, A.A., Lukitsch, M.J., Balogh, M.P., Irish, N., and Alpas, A.T. (2011). High temperature tribological behavior of W-DLC against aluminum. **Surface and Coating Technology**. 206: 1905–1912.

Gou, W., Li, G., Chu, X., and Zhong, B. (2007). Effect of negative self-bias voltage on microstructure and properties of DLC films deposited by RF glow discharge. **Surface and Coatings Technology**. 201: 5043–5045.

Grill, A. (1997). Tribology of diamond like carbon and related materials: An updated review. **Surface and Coating Technology**. 94–95: 507–513.

Grill, A. (1999). Diamond-like carbon: State of the art, **Diamond and Related Materials**. 8: 428–434.

Grillo, S.E., and Field, J.E. (2003). The friction of natural and CVD diamond. **Wear**. 254: 945–949.

Guo, C.Q., Pei, Z.L., Fan, D., Gong, J., and Sun, C. (2015). Microstructure and tribomechanical properties of (Cr, N)-DLC/DLC multilayer films deposited by

a combination of filtered and direct cathodic vacuum arcs. **Diamond and Related Materials**. 60: 66–74.

Guo, T., Kong, C., Li, X., Guo, P., Wang, Z., and Wang, A. (2017). Microstructure and mechanical properties of Ti/Al co-doped DLC films: dependence on sputtering current, source gas, and substrate bias. **Applied Surface Science**. 410: 51–59.

Hähner, G. (2006). Near edge X-ray absorption fine structure spectroscopy as a tool to probe electronic and structural properties of thin organic films and liquids. **Chemical Society Reviews.** 35: 1244–1255.

Harris, S.J., Weiner, A.M., and Meng, W.J. (1997). Tribology of metal-containing diamond-like carbon coatings. **Wear**. 211: 208–217.

Hassan, M.A., Bushroa, A.R., and Mahmoodian, R. (2015). Identification of critical load for scratch adhesion strength of nitride-based thin films using wavelet analysis and a proposed analytical model. **Surface and Coatings Technology**. 277: 216–221.

Hiratoko, T., Yoshiasa, A., Nakatani, T., Okube, M., Nakatsuka, A., and Sugiyama, K. (2013). Temperature dependence of pre-edge features in Ti K-edge XANES spectra for $ATiO_3$ (A = Ca and Sr), A_2TiO_4 (A = Mg and Fe), TiO_2 rutile and TiO_2 anatase. **Journal of Synchrotron Radiation**. 20: 641–643.

Hiratsuka, M., Nakamori, H., Kogo, Y., Sakurai, M., Ohtake, N., and Saitoh, H. (2013). Correlation between optical properties and hardness of diamond-like carbon films. **Journal of Solid Mechanics and Materials Engineering**. 7: 187–198.

Hirvonen, J.P., Koskinen, J., Anttila, A., Lappalainen, R., Toivonen, R., Arminen, E., and Trkula, M. (1990). Characterization and unlubricated sliding of ion-beam-deposited hydrogen-free diamond-like carbon films. **Wear**. 141: 45–58.

Irmer G., and Dorner-Reisel, A. (2005). Micro-Raman studies on DLC coatings. **Advanced Engineering Materials.** 8: 694–705.

Ishpal, Kumar, S., Dwivedi, N., and Rauthan, C.M.S. (2012). Investigation of radio frequency plasma for the growth of diamond like carbon films. **Physics of Plasmas**. 19: 033515-1–033515-14.

Jacop, W., and MÖller, W. (1993). On the structure of thin hydrocarbon films. **Applied Physics Letters**. 63: 1771–1773.

Jahanmir, S., Deckman, D.E., Ives, L.K., Feldman, A., and Farabaugh, E. (1989). Tribological characteristics of synthesized diamond films on silicon carbide. **Wear**. 133: 73–81.

Jimenez, J., Gago, R., Albella, J.M., and Terminello, L.J. (2001). X-Ray absorption studies of bonding environments in graphitic carbon nitride. **Diamond and Related Materials**. 10: 1170–1174.

Jo, Y.J., Zhang, T.F., Son, M.J., Kim, KH. (2018). Synthesis and electrochemical properties of Ti-doped DLC films by a hybrid PVD/PECVD process. **Applied Surface Science**. 433: 1184–1191.

Jüttner, B. (1987). Characterization of the cathode spot. **IEEE Transaction on Plasma Science**. 15: 474−480.

Kalin, M., Roman, E., Ožbolt, L., Vižintin, J. (2010). Metal-doped (Ti, WC) diamond-like-carbon coatings: Reactions with extreme-pressure oil additives under tribological and static conditions. **Thin Solid Films**. 518: 4336–4344.

Kamiya, M., Tanoue, H., Takikawa, H., Taki, M., Hasegawa, Y., and Kumagai, M. (2009). Preparation of various DLC films by T-shaped filtered arc deposition and the effect of heat treatment on film properties. **Vacuum**. 83: 510–514.

Kishimoto, S., Hashiguchi, T., Ohshio, S., and Saitoh, H. (2008). Density investigation by X-ray reflectivity for thin films synthesized using atmospheric CVD. **Chemical Vapor Deposition**. 14: 303–308.

Klaffke, D., Brand, J., Brand, C., and Wittorf, R. (2005). Tribological characterisation of *a*-C: H coatings at room temperature: Effect of counterbody material. **Tribotest**. 11: 213–232.

Kociubczyk, A., Mendez, C., Gregorutti, R., and Ares, A. (2015). Electrochemical tests in stainless steel surgical implants. **Procedia Materials Science**. 9: 335–340.

Koidl, P., Wagner, C., Dischler, B., Wagner, J., and Ramsteiner, M. (1990). **Materials Science Forum**. 52: 41–70.

Konca, E., Cheng, Y.T., Weiner, A.M., Dasch, J.M., and Alpas, A.T. (2005). Effect of test atmosphere on the tribological behaviour of the non-hydrogenated diamond-like carbon coatings against 319 aluminum alloy and tungsten carbide. **Surface and Coating Technology**. 200: 1783–1791.

Konkhunthot, K., Photongkam, P., and Wongpanya, P. (2019). Improvement of thermal stability, adhesion strength and corrosion performance of diamond-like carbon films with titanium doping. **Applied Surface Science**. 469: 471–486.

Konkhunthot, K., Tunmee, S., Zhou, X.L. Komatsu, K., Photongkam, P., Saitoh, H., and Wongpanya, P. (2018). The correlation between optical and mechanical properties of amorphous diamond-like carbon films prepared by pulsed filtered cathodic vacuum arc deposition. **Thin Solid Films**. 653: 317–325.

Koskinen, J., Hirvonen, J.P., Lappalainen, R., Anttila, A. (1994). **Diamond and Related Materials**. 3: 52–55.

Lam, L., Kong, K.V., Olivo, M., and Leong, W.K. (2016). Vibrational spectroscopy of metal carbonyls for bio-imaging and -sensing. **Analyst. 141**: 1569-1586.

Lee, J., Collins, R.W., Veerasamy, V.S., and Robertson, J. (1998). Analysis of the ellipsometric spectra of amorphous carbon thin films for evaluation of the sp^3-bonded carbon content. **Diamond and Related Materials**. 7: 999–1009.

Lenardi, C., Piseri, P., Briois, V., Bottani, C.E., Li Bassi, A., and Milani, P. (1999). Near-edge X-ray absorption fine structure and Raman characterization of amorphous and nanostructured carbon films. **Journal of Applied Physics**. 85: 7159–7167.

Leng, Y.X., Chen, J.Y., Yang, P., Sun, H., Wan, G. J., and Huang, N. (2003). Mechanical properties and thermomechanical stability of diamond-like carbon films synthesized by pulsed vacuum arc plasma deposition. **Surface and Coating Technology**. 173: 67–73.

Lengeler, B., Campagna, M., and Rosei, K. (1990). **X-ray Absorption and Reflection in the Hard X-Ray Range, Photoemission and Absorption and reflection in Solids and Interfaces with Synchrotron Radiation**. Amsterdam: North Holland.

Liang, C.H., Huang, C.F., and Tsai, H.Y. (2015). The influence of substrate bias voltages on structure, mechanical properties and anti-corrosion performance of Cr doped diamond- like carbon films deposited by steered cathodic arc evaporation. **Thin Solid Films**. 597: 88–96.

Lifshitz, Y. (1996). Hydrogen-free amorphous carbon films: Correlation between growth conditions and properties. **Diamond and Related Materials**. 3–5: 388–400.

Lifshitz, Y. (1999). Diamond-like carbon–present status, **Diamond and Related Materials**. 8: 1659–1676.

Lifshitz, Y., Kasi, S.R., and Rabalais, J.W. (1989). Subplantation model for film growth from hyperthermal species: application to diamond. **Physical Review Letters**. 62: 1290–1293.

Lifshitz, Y., Kasi, S.R., Rabalais, J.W., and Eckstein, W. (1990). Subplantation model for film growth from hyperthermal species. **Physical Review B**. 41: 10468–10480.

Lin, Y., Zia, A.W., Zhou, Z., Shum, P.W., and Li, K.Y. (2017). Development of diamond-like carbon (DLC) coatings with alternate soft and hard multilayer architecture for enhancing wear performance at high contact stress. **Surface and Coatings Technology**. 320: 7–12.

Lin, Y.H., Lin, H.D., Liu, K.C., Huang, M.W., Chen, Y.C., Chen, J.R., and Shih, H.C. (2009). Annealing effect on the structural, mechanical and electrical properties of titanium-doped diamond-like carbon films. **Thin Solid Films**. 518: 1503–1507.

Lippitz, A., Koprinarov, I., Friedrich, J.F., Unger, W.E.S., Weiss, K., and Wöll, Ch. (1996). Surface analysis of metallized poly (bisphenol A carbonate) films by X-ray absorption spectroscopy (NEXAFS). **Polymer**. 37: 3157-3160.

Liu, D., Benstetter, G., Lodermeier, E., and Vancea, J. (2003).Influence of the incident angle of energetic carbon ions on the properties of tetrahedral amorphous carbon (ta-C) films. **Journal of Vacuum Science and Technology A**. 21: 1665–1670.

Liu, H., Tanaka, A., and Umeda, K. (1999). The tribological characteristics of diamond-like carbon films at elevated temperatures. **Thin Solid Films**. 346: 162–168.

Liu, L., Wang, T., Huang, J., He, Z., Yi, Y., and Du, K. (2016). Diamond-like carbon thin films with high density and low internal stress deposited by coupling DC/RF magnetron sputtering. **Diamond and Related Materials**. 70: 151–158.

Liu, Y., Erdemir, A., and Meletis, E.I. (1996). A study of the wear mechanism of diamond-like carbon films. **Surface and Coating Technology**. 82: 48-56.

Lossy, R., Pappas, D.L., Roy, R.A., Doyle, J.P., Cuomo, J.J., Buley, J. (1995). Properties of amorphous diamond films prepared by a filtered cathodic arc. **Journal of Applied Physics**. 77: 4750–4756.

Lubwama, M., Corcoran, B., Rajani, K.V., Wong, C.S., Kirabira, J.B., Sebbit, A., McDonnell, K.A., Dowling, D., and Sayers, K. (2013). Raman analysis of DLC and Si-DLC films deposited on nitrile rubber. **Surface and Coatings Technology**. 232: 521–527.

Lung, B.H., Chiang, M.J., and Hon, M.H. (2001). Growth characterization and properties of diamond-like carbon films by electron cyclotron resonance chemical vapor deposition. **Thin Solid Films**. 392: 16–21.

Luo, J.K., Fu, Y.Q., Le, H.R., Williams, J.A., Spearing, S.M., Milne, W.I. (2007). Diamond and diamond-like carbon MEMS. **Journal of Micromechanics and Microengineering**. 17: 147–163.

Lyklema, J. (1995). **Fundamentals of Interface and Colloid Science: Soft Colloids**. The Netherlands: Elsevier Academic Press.

Lyklema, J. (2009). Quest for ion–ion correlations in electric double layers and overcharging phenomena. **Advances in Colloid and Interface Science**. 147–148: 205–213.

Ma, G., Gong, S., Lin, G., Zhang, L., and Sun, G. (2012). A study of structure and properties of Ti-doped DLC film by reactive magnetron sputtering with ion implantation. **Applied Surface Science.** 258: 3045– 3050.

Mandal, P., Arutiun, E., Papken, H. (2015). Tribological behaviour of Mo − W doped carbon-based coating at ambient condition. **Tribology International**. 90: 135– 147.

Mangolini, F., McClimon, J.B., Rose, F., and Carpick, R.W. (2014). Accounting for nanometer-thick adventitious carbon contamination in X-ray absorption spectra of carbon-based materials. **Analytical Chemistry**. 86: 12258–1265.

Marshall, P. (1984). **Austenitic stainless steel: Microstructure and mechanical properties**. Essex: Elsevier Applied Science Publishers.

Martinez-Martinez, D., Lopez-Cartes, C., Gago, R., Fernandez, A., Sanchez-Lopez, J.C. (2009).Thermal Stability and Oxidation Resistance of Nanocomposite TiC/a-C Protective Coatings. **Plasma Processes and Polymers**. 6: 462–467.

Matthes, B., Brozeit, E., Aromaa, J., Ronkainen, H., Hannula, S.P., Leyland, A., and Matthes, A. (1991). Corrosion performance of some titanium-based hard coatings. **Surface and Coatings Technology**. 49: 489–495.

McKenzie, D.R., Yin, Y., Marks, N.A., Davis, C.A., Pailthorpe, B.A., Amaratunga, G.A.J., and Veerasamy, V.S. (1994). Hydrogen-free amorphous carbon preparation and properties. **Diamond and Related Materials**. 3: 353–360.

McKenzie, D.R., Muller, D., Pailthorpe, B.A., Wang, Z.H., Kravtchinskaia, E., Segal, D., Lukins, P.B., Swift, P.D., Martin, P.J., Amaratunga, G., Gaskell, P.H., and Saeed, A. (1991). **Diamond and Related Materials**. 1: 51−59.

Meletis, E.I., Erdemir, A., and Fenske, G.R. (1995). Tribological characteristics of DLC films and duplex plasma nitriding/DLC coating treatments. **Surface and Coating Technology**. 73: 39–45.

Merkulov, V.I., Lowndes, D.H., Jellison Jr, G.E., Puretzky, A.A., and Geohegan D.B. (1998). Structure and optical properties of amorphous diamond films prepared by ArF laser ablation as a function of carbon ion kinetic energy. **Applied Physics Letters**. 73 (1998) 2591–2593.

Miki, Y., Nishimoto, A., Sone, T., and Araki, Y. (2015). Residual stress measurement in DLC films deposited by PBIID method using Raman microprobe spectroscopy. **Surface and Coatings Technology**. 283: 274–280.

Milošev, I., Huković, M.M., and Strehblow, H.H. (2000). Passive film on orthopaedic TiAlV alloy formed in physiological solution investigated by X-ray photoelectron spectroscopy. **Biomaterials**. 21: 2103–2113.

Mirkarimi, P.B., Medlin, D.L., McCarty, K.F., Dibble, D.C., and Clift, W.M. (1997). The synthesis, characterization, and mechanical properties of thick, ultrahard cubic boron nitride films deposited by ion-assisted sputtering. **Journal of Applied Physics**. 82: 1617–1625.

Miyoshi, K., Wu, R.L.C., and Garscadden, A. (1992). Friction and wear of diamond and diamondlike carbon coatings. **Surface and Coating Technology**. 54−55: 428–434.

Modabberasl, A., Kameli, P., Ranjbar, M., Salamati, H., and Ashiri, R. (2015). Fabrication of DLC thin films with improved diamond-like carbon character by the application of external magnetic field. **Carbon**. 94: 485–493.

Mori, T., Fujii, N., Xiong, Y., and Saitoh, T. (1995). Optical study of ion-deposited diamond-like carbon films using spectroscopic ellipsometry. **Thin Solid Films**. 270: 215–219.

Moura, C.C., Tare, R.S., Oreffo, R.O.C., and Mahajan, S. (2016). Raman spectroscopy and coherent anti Stokes Raman scattering imaging: prospective tools for monitoring skeletal cells and skeletal regeneration, **Journal of The Royal Society Interface**. 13: 1–12.

Mutafov, P., Lanigan, J., Neville, A., Cavaleiro, A., and Polcar, T. (2014). DLC-W coatings tested in combustion engine−Frictional and wear analysis. **Surface and Coating Technology**. 260: 284–289.

Najafpour, M.M., Moghaddam, N.J., Hosseini, S.M., Madadkhani, S., Hotynska, M., Mehrabani, S., Bagheri, R., and Song, Z.L. (2017). Nanolayered manganese oxide: Insights from inorganic electrochemistry. **The Royal Society of Chemistry**. 1–3: 1–13.

Nakamatsu, K., Nagase, M., Igaki, J., Namatsu, H., and Matsui, S. (2005). Mechanical characteristics and its annealing effect of diamondlike-carbon nanosprings fabricated by focused-ion-beam chemical vapor deposition. **Journal of Vacuum Science and Technology B**. 23: 2801–2805.

Narayan, R.J. (2005). Laser processing of diamond-like carbon-metal composites. **Applied Surface Science**. 245: 420–430.

Netz, R.R. (2001). Static van der Waals interactions in electrolytes. **The European. Physical Journal E**. 5: 189–205.

Netz, R.R., and Orland, H. (2000). Beyond Poisson-Boltzmann: Fluctuation effects and correlation functions. **The European. Physical Journal E**. 1: 203–214.

North America Stainless. (2010). Long Products Stainless Steel Grade Sheet. North America Stainless, California, US, Available from: (https://www.northamericanstainless.com/wp-content/uploads/2010/10/Grade-304-304L.pdf). Assessed date: Jan 11, 2019.

Okamoto, R., and Onuki, A. (2011). Charged colloids in an aqueous mixture with a salt. **Physics Review E**. 84: 051401-1–05401-19.

Oliveira, V.M.C.A., Aguiar, C., Vazquez, A.M., Robin, A.L.M., and Barboza, M.J.R. (2017). Corrosion Behavior Analysis of Plasma-assisted PVD Coated Ti-6Al-4V alloy in 2 M NaOH Solution. **Materials Research**. 20: 436–444.

Oliver, W.C., and Pharr, G.M. (1992). An improved technique for determining hardness and elastic modulus using load and displacement sensing indentation experiments. **Journal of Materials Research**. 7: 1564−1583.

Oliver, W.C., and Pharr, G.M. (2004). Measurement of hardness and elastic modulus by instrumented indentation: Advances in understanding and refinements to methodology. **Journal of Materials Research**. 19: 3–20.

Outka, D.A., and StÖhr, J. (1988). Curve fitting analysis of near edge core excitation spectra of free, adsorbed, and polymeric molecules. **The Journal of Chemical Physics**. 88: 3539–3554.

Pandiyaraj, K.N., Heeg, J., Lampka, A., Junge, F., Barfels, T., Wienecke, M., Rhee, Y.H., and Kim, H.W. (2012). In vitro cyto and blood compatibility of titanium containing diamond-like carbon prepared by hybrid sputtering method. **Plasma Science and Technology**. 14: 829–836.

Pang, X., Yang, H., Gao, K., Wang, Y., and Volinsky, A.A. (2011). AlTiN layer effect on mechanical properties of Ti-doped diamond-like carbon composite coatings. **Thin Solid Films**. 519: 5353–5357.

Park, S.J., Lee, K.R., and Ko, D.H. (2004). Tribochemical reaction of hydrogenated diamond-like carbon films: A clue to understand the environmental dependence. **Tribology International**. 37: 913–921.

Parratt, L.G., (1954). Surface studies of solids by total reflection of X-rays. **Physical Review**. 95: 359–369.

Penner-Hahn, J.E. (2003). X-ray absorption spectroscopy. **Comprehensive Coordination Chemistry II**. 2: 159–186.

Phase, D.M., and Sathe, V. (2004). In situ photoelectron spectroscopy study of TiCxNy films synthesized through reactive ion beam mixing. **Journal of Physics D: Applied Physics**. 37: 1696–1700.

Pierson, H.O. (1993). **Handbook of Carbon, Graphite, Diamond and Fullerenes: Properties, Processing and Applications**. New Jersey: Noyes Publications.

Prawer, S., Nugent, K.W., Lifshitz, Y., Lempert, G.D., Grossman, E., Kulik, J., Avigal, I., and Kalish, R. (1996). Systematic variation of the Raman spectra of DLC films as a function of sp^2:sp^3 composition. **Diamond and Related Materials**. 5: 433–438.

Qiang, L., Zhang, B., Zhou, Y., and Zhang, J. (2013). Improving the internal stress and wear resistance of DLC film by low content Ti doping. **Solid State Sciences**. 20: 17–22.

Ray, S.C., Tsai, H.M., Chiou, J.W., Bose, B., Jan, J.C., Kumar, K., Pong, W.F., Dasgupta, D., and Tsai, M.H. (2004). X-ray absorption spectroscopy (XAS)

study of dip deposited a-C:H(OH) thin films. **Journal of Physics: Condensed Matter**. 16: 5713–5719.

Reichelt, R. (2007). Scanning Electron Microscopy, **In: Science of Microscopy** (Hawkes, P.W., and Spence, J.C.H. (Eds.)), New York: Springer. pp. 133–272.

Reinke, P., Jacop, W., and MÖller, W. (1993). Influence of the ion energy on the growth and structure of thin hydrocarbon films. **Journal of Applied Physics**. 74: 1354–1361.

Robertson, J. (1986). Amorphous carbon. **Advances in Physics**. 35: (1986) 317–374.

Robertson, J. (1992). Mechanical properties and structure of diamond-like carbon. **Diamond and Related Materials**. 1: 397–406.

Robertson, J. (1993). Deposition mechanisms for promoting sp^3 bonding in diamond-like carbon. **Diamond and Related Materials**. 2: 984–989.

Robertson, J. (1996). Amorphous carbon, **Current Opinion Solid State and Materials Science**. 1: 557−561.

Robertson, J. (2002). Diamond-like amorphous carbon. **Materials Science and Engineering: R: Reports**. 37: 129−281.

Robertson, J. (2002). Diamond-like amorphous carbon. **Materials Science Engineering R**. 37: 129–281.

Robertson, J. (2003). Requirements of ultrathin carbon coatings for magnetic storage technology. **Tribology International**. 36: 405–415.

Robertson, J. (2008). Classification of Diamond-like Carbons. **In: Tribology of diamond-like carbon films: Fundamentals and applications** (Donnet, C., and Erdemir, A. (Eds.)), Boston: Springer. pp. 13–24.

Ronkainen, H., and Holmberg, K. (2008). **In: Tribology of Diamond-like Carbon films: Fundamental and Applications** (Donnet, C., and Erdemir, A. (Eds.)), New York: Springer. 155−200.

Ronkainen, H., Koskinen, J., Likonen, J., Varjus, S., and Vihersalo, J. (1994). Characterization of wear surfaces in dry sliding of steel and alumina on hydrogenated and hydrogen-free carbon films. **Diamond and Related Materials**. 3: 1329–1336.

Ronkainen, H., Likonen, J., Koskinen, J., and Varjus, S. (1996). Effect of tribofilm formation on the tribological performance of hydrogenated carbon coatings. **Surface and Coating Technology**. 79: 87–94.

Ronkainen, H., Varjus, S., Koskinen, J., and Holmberg, K. (2001). Differentiating the tribological performance of hydrogenated and hydrogen-free DLC coatings. **Wear**. 249: 260–266.

Ronkainen, H., Varjus, S., and Koskinen, J. (1992). Tribological properties of diamond-like carbon films. **Tribologia**. 11: 133–141.

Rosenbloom, S.N., and Corbett, R.A. (2007). **An Assessment of ASTM F2129 Electrochemical Testing of Small Medical Implants − Lessons Learned**. Delaware: Corrosion Testing Labs Inc. pp. 1–10.

Rüdiger, C., Maglia, F., Leonardi, S., Sachsenhauser, M., Sharp, I.D., Paschos, O., and Kunze, J. (2012). Surface analytical study of carbothermally reduced titania films for electrocatalysis application. **Electrochimica Acta**. 71: 1–9.

Sakurai, K., Mizusawa M., and Ishii, M. (2008). Significance of Frequency Analysis in X-ray Reflectivity: Towards analysis which does not depend too much on

models. **Transactions of the Materials Research Society of Japan**. 33: 523–528.

Sanders, D.M., and Anders, A. (2000). Review of cathodic arc deposition technology at the start of the new millennium. **Surface and Coating Technology**. 133−134: 78−90.

Santra, T.S., Liu, C.H., Bhattacharyya, T.K., Patel, P., and Barik, T.K. (2010). Characterization of diamond-like nanocomposite thin films grown by plasma enhanced chemical vapor deposition. **Journal of Applied Physics**. 107: 124320-1–124320-9.

Schematic diagram and Photograph of X-PEEM system, digital image of Synchrotron Light Research Institute (SLRI), Nakhon Ratchasima, Thailand. Available from: (https://www.slri.or.th/en/bl32b-peem.html). Assessed date: Jan 10, 2019.

Schematic of a typical XPS setup, digital image of Experimental Physics, Saarland University, 66123 Saarbrücken, Germany. Available from: (https://jacobs.physik.uni-saarland.de/home/index.php?page=forschung/UHV-Lab-1). Assessed date: Jan 11, 2019.

Schwan, J., Ulrich, S., Roth, H., Ehrhardt, H., Silva, S.R.P, Robertson, J., Samlenski, R., and Brenn, R. (1996). Tetrahedral amorphous carbon films prepared by magnetron sputtering and dc ion plating. **Journal of Applied Physics**. 79: 1416–1422.

Siegal, M.P., Barbour, J.C., Provencio, P.N., Tallant, D.R., Friedmann, T.A. (1998). Amorphous-tetrahedral diamondlike carbon layered structures resulting from film growth energetics. **Applied Physics Letters**. 73: 759–761.

Silva, F.J.G., Martinho, R.P., and Baptista, A.P.M. (2014). Characterization of laboratory and industrial CrN/CrCN/diamond-like carbon coatings. **Thin Solid Films**. 550: 278–284.

Singh, S.B., Poswal, A.K., Pandey, M., Tokas, R.B., Chand, N., Dhara, S., Sundaravel, B., Nair, K.G.M., Sahoo, N.K., and Patil, D.S. (2009). X-ray reflectivity studies on DLC films deposited by microwave ECR CVD: Effect of substrate bias. **Surface and Coatings Technology**. 203: 986–991.

Sinha, S.K., Sirota, E.N., Garoff, S., Stanley, H.B. (1988). X-ray and neutron scattering from rough surfaces. **Physical Review B**. 38: 2297–2311.

Soin, N., Roy, S.S., Ray, S.C., Lemoine, P., Rahman, M.A., Maguire, P.D., Mitra, S.K., and McLaughlin, J.A. (2012). Thickness dependent electronic structure of ultra-thin tetrahedral amorphous carbon (*ta*-C) films. **Thin Solid Films**. 520: 2909–2915.

Song, W., Kim, Y., Jung, D.S., Lee, S., Jung, W., Kwon, O.J., Kim, H.K., Kim, M.S., An, K.S., and Park, C.Y. (2013). Boron and nitrogen co-doping of diamond-like carbon film for transparent conductive films. **Applied Surface Science**. 284: 53–58.

Soriano, L., Abbate, M., de Groot, F.M.F., Alders, D., Fuggle, J.C., Hofmann, S., Petersen, H., and Braun, W. (1993). Chemical analysis of passivated and oxidized layers on FeCr and FeTi alloys by soft X-ray absorption spectroscopy. **Surface and Interface Analysis**. 20: 21–26.

Stansbury, E.E., and Buchana, R.A. (2000). **Fundamentals of Electrochemical Corrosion**. ASTM International. Ohio: Materials Park.

Stöhr, J. (1992). **NEXAFS spectroscopy** (p. 25). New York: Springer-Verlag Berlin Heidelbergp.

Stoyanov, E., Langenhorst, F., and Steinle-Neumann, G. (2007). The effect of valence state and site geometry on Ti $L_{3,2}$ and O K electron energy-loss spectra of Ti_xO_y phases. **American Mineralogist**. 92: 577–586.

Sugimoto, I., Honda, F., and Inoue, K. (2013). Analysis of wear behavior and graphitization of hydrogenated DLC under boundary lubricant with MoDTC. **Wear**. 305: 124–128.

Svahan, F., Kassman-Rudolphi, A., and Wallén, E. (2003). The influence of surface roughness on friction and wear of machine element coatings. **Wear**. 254: 1092–1098.

Synchrotron Light Source, digital image of Synchrotron Light Research Institute (SLRI), Nakhon Ratchasima, Thailand. Available from: (https://www.slri.or.th/en/what-is-synchrotron-light.html). Assessed date: Jan 10, 2019.

Tai, C., Lee, S.C., Wei, C.H., and Tyan, S.L. (2006). Correlation between I_D/I_G ratio from visible Raman spectra and sp^2/sp^3 ratio from XPS spectra of annealed hydrogenated DLC film. **Materials transactions**. 47: 1847–1852.

Tallant, D.R., Parmeter, J.E., Siegal, M.P., and Simpson, R.L. (1995). The thermal stability of diamond-like carbon. **Diamond and Related Materials**. 4: 191–199.

Tanaka, A., Nishibori, T., Suzuki, M., and Maekawa, K. (2004). Characteristics of friction surfaces with DLC films in low and high humidity air. **Wear**. 257: 297–303.

ThyssenKrupp Materials. (2017). Stainless steel 304 1.4301. ThyssenKrupp Materials, West Midlands, UK. Available from: (https://www.thyssenkrupp-materials.co.uk/stainless-steel-304-14301.html). Assessed date: Jan 11, 2019.

Tompkins H.G., and McGahan, W.A. (1999). **Spectroscopic ellipsometry and reflectometry: A User's Guide**. New York: John Wiley & Sons.

Toner, B.P., Dunham, D., Droubay, T., Kikuma J., and Denlinger, J. (1996). X-ray Photoemission Electron Microscopy: Magnetic circular dichroism imaging and other contrast mechanisms. **Journal of Electron Spectroscopy and Related Phenomena**. 78: 13-18.

Trava-Airoldi, V.J., Bonetti, L.F., Capote, G., Fernandes, J.A., Blando, E., Hübler, R., Radi, P.A., Santos, L.V., and Corat, E.J. (2007). DLC film properties obtained by a low cost and modified pulsed-DC discharge. **Thin Solid Films**. 516: 272–276.

Tsai, H., and Bogy, D.B. (1987). Characterization of diamondlike carbon films and their application as overcoats on thin film media for magnetic recording. **Journal of Vacuum Science and Technology A**. 5: 3287–3312.

Tzeng, Y., Yoshikawa, M., Murakawa, M., and Feldman A. (1991). **Applications of Diamond Films and Related Materials**. New York: Elsevier Science.

Utsumi, T., Oka, Y., Fujiwara, E., and Yatsuzuka, M. (2007). Effect of a hard supra-thick interlayer on adhesion of DLC film prepared with PBIID process. **Nuclear Instruments and Methods in Physics Research B.** 257: 706–709.

Van der Lee, A., Roualdes, S., Berjoan, R., and Durand, J. (2001). Mass density determination of thin organosilicon films by X-ray reflectometry. **Applied Surface Science.** 173: 115–121.

Velasco-Velez, J.J., Davaasuren, B., Scherzer, M., Cap, S., Willinger, M., Guo, J.H., Schlögl, R., and Knop-Gericke, A. (2016). Exploring the incorporation of nitrogen in titanium and its influence on the electrochemical corrosion resistance in acidic media. **Surface Science**. 650: 272–278.

Viswanathan, S., Reddy, M.M., Mohan, L., Bera, P., Barshilia, H.C., and Anandan, C. (2017). Corrosion and wear properties of Ti/tetrahedral amorphous carbon multilayered coating. **Journal of Bio- and Tribo-Corrosion**. 3: 1–10.

Voevodin, A.A., and Zabinski, J.S. (2000). Supertough wear-resistant coatings with 'chameleon'surface adaptation. **Thin Solid Films**. 370: 223–231.

Voevodin, A.A., Phelps, A.W., Zabinski, J.S., and Donley, M.S. (1996). Friction induced phase transformation of pulsed laser deposited diamond-like carbon. **Diamond and Related Materials**. 5: 1264–1269.

Wang, J.S., Sugimura, Y., Evans, A.G., and Tredway, W.K. (1998). The mechanical performance of DLC films on steel substrates. **Thin Solid Films**. 1-2: 163.

Wang, P., Wang, X., Xu, T., Liu, W., and Zhang, J. (2007). Comparing internal stress in diamond-like carbon films with different structure. **Thin Solid Films**. 515: 6899–6903.

Wang, Q.Z., Zhou, F., Zhou, Z.F., Yang, Y., Yan, C., Wang, C.D., Zhang, W.J., Li, L.K.Y., Bello, I., and Lee, S.T. (2012). Influence of Ti content on the structure and tribological properties of Ti-DLC coatings in water lubrication. **Diamond and Related Materials**. 25: 163–175.

Wang, S., Zhu, J.Q., Wang, J.Z., Yin, X.B., and Han, X. (2011). Raman spectroscopy and mechanical properties of multilayer tetrahedral amorphous carbon films. **Thin Solid Films**. 519: 4906–4909.

Wang, Y., Wang, J., Zhang, G., Wang, L., and Yan, P. (2012). Microstructure and tribology of TiC(Ag)/a-C: H nanocomposite coatings deposited by unbalanced magnetron sputtering. **Surface and Coating Technology** 206: 299−308.

Weiler, M., Sattel, S., Jung, K., Ehrhardt, H., Veerasamy, V.S., and Robertson, J. (1994). Highly tetrahedral, diamond-like amorphous hydrogenated carbon prepared from a plasma beam source. **Applied Physics Letters**. 64: 2797–2799.

Wormington, M., Pape, I., Hase, T.P.A., Tanner, B.K., and Bowen, D.K. (1991). Evidence for grading at polished surfaces from grazing-incidence X-ray scattering. **Philosophical Magazine Letters**. 74: 211–216.

Wu, J.B., Chang, J.J., Li, M.Y., Leu, M.S., and Li, A. (2007). Characterization of diamond-like carbon coatings prepared by pulsed bias cathodic vacuum arc deposition. **Thin Solid Films**. 516: 243–247.

Wu, Y., Chen, J., Li, H., Ji, L., Ye, Y., and Zhou, H. (2013). Preparation and properties of Ag/DLC nanocomposite films fabricated by unbalanced magnetron sputtering. **Applied Surface Science**. 284: 165– 170.

Yu, Y.J. Kim, J.G. Cho, S.H. and Boo, J.H. (2003). **Surface and Coatings Technology**. 162: 161–166.

Zeng, A., Neto, V.F., Gracio, J.J., and Fan, Q.H. (2014). Diamond-like carbon (DLC) films as electrochemical electrodes. **Diamond and Related Materials**. 43: 12– 22.

Zhang, J., Yu, X., Zhao, X., and Zhang, L. (2007). Influence of interfacial carbonization on the structure and mechanical properties of multilayered Cr-containing diamond-like carbon films. **The Journal of Physical Chemistry C.** 121: 6781– 6787.

Zhang, Q., Yoon, S.F., Rusli, J.A. and Yang, H. (1998). Deposition of hydrogenated diamondlike carbon films under the impact of energetic hydrocarbon ions. **Journal of Applied Physics**. 84: 5538–5542.

Zhang, S., Bui, X.L., and Li, X. (2006). Thermal stability and oxidation properties of magnetron sputtered diamond-like carbon and its nanocomposite coatings. **Diamond and Related Materials**. 15: 972–976.

Zhang, W., Tanaka, A., Wazumi, K.K., and Koga, Y. (2003). Tribological properties of diamond-like carbon films in low and high moist air. **Tribology Letters**. 14: 123–130.

Zhang, Y.B., Lau, S.P., Sheeja, D., and Tay, B.K. (2005). Study of mechanical properties and stress of tetrahedral amorphous carbon films prepared by pulse biasing. **Surface and Coatings Technology**. 195: 338 – 343.

Zhao, F., Li, H., Ji, L., Wang, Y., Zhou, H., and Chen, J. (2010). Ti-DLC films with superior friction performance. **Diamond and Related Materials**. 19: 342–349.

Zhou, S., Wang, L., and Xue, Q. (2012). Duplex doped nanocomposite carbon-based coating with self-lubricating performance. **Diamond and Related Materials**. 21: 58−65.

Zhou. W., and Wang, Z.L. (2007). Scanning Microscopy for Nanotechnology: Techniques and Applications. **In: Fundamentals of Scanning Electron Microscopy** (Zhou, W., Apkarian, R.P. Wang, Z.L., and Joy, D. (Eds.)), New York: Springer. pp. 1–40.

Zou, Y.S., Wu, Y.F., Yang, H., Cang, K., Song, G.H., Li, Z.X., and Zhou, K. (2011). The microstructure, mechanical and friction properties of protective diamond like carbon films on magnesium alloy. **Applied Surface Science**. 258: 1624–1629.

APPENDICES
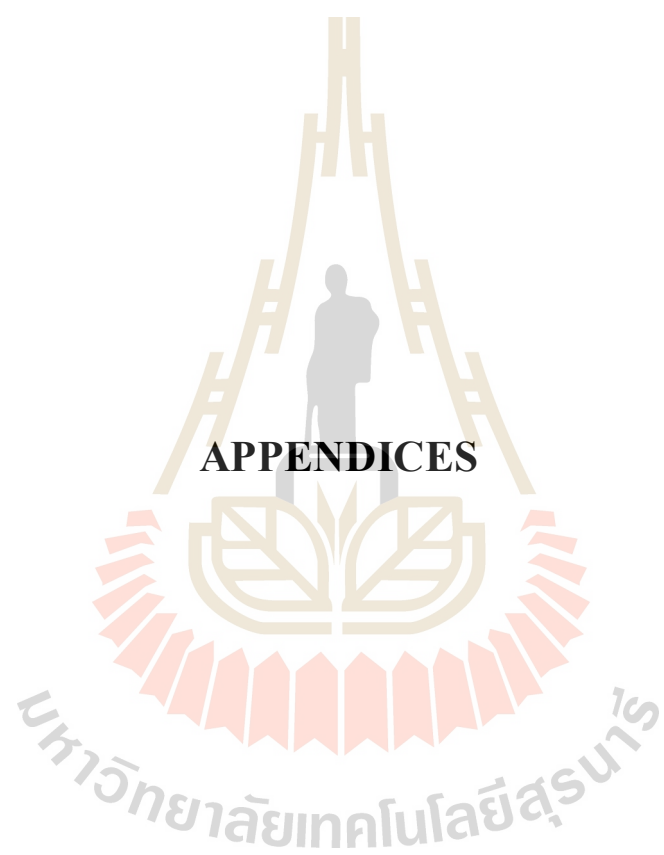
APPENDIX A

FABRICATION OF THE W-DOPED DLC FILM

In this PhD thesis, the Ti incorporation into the DLC films has been carried out to obtain improved properties, such as internal stress, adhesion strength, tribological properties, and corrosion protection performance of the DLC films. In addition to the study of the Ti-doped DLC films, many research groups, however, have investigated the W incorporation into DLC films, the so-called the W-doped DLC film, and reported their outstanding mechanical properties and tribological performance. For example, Mutafov *et al*. (2014) fabricated W-doped DLC film by reactive magnetron sputtering from the graphite target and composite target between the W and the graphite. From the experiments, they found excellent wear resistance of the W-doped DLC films due to the formation of a very thin solid tribolayer formed on oil additives during the engine tests. One group revealed that the adhesion strength of the W-doped DLC film deposited on 316L stainless steel substrates was significantly improved when the W atoms were introduced at 3.08 at.%. The lowest value of the wear rates was obtained as the W-doped DLC films were tested under dry and lubrication conditions (Fu *et al*., 2013). Another study associated the fabrication of Ti and W co-doped DLC film on Si substrates by co-sputtering the Ti and W targets in the mixed atmosphere of CH_4 and Ar reactive gas. The results exhibited that the incorporation of the W atoms into the DLC film led to the reduction in the internal stress and enhanced the hardness to 12.7 GPa when the W was increased to 2.6 at.%. The tribological performance in terms of

friction and wear resistance was also significantly improved by the addition of the W atoms (Qiang *et al*., 2015). In addition to the above-mentioned investigations of research groups, there have been attempts to produce and study the microstructure and properties of the W-doped DLC film in correlation with the Ti-doped DLC films here.

A1. EXPERIMENTAL PROCEDURES

In the first step, the W rod used as the cathode material was bought from several suppliers including the Nilaco Corporation (99.50% purity W), ESPI Metals (99.95% purity W), and Goodfellow (99.95% purity W) and different sizes 6.35, 8.00, 9.53 mm in diameter to compare and search for the appropriate deposition conditions for the W-doped DLC film. While the W rods were being shipped, the ceramic insulator was machined to fit the dimension of the W that had been ordered before being inserted into the cathodic arc source for generating the W plasma. The other cathodic arc source was the graphite rod for producing the C plasma. To trigger the arc plasma, the arc current which was electrically connected to the W cathode was driven at the arc voltage between 0.45 and 0.98 kV. This arc voltage was very close to the limitation of the arc plasma power supply at the maximum arc voltage of 1.0 kV. In order to avoid damage to the electronic components, for example, an insulated-gate bipolar transistor (IGBT) and a diode bridge which were inside the power supply, the arc voltage should be maintained at less than 1.0 kV. The duty cycle was varied in a wide range of 0.001–60%. The pulse repetition rate was tuned from 1 to 6 Hz. The maximum and minimum points of this system were selected in the fabrication of the W-doped DLC films in this experiment. However, even though the above-mentioned deposition conditions were used, the phase transition from solid cathode material to vapor or plasma did not occur.

The arc only occurred on the conductive path, e.g., the graphite layer coated on an insulator surface to allow the current from the cathode cross over to generate the plasma, and it just stopped when the conductive path had gone.

From the experiments, it is very essential to understand the mechanisms of the vacuum arcs generated at the cathode spots via the current-carrying plasma (Anders, 2001, 2008; Anders *et al*., 2001) and consider the variables that determine the difficulty of generating vapor or plasma of the cathode materials. The cohesive energy of the cathode materials is one of the vital variables that determine the energy for the phase transition of the cathode materials from solid to plasma or for ionization. Therefore, cathode materials with a large cohesive energy require more energy input for ionization and acceleration of ions toward the substrate. Additionally, there is a correlation between the cohesive energy and the boiling (point) temperature. The boiling point of the cathode material is known and relates to the strength or energy of the atomic bonds of the cathode material. Another consideration is the arc burning voltage which refers to the potential difference between the cathode and anode. It also determines the energy dissipation in the arc plasma. All of the variables yield the same effect that makes the ionization of the cathode materials more difficult when they require more energy. Table A shows the cohesive energy, arc burning voltage, and boiling point of the cathode materials in this thesis (Anders, 2001, 2008 Anders *et al*., 2001).

Table A.1 The summarized data of the cohesive energy, arc burning voltage, and boiling point of the cathode materials.

Element	Cohesive energy (eV/atom)	Arc burning voltage (V)	Boiling point (°C)
Ti	4.85	21.3	3287
C	7.37	29.6	4027
W	8.99	31.9	5555

As seen in Table A.1, the W has the highest cohesive energy, arc burning voltage, and boiling point compared to other elements, followed by the C and Ti, respectively. This is the reason why the ionization of the W becomes more difficult than for the other cathode materials. Therefore, the synthesis of the W-doped DLC film requires more energy or power input than the pulsed two-FCVA system can provide. To overcome this problem, high energy input and arc burning voltage are required for the phase transition from solid to plasma. In addition to the energy input, the application of the trigger system can be helpful to stimulate the initial arc to plasma and is needed to encourage the stability of the further arc over the cathode surface.

A.2 REFERENCES

Anders, A. (2001). Energetics of vacuum arc cathode spots. **Applied Physics Letters**. 78: 2837–2839.

Anders, A., (2008). **Cathodic Arcs: From Fractal Spots to Energetic Condensation**. New York: Springer Science + Business Media.

Anders, A., Yotsombat, B., and Binder, R. (2001). Correlation between cathode properties, burning voltage, and plasma parameters of vacuum arcs. **Journal of Applied Physics**. 89: 7764–7771.

APPENDIX B

PUBLICATIONS AND PRESENTATIONS

B.1   List of publications

Konkhunthot, K., Tunmee, S., Zhou, X.L. Komatsu, K., Photongkam, P., Saitoh, H., and Wongpanya, P. (2018). The correlation between optical and mechanical properties of amorphous diamond-like carbon films prepared by pulsed filtered cathodic vacuum arc deposition. **Thin Solid Films**. 653: 317–325.

Konkhunthot, K., Photongkam, P., and Wongpanya, P. (2019). Improvement of thermal stability, adhesion strength and corrosion performance of diamond-like carbon films with titanium doping. **Applied Surface Science**. 469: 471–486.

B.2   List of oral presentations

Konkhunthot, K. (September 2015). The DC Bias Voltage Effects on the Structure and Corrosion Resistance of DLC Films Synthesized by FCVA Technique. In: **International Symposium on Engineering and Applied Science: Higher Education Forum**. Kuala Lumpur, Malaysia.

Konkhunthot, K. (June 2017). Investigation of diamond-like carbon films deposited by pulsed filtered cathodic vacuum arc technique. In: **The 18th RGJ.- Congress, Global Sustainability: Lesson Learned From the Royal Projects.** Richmond Stylish Convention Hotel, Nonthaburi, Thailand.

Article published in Thin Solid Films

The correlation between optical and mechanical properties of amorphous diamond-like carbon films prepared by pulsed filtered cathodic vacuum arc deposition

Natthaphong Konkhunthot[a,b], Sarayut Tunmee[c], XiaoLong Zhou[d], Keiji Komatsu[b], Pat Photongkam[c], Hidetoshi Saitoh[b], Pornwasa Wongpanya[a,*]

[a] School of Metallurgical Engineering, Institute of Engineering, Suranaree University of Technology, Nakhon Ratchasima 30000, Thailand
[b] Graduate School of Engineering, Nagaoka University of Technology, 1603-1 Kamitomioka-machi, Nagaoka, Niigata 940-2188, Japan
[c] Synchrotron Light Research Institute (Public Organisation), 111 University Avenue, Muang District, Nakhon Ratchasima 30000, Thailand
[d] Functional Thin Films Research Center, Shenzhen Institutes of Advanced Technology, Chinese Academy of Sciences, Shenzhen 518055, China

ARTICLE INFO

ABSTRACT

Diamond-like carbon (DLC) films were deposited by pulsed filtered cathodic vacuum arc (FCVA) deposition. The microstructure, mechanical and optical properties of DLC films have been investigated as functions of the variation in the substrate negative direct current bias voltage (V_{bias}) from 0.0 to 1.5 kV. Raman and X-ray photoelectron spectroscopy results show a correlation between the I_D/I_G ratio and the microstructure in terms of the sp^3/sp^2 ratio to V_{bias}. This fact shows that a significant change in the sp^3 content, which is attributed to the transformation from graphite-like to diamond-like, is accompanied by a decreasing I_D/I_G ratio. The relatively high mass density of the films in the range of 2.51 to 2.79 g/cm^3 can be obtained with biasing. The mechanical properties, i.e., the hardness and elastic modulus, were 13–25 and 114–145 GPa, respectively. The improvement of the mechanical properties is due to the formation of the compressive residual stress and the local density depending on V_{bias}. The relationship between the refractive index and the I_D/I_G ratio agree well with the microstructure and mechanical properties of DLC films. All of these results indicate a vital role of V_{bias} in determining the DLC properties.

1. Introduction

Diamond-like carbon (DLC) films have been receiving much attention in recent years due to their unique properties, such as high hardness, high wear resistance, low friction coefficient, thermal conductivity, optical transparency, chemical inertness, and biological compatibility [1–6]. These properties of DLC films are suitable for various applications, such as protective coatings for magnetic storage, cutting tools, optical components, automotive parts, and antireflective coatings [7–10]. A large number of deposition techniques, such as radio frequency plasma enhanced chemical vapor deposition, electron cyclotron resonance chemical vapor deposition, magnetron sputtering deposition, and filtered cathodic vacuum arc (FCVA), have been successfully used to synthesize DLC films [1,10–13]. FCVA deposition offers outstanding advantages by producing the hydrogen-free tetrahedral amorphous (ta-C) films with a high fraction of sp^3 content. The ta-C films yield a wide range of desirable properties, such as superior mechanical hardness, low friction coefficient, optical transparency

compared with those of the hydrogenated ta-C:H films [14,15], which is useful for optical and mechanical applications. The fact is that the ion energy determines optical and mechanical properties and microstructure of DLC films, and the FCVA deposition, as an energetic and plasma-based method, generates a highly ionized plasma [16]; the energetic ions generated by the FCVA can be precisely controlled by adjusting V_{bias}. Additionally, the FCVA is appropriate for reducing the number of macro-particles; so that high-quality DLC films can be produced [17,18].

The mechanical and optical properties of DLC films strongly depend on their microstructure, especially the sp^3/sp^2 ratio. Currently, the microstructure of DLC has been characterized using ^{13}C nuclear magnetic resonance, Raman spectroscopy, electron energy-loss spectroscopy, and X-ray absorption spectroscopy. In particular, Raman spectroscopy, a nondestructive and comparatively simple technique, has been shown to be an excellent tool for assessing the intensity ratio of the D and G bands (I_D/I_G) and the residual stress (σ). Formation of the I_D/I_G ratio and σ in the films is related to the variation in the carbon

network structure in terms of the sp^3/sp^2 ratio and also corresponds to their mechanical and optical properties. X-ray photoelectron spectroscopy (XPS) is a surface-sensitive quantitative spectroscopic technique for analyzing the carbon bonding configuration and the sp^3/sp^2 ratio of DLC films. The exploration of a new approach to determine the mass density (ρ), thickness (t), and roughness of DLC films is essential. Currently, X-ray reflectivity (XRR) is extensively employed for measuring multi-layer thin films [19,20]. Additionally, the optical properties, such as the refractive index (n) and the extinction coefficient (k), can be accurately measured using spectroscopic ellipsometry (SE) [21–23]. Recent investigations show the correlation between optical properties and microstructure of DLC films deposited by microwave plasma assisted chemical vapor and FCVA [21,23,24]; however, there has not yet been an extensive study of how optical and mechanical properties correlate to σ and ρ as well as the sp^3/sp^2 ratio of DLC films, which can be beneficial in optimizing optical and mechanical properties. Therefore, the study is comprehensively investigated and systematically conducted here.

In this study, we investigate optical, mechanical and physical properties of DLC films deposited by pulsed FCVA at various V_{bias}. The main objective is to examine the microstructure and mechanical properties of DLC films and to elucidate the relationship of the σ and the ρ to V_{bias}. Additionally, the correlation between the n and the I_D/I_G ratio on the H and the sp^3 content was discussed and established.

2. Experimental details

First, the p-type (100) oriented silicon (Si) was prepared into size $10 \times 10 \, \text{mm}^2$ substrates. The substrates were ultrasonically cleaned with ethanol and acetone for 15 min before being introduced into the deposition chamber. The chamber was evacuated to a base pressure of 3×10^{-3} Pa using a roughing pump and turbomolecular pump, sequentially. The photograph and schematic diagram of the pulsed-FCVA system are shown in Fig. 1(a) and (b). The pulsed-FCVA system has two vacuum arc plasma sources. Each of them has its own macro-particle filter and can be independently controlled by using the arc power supply controller that is capable of operating two sources simultaneously, i.e., doping and multi-layered depositions. Extraordinary conditions achieved in this system have several potential advantages, enabling to incorporate an element into DLC structure and to produce the multi-layered depositions. High purity graphite (99.99%) and titanium (99.50%) rods were installed individually on the cathodic arc sources. To trigger the initial arc, the deposition of the conductive path from cathode materials between the cathode and insulator was needed to allow the current to initiate the plasma. The arc current was driven at a voltage of -0.8 kV with pulse repetition rates of 1.0 and 1.25 Hz for the graphite and titanium cathodes, respectively, under a duty cycle of 50% to maintain the balance between the cathode consumption and arc stability during deposition. The macro-particles and neutral atoms were filtered out using an open architecture, namely a 90° bends magnetic filter, which was electrically connected in series with the arc discharge. The bend filter coil was made of a copper tube with a 45 mm inner diameter. The distance between the outlet of the coil and the substrate was 25 mm. Prior to deposition, a bombardment with titanium (Ti) ions was carried out for 5 min at V_{bias} of 1.5 kV to remove any surface oxides and create an active surface for DLC films. A Ti intermediate layer of ~ 20 nm prepared at V_{bias} of 1.0 kV was subsequently deposited on the Si substrate to serve as a bond-coat between the film and the substrate; this is represented as a Ti/Si substrate. This strategy not only allows Ti ions to be deposited on the Si substrate as magneton sputtering, but also allows the Ti ions to be implanted into the Si sublayer, which leads to excellent adhesion of a Ti intermediate layer for DLC films. Finally, the DLC films were deposited on the Ti/Si substrate by the pulsed-FCVA deposition with the various V_{bias} of 0.0, 0.5, 1.0, and 1.5 kV at room temperature. During deposition, the working pressure was 3×10^{-2} Pa due to the outgassing from the cathode materials. The deposition time

was 30 min for each condition. With the thickness results determined by XRR, the DLC film growth rates at the three different V_{bias} of 0.5, 1.0, and 1.5 kV were estimated to be 3.5, 4.8, and 3.3 nm/min, respectively.

A laser Raman microscope spectroscopic device (HORIBA, Jobin-Yvon, LabRAM Infinity) was used to study the microstructure of the amorphous carbon films. The Raman spectra of the films were obtained in the backscattering mode using an Ar$^+$ laser with the wavelength of 514.5 nm at a power of 5 mW. The Raman spectra were acquired over the range of 1000–2000 cm^{-1} at a 1 cm^{-1} resolution. The Raman parameters consisting of the D and G bands, the I_D/I_G ratio, and the full width at half maximum (FWHM) of the films were investigated and obtained by fitting the Raman spectra with two Gaussians functions. Taking into account the Raman parameters, the σ and clustering size of the sp^2 sites (L_a) of the films were also evaluated. By using the I_D/I_G ratio, the L_a of the films can be determined using the empirical equation:

$$\frac{I_D}{I_G} = C'(\lambda) L_a^2, \tag{1}$$

where $C'(514 \, \text{nm}) \sim 0.0055$ [25]. The methodology for calculating σ will be described in the Microstructure analysis section.

The XPS apparatus (JEOL, JPS-9010TR) was utilized to obtain the surface chemical composition and the sp^3/sp^2 bonding ratio of the DLC films with a Mg K_α X-ray source. The emitted photoelectron was recorded using a hemispherical electron energy analyzer at the pass energy of 20 eV with a step size of 0.1 eV and a dwell time of 10 s. The operation was performed in the ultrahigh vacuum condition of $\sim 10^{-6}$ Pa. Before the measurements, the native oxide layers were removed by bombardment with Ar$^+$ ions with a kinetic energy of 1 kV for 1 min.

The ρ, t, and roughness were measured by XRR with a Cu K_α radiation source at the wavelength of 1.54 Å. The XRR measurements were carried out by varying the incident angle in the range of 0.2–2.5° with a scanning step of 0.004°. The reflection intensity was achieved using an X-ray diffraction apparatus (M03XHFMXP3, MacScience). The XRR profiles were simulated using a GXRR software, which is a commercial package for analysis that is based on Parratt's theory [26].

The hardness (H) and elastic modulus (E) of the DLC films were investigated by a pico-indentation measurement using a FISCHER H-100 system with a diamond Vickers tip. Six indentations were conducted to obtain satisfactory statistical reliability and average values for each sample. A fused SiO$_2$ standard was performed to ensure that the pico-indentation system remained calibrated. An ultra-low applied load of 0.1 mN with the maximum indentation depth of < 10% of the film thickness was consistently used to avoid the influence of the Si substrate. The measurements of the parameters were carried out at the loading and unloading rates of 0.01 mN/s. The indenter was moved constantly with a speed of 0.1 nm/s and paused at the maximum load for a holding time of 10 s. The measured values of H and E are obtained based on the Oliver and Pharr method [27,28].

The n and k of the DLC films were measured by an SE apparatus (HORIBA, Jobin-Yvon, UVISEL-23301010I) [29]. A Xenon arc lamp that was operated at a power of 75 W was applied to generate the light beam with a spot size of 500 µm^2. The measurement is performed using two independent monochromators at the light reflection angle of 70° and the temperature of ~ 20 °C with an appropriate fitting model in the wavelength from 300 to 1000 nm. The standard and fitting models were used to simulate the optical constants, as presented in Fig. 2. The standard model included a DLC layer and a Ti layer deposited on the Si substrate, and the fitting model consisted of a DLC layer + voids, a DLC layer, and a Ti layer deposited on the Si substrate. With a minimal mean square error, the measured data will be reliable. The n and k can be determined by defining the void volume to be 50% using the Bruggeman effective medium approximation (B-EMA) [29,30].
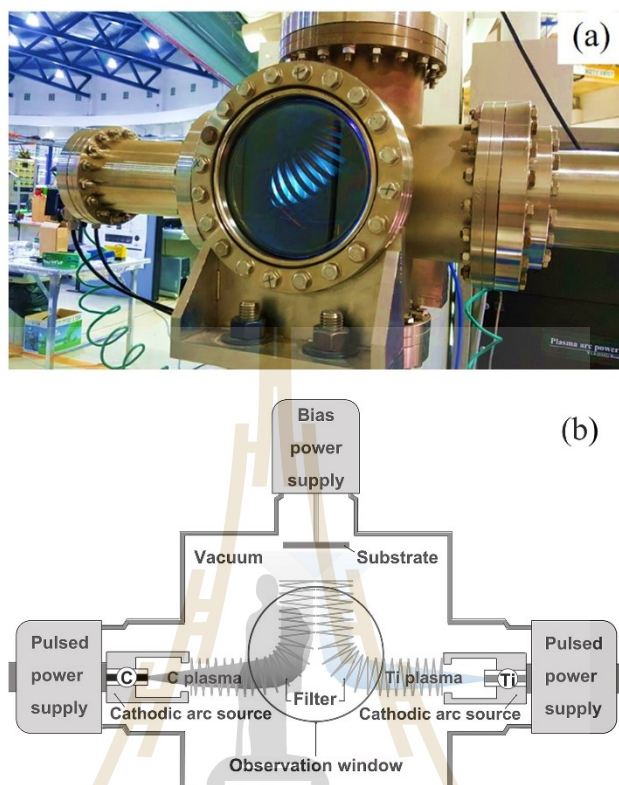
Fig. 1. The photograph (a) and schematic diagram (b) of an in-house developed pulsed-FCVA system used for film deposition in this work.

3. Results and discussion

3.1. Microstructure analysis

Fig. 3 shows the Raman spectra of the DLC films that were deposited at various V_{bias}. The spectra of glassy carbon and highly ordered pyrolytic graphitic (HOPG) are also plotted here for comparison. DLC-0, DLC-1, DLC-2, and DLC-3 were used to denote the films that were prepared with V_{bias} of 0.0, 0.5, 1.0, and 1.5 kV, respectively. For quantitative analysis, all the Raman spectra were fitted into two main Raman bands in the wavenumber range of 900–1900 cm^{-1} for visible excitations. The Raman spectra can be deconvoluted into two typical Gaussian functions, represented as the D band (~1350 cm^{-1}) and the G band (~1540 cm^{-1}), which are consistent with the values reported by others [31]. The D band is attributed to the breathing mode of the sp^2 sites due to the disordered structure in the sixfold aromatic rings, and the G band is related to the stretching of all of the sp^2 sites in both the rings and chains [25,33,34]. A peak at approximately 950 cm^{-1} is attributed to the second-order phonon scattering of the underlying Si substrate [32]. The intensity of the spectrum is indicative of the optical transparency of the films, depending on the sp^3-bonded carbon atoms.

In this study, the obtained Raman parameters consist of the position of D and G bands, the I_D/I_G ratio, the FWHM(D), the FWHM(G), σ, and L_a, as presented in Table 1.

The variation in the I_D/I_G ratio and σ as a function of various V_{bias} are shown in Fig. 4. The inset shows the correlation between the G band position and the FWHM(G) depending on V_{bias}. The I_D/I_G ratio reveals qualitative information on the values of the sp^3/sp^2 ratio and L_a in the films [35]. In Fig. 4, the I_D/I_G ratio is slightly decreased by the application of V_{bias}. It passed through the minimum value at V_{bias} of 1.0 kV and then increased with the further increase of V_{bias}. The evolution of the I_D/I_G ratio is due to the variation in the carbon network structure, which depends on the energetic ions. According to the three-stage model proposed by Ferrari and Robertson [35], the decrease in the I_D/I_G ratio is related to the transition from ordered graphite to sp^3 bonded *ta*-C, accompanied with the change of the sp^2 configuration from rings to chains. Based on the model, the conversion of C-sp^2 (graphite-like phase) to C-sp^3 (diamond-like phase) in the carbon network structure occurs under variation of V_{bias} from 0.0 to 1.5 kV, and the maximum sp^3 content is thus expected to be achieved with the minimum I_D/I_G ratio, as shown at V_{bias} of 1.0 kV in Fig. 4.

Furthermore, the variations in the G band position as a function of

(a)

Standard Model

Fig. 3. Raman spectra for the DLC films deposited at various V_{bias} in the range of 0.0 to 1.5 kV, glassy carbon, and HOPG.

(b)

Fitting Model

Table 1
Detailed parameters obtained from Raman analysis: D and G bands position, FWHM(D), FWHM(G), I_D/I_G ratio, L_a, and σ of the films deposited at various V_{bias}.

Sample code	V_{bias} (kV)	D band		G band		I_D/I_G ratio	L_a (nm)	σ (GPa)
		Position (cm⁻¹)	FWHM (cm⁻¹)	Position (cm⁻¹)	FWHM (cm⁻¹)			
DLC-0	0.0	1347.39	239.33	1531.42	207.59	0.33	7.7	0
DLC-1	0.5	1331.08	214.15	1543.19	235.48	0.23	6.5	2.00
DLC-2	1.0	1321.13	209.56	1545.64	238.46	0.21	6.1	2.41
DLC-3	1.5	1337.16	226.30	1540.34	232.18	0.25	6.7	1.51

Fig. 2. The standard (a) and fitting (b) models used for simulating the optical constants (n and k) of the DLC films.

V_{bias} are studied. The G band positions for DLC-0, DLC-1, DLC-2, and DLC-3 were 1531.42 ± 0.77, 1543.19 ± 0.77, 1545.64 ± 0.77, and 1540.34 ± 0.77 cm⁻¹, respectively, as presented in Table 1. The shifts of the G band are correlated with stress conditions within the DLC films, such that the magnitude of the σ can be calculated using the following equation [36–39]:

$$\sigma = 2G\left[\frac{1+\upsilon}{1-\upsilon}\right]\left[\frac{\Delta w}{w_0}\right], \qquad (2)$$

where G is the shear modulus [40] (G = 70 GPa), υ is the Poison's ratio [40] (~0.3), Δw is the shift in the Raman wavenumber of the G band, and w_0 is the Raman wavenumber of reference. By choosing the G band position of the DLC-0 as the reference Raman wavenumber in Eq. (2), the relative compressive σ of the DLC films at various V_{bias} can be calculated to be 1.99 ± 0.10, 2.41 ± 0.12, and 1.33 ± 0.08 GPa for DLC-1, DLC-2, and DLC-3, respectively. The G band position shifts

Fig. 4. The I_D/I_G ratio and σ as a function of the various V_{bias}. The inset is the relationship between the G band positions and the FWHM(G) as a function of V_{bias}.

upward to a higher wavenumber in the Raman spectra due to the formation of clusters of the carbon networks in the films [38]. This is indicative of the large amounts of the σ compared to that of DLC-0.

Fig. 4 illustrates that the σ is inversely proportional to the I_D/I_G ratio. Therefore, when the σ exists in the films in this study, it is thought that the sp^3 phase will appear. The σ arises as a result of the relationship between the interatomic force constant and interatomic separation. This is associated with the atomic vibrational frequency [36,37]. In the case of the materials subjected to mechanical compression, bond lengths decrease, force constants increase, and vibrational frequencies increase [36,37]. Thus, it is supposed that the interatomic distance decreases when the compressive σ exists in the film, which results in the increase of the density as presented in the XRR analysis. The existence of the σ is thought to be due to the impinging ions during the deposition of the film, as previously described in terms of the subplantation model [40,41]. According to this model, the bombarding species in the plasma cause an increase of the atomic packing density, resulting in the increase of the intrinsic stress [36,37,39] and favoring the formation of the sp^3 phase in the films. As V_{bias} increases further, however, the stress decreases; the stress relief occurs due to the bombarding of the energetic ions at a high V_{bias}.

A similar trend of the FWHM(G) and the G band position is observed for variations of the disordered structure and L_a. The L_a of the films was determined by Eq. (1) [25] to be 7.8, 6.2, 6.0, and 6.6 nm for DLC-0, DLC-1, DLC-2, and DLC-3, respectively. These results elucidate that the L_a changes under the impact of V_{bias}. The decrease in the L_a is considered to depend on the decrease in the I_D/I_G ratio and increase in the FWHM(G). Similar results to ours were obtained elsewhere in the literature [42]. Therefore, it should be noted that films with a small value of the L_a are observed to have sp^3 bonding.

Fig. 5(a) and (b) show the C 1s and O 1s XPS spectra of the DLC films at various V_{bias}. In Fig. 5(a), the C 1s XPS spectra reveal the existence of the bonding states of the carbon atoms. To determine the sp^3/sp^2 ratio of the films, the C 1s XPS spectra were deconvoluted into three Gaussian peaks. The peaks centered at approximately 284.3 eV and 285.3 eV were defined to be the C=C bonds and C–C bonds. Another peak in the binding energy range of 286.0–287.0 eV is due to the C–OH bonds and C–O and/or O–C=O bonds, which are associated with the air or gas exposure of the dangling bonds [43–46]. The presence of the oxygen in the film surface is shown in Fig. 5(b). The existence of the chemical bonding species in the range of 531.3 to 532.9 eV is attributed to the C–O and C–OH bonds [44–47]. The sp^3/sp^2 ratio of the carbon atoms was estimated by the ratio of the peak area to the total peak area. The ratios of the sp^3/sp^2 and oxygen (O) percentage in the films were obtained from the fitting and are listed in Table 2. As shown in Table 2, the O content sharply decreases from 11.36 to 3.52 at% as V_{bias} increases from 0.0 to 0.5 kV indicating the effects of the increasing V_{bias} on the relative O percentage in the films as supported by others [48]. There is a slight change in the range of 3.52–5.40 at% as V_{bias} increases further from 0.5 to 1.5 kV. This means that there is no significant change in the O content as higher V_{bias} are applied. The results show the significant improvement of the sp^3 bonding along with the decrease in the O content under the negative biasing condition, particularly at V_{bias} of 1.0 kV.

As mentioned previously, it is interesting to further investigate the change in the structure and property of the films with different V_{bias}. According to the Raman and XPS results, the sp^3 contents can be controlled by adjusting the ion energy via V_{bias}. In the case of intermediate energies, the positive ions are accelerated toward the substrate with a relatively high speed. Thus, the ions are capable of penetrating the subsurface layer, invading the subsurface interstitial sites, and producing a higher local density. Ion implantation is associated with the compressive stress under the deposition condition, which in turn promotes the stabilization of the sp^3 phase. As the ion energies further increase the thermalization and relaxation stages allow the excess density to relax, causing the loss of the σ and sp^3 bonding [10,49,50], as

occurred at V_{bias} of 1.5 kV.

3.2. Density and thickness analysis

Fig. 6 shows the XRR results of the DLC films at various V_{bias} for the incident angle range of 0.2–2.5°. The black and red curves represent the experimental and simulated XRR profiles. The accurate values of ρ and t of the films can be achieved with the minimum reliability factor of 0.02–0.05, indicating that the simulation was adequate for the

Fig. 5. The C 1s (a) and O 1s (b) XPS spectra for the DLC films deposited at various V_{bias}.

Table 2

Summarized results of ρ, t, n, k, sp^3/sp^2 ratio, and O content of the films deposited at various V_{bias} obtained from XRR, SE, and XPS.

Sample code	V_{bias} (kV)	ρ (g/cm^3)	t (nm)	n ($\lambda = 550$ nm)	k	sp^3/sp^2 ratio	O content (at%)
DLC-0	0.0	–	–	2.10	0.43	0.30	11.36
DLC-1	0.5	2.73	105.04	2.64	0.61	0.39	3.52
DLC-2	1.0	2.79	143.66	2.68	0.53	0.46	5.40
DLC-3	1.5	2.51	98.66	2.58	0.49	0.34	5.33
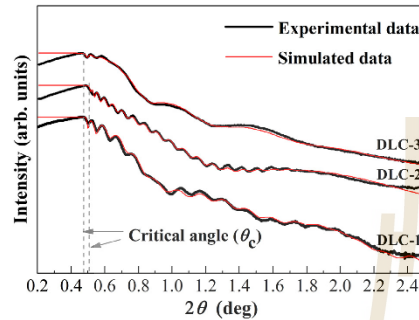
Fig. 6. X-ray reflectivity for the DLC films deposited at various V_{bias}.

measured sample. The reflectivity profiles contain a critical angle (θ_c) and interference fringe providing the information of the average electron density and total thickness, respectively. At a low angle, the θ_c is simulated, and thus ρ can be obtained, which is formulated by the following expression [19,51–54]:

$$\rho = \left[\frac{\pi\theta_c^2}{N_A r_c \lambda^2} \right] \left[\frac{X_C(M_C - M_H) + M_H}{X_C(Z_C - Z_H) + Z_H} \right], \tag{3}$$

where θ_c is the critical angle in radians, r_c is the classical electron radius, N_A is Avogadro's number, λ is the wavelength used by the instrument, X_C and X_H are the relative atomic fraction of C and H (note that the atomic fraction of X_H is a form of $1–X_C$), Z_C and Z_H are the atomic numbers of C and H, and M_C and M_H are the molar mass of C and H, respectively. Moreover, the relationship between ρ and t is described as follows [54]:

$$\rho = \frac{\sum \rho_i t_i}{\sum t_i}, \tag{4}$$

where ρ_i and t_i are the density and thickness of each layer. By placing ρ from Eq. (3) into Eq. (4), we finally find the film thickness.

From the measurements, DLC-0 should not be used because film delamination is observed. Hence, its ρ and t are not able to be measured exactly by this method and are not shown here. The detailed fittings of these XRR profiles are summarized in Table 2. The ρ of DLC-1, DLC-2, and DLC-3 are 2.73 ± 0.03, 2.79 ± 0.03, and 2.51 ± 0.03 g/cm^3, respectively. The presence of the ρ has a significant influence from V_{bias}. The interference fringes are observed for all samples, indicating that the deposited films in this work are more than a single layer, which are so-called multilayer films [19,55]. The maximum ρ of 2.79 g/cm^3 can be obtained at V_{bias} of 1.0 kV for DLC-2. It is, however, seen that DLC-3 displays a slightly different XRR profile with larger periods than the others. This is because of the decrease in ρ and t, as presented in Table 2. The ρ of DLC-3 (2.51 g/cm^3) is lower than that of DLC-1 (2.73 g/cm^3), indicating that the density is no longer developed as V_{bias} increases beyond 1.0 kV. The reduction of ρ with the further increase of

V_{bias} is due to the relaxation of the excess local density and compressive stress within the carbon networks structure. This relaxation occurs due to the increasing substrate temperature at high energies of the ions, which is associated with the graphitization process [56]. Furthermore, the ρ depends on the sp^3 content, such that for an increase in the ρ, the sp^3 content also increases. In contrast, the ρ decreases for the samples that primarily have sp^2 bonding, corresponding to an increase in the I_D/I_G ratio. The t of the deposited films are 105.0, 143.6, and 98.7 nm for DLC-1, DLC-2, and DLC-3, respectively. The t increases as V_{bias} increases from 0.5 to 1.0 kV but then decreases as V_{bias} increases further. This is because the deposition process is less prominent than the self-sputtering of substrate materials under the higher ion energy, and thus the sputtering yields must be less than the deposition process so that film growth can occur [40]. The diffusion layer between the DLC film and the Ti layer is approximately 2.70 ± 0.9 nm thick, is approximately unchanged during the deposition, and has a density of 4.37 ± 0.8 g/cm^3. The diffusion layer consists of the mixture of the carbon ion impingements into the surface of the Ti layer. The impingement of the relatively high energy ions that were generated at larger V_{bias} is the main reason for the monotonic increases of the surface roughnesses of 3.77, 4.17, and 5.11 for DLC-1, DLC-2, and DLC-3, respectively.

3.3. Mechanical properties analysis

H and E as important factors, which in turn affect the sp^3/sp^2 ratio of the films, were investigated by pico-indentation tests. The loading versus indentation depth curves of the DLC films at various V_{bias} are shown in Fig. 7. The indentation depth of each sample at the ultra-low applied load of 0.1 mN is in the range of 8–11 nm and < 10% of the film thickness. Thus, it is reasonable to neglect the substrate effect during the pico-hardness test [57–61]. In Fig. 7, the indentation depth of the deposited film decreases and reaches its lowest value of approximately 8 nm as V_{bias} increases from 0.0 to 1.0 kV and then slightly increases by approximately 9.5 nm with the further increase of V_{bias} to 1.5 kV. The H of DLC-1 and DLC-2 have been improved significantly compared to DLC-0 by reducing the indentation depth, indicating that V_{bias} is powerful for changing the mechanical properties of DLC films.

Fig. 8 and its inset demonstrate the correlation between H and E, and the correlation of the ρ and σ of the DLC films and V_{bias}. The H and E results are summarized in Table 3. In Fig. 8, H and E reach the maximum value of 24.83 and 148.66 GPa, respectively, at V_{bias} of 1.0 kV. These results suggest that the C—C network structure in the DLC films transforms as V_{bias} is applied. Consistent with other reports [61–68], the increasing ρ and σ correlate well with H and E, as presented in the inset of Fig. 8. One can see that H and E profoundly increase as V_{bias} increases from 0.5 to 1.0 kV. However, they seem to
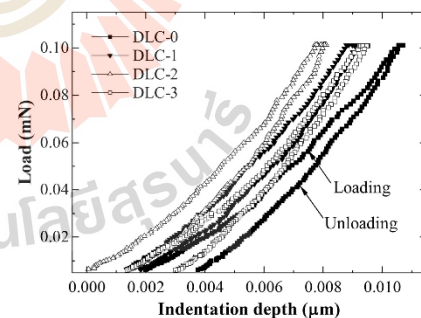
Fig. 7. Indentation depth curves for the DLC films deposited at various V_{bias}.
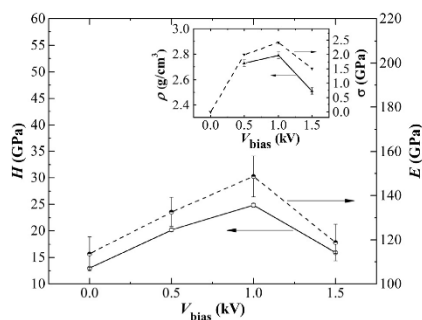
Fig. 8. The H and E for the DLC films deposited at various V_{bias}. The inset is the correlation between ρ and σ and V_{bias}.

Table 3
The H and E of the films deposited at various V_{bias} obtained from pico-indentation.

Sample code	V_{bias} (kV)	H (GPa)	E (GPa)
DLC-0	0.0	12.93 ± 0.95	113.64 ± 7.66
DLC-1	0.5	20.18 ± 1.23	132.57 ± 6.62
DLC-2	1.0	24.83 ± 2.10	148.66 ± 9.20
DLC-3	1.5	15.94 ± 1.41	118.68 ± 8.22

decrease as V_{bias} increases further to 1.5 kV. An ion sub-plantation model is used to explain this property change [10,40,49,50]. It is reported that at a high V_{bias} the dissipation of excess heat generated by the impinging of high energetic ions could relax the high local stress and density, resulting in the reduction of H and E [69].

H shows a relatively low value compared to the other DLC films deposited by FCVA, ranging between 20 and 80 GPa [61,70–72]. This low value is caused by the relatively high oxygen content, which exists during the film deposition at high base pressure condition, as was found using XPS. The influence of base pressure and residual gas pressure during the film deposition leading to the observed reduction in mechanical properties has also been evidenced in the literature [73,74]. It should be noticed that the best condition that provided the highest H (~25 GPa) and density (2.79 g/cm³) is nearly comparable for the ta-C films with the H > 20 GPa and density close to 3 g/cm³ [10,75,76]. All of this indicates that films that are deposited at the appropriate V_{bias} will be ta-C films. Additionally, future experiments should consider finer steps of V_{bias} to investigate the mechanical properties of the films in more details.

3.4. Optical properties analysis

Fig. 9(a) and (b) show the n and k versus wavelength of the DLC films at various V_{bias}. The n value tends to increase with the increasing wavelength and seems to saturate even up to 750 nm for the biased samples. DLC-0 shows a different behavior: the n value decreases as the wavelength increases. The k values gradually decrease with the increasing wavelength for the films that were deposited under V_{bias}. This implies that the biased films become transparent at higher wavelengths, typically beyond 800 nm; however, a slight change was observed in the case of the k values for biased samples. The films that were prepared without V_{bias} show some difference. With the further increase in wavelength, the k value also increases. The optical data of n and k collected at the wavelength of 550 nm are depicted in Table 2. The n and k of the films are found to be in the range of 2.10–2.68 and 0.43–0.61,
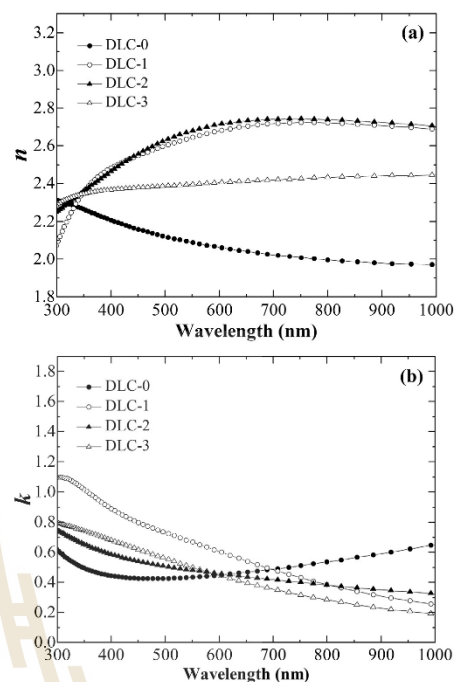
Fig. 9. The optical constants n (a) and k (b) of the DLC films deposited at various V_{bias} as a function of the wavelength in the range of 300–1000 nm.

respectively. It has been previously reported that the decrease in k and the increase in n are associated with increased transparency and the sp^3 bonding of the films [77,78]. From the measurements, the k value has almost no change from the application of V_{bias}. The k value remains approximately constant at 0.52 ± 0.09, which indicates that the film transparency has small change as V_{bias} increases. This might be the influence of the pre-coated Ti layer, which is a practically non-transparent material [79]. Therefore, in the present work, we only focus on the relationship between the n value and the film properties. The value of n becomes small with a lower sp^3 content, as found by XPS, while V_{bias} increases above or decreases below 1.0 kV, as shown in Table 2.

Taking into account the relationship between the n value and the I_D/I_G ratio has not been systematically investigated; an established relationship as a function of V_{bias} was plotted, as shown in Fig. 10. An inverse proportion between the n value and the I_D/I_G ratio was observed. The value of n first increases with the increasing V_{bias} and then reaches the maximum value of 2.68 at V_{bias} of 1.0 kV. As V_{bias} increases further, it drops slightly. Meanwhile, with the same V_{bias}, the I_D/I_G ratio reaches the minimum value of 0.21. These observation results agree well with the sp^3/sp^2 ratio, ρ, H, and E.

Regarding these observations, the established correlation between the n and the I_D/I_G ratio on the properties of the DLC films deposited by pulsed FCVA with the function of V_{bias} should be emphasized. The correlation can be used to infer the sp^3/sp^2 ratio, H and ρ of the films using either the n or the I_D/I_G ratio obtained from comparatively simple and non-destructive analytical methods, i.e., SE and Raman
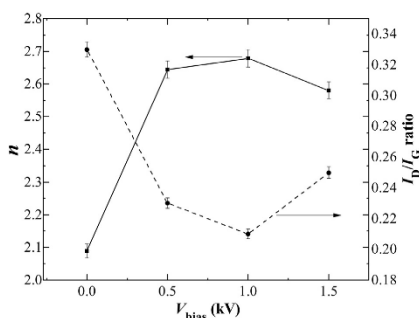
Fig. 10. The correlation between V_{bias} and both the n and the I_D/I_G ratio for the DLC films.

spectroscopy [35]. The correlation can thus be used to reduce the number of samples in experiments. Production of DLC films, which have relatively high ρ, sp^3 carbon bonding, good mechanical properties, and a high value of n, via the pulsed-FCVA technique is possible by applying the proper V_{bias} of 1.0 kV.

4. Conclusions

DLC films were deposited on Si (100) substrate by the pulsed-FCVA deposition at various V_{bias} from 0.0 to 1.5 kV. The microstructures and mechanical and optical properties of the films were investigated. The XRR showed that the DLC films have a relatively high ρ in the range of 2.51–2.79 g/cm^3 with t in the range of 98.7–143.9 nm. The Raman and XPS analysis show the significant dependence of the I_D/I_G and sp^3/sp^2 ratios for the films deposited at V_{bias} of 1.0 kV. The H and E of the films increase with the cumulative σ. The existence of the σ with the alteration of V_{bias} can be explained using the sub-plantation model. The n values correlate well with the I_D/I_G ratios, which are consistent with the other physical and mechanical properties of the films, such as ρ, H, and E. With its simple and reliable analytical method, this established correlation between the n values and the I_D/I_G ratios is useful for signifying the important quality of DLC films, which can be applied for efficient quality control and development in industrial applications. The optimum condition for DLC deposition can be obtained with V_{bias} of 1.0 kV. Consequently, the mechanical and optical properties of DLC films can be modified directly by transforming the microstructure by manipulating V_{bias}.

Acknowledgements

References

[1] J. Robertson, Amorphous carbon, Solid State Mater. Sci. 1 (1996) 557–560.
[2] T.S. Santra, C.H. Liu, T.K. Bhattacharyya, P. Patel, T.K. Barik, Characterization of diamond-like nanocomposite thin films grown by plasma enhanced chemical vapor deposition, J. Appl. Phys. 107 (2010) 124320-1–124320-9.
[3] W. Song, Y. Kim, D.S. Jung, S. Lee, W. Jung, O.J. Kwon, H.K. Kim, M.S. Kim, K.S. An, C.Y. Park, Boron and nitrogen co-doping of diamond-like carbon film for transparent conductive films, Appl. Surf. Sci. 284 (2013) 53–58.
[4] A.S. Chaus, T.N. Fedosenko, A.V. Rogachev, L. Čaplovič, Surface, microstructure, and optical properties of copper-doped diamond-like carbon coating deposited in pulsed cathodic arc plasma, Diam. Relat. Mater. 42 (2014) 64–70.
[5] F.J.G. Silva, R.P. Martinho, A.P.M. Baptista, Characterization of laboratory and industrial CrN/CrCN/diamond-like carbon coatings, Thin Solid Films 550 (2014) 278–284.
[6] S. Wang, J.Q. Zhu, J.Z. Wang, X.B. Yin, X. Han, Raman spectroscopy and mechanical properties of multilayer tetrahedral amorphous carbon films, Thin Solid Films 519 (2011) 4906–4909.
[7] J. Vetter, 60 years of DLC coatings: historical highlights and technical review of cathodic arc processes to synthesize various DLC types, and their evolution for industrial applications, Surf. Coat. Technol. 257 (2014) 213–240.
[8] N.Y. Xu, S.H. Tsang, E.H.T. Teo, X.C. Wang, C.M. Ng, B. kang Tay, Effect of initial sp^3 content on bonding structure evolution of amorphous carbon upon pulsed laser annealing, Diam. Relat. Mater. 30 (2012) 48–52.
[9] F. Piazza, D. Grambole, D. Schneider, C. Casiraghi, A. Ferrari, J. Robertson, Protective diamond-like carbon coatings for future optical storage disks, Diam. Relat. Mater. 14 (2005) 994–999.
[10] J. Robertson, Diamond-like amorphous carbon, Mater. Sci. Eng. R 37 (2002) 129–281.
[11] J. Matlak, K. Komvopoulos, Friction properties of amorphous carbon ultrathin films deposited by filtered cathodic vacuum arc and radio-frequency sputtering, Thin Solid Films 579 (2015) 167–173.
[12] A. Grill, Diamond-like carbon: state of the art, Diam. Relat. Mater. 8 (1999) 428–434.
[13] D. Sheeja, B.K. Tay, S.P. Lau, X. Shi, J. Shi, Y. Li, X. Ding, E. Liu, Z. Sun, Characterization of ta-C films prepared by a two-step filtered vacuum arc deposition technique, Surf. Coat. Technol. 127 (2000) 247–251.
[14] C.Y. Cheng, F.C.N. Hong, Growth of hydrogen-free diamond-like carbon films by a particle-free hollow-cathode arc ion plating system, Thin Solid Films 498 (2006) 206–211.
[15] A. Modabberasl, P. Kameli, M. Ranjbar, H. Salamati, R. Ashiri, Fabrication of DLC thin films with improved diamond-like carbon character by the application of external magnetic field, Carbon 94 (2015) 485–493.
[16] P. Wang, X. Wang, Y. Chen, G. Zhang, W. Liu, J. Zhang, The effect of applied negative bias voltage on the structure Ti-doped a-C:H films deposited by FCVA, Appl. Surf. Sci. 253 (2007) 3722–3726.
[17] X.Z. Ding, B.K. Tay, S.P. Lau, P. Zhang, X.T. Zeng, Structural and mechanical properties of Ti-containing diamond-like carbon films deposited by filtered cathodic vacuum arc, Thin Solid Films 408 (2002) 183–187.
[18] H. Takikawa, K. Izumi, R. Miyano, T. Sakakibara, DLC thin film preparation by cathodic arc deposition with a super droplet-free system, Surf. Coat. Technol. 163–164 (2003) 368–373.
[19] A.C. Ferrari, A. LiBassi, B.K. Tanner, V. Stolojan, J. Yuan, L.M. Brown, S.E. Rodil, B. Kleinsorge, J. Robertson, Density, sp^3 fraction, and cross-sectional structure of amorphous carbon films determined by X-ray reflectivity and electron energy-loss spectroscopy, Phys. Rev. B 62 (2000) 89–103.
[20] A. LiBassi, A.C. Ferrari, V. Stolojan, B.K. Tanner, J. Robertson, L.M. Brown, Density, sp^3 content and internal layering of DLC films by X-ray reflectivity and electron energy loss spectroscopy, Diam. Relat. Mater. 9 (2000) 771–776.
[21] M. Pandey, D. Bhatacharyya, D.S. Patil, K. Ramamchandran, N. Venkatramani, A.K. Das, Structural and optical properties of diamond like carbon films, J. Alloys Compd. 386 (2005) 296–302.
[22] J. Mistrik, P. Janicek, A. Taylor, F. Fendrych, L. Fekete, A. Jager, M. Nesladek, Spectroscopic ellipsometry characterization of nano-crystalline diamond films prepared at various substrate temperatures and pulsed plasma frequencies using microwave plasma enhanced chemical vapor deposition apparatus with linear antenna delivery, Thin Solid Films 571 (2014) 230–237.
[23] J. Zhu, J. Han, X. Han, S. Meng, A. Liu, X. He, Optical properties of amorphous diamond films evaluated by non-destructive spectroscopic ellipsometry, Opt. Mater. 28 (2006) 473–479.
[24] M. Vinnichenko, R. Gago, N. Huang, Y.X. Leng, H. Sun, U. Kreissig, M.P. Kulish, M.F. Maitz, Spectroscopic ellipsometry investigation of amorphous carbon films with different sp^3 content: relation with protein adsorption, Thin Solid Films 455–456 (2004) 530–534.
[25] A.C. Ferrari, J. Robertson, Interpretation of Raman spectra of disordered and amorphous carbon, Phys. Rev. B 61 (2000) 14095–14107.
[26] L.G. Parratt, Surface studies of solids by total reflection of X-rays, Phys. Rev. 95 (1954) 359–369.
[27] W.C. Oliver, G.M. Pharr, Measurement of hardness and elastic modulus by instrumented indentation: advances in understanding and refinements to methodology, J. Mater. Res. 19 (2004) 3–20.
[28] W.C. Oliver, G.M. Pharr, An improved technique for determining hardness and elastic modulus using load and displacement sensing indentation experiments, J. Mater. Res. 7 (1992) 1564–1583.
[29] D.E. Aspnes, Optical properties of thin films, Thin Solid Films 89 (1982) 249–262.
[30] T. Mori, N. Fujii, Y. Xiong, T. Saitoh, Optical study of ion-deposited diamond-like carbon films using spectroscopic ellipsometry, Thin Solid Films 270 (1995) 215–219.
[31] B.H. Lung, M.J. Chiang, M.H. Hon, Growth characterization and properties of diamond-like carbon films by electron cyclotron resonance chemical vapor deposition, Thin Solid Films 392 (2001) 16–21.
[32] S. Prawer, K.W. Nugent, Y. Lifshitz, G.D. Lempert, E. Grossman, J. Kulik, I. Avigal, R. Kalish, Systematic variation of the Raman spectra of DLC films as a function of sp^2:sp^3 composition, Diam. Relat. Mater. 5 (1996) 433–438.
[33] C. Casiraghi, A.C. Ferrari, J. Robertson, Raman spectroscopy of hydrogenated

amorphous carbon, Phys. Rev. B 72 (2005) 1–14.

[34] C. Casiraghi, F. Piazza, A.C. Ferrari, D. Grambole, J. Robertson, Bonding in hydrogenated diamond-like carbon by Raman spectroscopy, Diam. Relat. Mater. 14 (2005) 1098–1102.

[35] A.C. Ferrari, J. Robertson, Raman spectroscopy of amorphous, nanostructured, diamond-like carbon, and nanodiamond, Phil. Trans. R. Soc. A 362 (2004) 2477–2512.

[36] R.J. Narayan, Laser processing of diamond-like carbon-metal composites, Appl. Surf. Sci. 245 (2005) 420–430.

[37] M. Lubwama, B. Corcoran, K.V. Rajani, C.S. Wong, J.B. Kirabira, A. Sebbit, K.A. McDonnell, D. Dowling, K. Sayers, Raman analysis of DLC and Si-DLC films deposited on nitrile rubber, Surf. Coat. Technol. 232 (2013) 521–527.

[38] Y. Miki, A. Nishimoto, T. Sone, Y. Araki, Residual stress measurement in DLC films deposited by PBIID method using Raman microprobe spectroscopy, Surf. Coat. Technol. 283 (2015) 274–280.

[39] K. Nakamatsu, M. Nagase, J. Igaki, H. Namatsu, S. Matsui, Mechanical characteristics and its annealing effect of diamondlike-carbon nanosprings fabricated by focused-ion-beam chemical vapor deposition, J. Vac. Sci. Technol. B 23 (2005) 2801–2805.

[40] Y. Lifshitz, S.R. Kasi, J.W. Rabalais, Subplantation model for film growth from hyperthermal species: application to diamond, Phys. Rev. Lett. 62 (1989) 1290–1293.

[41] Y. Lifshitz, S.R. Kasi, J.W. Rabalais, W. Eckstein, Subplantation model for film growth from hyperthermal species, Phys. Rev. B 41 (1990) 10468–10480.

[42] A.C. Ferrari, S.E. Rodil, J. Robertson, Interpretation of infrared and Raman spectra of amorphous carbon nitrides, Phys. Rev. B 67 (2003) 1–20.

[43] J.S. Chen, S.P. Lau, Z. Sun, B.K. Tay, G.Q. Yu, F.Y. Zhu, D.Z. Zhu, H.J. Xu, Structural and mechanical properties of nitrogen ion implanted ultra high molecular weight polyethylene, Surf. Coat. Technol. 138 (2001) 33–38.

[44] M.H. Ahmed, J.A. Byrne, J. McLaughlin, W. Ahmed, Study of human serum albumin adsorption and conformational change on DLC and silicon doped DLC using XPS and FTIR spectroscopy, J. Biomed. Nanotechnol. 4 (2013) 194–203.

[45] C. Rüdiger, F. Maglia, S. Leonardi, M. Sachsenhauser, I.D. Sharp, O. Paschos, J. Kunze, Surface analytical study of carbothermally reduced titania films for electrocatalysis application, Electrochim. Acta 71 (2012) 1–9.

[46] D.M. Phase, V. Sathe, In situ photoelectron spectroscopy study of TiCxNy films synthesized through reactive ion beam mixing, J. Phys. D. Appl. Phys. 37 (2004) 1696–1700.

[47] I. Milošev, M.M. Huković, H.H. Strehblow, Passive film on orthopaedic TiAlV alloy formed in physiological solution investigated by X-ray photoelectron spectroscopy, Biomaterials 21 (2000) 2103–2113.

[48] J.C. Damasceno, S.S. Camargo Jr., Plasma deposition and characterization of silicon oxide-containing diamond-like carbon films obtained from CH$_4$:SiH$_4$:O$_2$ gas mixtures, Thin Solid Films 516 (2008) 1890–1897.

[49] J. Robertson, Deposition mechanisms for promoting sp^3 bonding in diamond-like carbon, Diam. Relat. Mater. 2 (1993) 984–989.

[50] A.C. Ferrari, S.E. Rodil, J. Robertson, W.I. Milne, Is stress necessary to stabilise sp^3 bonding in diamond-like carbon? Diam. Relat. Mater. 11 (2002) 994–999.

[51] P.K. Chu, L. Li, Characterization of amorphous and nanocrystalline carbon films, Mater. Chem. Phys. 96 (2006) 253–277.

[52] Q. Zhang, S.F. Yoon, J. Ahn Rusli, H. Yang, Deposition of hydrogenated diamondlike carbon films under the impact of energetic hydrocarbon ions, J. Appl. Phys. 84 (1998) 5538–5542.

[53] L. Liu, T. Wang, J. Huang, Z. He, Y. Yi, K. Du, Diamond-like carbon thin films with high density and low internal stress deposited by coupling DC/RF magnetron sputtering, Diam. Relat. Mater. 70 (2016) 151–158.

[54] S. Kishimoto, T. Hashiguchi, S. Ohshio, H. Saitoh, Density investigation by X-ray reflectivity for thin films synthesized using atmospheric CVD, Chem. Vap. Depos. 14 (2008) 303–308.

[55] A. van der Lee, S. Roualdes, R. Berjoan, J. Durand, Mass density determination of thin organosilicon films by X-ray reflectometry, Appl. Surf. Sci. 173 (2001) 115–121.

[56] I. Sugimoto, F. Honda, K. Inoue, Analysis of wear behavior and graphitization of hydrogenated DLC under boundary lubricant with MoDTC, Wear 305 (2013) 124–128.

[57] A.C. Fischer-Cripps, Critical review of analysis and interpretation of nanoindentation test data, Surf. Coat. Technol. 200 (2006) 4153–4165.

[58] T. Andriollo, J. Thorborg, J. Hattel, Analysis of the equivalent indenter concept used to extract Young's modulus from a nano-indentation test: some new insights into the Oliver-Pharr method, Model. Simul. Mater. Sci. Eng. 25 (2017) 1–22.

[59] C.H. Liang, C.F. Huang, H.Y. Tsai, The influence of substrate bias voltages on structure, mechanical properties and anti-corrosion performance of Cr doped diamond-like carbon films deposited by steered cathodic arc evaporation, Thin Solid Films 597 (2015) 88–96.

[60] P.B. Mirkarimi, D.L. Medlin, K.F. McCarty, D.C. Dibble, W.M. Clift, The synthesis, characterization, and mechanical properties of thick, ultrahard cubic boron nitride films deposited by ion-assisted sputtering, J. Appl. Phys. 82 (1997) 1617–1625.

[61] C.Q. Guo, Z.L. Pei, D. Fan, J. Gong, C. Sun, Microstructure and tribomechanical properties of (Cr, N)-DLC/DLC multilayer films deposited by a combination of filtered and direct cathodic vacuum arcs, Diam. Relat. Mater. 60 (2015) 66–74.

[62] Y. Lin, A.W. Zia, Z. Zhou, P.W. Shum, K.Y. Li, Development of diamond-like carbon (DLC) coatings with alternate soft and hard multilayer architecture for enhancing wear performance at high contact stress, Surf. Coat. Technol. 320 (2017) 7–12.

[63] C. Tai, S.C. Lee, C.H. Wei, S.L. Tyan, Correlation between I_D/I_G ratio from visible Raman spectra and sp^3/sp^2 ratio from XPS spectra of annealed hydrogenated DLC film, Mater. Trans. 47 (2006) 1847–1852.

[64] T. Guo, C. Kong, X. Li, P. Guo, Z. Wang, A. Wang, Microstructure and mechanical properties of Ti/Al co-doped DLC films: dependence on sputtering current, source gas, and substrate bias, Appl. Surf. Sci. 410 (2017) 51–59.

[65] J. Robertson, Mechanical properties and structure of diamond-like carbon, Diam. Relat. Mater. 1 (1992) 397–406.

[66] Y.B. Zhang, S.P. Lau, D. Sheeja, B.K. Tay, Study of mechanical properties and stress of tetrahedral amorphous carbon films prepared by pulse biasing, Surf. Coat. Technol. 195 (2005) 338–343.

[67] W. Gou, G. Li, X. Chu, B. Zhong, Effect of negative self-bias voltage on microstructure and properties of DLC films deposited by RF glow discharge, Surf. Coat. Technol. 201 (2007) 5043–5045.

[68] S. Chowdhury, M.T. Laugier, I.Z. Rahman, Effect of target self-bias voltage on the mechanical properties of diamond-like carbon films deposited by RF magnetron sputtering, Thin Solid Films 468 (2004) 149–154.

[69] S.B. Singh, A.K. Poswal, M. Pandey, R.B. Tokas, N. Chand, S. Dhara, B. Sundaravel, K.G.M. Nair, N.K. Sahoo, D.S. Patil, X-ray reflectivity studies on DLC films deposited by microwave ECR CVD: effect of substrate bias, Surf. Coat. Technol. 203 (2009) 986–991.

[70] J. Robertson, Requirements of ultrathin carbon coatings for magnetic storage technology, Tribol. Int. 36 (2003) 405–415.

[71] M. Kamiya, H. Tanoue, H. Takikawa, M. Taki, Y. Hasegawa, M. Kumagai, Preparation of various DLC films by T-shaped filtered arc deposition and the effect of heat treatment on film properties, Vacuum 83 (2009) 510–514.

[72] Y.S. Zou, Y.F. Wu, H. Yang, K. Cang, G.H. Song, Z.X. Li, K. Zhou, The microstructure, mechanical and friction properties of protective diamond like carbon films on magnesium alloy, Appl. Surf. Sci. 258 (2011) 1624–1629.

[73] J.B. Wu, J.J. Chang, M.Y. Li, M.S. Leu, A. Li, Characterization of diamond-like carbon coatings prepared by pulsed bias cathodic vacuum arc deposition, Thin Solid Films 516 (2007) 243–247.

[74] N. Dwivedi, S. Kumar, H.K. Malik, Role of base pressure on the structural and nanomechanical properties of metal/diamond-like carbon bilayers, Appl. Surf. Sci. 274 (2013) 282–287.

[75] J.K. Luo, Y.Q. Fu, H.R. Le, J.A. Williams, S.M. Spearing, W.I. Milne, Diamond and diamond-like carbon MEMS, J. Micromech. Microeng. 17 (2007) 147–163.

[76] A. Grill, Tribology of diamondlike carbon and related materials: an updated review, Surf. Coat. Technol. 94–95 (1997) 507–513.

[77] J. Lee, R.W. Collins, V.S. Veerasamy, J. Robertson, Analysis of the ellipsometric spectra of amorphous carbon thin films for evaluation of the sp^3-bonded carbon content, Diam. Relat. Mater. 7 (1998) 999–1009.

[78] M. Hiratsuka, H. Nakamori, Y. Kogo, M. Sakurai, N. Ohtake, H. Saitoh, Correlation between optical properties and hardness of diamond-like carbon films, J. Solid. Mech. Mater. Eng. 7 (2013) 187–198.

[79] A. Axelevitch, B. Gorenstein, G. Golan, Investigation of optical transmission in thin metal films, Phys. Procedia 32 (2012) 1–13.

Full Length Article

Improvement of thermal stability, adhesion strength and corrosion performance of diamond-like carbon films with titanium doping

Natthaphong Konkhunthot[a,b], Pat Photongkam[b], Pornwasa Wongpanya[a,*]

[a] School of Metallurgical Engineering, Institute of Engineering, Suranaree University of Technology, Nakhon Ratchasima 30000, Thailand
[b] Synchrotron Light Research Institute (Public Organization), 111 University Avenue, Muang District, Nakhon Ratchasima 30000, Thailand

ARTICLE INFO

ABSTRACT

Ti-doped diamond-like carbon (Ti-doped DLC) films were deposited on 304 stainless steel through a pulsed filtered cathodic vacuum arc deposition with an individual cathodic arc source. Structural dependent thermal stability, mechanical properties, adhesion, and corrosion performance were thoroughly investigated as a function of the Ti content. Only 0.8 at.% Ti content in the DLC films offers the relatively high hardness (28.8 GPa), high corrosion resistance, enhanced adhesion strength as well as improved thermal stability compared to the undoped DLC films. The reduction in the internal stress and the sp^3 content associated with a slight decrease in the mechanical properties is due to from Ti doping. Higher thermal stability is due to the TiC phase in the Ti-doped DLC structure. Enhancement of the adhesion strength is owing to the relief of the internal stress and the occurrence of the strong atomic intermixing bond at a Ti-doped DLC/Ti intermediate layer interface. Interestingly, the formation of the TiO_2 film on the Ti-doped DLC surface due to a small amount of Ti doping significantly exhibited a better corrosion performance. Ti-doped DLC films, therefore, are a promising coating for tribological applications.

1. Introduction

AISI 304 stainless steel is one of the most versatile and extensively used in a variety of industrial applications because of its good corrosion resistance, high strength, and formability at a relatively lower cost [1–3]. Nevertheless, there have been still restrictions in some advanced engineering and tribological applications requiring excellent hardness, high wear and corrosion resistance, and a smooth contact surface. Several kinds of surface modification have been adopted, such as physical vapor deposition, chemical vapor deposition, etc. for enhancement of surface properties in engineering parts. The outstanding mechanical and chemical properties of excellent hardness and antiwear, low-friction, and chemical inertness [4–9], make DLC film as a protective coating of great interest in numerous applications from tribological protective coating to biomedical materials like wear-resistant coatings, electrical devices, food storage, and medical components [10–12]. Among the applications, a certain component usually encountered the localized heat and corrosive conditions, causing deteriorations of DLC films. With regard to these issues, the investigation of the films' thermal stability and corrosion performance is essential to understand their reliable long-term performance. In the adoption of DLC films in thermal conditions, there is a classical problem in DLC production concerning the existence of hydrogen in the DLC film – the so-called hydrogenated amorphous carbon – often at a relatively higher temperature beyond 200 °C, that experiences hydrogen desorption leading to the conversion of the sp^3 to sp^2 hybridized bonds in the films [13–15]. Subsequently, the desirable properties, especially for abrasive wear, hardness, and slickness, are degraded. Extensive research has, thus, been performed on hydrogen-free DLC films, particularly relating to tetrahedral amorphous carbon (ta-C) with a high sp^3 content [16]. For the synthesis of the ta-C films, the filtered cathodic vacuum arc (FCVA) has been adopted recently with the reason that it employs a small material rod (8-mm diameter) and does not require the reactive and/or background gas. It is, therefore, the eco-friendly [17] and cost-effective surface modification process, which is capable of high-quality DLC production. However, the drawback is that a large intrinsic residual internal stress can be generated during the film deposition known as subplantation [18–22], resulting in the film's delamination [11,16,23,24] due to poor adhesion to the substrate, particularly on the stainless steel substrate, and thus restricting further applications. Two effective strategies have stimulated considerable interest in solving this problem: (i) the intentional introduction of elements and (ii) the deposition of an intermediate layer [25–28]. In recent times, Ti has been employed as a doping element and/or metallic intermediate layer for

* Corresponding author.
 E-mail address: pornwasa@sut.ac.th (P. Wongpanya).

several reasons, i.e., it has good adhesion to all substrates and reacts readily with C atoms, leading to the formation of TiC phases and, thus, providing relief of the residual internal stress and exceptional tribological properties [25–29]. The sp^3/sp^2 ratio is one of the most important parameters determining the DLC's properties. Near edge X-ray absorption fine structure (NEXAFS) spectroscopy is sensitive to the geometric structure of localized C atoms, and it is capable of practically evaluating the sp^3/sp^2 ratio and bonding configuration of the DLC films as a function of the Ti. The mechanical properties were accurately measured using the nano-indentation system, which is a suitable method for amorphous thin films [30–31]. The potentiodynamic polarization test was carried out to investigate the corrosion resistance of the films. X-ray photoemission electron microscopy (X-PEEM) in conjunction with NEXAFS and scanning electron microscopy (SEM) are effective techniques and can provide the local surface morphologies and structural dependent corrosion resistance. Apart from that, the tribological performance, particular the adhesion strength of the films has been evaluated to meet the specific requirement of the protective coatings.

The purpose of this study is to prepare the Ti-doped DLC films on AISI 304 stainless steel substrates with a Ti bond-coat by pulsed two-FCVA deposition and attempt to relate the roles of Ti doping with the thermal stability, mechanical properties, adhesion strength, and corrosion-induced structural transformation. Thermal stability is investigated by a vacuum thermal annealing at various temperatures ranging from room temperature (RT ≈ 25 °C) to 500 °C in real-time analysis. The correlation of structural and mechanical and corrosion properties was also investigated through the nano-indentation test and potentiostat analyzer. Additionally, the measurement of the adhesion strength has been focused on because it is the most significant parameter for a protective coating in tribological applications.

2. Experimental procedures

2.1. Film deposition

AISI 304 austenitic stainless steel (SS) substrate and Si (1 0 0) wafer (approximate size of $10 \times 10 \, mm^2$) were ultrasonically pre-cleaned in ethanol and acetone for 15 min at each step in order to remove any grease contaminations and subsequently were dried by the nitrogen gas before being loaded into the deposition chamber. Two sets of undoped (pure) DLC and Ti-doped DLC films were deposited using a pulsed two-FCVA deposition in this study. The first set comprised the films deposited on the SS substrate, ground and polished to the surface roughness of $R_a = 30 \, nm$ and these were used for nano-mechanical, nano-scratch, and corrosion tests, while a second set comprised the films deposited on the Si substrate and they were used for elementary composition, microstructure, and bonding configuration measurements. Prior to the DLC deposition, the vacuum chamber was evacuated to a base pressure of 2.0×10^{-3} Pa by a turbomolecular pump backed up by a roughing pump. The graphite cathode (99.99% pure, 8 mm in diameter) and titanium cathode (99.50% pure, 8 mm in diameter) were inserted separately on the cathodic arc source. For a vacuum arc discharge, the main arc was initiated via the conductive path deposited on a ceramic insulator surface between the cathode and anode, which allows plasma to generate from the cathode spot. The macro-particles and uncharged atoms originated from the plasma were filtered out through a 90°-curved magnetic filter system, which was electrically connected in a series with the arc discharge. Before the DLC deposition, the bombardment of Ti ions was initially performed at a high direct current (dc) bias voltage of −1500 V for 5 min to remove any surface oxide layers and to create a diffusion interface between the substrate and the DLC films. A 20 nm thickness of the Ti adhesive layer, representing a Ti bond-coat, was first deposited onto the substrate to enhance the adhesion between the film and the substrate. While the mixing of the Ti$^+$ and C$^+$ plasma was supplied simultaneously to form the Ti-doped DLC films at a dc substrate bias voltage of −1000 V, the working pressure of

the system was increased up to 3.0×10^{-3} Pa. The DLC film deposition procedure has been stated in detail previously [22]. The concentration levels of the Ti-incorporated DLC films were controlled through the applied arc voltage (650 and 800 V) to a Ti cathode; these samples subsequently are denoted as Ti-DLC1 and Ti-DLC2. The pure DLC film was also prepared here for comparison. The same condition as the Ti-DLC films is maintained for the pure DLC film unless the applied arc voltage is determined at the single value of 800 V. The deposition time was kept at 30 min for all the specimens.

2.2. Elementary composition and surface morphology of the films

The elemental compositions of the pure DLC and Ti-DLC films were determined by an XPS (XPS; PHI5000 Versaprobe, ULVAC-PHI, Japan) using a monochromatic Al K_α radiation as an excitation source (1486.6 eV) at the beamline 5.3: SUT-NANOTEC-SLRI XPS, SLRI, Thailand. The photoelectrons were recorded in the C 1s, O 1s, and Ti 2p electron shell with the following conditions: a spot size on the sample of 100 μm, the 10 nm depth, the pass energy of 46.95 eV, the step increment of 0.1 eV, and the dwell time of 100 eV. The measurements were carried out within an ultra-high vacuum (UHV) of $\sim 10^{-7}$ Pa. The samples were sputtered with Ar$^+$ ions before measurement with a kinetic energy of 2000 V for 12 s to remove any surface oxides and residual contaminations. The quantitative analysis was accomplished using MultiPak Spectrum: ESCA software. The surface morphologies of all the films before and after the electrochemical experiments were studied via SEM technique using FEI QUANTA 450, equipped with the Oxford Instrument electron energy dispersive spectroscopy (EDS). The elementary composition of the films was also analyzed using EDS.

2.3. Microstructure of the films

The microstructural information of the pure DLC and Ti-DLC films was determined by a dispersive Raman spectroscopic device (BRUKER RamanScope, SENTERRA, OPUS) with an Ar$^+$ laser as an excitation source (λ = 532 nm), operated at 12.5 mW. The focusing spot on the sample is approximately $4 \, \mu m^2$. The spectral resolution of the visible spectrometer is about 3 cm^{-1}. The Raman results of the films were recorded in the range of 800–2000 cm^{-1} under a backscattering configuration. The Raman parameters, such as the intensity ratio of the D and G bands (I_D/I_G ratio), the position of the D and G bands, and full width at half maximum (FWHM) of the deposited films were achieved by fitting the Raman spectra with two Gaussian line shapes using the OriginPro software.

2.4. Local imaging and chemical bonding structure of the films

More detailed information in the local morphology and local bonding structure on pure DLC and Ti-DLC films before and after the thermal annealing and the corrosion tests was investigated by the X-PEEM in conjunction with NEXAFS spectroscopy using SPELEEM (spectroscopic photoemission and low energy electron microscope, ELMITEC Elektronenmikroskopie GmbH, Germany) at the beamline 3.2Ub: PEEM, SLRI, Thailand. The spectroscopic analysis on microscopic imaging, frequently called a spectromicroscopy technique, is an attractive and powerful tool for analyzing the chemically heterogeneous materials. The analyzer of SPELEEM acts as a low pass electron energy filter with a few eV bandwidths near the photoelectron threshold, at which the electrons are readily emitted at particular photon energies. Therefore, the high spatial resolution of ~1 nm can be achieved.

In the X-PEEM chamber, the monochromatic soft X-ray with high intensity and high energy resolution from the synchrotron radiation was focused onto the sample's surface using X-ray mirrors. The emitted electrons near the minimum of the secondary electron mean free path was accelerated into the microscope by a potential difference of 20 kV

between the sample and the objective lens. The resolution and transmission of the microscope were then defined at the objective lens in connection with a contrast aperture. Subsequently, the intermediate lens and projective lens collected and magnified the image onto a microchannel plate or a phosphor screen. Finally, the digital signal or the electrons on the screen will be converted into a visible image and captured by a couple-charged device (CCD) camera, which can be processed supplementary by a personal computer. Because the parallel image-acquisition is used, the technique is quite fast. Therefore, it allows us to analyze the image sequence acquired at different energies, also called a stack. The series of the stack can be transformed to a video record, enabling comprehension of the processes in real-time.

In this study, the C K-edge, O K-edge, and Ti $L_{3,2}$-edge X-PEEM images were collected and stacked using ImageJ software for analyzing the particular areas. The corresponding C K-edge, O K-edge, and Ti $L_{3,2}$-edge NEXAFS spectra acquired in the X-PEEM images were obtained for identifying the local bonding configurations of the particular area operated under a UHV of $\sim 3 \times 10^{-10}$ Pa. The photon energy of the beamline covered the range of 40–1040 eV at an image resolution of 30 nm. The synchrotron radiation source was generated at a storage ring with a beam energy of 1.2 GeV. The dispersed synchrotron radiation was incident at an angle of 17° with respect to the specimen normal. NEXAFS results were recorded in the partial electron yield (PEY) mode, which traditionally utilizes a bias voltage of -20 kV on the detector equipped with an energy analyzer. The absorption signals were given by normalizing the out-coming emitted electron intensity from a freshly flashed Si (1 0 0) wafer in the same photon energy range. The highly oriented pyrolytic graphite (HOPG), representing the complete sp^2 structure, was used as the reference material for energy calibration and quantitatively calculating the absolute sp^2 fraction. The C K-edge, O K-edge, and Ti $L_{3,2}$-edge NEXAFS spectra were achieved in the energy range of 270–350 eV, 520–560 eV, and 445–475 eV, respectively, with a scanning step of 0.1 eV.

2.5. Mechanical properties and adhesion of the films

The nano-mechanical properties, such as the hardness and reduced Young's modulus of our samples were performed by a nano-indentation test with NanoTest (Micro Materials, UK), which is a modular system for nano-indentation, nano-scratch, and nano-impact testing. This technique is a pendulum-based depth-sensing method, which is the most reliable method for measuring the amorphous carbon thin films. The specimen is vertically mounted on the platform, and the normal load is electromagnetically applied. A flowing current through the coil causes the pendulum to rotate and induces the diamond probe to penetrate the sample. Meanwhile, the displacement is measured using the parallel capacitor plate, providing the resolution at the nanometer level. Six repeated measurements were carried out for each sample using a Berkovich type of indenter to acquire the statistical reliability and average value. The maximum penetration depth for the films was kept at approximately 20 nm, which is less than 15% [32–35] of the total film thickness, to avoid the substrate effect. The film thickness was investigated to be ~144 nm using the X-ray reflectometry (XRR) that are not shown here and the procedure measurement has been described in detail in our work [22]. The loading and unloading curves were conducted at a rate of 0.1 mN/s with a holding time of 10 s. The hardness and reduced Young's modulus were carried out from the load-displacement curves based on the Oliver-Pharr method [36,37], which has been considered as an accurate method for evaluating contact hardness [38].

In the case of the nano-scratch testing, moving of the platform is employed. Friction and acoustic emission were also monitored during the scratch tests. For the adhesion analysis, at least three repeated scratches were measured for each sample with a conical diamond tip (90° angle, 5 μm of final radius). A pre-scratching procedure is essential to eliminate the surface roughness effect, topography, slope, and

instrument bending [39,40]. In a multipass wear test mode, the scratch procedure included three sequential scans at 30 μm/s over a 5000 μm scan length as follows: (i) a preliminary topography scan at 2.0 mN constant load, (ii) a scratch scan at 3.0 mN/s applied load, ramped after 50 μm, to a maximum load of 500 mN, and (iii) a final subsequent topography scan at 2.00 mN constant load over the scratched track. The very low speed was kept to reduce the thermal effect, leading to the graphitization of the DLC. The residual scratch tracks were imaged by an SEM microscope and a digital capture system compared with the nano-scratch test results. The nano-indentation and nano-scratch tests were conducted under a relative humidity of approximately 50% and temperature of 27 ± 0.5 °C.

2.6. Corrosion properties of the films

The corrosion resistance of the samples was performed in an aerated 3.5 wt% sodium chloride (NaCl) solution with the following composition: 3.5 g/l NaCl in distilled water (pH ≈ 6.6) at 27 ± 0.5 °C using an Autolab potentiostat PGSTAT 128 N (Metrohm AG, Switzerland). The pH of the aqueous solution was adjusted with a 1 M hydrochloric acid (HCl) to 2.0. In this case, several species dissolved in the NaCl solution, such as Cl^-, H^+, and OH^- can affect the corrosion. The active species is a key factor in determining the rate of the corrosion. Thereby, more aggressive destruction might be observed for the films tested in this study. The electrochemical cell of a standard three-electrode system was set up for the electrochemical experiments composed of a saturated silver to silver chloride (Ag/AgCl) with potassium chloride (KCl) 3.0 M as the reference electrode (RE), a graphite rod (purity of 99.99%) as the counter electrode (CE), and tested specimens as the working electrode (WE), respectively. The RE was connected to a capillary glass tube, the end of which was kept very close to the WE surface to minimize the ohmic drop or iR drop. The WE was pressed between an O-ring and a copper plate with an exposed area inside of 0.28 cm². The setup of an electrochemical cell is shown in Fig. 1. The samples were soaked in the solution for 30 min to stabilize the open circuit potential (OCP) or steady state potential. The potentiodynamic polarization tests were acquired at a scan rate of 0.167 mV/s and a sweeping range from -500 mV below the OCP, in the cathodic region, and to $+500$ mV above the OCP, in the anodic region. The corrosion potential (E_{corr}) and corrosion current density (i_{corr}) were received from the Tafel extrapolation method. The corrosion rate (CR) in millimeters per year (mm/year) was estimated using the following equation [41,42]:

$$CR = \frac{K \times i_{corr} \times EW}{\rho} \qquad (1)$$

where K is the constant value (0.13) that define the unit of the CR, and
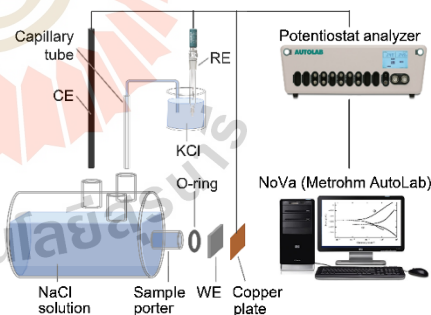
Fig. 1. The schematic of an electrochemical cell with a standard three-electrode system, i.e., RE, CE, and WE for measuring electrode potentials.

EW is the equivalent weight, which can be obtained using the following equation:

$$EW = \frac{1}{N_{EQ}} \tag{2}$$

where $N_{EQ} = \Sigma\left(\frac{f_i n_i}{W_i}\right)$, in which f_i is the mole fraction of the alloying elements, n_i is the number of electrons transferred during the corrosion, and W_i is the atomic weight of the alloying elements. The density (ρ) of each film was measured using the XRR method to be 2.79, 2.68, and 2.49 g/cm^3 for the pure DLC, Ti-DLC1, and Ti-DLC2, respectively, and the measurement technique can be seen from the previous work [22]. By using the electrochemical parameters, the porosity (P) of the films can be calculated using the empirical equation [43]:

$$P = \frac{R_p^0}{R_p} \times 10^{-|\Delta E_{corr}|/\beta_a} \tag{3}$$

where R_p^0 and R_p are the polarization resistance of the substrate and the film, ΔE_{corr} is the potential difference between the corrosion potential of the substrate and the film, and β_a is the anodic Tafel slope for the substrate. In addition, the protective efficiency (P_i), which is an important parameter in the corrosion performance, was also evaluated using Eq. (4) [44]:

$$P_i = 100\left(1 - \frac{i_{corr}}{i_{corr}^0}\right) \tag{4}$$

where i_{corr}^0 and i_{corr} are the corrosion current density of the substrate and the films, respectively.

2.7. Metallic ion release of the films

The metallic ions' concentration released into the solution was collected and analyzed by an inductively coupled plasma-mass spectrometry (ICP-MS Agilent 7500ce, USA) to confirm the results acquired from the corrosion test. The collected solution of 8 mL from individual samples was filled into a plastic tube before being put on the tray of the ICP-MS system. To measure the Ti, chromium (Cr), manganese (Mn), iron (Fe), nickel (Ni), and molybdenum (Mo), the solutions with the exact values of these elements with the following concentrations: 0.001, 0.03, 0.05, 0.07, and 0.1 mg/L, respectively, must be utilized as a standard calibration. The helium collision mode, together with reaction cell technology and internal standard calibration were adopted. Four samples were employed in the measurement to acquire the average statistical analysis.

3. Results and discussion

3.1. Surface morphology and elementary analysis

The surface morphologies of all the films were characterized by the SEM technique. The SEM images of the pure DLC and Ti-DLC films look similar as shown in Fig. 2. All the films are very smooth and with a dense surface without spalling or delamination, indicating the good adhesion of the films to the substrates. No observation of grains or columnar structures for all the films confirms that the films are amorphous structures. A few macro-particles were randomly found on the films' surfaces, even though the magnetic filter is employed. The presence of the macro-particles can be perceived as a minor drawback in some of the mechanical and tribological applications, but they are of primary concern as a particular protective coating for corrosion applications. EDS was also employed to confirm the existence of Ti atoms in the Ti-DLC films. The spot area on the samples was projected at 3 mm^2. The EDS spectra of all the films reveal the main intensity of the C and Si peaks originating from the DLC film and the underlying Si substrate. A weak intensity of the Ti peak originating can also be detected in the spectra of the Ti-DLC films, indicating that the Ti-DLC films can be

successfully synthesized using the pulsed two-FCVA deposition.

The quantitative elemental analysis of all the films was measured by the XPS technique. The variation in the elementary composition has been given in Table 1. The Ti was approximately 0.8 and 2.1 at.% for the Ti-DLC1 and Ti-DLC2, respectively, which is proportional to the applied arc voltages of 650 and 800 V. It is confirmed that the use of the arc voltages is an efficient method to control the amount of the Ti in the Ti-DLC films. With the increase in the arc voltage from 650 to 800 V, the amount of Ti and O in the Ti-DLC films increases from 0.8 to 2.1 at. % and from 3.4 to 5.3 at.%, respectively, accompanied with a decrease in C from 95.8 to 92.6 at.%. The increase in the O percentage with the increasing Ti content may be attributed to the formation of the surface oxide layer after the films are exposed to air [45], which could probably be regarded as absorbed O atoms on the Ti-DLC surface. However, the formed oxide layer was found to protect the diffusion of the active ions or water molecules into the sublayer, thus impeding the destruction of these species to the cross-link carbon network structure, which will be further described in the Corrosion performance analysis section.

3.2. Raman spectroscopy analysis

Raman spectroscopy is a standard nondestructive and comparatively simple technique, which is widely used to accomplish the microstructural information of amorphous carbon films [46–48]. Fig. 3 illustrates the Raman spectra of the pure DLC, Ti-DLC1, and Ti-DLC2, respectively, over a range from 800 to 2000 cm^{-1}. The spectra were fitted into two Gaussians bands. The main band located at ~1545 cm^{-1} is designated as the "G" band for the zone center phonons of the symmetric E_{2g} stretching mode of all the sp^2 sites [47,48]. A small shoulder band at ~1355 cm^{-1} is represented as the "D" band for the zone-edge K-point phonon of symmetric A_{1g} breathing mode of the sp^2 sites due to the bond angle's disordered structure in the sixfold aromatic rings [47,48]. The square shape peak at ~950 cm^{-1} corresponds to the second-order Raman spectrum from the underlying Si substrate, which implies the optical transparency of the films [38]. Table 2 illustrates the variations in the G band position, full width at half maximum of the G band FWHM(G), and I_D/I_G ratio for all the films, obtained from the fitting of the Raman spectra. The Raman results show that the position of the G band shifts to a lower wavenumber as the Ti content increases. The shift of the G band position is associated with the change in the graphite cluster size and the internal stress in the films [47]. The relationship between the shift of the G band position and the internal stress as a function of negative bias voltage has been previously investigated [22]. It was found that the shift of the G band to a higher wavenumber is due to the increase in the internal stress. Further results showed that the increasing internal stress is a result of the large density and high sp^3 bonding originated by the subplantation process.

For our results, the shift of the G band position toward the lower wavenumber with Ti doping means that the residual internal stress in the Ti-DLC films has been decreased. This reduction can be explained using the following three factors: (i) a decrease in the sp^3 hybridization due to the Ti doping can lead to the reduced internal stress; (ii) the reduction in the internal stress is caused by the increase of the adatom mobility induced by the bombardment with Ti ions and, as the new degree of freedom increases, the intense local density and stress of the sp^3 sites can relax; and (iii) the distortion of the atomic bond-angle disorder can exist by Ti incorporation resulting in a significant reduction in the internal stress of the system [49–51]. The reduced internal stress in the Ti-DLC films is related to the film adhesion, which will be further described in the Adhesion analysis section. Additionally, the decrease in the FWHM(G) and the increase in the I_D/I_G ratio are observed as the Ti content increases. This observation is because of the increase in the number or size of the sp^2-bonded clusters [47]. Therefore, the sp^2 carbon bonding is found to increase with the increasing I_D/I_G ratio. The Raman results are in good agreement with the NEXAFS and mechanical property results.
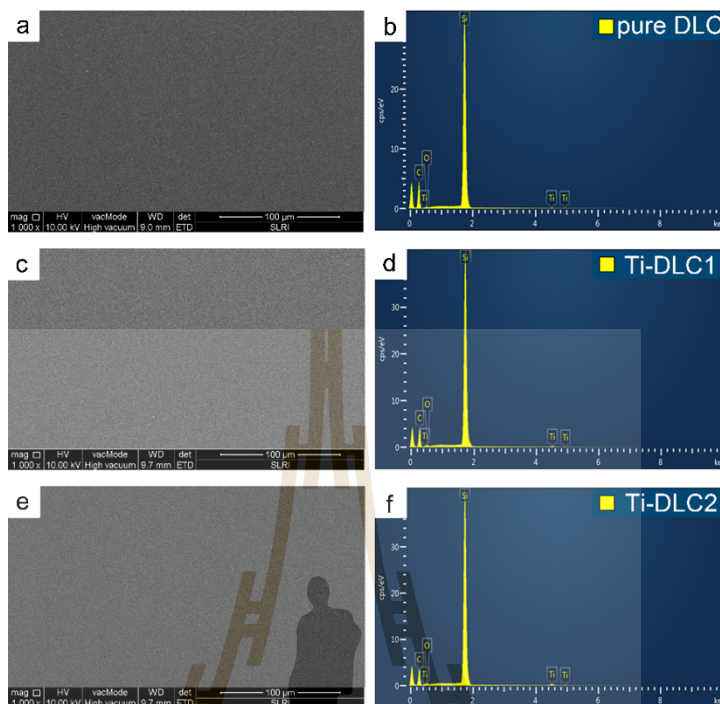
Fig. 2. The SEM micrographs (a) pure DLC, (c) Ti-DLC1, and (e) Ti-DLC2, respectively, and the EDS spectra of (b) pure DLC, (d) Ti-DLC1, (f) Ti-DLC2, respectively.

Table 1
Elementary composition of the pure DLC, Ti-DLC1, and Ti-DLC2, respectively, acquired from the XPS analysis.

Sample code	Applied arc voltage (−V)		Content (at.%)		
	C cathode	Ti cathode	C	O	Ti
Pure DLC	800	–	97.8	2.2	–
Ti-DLC1	800	650	95.8	3.4	0.8
Ti-DLC2	800	800	92.6	5.3	2.1

3.3. Local bonding structure and thermal stability analysis

The local bonding configurations of the Ti-DLC films as a function of the thermal annealing were investigated on the basic of the NEXAFS spectroscopy compared to the pure DLC film. Fig. 4(a)–(c) shows the C K-edge NEXAFS spectra of the pure DLC, Ti-DLC, and Ti-DLC2, respectively, with the variation of thermal annealing in the range of RT to 500 °C. The heterogeneities in the chemical bonding configuration are demonstrated in these spectral features. The pre-edge resonance at a photon energy of ~285.4 eV corresponds to the transition of the C $1s$ core-level electrons into states of the unoccupied π^* symmetry orbitals principally originating from the sp^2 (C=C) and also the contribution of the sp (C≡C) sites if present. The broad band region between 288 and
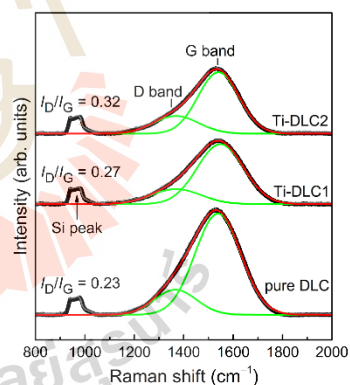
Fig. 3. Raman spectra of pure DLC, Ti-DLC1, and Ti-DLC2, respectively. The black and red lines represent the experimental and fitted curves. The deconvolution of the D and G bands is presented in the green lines.

Table 2
Variations of the G band position, FWHM(G), and I_D/I_G ratio of all the films.

Sample code	G-band position (cm^{-1})	FWHM(G)	I_D/I_G ratio
Pure DLC	1546.5	220.9	0.23
Ti-DLC1	1545.4	218.5	0.27
Ti-DLC2	1540.7	194.8	0.32

335 eV is due to the overlapping C 1s into the unoccupied σ^* transition at the sp, sp^2, and sp^3 sites within the films.

In Fig. 4, it is notable that the spectra of the Ti-DLC films have the analogous features to those of the pure DLC film, indicating that most of the atomic bonding structure does not change significantly as long as the concentration level of the Ti atoms is in a low value. It can be observed that the intensity ratio of the pre-edge peak and broad region of the Ti-DLC films increases slightly compared to the pure DLC films, indicating that the Ti doping induces the formation of graphitic (sp^2) bonds, a process called graphitization. Additionally, the intensity ratios are increased as the annealing temperature rises, which points to the conversion of the sp^3 to sp^2 hybridized bonding by the thermal annealing.

Fig. 5(a)–(c) shows the Ti $L_{3,2}$-edge NEXAFS spectra of the pure DLC, Ti-DLC1, and Ti-DLC2, respectively. From Fig. 5, the Ti atoms were successfully incorporated into the Ti-DLC structure by mixing of the Ti^+ and C^+ plasma, whereas the pure DLC film has no evidence of Ti intensity. The four dominant resonances can be observed clearly for the Ti-DLC films before and after the annealing temperature below 400 °C. The first two features located at ~458 and 460 eV are assigned to the excitations of the L_3-edge core level from the Ti $2p_{3/2}$ to unoccupied Ti $3d_{5/2}$ electronic states, while features located at ~464 and 465 eV correspond to the L_2-edge core level from the Ti $2p_{1/2}$ to empty Ti $3d_{3/2}$ electronic states. The double-peak structure of the $L_{3,2}$-edge corresponds to the spin-orbit coupling, splitting the energy levels into two sublevels with the empty t_{2g} and e_g symmetry of the 3d orbital. In Fig. 5(b) and (c), the spectral features and positions of the Ti-DLC films are a resemblance to the TiC powder [52]. Similar results were also investigated by several authors [53–56] who have reported the formation of the Ti–C bonds and/or the amorphous TiC phases dispersed in an amorphous DLC matrix of the Ti-DLC films prepared using the different methods with the Ti content in the range of 0.62–2.80 at.%. However, at a very low Ti concentration (< 0.42 at.%) [49], it was found that the Ti atoms cannot bond with the C atoms, but rather in the form of a solid solution [54]. The TiC phase, in this study, is a vital cause for the reduction of the meta-stable C-sp^3 hybridized bonding

owing to a replacement of the C–C bonds by the Ti–C bonds, as confirmed by the NEXAFS analysis. On the other hand, the oxidation of the Ti can take place thermodynamically on the Ti-DLC surface when the sample is exposed to air, representing as the residual TiO_2 surface, as described by the O K-edge spectra in Fig. 6. It is, therefore, difficult to eliminate completely the O contaminations and they could not be neglected. From the above results, it is deduced that the Ti atoms in the Ti-DLC films existed mainly in forms of TiC rather than TiO_2 when the Ti content of 0.8–2.1 at.% is kept.

Regarding the thermal effects, the spectra of the Ti-DLC films exhibit distinct features when the annealing temperature increases beyond 300 °C. The change in the line-shape has taken place along with an absence of the double-peak structure, which is attributed to the disappearance of the carbonate surface contaminations [57,58]. This phenomenon might be from the chemisorbed O at the Ti-DLC surface as CO and/or CO_2. After the disappearance of the carbonation, it leaves the oxide of the Ti behind, in particular for the monoxide (TiO) [59] without the appearance of the $L_{3,2}$-edge doubled structures. Additionally, Martinez et al. [57] have subsequently reported a decrease in the oxidation resistance with the presence of the TiO.

The O K-edge NEXAFS spectra of the pure DLC, Ti-DLC1, and Ti-DLC2 respectively, at different annealing temperatures are shown in Fig. 6(a)–(c) and these spectra are correspondent to the natural oxidation on the DLC surface. The O K-edge NEXAFS spectra of the pure DLC films can be divided into two regions: the first region at about 528 eV corresponds to the O $1s \to \pi^*$ transitions originated from the carbonyl and carboxyl groups of the O atoms double-bonded to the C atoms (C=O), and the second broad region between 533 eV and 550 eV assigns to the O $1s \to \pi^*$ (C–O–C), and the O $1s \to \sigma^*$ (–OH) transitions. The O K-edge spectra of the Ti-DLC films feature a slight change compared to the pure DLC films because of a tiny level of the Ti atoms. There are still different spectral features observed for the Ti-DLC films. The observed peaks at 531 eV and 534 eV correspond to the O 2p states with the empty Ti 3d states [60]. An observed broad section of 537–550 eV corresponds to the O 2p states hybridized with the Ti 4s and Ti 4p states. The Ti-DLC spectra resemble the formation of the residual TiO_2 surface [61]. The features of the O K-edge NEXAFS spectra of the Ti-DLC films remain the same spectra as those of the pure DLC films, indicating no obvious change in the local bonding configuration. The features of the spectra exhibit a slight reduction in both the first and second broad regions, which corresponds to the disappearance of the carbonate surface contamination at a high temperature.

The relative sp^2 fraction has been comprehended as the most important information in determining the DLC properties that can be
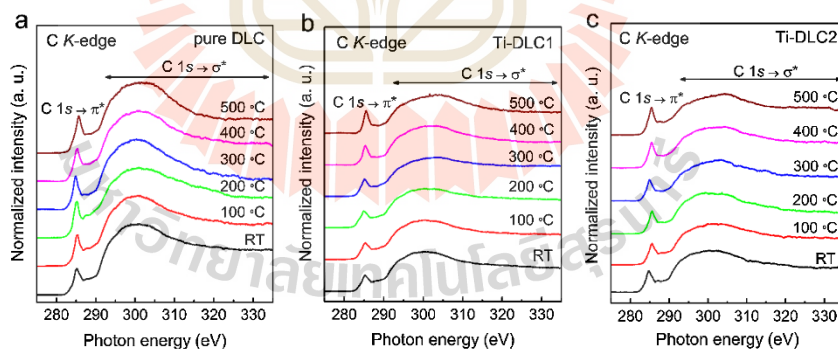
Fig. 4. C K-edge NEXAFS spectra of DLC (a) pure DLC, (b) Ti-DLC1, and (c) Ti-DLC2 as a function of thermal annealing in the range of room temperature (RT) to 500 °C.
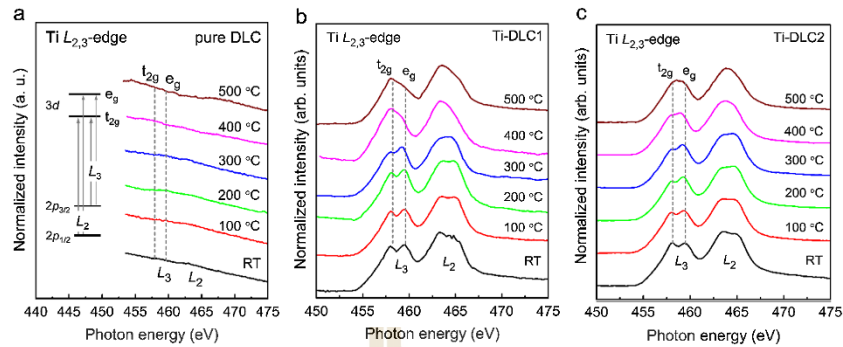
Fig. 5. Ti $L_{3,2}$-edge NEXAFS spectra of DLC (a) pure DLC, (b) Ti-DLC1, and (c) Ti-DLC2 as a function of thermal annealing in the range of room temperature (RT) to 500 °C.
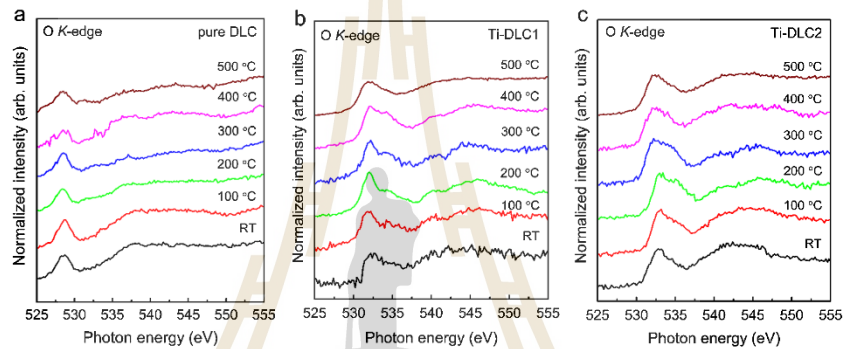
Fig. 6. O K-edge NEXAFS spectra of DLC (a) pure DLC, (b) Ti-DLC1, and (c) Ti-DLC2 as a function of thermal annealing in the range of room temperature (RT) to 500 °C.

obtained from the C K-edge NEXAFS spectrum by normalizing the area of the pre-edge resonance corresponding to the C $1s \rightarrow \pi^*$ transitions at ~285.4 eV with the area of a large section of the spectrum range of 288–335 eV. The C K-edge spectrum is deconvoluted using the Igor Pro 6.3 software to evaluate the relative sp^2 fraction. Fig. 7 illustrates an example of the C K-edge NEXAFS spectrum of the pure DLC film before annealing. The subtraction and deconvolution are carried out to obtain the multiple peaks. The additional resonances in the intermediate region between the π^* and the σ^* states are found at ~286.7, ~288.0, and ~289.4 eV, which are used to ascribe to the transition of the C $1s$ into the σ^* (C–H), π^* (C=O) and/or π^* (C≡C), and σ^* (C–C) states, respectively. The other higher resonances are also shown at ~296.2 and ~302.3 eV, which can be assigned to the transition of the C $1s$ into the σ^* (C=C) and σ^* (C≡C) [62;63]. Because there is no hydrogen employed in the FCVA system, the σ^* (C–H) states are assigned to the hydrogen saturation of the surface carbon dangling bonds [64]. While, the π^* (C=O) contribution to the residual presence of the oxidized carbon, such as graphite oxide, which can occur easily on the DLC surface as a result of the water molecules and active species or even oxygen functional groups [62] from the environment.

The absolute value of the $sp^2/(sp^2 + sp^3)$ ratio was estimated by comparing the C K-edge NEXAFS spectrum the films to that of the HOPG using the following expression:

$$f_{sp^2} = \frac{I_{\text{sam}}^{\pi^*} I_{\text{ref}}(\Delta E)}{I_{\text{ref}}^{\pi^*} I_{\text{sam}}(\Delta E)} \qquad (5)$$

where $I_{\text{sam}}^{\pi^*}$ and $I_{\text{ref}}^{\pi^*}$ are the areas of the π^*(C=C) resonance of the films and HOPG reference, and $I_{\text{sam}}(\Delta E)$ and $I_{\text{ref}}(\Delta E)$ are the areas calculated under the remainder of each spectrum between 288 eV and 335 eV of the films and reference [65–67].

The $sp^2/(sp^2 + sp^3)$ ratios of the pure DLC, Ti-DLC1, and Ti-DLC2 as a function of thermal annealing increase continuously, as shown in Fig. 8, consistent with the increase in the intensity ratio of a pre-edge peak and the decrease in the broad band region, as previously described in the Local bonding structure and thermal stability analysis section. The $sp^2/(sp^2 + sp^3)$ ratios of the pure DLC, Ti-DLC1, and Ti-DLC2 start at 0.33, 0.40, and 0.44, respectively. The pure DLC film exhibits a different response to thermal annealing compared to the Ti-DLC films. The pure DLC film starts with a lower $sp^2/(sp^2 + sp^3)$ ratio, but this ratio increases dramatically to 0.43 and 0.58 for the annealing temperature of up to 300 °C and 500 °C, respectively, indicating that considerable graphitization has occurred. In contrast, the $sp^2/(sp^2 + sp^3)$ ratios of the Ti-DLC1 and Ti-DLC2 increase gradually up to 0.47 and 0.50, indicating a minor changed ratio compared to the pure DLC film. The fact is that the Ti doping into the DLC structure can stabilize the sp^3 phases in Ti-DLC films, as demonstrated by a slight change in the $sp^2/$

N. Konkhunthot et al.

Applied Surface Science 469 (2019) 471–486
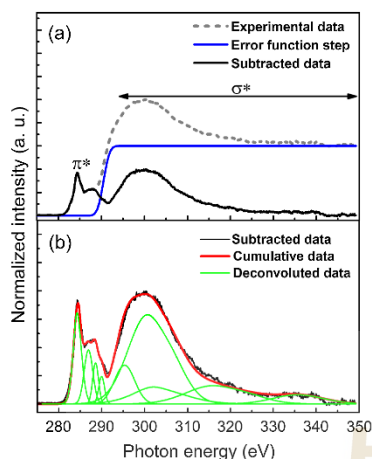
Fig. 7. C *K*-edge NEXAFS spectrum of pure DLC at RT before and after subtraction (a). An error function step was used here to fit the edge jumping at ionization potential as demonstrated by a blue line. The deconvolution into the multi-Gaussian peaks of the C *K*-edge NEXAFS spectrum (b).
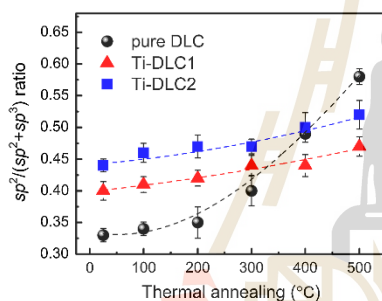
Fig. 8. The correlation of the absolute $sp^2/(sp^2 + sp^3)$ ratio on the thermal annealing of pure DLC, Ti-DLC1, and Ti-DLC2, respectively.

$(sp^2 + sp^3)$ ratios with the increase of the annealing temperature. Such behavior implies that the graphitization of the Ti-DLC films occurs at a slower rate and higher temperature compared to the pure DLC film. The higher thermal stability of the Ti-DLC films might be attributed to the formation of the TiC phase dispersed in the DLC matrix, as confirmed by the NEXAFS results in Fig. 5(b) and (c). It is known that the metal carbide, such as TiC, exhibits the natural stability even at an annealing temperature up to 600 °C [25], which inhibits the graphitization of the Ti-DLC films and thus stabilizes the DLC structure [68,69].

3.4. Mechanical properties

The nano-mechanical properties of all samples, such as hardness (*H*), reduced Young's modulus (*E*), plastic index parameter (*H/E*), and elastic recovery (*%ER*) have been evaluated by the nano-indentation load and indentation displacement curves as shown in Fig. 9 based on the standard Oliver and Pharr method [37]. Table 3 shows the
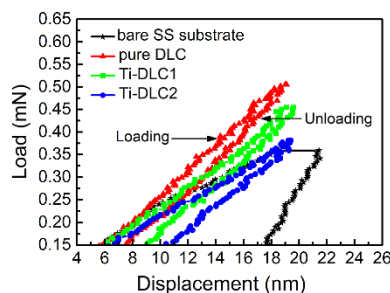
Fig. 9. Nano-indentation load versus indentation displacement curves of bare SS substrate, pure DLC, Ti-DLC1, and Ti-DLC2, respectively.

Table 3
Nano-indentation results of all the samples.

Sample code	Hardness *H*, (GPa)	Reduced Young's modulus *E*, (GPa)	plastic index parameter *H/E*	Elastic recovery *ER*, (%)
Bare substrate	5.6 ± 1.60	254.0 ± 5.41	0.022	17
Pure DLC	32.8 ± 2.19	234.7 ± 7.08	0.139	60
Ti-DLC1	28.8 ± 1.01	215.0 ± 6.54	0.134	54
Ti-DLC2	27.6 ± 1.48	213.0 ± 5.84	0.130	46

summarized nano-mechanical values acquired from the nano-indentation test. Fig. 9 illustrates a typical nano-indentation load versus indentation displacement curves of the bare SS substrate, pure DLC, Ti-DLC1, and Ti-DLC2, respectively. It is obvious that the bare substrate exhibits a highly plastic deformation, which is a typical feature of most metals [70]. A high degree of permanent plastic deformation occurs to a bare substrate, and is indicated by a small difference between the maximum displacement and residual displacement after load removal. In contrast, the predominantly elastic recovery of the curve was observed for the pure DLC, Ti-DLC1 and Ti-DLC2, consecutively. A higher elastic reaction is because of the relaxation of the elastic strain within the DLC structure, which indicates a typically hard and adherent film [71,72]. The elastic recovery is strongly dependent on the sp^3 content in the film. Therefore, the elastic recovery of Ti-DLC films experiences a slight decrease with the Ti doping. The pure DLC film exhibits a maximum applied load at the same displacement associated with the minimum residual displacement compared to the Ti-DLC films. The highest performance against the plastic deformation and elastic recovery of the pure DLC film is mainly associated with the larger sp^3 content in the DLC structure, as confirmed by the NEXAFS results.

As shown in Table 3, the nano-mechanical properties, including the *H*, *E*, *H/E*, and *%ER* of a bare substrate are highly enhanced with the application of the pure DLC and Ti-DLC films. For example, the *H* increases at least more than five times when the Ti-DLC2 is applied. The *H* and *E* of the DLC films reach the highest values of 32.8 GPa and 234.7 GPa, respectively, for the pure DLC film. Additionally, those values continuously decrease as the Ti content increases. The nano-mechanical values of all the films show consistent results with the sp^3 content. A slight decrease in the *H* and *E*, as with the increase in Ti, is related to the increase in the sp^2/sp^3 ratio in the DLC structure, as confirmed by the NEXAFS analysis. In this study, the *H* values of all the deposited films are nearly comparable to those of the *ta*-C films [24,73,74] and thus can protect from scratches and wear efficiently [71].

The *H/E* and *%ER* are valuable parameters in the mechanical properties, and are used to describe the elastic-plastic behavior and are

intimately related to the wear resistance of the films [33]. Therefore, the DLC films with a higher *H/E* exhibit higher wear resistance [33]. The bare SS substrate with the elastic-plastic behavior shows a lower *H/E* value as shown in Table 3, owing to a large amount of mechanical work generated during the plastic deformation. In contrast, the pure DLC film exhibits the highest elastic behavior; therefore, it might have the highest wear resistance. A slight decrease in the *H/E* found in the Ti-DLC films might imply that the low level of Ti doped into the DLC structure has little impact on the mechanical properties.

The elastic recovery (*%ER*) is calculated through the following expression:

$$\%ER = \left(\frac{d_{max} - d_{res}}{d_{max}} \right) \times 100 \tag{6}$$

where d_{max} and d_{res} are the displacements at the maximum load and residual displacement after the load removal. The maximum value of the *%ER* is found in the pure DLC film followed by the Ti-DLC1, Ti-DLC2, and bare substrate, respectively, similar to the *H* value. As for all the above results, the nano-mechanical properties of the Ti-DLC films are still considerably good value as long as the Ti doping is low. However, other properties, such as adhesion and corrosion, have been further evaluated and are discussed in the next section as to whether or not Ti-DLC films represent a protective coating for mechanical and tribological applications.

3.5. Adhesion analysis

It is feasible that a hard-DLC can delaminate prematurely from the underlying substrate during sliding contact by the external normal and/or shear forces due to inferior adhesion strength. Therefore, one of the most important properties and playing a vital role in tribological applications is the film adhesion that is not attributed to the mechanical properties, particularly the *H* and *E* [75]. In the adhesion analysis, the critical load (L_c) is known as a crucial parameter associated with the tribological performance in terms of adhesion strength [36,76] and can easily be identified as a point at which there is an abrupt increase in the friction force and/or at the critical coating spallation or delamination. Fig. 10(a)–(c) shows the typical scratch results for the pure DLC, Ti-DLC1, and Ti-DLC2, respectively. The integrated SEM micrograph inspection is compared to realize the coating adhesion failure. A variation of the acoustic emission spectra is also monitored during the scratch test for evaluating the coating adhesion failures at the phase interfaces, which is consistent with the L_c. There are two distinct stages of the L_c with regard to the SEM morphology as shown in the inset of Fig. 10. The first stage, the L_{c1}, is the applied normal load at which the first cohesive failure consists of the plastic deformation along the edge, parallel or edge crack, and fine crack, and it is rather difficult to define. The other stage, the L_{c2}, is the point of the subsequent adhesion failure containing the external transverse crack and the first delamination [39]. The L_{c2} is defined as the maximum adhesion strength of the films before the film delamination happens. From the scratch results, the L_{c1} and L_{c2} occur at 164, 178, and 181 mN, and 203, 220, and 224 mN for the pure DLC, Ti-DLC1, and Ti-DLC2, respectively. It is notable that the L_c increases with the increasing Ti content, indicating the enhancement of the scratch adhesion strength of the Ti-DLC films. There is no correlation observed between the L_c and the *H* and *E*; rather it depends on the internal stress condition, which is a direct function of the elastic stored energy in the films. The accumulation of the elastic stored energy is a cause of the separation of the films from the substrate. If the adhesive energy cannot overcome the elastic stored energy, the deposited films, in this case, will peel off [40,77]. The decrease in the internal stress, in this study, is associated with the increase of the Ti content as confirmed by the Raman analysis that showed the enhancement of the L_c of the films. The sp^2 (C=C) sites can affect the adhesion strength of the films. The sp^2 (C=C) bonds have a shorter bond length than the sp^3 (C–C) bonds, a
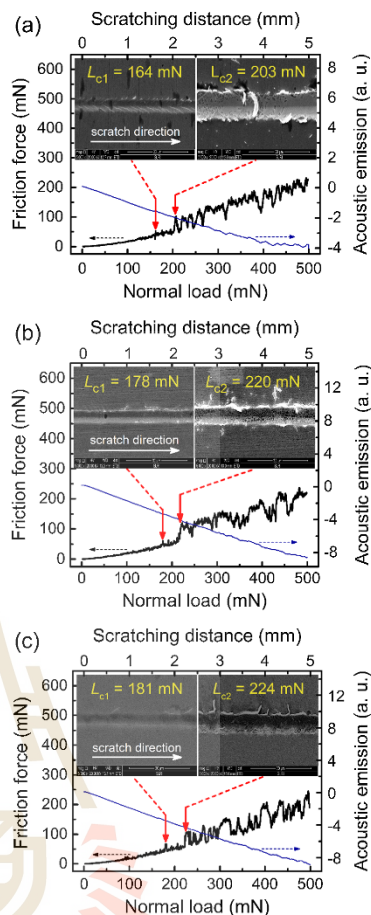
Fig. 10. Typical scratch curves of (a) pure DLC, (b) Ti-DLC1, and (c) Ti-DLC2, respectively. Inset demonstrates the SEM micrographs of the corresponding scratch tracks at a point of the L_{c1} and L_{c2}, respectively.

large number of the sp^2 (C=C) bonds in Ti-DLC films, therefore, correspondingly reduces the strain within the DLC structure, which results in the improvement of the L_c [78]. Another important reason involves the atomic intermixing at an interface between the top DLC film and the Ti intermediate layer. A Ti-DLC/Ti interface, herein, possesses a relatively higher bonding strength than a pure DLC/Ti interface owing to the formation of the compound phase between the Ti and C atoms, TiC; the adhesion strength of the Ti-DLC films, subsequently, has been significantly improved through the strong bonding strength at a diffusion interface.

The inset in Fig. 10(a)–(c) reveals the SEM morphologies of three scratch tracks for all the films, as displayed in the L_{c1} and L_{c2} regions, respectively. The initial stain failure was seen as depicted in the L_{c1}

region where the edge and fine cracks on the scratch tracks can be obviously be observed for the pure DLC, while the Ti-DLC1 and Ti-DLC2 exhibit the slight edge cracks, particularly the Ti-DLC2 showing a relatively smooth scratch track with the minor edge and fine cracks. The failure of adhesion strength occurs at the L_{c2} when the deformation cracks and exfoliations are found on the scratch track. The scratch track, in this stage, is seriously damaged and the films have spalled off at the localized scratch region until the substrate is exposed, indicating a point at which the failure of the adhesion strength of the films takes place. The brittle fractures, as illustrated by the segment cracks and splits along both sides of the scratch track, are obviously seen in the pure DLC film but are found only a little in the Ti-DLC1. On the other hand, the Ti-DLC2 reveals only splits with exfoliations at the upper edge of the scratch track without any brittle fractures, confirming the improvement of the adhesion strength with Ti doping. These observations are according to the elastic recovery revealed by the nano-indentation test results shown in Table 3 that the pure DLC film with a predominant elastic recovery may be damaged by the brittle behavior. In contrast, the incorporation of the Ti atoms allows the Ti-DLC films, with a lower elastic recovery, to deform during the scratches and in turn improves the toughness and adhesion strength of the Ti-DLC films. From this point of view, it is elucidated that the scratch adhesion strength of the films depends mostly on the residual internal stress and the atomic intermixing at a diffusion interface. Therefore, the combined properties of the Ti-DLC films including the low residual stress and the strong bonding strength at the interface provide superior toughness and adhesion strength without much sacrifice of the mechanical properties, which are necessary for tribological applications.

3.6. Corrosion performance analysis

The corrosion performance of bare SS substrate, pure DLC, and Ti-DLC films is investigated through the potentiodynamic polarization test. The polarization curve of all the films and a bare substrate are shown in Fig. 11. The corrosion parameters, such as E_{corr}, i_{corr}, β_a, β_c, R_p, and CR deduced from the Tafel extrapolation method are given in Table 4. The polarization curves of the bare SS substrate experience a massive improvement with the application of the DLC films. The polarization curves of the deposited films shift toward a more positive region of the E_{corr} and the orders of magnitude decrease in the i_{corr}. In comparison between the pure DLC and Ti-DLC films, we found that the Ti-DLC films, particularly for Ti-DLC1 reveal higher corrosion resistance than that of the pure DLC film, as demonstrated by the increase in the E_{corr} and decrease in the i_{corr} as can be observed in Table 4. The E_{corr} and i_{corr} of the pure DLC film are $-146.02\,\text{mV}$ and $14.15\,\text{nA/cm}^2$,
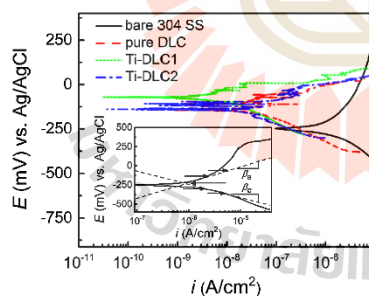
Fig. 11. Potentiodynamic polarization curves tested in an aerated 3.5 wt% NaCl solution of pH 2.0 at 27 ± 2 °C of bare SS substrate, pure DLC, Ti-DLC1, and Ti-DLC2, respectively. Inset demonstrates the example of the Tafel extrapolation method to acquire the simulated parameters for the bare SS substrate.

respectively, increasing by two times for the E_{corr} to $-70.70\,\text{mV}$ and decreasing by fivefold for the i_{corr} to $3.25\,\text{nA/cm}^2$ for the Ti-DLC1. The enhanced corrosion performance is a result of the formed oxides, TiO_2, or the metal carbide, TiC, enriched on the Ti-DLC surface that acts as the primary diffusion barrier against the penetration of the active ions, water molecules, and oxygen into the sublayer, and thus guards against the destruction of the aqueous solution of an amorphous carbon structure.

The porosity (P) and protective efficiency (P_i) were also estimated to assess the corrosion performance thoroughly, as shown in Fig. 12. It is remarkable that the amount of the P correlates well with the R_p and influences directly on the resistivity and durability of the DLC films. Ti-DLC films have a smaller amount of P than that of the pure DLC film, which results in the reduction of the aggressive ion diffusion path in the Ti-DLC films. The films with a large amount of P will show severe delamination, as confirmed by the SEM analysis (Fig. 13). Aggressive ions in the solution easily penetrate into the film/sublayer interface due to the P that results in the films peeling off; subsequently, the metallic substrate is attacked, and the metallic ions are released. The higher i_{corr} and CR of the films are, thus, mainly from a large amount of P. The estimated P_i of the DLC films shows a slight increase as the Ti content increases. The Ti-DLC1 has the highest P_i of 99.36% associated with the lowest P, which is in good accordance with the results of the P, E_{corr}, and i_{corr}. As a result, the Ti incorporation into the DLC films is an efficient approach that provides a corrosion-protective coating in the acidic and saline solution.

3.7. Metallic ions release analysis

An approximate solution of 8 mL from the individual sample was collected after the corrosion test, and the released metallic ions were examined using the ICP-MS technique. From the potentiodynamic results, it confirms that the corrosion resistance of a bare SS substrate has been improved evidently with the application of the DLC films; the released metallic ions of a bare substrate are thus not capable of being measured, and only those of the deposited films were evaluated through this technique. The ICP-MS results illustrate that the pure DLC film releases the maximum concentration of metallic ions with the following quantities: (Fe: 0.5559 mg/L, Cr: 0.0805 mg/L, Ni: 0.0323 mg/L, Mn: 0.0093 mg/L, and Ti: 0.0029 mg/L) (see details in Table 5). Two crucial parameters, an electrochemical potential (E) and a pH, explain the mechanisms of the released metallic ions into an aqueous solution. The Pourbaix diagrams are known as the E-pH diagrams providing the possibility of the predominant forms and/or phases in which the elements exist in an aqueous electrochemical system. Regarding the thermodynamic available data for the main species, the Pourbaix diagrams for Fe [79], Cr [80], Ni [81], Mn [82], and Ti [83] at the E (~ 0 and 300 mV) and pH ($=2$) region are mostly presented as aqueous species of Fe^{2+}, Cr^{3+}, Ni^{2+}, and Mn^{2+} ions, except for Ti, which is in a stable form as a TiO_2 film within a passivity region. It can be seen from the Pourbaix diagrams that the concentration of the released metallic ions depends on the number of elements contained in the samples. Because the substrate is the AISI 304 stainless steel consisting of Fe balanced, Cr 18–20, Ni 8–10, and Mn 2 wt%, the released metallic ions that are detected show a proportionate value to the number of the elements contained in the metallic substrate.

Taking into account the main elements, Ti is one of the most crucial factors in determining the number of the released metallic ions in this study. Ti forms readily as a TiO_2 film after exposure to the O atoms in the atmosphere and/or the solution; it, thus, protects the under-layer film from the destruction of the active species and inhibits the released metallic ions into the solution. As a result, the Ti-DLC films show the lower concentration of the released metallic ions as compared to the pure DLC films, which is consistent with the corrosion results. The surface morphology in Fig. 13 might be clarified by this observation. As seen in Fig. 13, the pure DLC film has been severely damaged as shown

Table 4

The corrosion parameters of all the samples obtained from the potentiodynamic polarization measurement.

Samples	E_{corr} (−mV)	i_{corr} (nA/cm^2)	β_a (V/decade)	β_c (V/decade)	R_p (×10^3 Ω cm^2)	CR (×10^{-2} mm/y)
Bare SS	163.400	507.870	119.960	259.430	19.412	1.886
Pure DLC	146.020	14.150	15.046	9.208	175.336	0.021
Ti-DLC1	70.695	3.252	25.507	11.988	1089.300	0.005
Ti-DLC2	138.950	5.203	7.882	7.988	331.212	0.010

Fig. 12. The porosity (P) and protective efficiency (P_i) of pure DLC, Ti-DLC1, and Ti-DLC2, respectively obtained from the potentiodynamic polarization testing.

Table 5

The concentration of released ions in the solution after the potentiodynamic polarization measurement.

Sample code	Concentration of metallic ions release (mg/L)				
	Fe	Cr	Ni	Mn	Ti
Pure DLC	0.5559	0.0805	0.0323	0.0093	0.0029
Ti-DLC1	0.1350	0.0160	0.0048	0.0029	0.0021
Ti-DLC2	0.4897	0.0587	0.0168	0.0084	0.0026

by the appearance of a larger number and size of pits, whereas the Ti-DLC films have few signs of corrosion traces, especially Ti-DLC1 with the smallest number and size of pits. Such evidence confirms the improvement in the surface properties of the DLC films with doped Ti. Thereby, the introduction of Ti atoms with an appropriate concentration is more applicable and suitable to surface-modified DLC films for applications in a corrosive environment. Another vital point is the
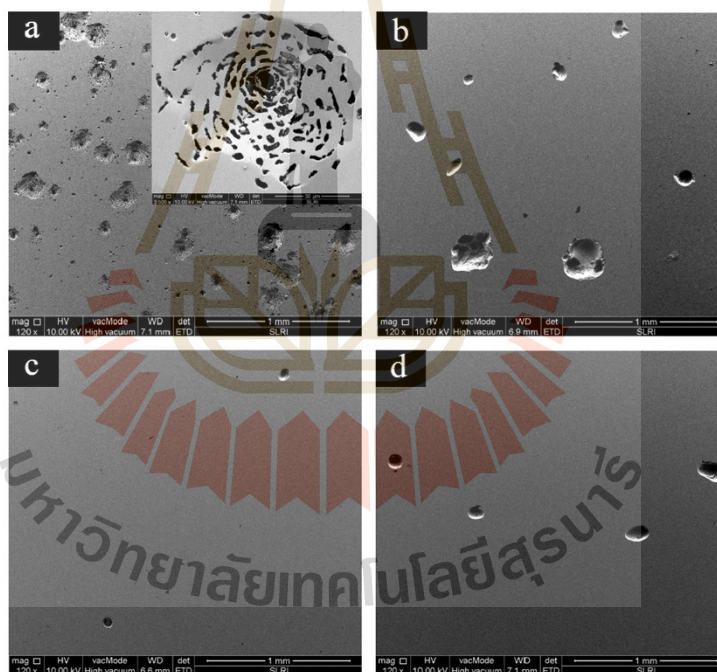
Fig. 13. SEM micrographs of (a) bare SS substrate with a high magnification, (b) pure DLC, (c) Ti-DLC1, and (d) Ti-DLC2, respectively.

formation of TiO_2, affecting the structural properties in terms of the sp^3/sp^2 ratio, and impacting on the corrosion mechanisms, which will be further discussed in the Structural analysis after electrochemical corrosion test section.

3.8. Surface morphology analysis after electrochemical corrosion tests

The surface morphologies of the bare SS substrate, pure DLC, Ti-DLC1, and Ti-DLC2 after the potentiodynamic test were characterized using the SEM, as shown in Fig. 13(a)–(d). Evidently, the surface morphologies of the bare SS substrate are severely damaged and are fully covered by the features of pits. As seen in Fig. 13(a), the pit growth in stainless steel shows the pit mouth at the center, surrounded by flask shapes and lacy metal covers. As shown in Fig. 13(b)–(d), SEM micrographs of the pure DLC and Ti-doped DLC films have no evidence of the severe damage as found in the bare substrate. Active ions, H^+, OH^-, and Cl^- dissolved in the aqueous solution, penetrate into the sublayer of the films, as demonstrated by the localized damage or corroded spots, resulting in the films' delamination. The pure DLC film demonstrates a larger damaged surface than that those of the Ti-DLC films. The corroded spot that formed into about 30 μm in size is observed in the pure DLC film. The size of such a spot is well correlated with the P. The damaged surfaces are ranked in order from the lowest to the highest as follows: the Ti-DLC1, Ti-DLC2, and pure DLC. The improvement in the corrosion resistance in the Ti-DLC films is from the formation of the metal carbide or oxide layer enriched on the Ti-DLC surface, as ascribed in the previous results. The SEM micrographs confirmed that the Ti-DLC1 is the best candidate employed as a corrosion-resistant coating under this condition.

3.9. Structural analysis after electrochemical corrosion test

X-PEEM and NEXAFS were implemented to verify the structural dependent corrosion resistance of the different regions on the DLC surface after the corrosion tests. The use of X-PEEM in conjunction with NEXAFS provides much surface sensibility and is an appropriate tool to obtain information of both imaging and spectroscopy of a nanoscale object. Fig. 14(a)–(c) demonstrates a stack of the C K-edge X-PEEM images of the pure DLC, Ti-DLC1, and Ti-DLC2, taken at the photon energies of 285.4, 288.0, 289.4, 296.2, and 302.3 eV, respectively (on the strong C 1s absorption peaks), corresponding to the deconvoluted resonances of the π^* (C=C), π^* (C=O) and/or π^* (C≡C), σ* (C–C), σ* (C=C), and σ* (C≡C) states, as seen in Fig. 7. The dark and bright regions in the X-PEEM images are correlated directly to the image
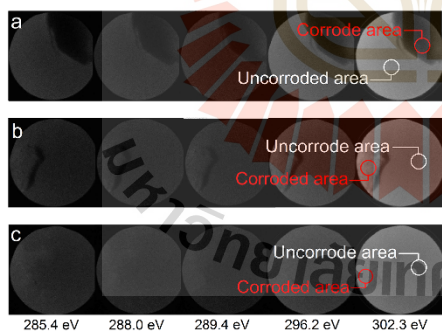
Fig. 14. A stack of the C K-edge X-PEEM image of (a) pure DLC, (b) Ti-DLC1, and (c) Ti-DLC2 at different photon energies of 285.4, 288.0, 289.4, 294.6, and 302.5 eV, respectively. The field of view of each image = 75 μm.
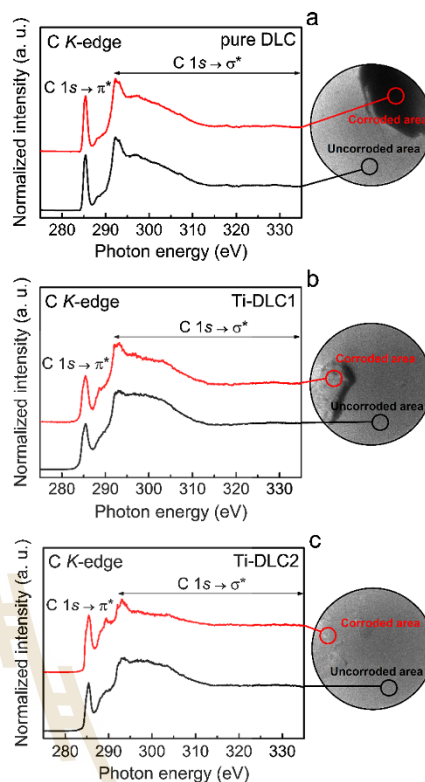
Fig. 15. C K-edge spectra and C K-edge X-PEEM images of (a) pure DLC, (b) Ti-DLCs, and (c) Ti-DLC2, respectively.

contrast mechanisms, such as topographic, work function, elemental, and chemical contrast. The element and chemical contrasts are the most substantial mechanisms in determining the distinctions of each region. Additionally, the chemical contrast is also associated with the electronic band structure like bonds and molecular orbitals; therefore, the area containing the predominant elements and/or bonds appeared brighter. The bright area can be observed outside the pit, representing to be an uncorroded area enriched with carbon atoms, whereas the darker area should be considered as a corroded area with a lower carbon atom content. By selecting the C K-edge X-PEEM image sequences at different photon energies, the regions containing the C species can be spatially resolved by the contrast while the image changes in regard to the changes in the C absorption peak intensity. The regions at the photon energies of 285.4, 288.0, and 289.4 eV appear nearly dark owing to the slight absorption of the C species at these energies, whereas the other ones at photon energies of 296.2 and 302.3 eV are bright because of the strong absorption of the C species. The bright regions, in this case, relate to the overlapping C $1s \rightarrow$ the σ* transitions at the sp^2 and sp^3 sites.

NEXAFS implementation is for the in-depth understanding of the corrosion-induced structural transformation of the DLC films. Fig. 15

shows the corresponding C K-edge NEXAFS spectra acquired from the C K-edge X-PEEM images for the pure DLC, Ti-DLC1, and Ti-DLC2. The C K-edge X-PEEM image of the pure DLC film sustained severe corrosion until deep into the sub-layer, as illustrated by the dark area where there is less of the signal of the C absorption. The pre-edge π^* (C=C) resonance located at ~285.4 eV obtained a greater increment together with a noticeable decrease in the overlapping C $1s \rightarrow$ the σ^* transition at the sp, sp^2, and sp^3 sites of a broad region between 288 and 335 eV. The $sp^2/(sp^2 + sp^3)$ ratios of the pure DLC film in the corroded and uncorroded areas are also estimated via Eq. (5) to be 0.89 and 0.88, which confirms a massive change in the carbon network structure compared to the pure DLC film before the corrosion test (0.33). No obvious difference in the ratio observed for the two areas indicates that most of the metastable C-sp^3 bonding from both areas is converted to the C-sp^2 bonding by interacting with the active species in the corrosive solution [84]. This observation is consistent with the spectral features of the C K-edge NEXAFS spectra of the pure DLC film after the corrosion test, which resembles the graphite oxide [85,86]. Considering the films with the high sp^2 bonding, the electron transfer and exchange at the film/solution interface will occur easily followed by the dissolution of the higher metallic ions.

In the case of the Ti-DLC films, a slight increase in the π^* (C=C) resonance and a slight decrease in the broad band are observed. For the Ti-DLC films, additional peaks observed at ~288–290 eV correspond to the σ (C–H) and the π^* (C=O) sites that might probably be the corrosion products on the Ti-DLC surface. By calculation, the $sp^2/(sp^2 + sp^3)$ ratios of the Ti-DLC1 and Ti-DLC2 in the corroded and uncorroded areas are 0.73 and 0.60, and 0.77 and 0.72, respectively. In this study, the active species in the acidic solution might be the main reason resulting in dramatic changes in the ratio in the DLC films. The results of the sp^2/sp^3 ratio in the Ti-DLC films before and after the corrosion test are not remarkably different compared to the pure DLC film, and it indicates that the Ti-DLC films are more noble and durable than the pure DLC film under the same solution.

The durability of the Ti-DLC films is confirmed by the further investigation acquired from the Ti $L_{3,2}$-edge spectra. Fig. 16 illustrates the corresponding Ti $L_{3,2}$-edge NEXAFS spectra obtained from the Ti $L_{3,2}$-edge X-PEEM images of the pure DLC, Ti-DLC1, and Ti-DLC2, respectively. The spectral features in two areas of the pure DLC film show a significant difference due to the severe damage. No signs of the intensity of the Ti $2p$ peak are observed in the uncorroded area, as shown by the bright area, whereas the spectral features of the Ti peak intensity can be noticeably observed in the corroded area, as demonstrated by the dark area. The appearance of the Ti in the pure DLC is due to the delamination of the entire DLC film, which leads to the detection of a Ti intermediate layer deposited on a bare substrate. Conversely, the Ti-DLC films exhibit the spectral features of the Ti peak from two areas. This spectrum is associated with the interactions of Ti–O bonds like the TiO_2 film, which can occur naturally on the Ti-DLC surface [61]. A slight difference between the Ti-DLC1 and Ti-DLC2 can be observed. A relatively higher intensity of the Ti peak is found for the Ti-DLC2 depending on the Ti content in the films. The appearance of the TiO_2 film is expected to enhance the corrosion resistance of the Ti-DLC films due to its stability in the acidic solution, as shown in the Pourbaix diagram [83]. The stable Ti-incorporated DLC surface acts as a diffusion barrier for interrupting the penetration of water molecules, active ions, and oxygen into the sublayer [87]; thus it prevents the destruction of the aqueous solution to the carbon cross-linking structure in terms of the sp^3/sp^2 ratio. Although the Ti-DLC2 exhibits almost the same spectral features as the Ti-DLC1, which should exhibit the similar behavior, the corrosion resistance is nearly the value for the pure DLC film. The fact is that a higher number of the Ti atoms can break up the continuity of the carbon network in the Ti-DLC structure. This can lead to the increase in the sp^2 hybridized carbon [87] and the electron transfer and exchange at the film/solution interface, enabling the corrosion to occur more rapidly. Regarding the discontinuity of the DLC matrix, it may cause
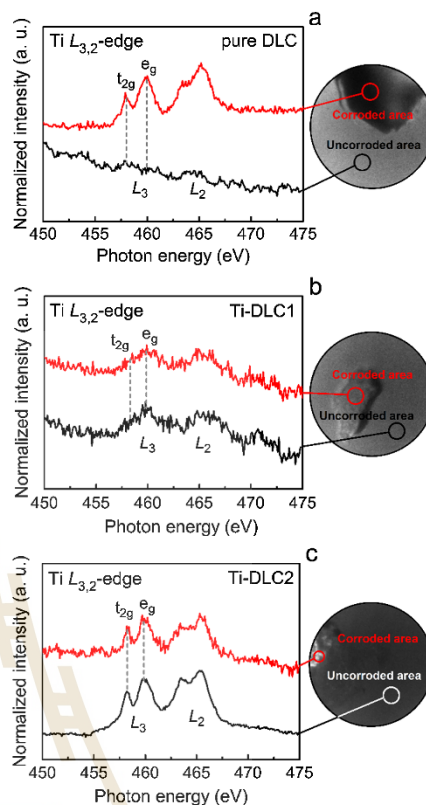
Fig. 16. Ti $L_{3,2}$-edge spectra and Ti $L_{3,2}$-edge X-PEEM images of (a) pure DLC, (b) Ti-DLC1, and (c) Ti-DLC2, respectively.

point defects, such as porosity, which is an origin of local corrosion, as seen by the SEM images in Fig. 13. The large degree of the sp^2 bonds and defects in the Ti-DLC2 can, therefore, lead to the reduction in the corrosion resistance even if the passive TiO_2 film is included.

The Fe $L_{3,2}$-edge NEXAFS spectra have been further analyzed to confirm the durability of the deposited films. Fig. 17 shows the corresponding Fe $L_{3,2}$-edge NEXAFS spectra and the Fe $L_{3,2}$-edge X-PEEM images of the pure DLC, Ti-DLC1, and Ti-DLC2, respectively. The results illustrate that there is a great distinction between two areas in the pure DLC film. The corroded area sustained severe detriments. The entire deposited films have spalled off until the spectral intensity of the Fe peak from the substrate beneath the deposited film is observed. It is found that the spectral shapes of the Fe peak acquired from the corroded area are similar to those from the AISI 304 stainless steel spectrum [89], confirming the delamination of the entire films. In contrast, no signal of the Fe peak intensity is detected in both areas of the Ti-DLC1. This means that the film remains in an acidic chloride solution, indicating the great durability of the Ti-DLC1, while the Ti-DLC2 shows the same behavior as the pure DLC film, but the Fe intensity detected in the corroded area, and the shapes of the Fe spectrum are similar to the
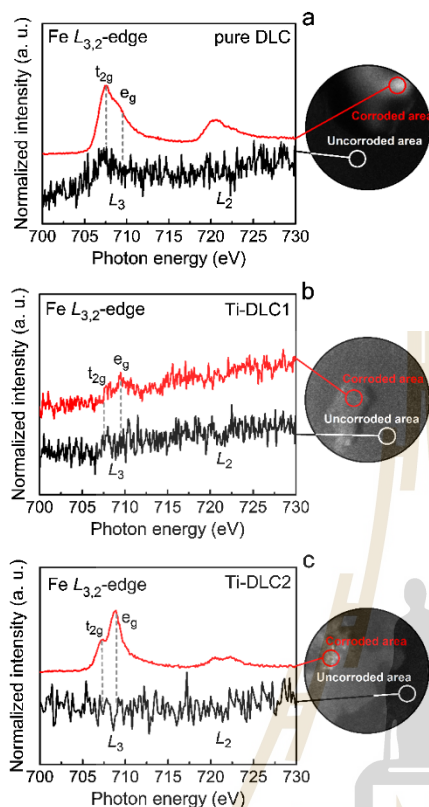
Fig. 17. Fe $L_{3,2}$-edge spectra and Fe $L_{3,2}$-edge X-PEEM images of (a) pure DLC, (b) Ti-DLCs, and (c) Ti-DLC2, respectively.

Fig. 18. Cr $L_{3,2}$-edge spectra and Cr $L_{3,2}$-edge X-PEEM images of (a) pure DLC, (b) Ti-DLCs, and (c) Ti-DLC2, respectively.

Fe_2O_3 or Fe_3O_4 spectrum [89], which correspond to the corrosion products formed at the pitting edge on the Ti-DLC2 surface. These observations show good consistency with the corrosion and SEM analysis. The Cr $L_{3,2}$-edge NEXAFS spectra are also investigated and shown in Fig. 18. The same trend as the Fe $L_{3,2}$-edge NEXAFS spectra is observed for the Cr spectrum. The spectral shapes of the Cr $L_{3,2}$-edge NEXAFS acquired from the corroded areas of the pure DLC and Ti-DLC2, look like the Cr oxides formed on the AISI304 stainless steel sample [88]. Furthermore, such spectral features are similar to the Cr_2O_3 spectrum [89], which is the stable oxide formed on the AISI304 stainless steel substrate.

Noticeably, the DLC films with the combined properties of enhanced thermal stability, excellent mechanical properties and adhesion, and good corrosion resistance can be obtained through the Ti doping at a very low concentration of 0.8 at.%. These attractive properties make it satisfactory as a protective corrosion resistant coating for mechanical and tribological applications. Further emphasis is that the films deposited by the FCVA system in the study are the comparatively simple and cost-effective plasma-based method, which is useful for the development of the modified DLC films.

4. Conclusions

In this study, the Ti-DLC films were synthesized on AISI 304 stainless steel substrate by pulsed two-FCVA deposition and their thermal stability, mechanical properties, adhesion strength, and corrosion performance were thoroughly investigated. The NEXAFS results indicate that the sp^3/sp^2 ratio decreases with the Ti doping, while the thermal stability of Ti-DLC films experiences an enhancement due to the formation of the TiC phase in the Ti-DLC matrix. The results of the Raman analysis show a notable reduction in the internal stress with the introduction of the Ti atoms. The mechanical properties of the Ti-DLC films decrease slightly as the Ti content increases, but their hardness is still retained at a relatively high value. The good adhesion strength of the Ti-DLC films corresponds to the reduction in the internal stress and the atomic intermixing formed at the Ti-DLC/Ti interface. The corrosion resistance has been improved evidently, which is attributed to the formation of a diffusion TiO_2 barrier on the Ti-DLC surface. Therefore, the optimum Ti concentration to maintain the combined outstanding properties, including high thermal stability, excellent mechanical properties, adhesion strength, and good corrosion resistance, has been

observed at a Ti content of 0.8 at.% and the Ti-DLC film becomes the preferred candidate for mechanical, and tribological applications.

Acknowledgement

Appendix A. Supplementary material

Supplementary data to this article can be found online at https://doi.org/10.1016/j.apsusc.2018.11.028.

References

[1] J.B.L. Francisco, D.G.E. Cynthia, C.H. Ramon, P.A.R. Susana, J.P.C. Manuel, E.L.S. Jose, M.S. Roberto, M.H.R. Jose, Influence of size on the microstructure and mechanical properties of an AISI 304L stainless steel: a comparison between bulk and fibers, Materials 8 (2015) 451–461, https://doi.org/10.3390/ma8020451.

[2] P. Marshall, Austenitic Stainless Steel: Microstructure and Mechanical Properties, Elsevier Applied Science Publishers Ltd, Essex, 1984.

[3] J. Beddoes, J.G. Parr, Introduction to Stainless Steels, third ed., ASM International, Ohio, 1999.

[4] J. Robertson, Amorphous carbon, Solid State Mater. Sci. 1 (1996) 557–560, https://doi.org/10.1016/S1359-0286(96)80072-6.

[5] T.S. Santra, C.H. Liu, T.K. Bhattacharyya, P. Patel, T.K. Barik, Characterization of diamond-like nanocomposite thin films grown by plasma enhanced chemical vapor deposition, 124320-1–124320-9, J. Appl. Phys. 107 (2010), https://doi.org/10.1063/1.3415548.

[6] W. Song, Y. Kim, D.S. Jung, S. Lee, W. Jung, O.J. Kwon, H.K. Kim, M.S. Kim, K.S. An, C.Y. Park, Boron and nitrogen co-doping of diamond-like carbon film for transparent conductive films, Appl. Surf. Sci. 284 (2013) 53–58, https://doi.org/10.1016/j.apsusc.2013.06.166.

[7] A.S. Chaus, T.N. Fedosenko, A.V. Rogachev, L. Čaplovič, Surface, microstructure, and optical properties of copper-doped diamond-like carbon coating deposited in pulsed cathodic arc plasma, Diam. Relat. Mater. 42 (2006) 64–70, https://doi.org/10.1016/j.diamond.2014.01.001.

[8] F.J.G. Silva, R.P. Martinho, A.P.M. Baptista, Characterization of laboratory and industrial CrN/CrCN/diamond-like carbon coatings, Thin Solid Films 550 (2014) 278–284, https://doi.org/10.1016/j.tsf.2013.11.042.

[9] S. Wang, J.Q. Zhu, J.Z. Wang, X.B. Yin, X. Han, Raman spectroscopy and mechanical properties of multilayer tetrahedral amorphous carbon films, Thin Solid Films 519 (2011) 4906–4909, https://doi.org/10.1016/j.tsf.2011.01.051.

[10] L. Hongxi, J. Yehua, Z. Rong, T. Baoyin, Wear behaviour and rolling contact fatigue life of Ti/TiN/DLC multilayer film fabricated on bearing steel by PIID, Vacuum 86 (2012) 848–853, https://doi.org/10.1016/j.vacuum.2011.02.015.

[11] A. Matthews, S.S. Eskildsen, Engineering applications for diamond-like carbon, Diam. Relat. Mater. 3 (1994) 902–911, https://doi.org/10.1016/0925-9635(94)90297-6.

[12] D. Roth, B. Rau, S. Roth, J. Mai, K.H. Dittrich, Large area and three-dimensional deposition of diamond-like carbon films for industrial applications, Surf. Coat. Technol. 74–75 (1995) 637–641, https://doi.org/10.1016/0257-8972(95)08338-3.

[13] A. Erdemir, C. Donnet, Tribology of diamond and diamond-like carbon films: an overview, in: G.W. Stachowiak (Ed.), Wear: Materials, Mechanisms and Practice, Wiley, London, 2005, pp. 1–7.

[14] H. Liu, A. Tanaka, K. Umeda, The tribological characteristics of diamond-like carbon films at elevated temperature, Thin Solid Films 345 (1999) 162–168, https://doi.org/10.1016/S0040-6090(98)01093-1.

[15] H.X. Li, T. Xu, C.B. Wang, J.M. Chen, H.D. Zhou, H.W. Liu, Annealing effect on the structure, mechanical and tribological properties of hydrogenated diamond-like carbon films, Thin Solid Films 515 (2006) 2153–2160, https://doi.org/10.1016/j.tsf.2006.04.018.

[16] A.C. Ferrari, B. Kleinsorge, N.A. Morrison, A. Hart, V. Stolojan, J. Robertson, Stress reduction and bond stability during thermal annealing of tetrahedral amorphous carbon, J. Appl. Phys. 85 (1999) 7191–7197, https://doi.org/10.1063/1.370531.

[17] A.D. Liu, H.X. Zhang, T.H. Zhang, MEVVA ion source development and its industrial applications at Beijing Normal University, Surf. Coat. Technol. 193 (2005) 65–68, https://doi.org/10.1016/j.surfcoat.2004.07.057.

[18] M. Lejeune, M. Benlahsen, R. Bouzerar, Stress and structural relaxation in amorphous hydrogenated carbon films, Appl. Phys. Lett. 84 (2004) 344–346, https://doi.org/10.1063/1.1637447.

[19] G. Gassner, P.H. Mayrhofer, C. Mitterer, J. Kiefer, Structure-property relations in Cr-C/a-C: H coatings deposited by reactive magnetron sputtering, Surf. Coat.

[20] Technol. 200 (2005) 1147–1150, https://doi.org/10.1016/j.surfcoat.2005.02.186.
G. Gassner, P.H. Mayrhofer, J. Patscheider, C. Mitterer, Thermal stability of nanocomposite CrC/a-C: H thin films, Thin Solid Films 515 (2007) 5411–5417, https://doi.org/10.1016/j.tsf.2006.12.149.

[21] F.M. d'Heurle, J.M.E. Harper, Note on the origin of intrinsic stresses in films deposited via evaporation and sputtering, Thin Solid Films 171 (1989) 81–92, https://doi.org/10.1016/0040-6090(89)90035-7.

[22] N. Konkhunthot, S. Tunmee, X.L. Zhou, K. Komatsu, P. Photongkam, H. Saitoh, P. Wongpanya, The correlation between optical and mechanical properties of amorphous diamond-like carbon films prepared by pulsed filtered cathodic vacuum arc deposition, Thin Solid Films 653 (2018) 317–325, https://doi.org/10.1016/j.tsf.2018.03.053.

[23] J. Robertson, Properties of diamond-like carbon, Surf. Coat. Technol. 50 (1992) 185–203, https://doi.org/10.1016/0257-8972(92)90001-Q.

[24] A. Grill, Tribology of diamond like carbon and related materials: an updated review, Surf. Coat. Technol. 94–95 (1997) 507–513, https://doi.org/10.1016/S0257-8972(97)00458-1.

[25] Y.H. Lin, H.D. Lin, K.C. Liu, M.W. Huang, Y.C. Chen, J.R. Chen, H.C. Shih, Annealing effect on the structural, mechanical and electrical properties of titanium-doped diamond-like carbon films, Thin Solid Films 518 (2009) 1503–1507, https://doi.org/10.1016/j.tsf.2009.09.096.

[26] X. Shia, L. Guo, Y. Bai, L. Qiao, Characterization of coating probe with Ti-DLC for electrical scanning probe microscope, Appl. Surf. Sci. 257 (2011) 7238–7244, https://doi.org/10.1016/j.apsusc.2011.03.099.

[27] R.J. Narayan, Laser processing of diamond-like carbon-metal composites, Appl. Surf. Sci. 245 (2005) 420–430, https://doi.org/10.1016/j.apsusc.2004.11.026.

[28] C. Liu, G. Li, W. Chen, Z. Mu, C. Zhang, L. Wang, The study of doped DLC films by Ti ion implantation, Thin Solid Films 475 (2005) 279–282, https://doi.org/10.1016/j.tsf.2004.08.051.

[29] F. Zhao, H.X. Li, L. Ji, Y.G. Wang, H.D. Zhou, J.M. Chen, Ti-DLC films with superior friction performance, Diam. Relat. Mater. 19 (2010) 342–349, https://doi.org/10.1016/j.diamond.2010.01.008.

[30] Y. Lifshitz, Hydrogen-free amorphous carbon films: correlation between growth conditions and properties, Diam. Relat. Mater. 5 (1996) 388–400, https://doi.org/10.1016/0925-9635(95)00445-9.

[31] R. Gago, M. Vinnichenko, H.U. Jäger, A.Y. Belov, I. Jiménez, N. Huang, H. Sun, M.F. Maitzl, Evolution of sp^2 networks with substrate temperature in amorphous carbon films: experiment and theory, 014120-1-014120-9, Phys. Rev. B 72 (2005), https://doi.org/10.1103/PhysRevB.72.014120.

[32] A. Modabberasl, P. Kameli, M. Ranjbar, H. Salamati, R. Ashiri, Fabrication of DLC thin films with improved diamond-like carbon character by the application of external magnetic field, Carbon 94 (2015) 485–493, https://doi.org/10.1016/j.carbon.2015.06.081.

[33] S. Ishpal, N. Kumar, C.M.S. Dwivedi, Rauthan, Investigation of radio frequency plasma for the growth of diamond like carbon films, 033515-1 033515-14, Phys. Plasmas 19 (2012), https://doi.org/10.1063/1.3694855.

[34] D. Liu, G. Benstetter, E. Lodermeier, J. Vancea, Influence of the incident angle of energetic carbon ions on the properties of tetrahedral amorphous carbon (ta-C) films, J. Vac. Sci. Technol. A 21 (2003) 1665–1670, https://doi.org/10.1116/1.1597888.

[35] V.J. Trava-Airoldi, L.F. Bonetti, G. Capote, J.A. Fernandes, E. Blando, R. Hübler, P.A. Radi, L.V. Santos, E.J. Corat, DLC film properties obtained by a low cost and modified pulsed-DC discharge, Thin Solid Films 516 (2007) 272–276, https://doi.org/10.1016/j.tsf.2007.06.100.

[36] W.C. Oliver, G.M. Pharr, Measurement of hardness and elastic modulus by instrumented indentation: advances in understanding and refinements to methodology, J. Mater. Res. 19 (2004) 3–20, https://doi.org/10.1557/jmr.2004.19.1.3.

[37] W.C. Oliver, G.M. Pharr, An improved technique for determining hardness and elastic modulus using load and displacement sensing indentation experiments, J. Mater. Res. 7 (1992) 1564–1583, https://doi.org/10.1557/JMR.1992.1564.

[38] Y.B. Zhang, S.P. Lau, D. Sheeja, B.K. Tay, Study of mechanical properties and stress of tetrahedral amorphous carbon films prepared by pulse biasing, Surf. Coat. Technol. 195 (2005) 338–343, https://doi.org/10.1016/j.surfcoat.2004.09.009.

[39] B.D. Beake, V.M. Vishnyakov, R. Valizadeh, J.S. Colligon, Influence of mechanical properties on the nanoscratch behaviour of hard nanocomposite TiN/Si₃N₄ coating on Si, J. Phys. D Appl. Phys. 39 (2006) 1392–1397, https://doi.org/10.1088/0022-3727/39/7/009.

[40] M.A. Hassan, A.R. Bushroa, R. Mahmoodian, Identification of critical load for scratch adhesion strength of nitride-based thin films using wavelet analysis and a proposed analytical model, Surf. Coat. Technol. 277 (2015) 216–221, https://doi.org/10.1016/j.surfcoat.2015.07.061.

[41] ASTM G102-89, Standard practice for calculation of corrosion rates and related information from electrochemical measurements, in Annual book of ASTM standards, vol. 03.02, 1990, pp. 416–422.

[42] R.V. Lakshmi, Y. Yoganandan, K.T. Kayya, B.J. Basa, Effective corrosion inhibition performance of Ce³⁺ doped sol-gel nanocomposite coating on aluminium alloy, Prog. Org. Coat. 76 (2013) 367–374, https://doi.org/10.1016/j.porgcoat.2012.10.004.

[43] B. Matthes, E. Brozeit, J. Aromaa, H. Ronkainen, S.P. Hannula, A. Leyland, A. Matthes, Corrosion performance of some titanium-based hard coating, Surf. Coat. Technol. 49 (1991) 489–495 https://doi.org/10.1016%2F0257-8972%2891%2990105-6.

[44] Y.J. Yu, J.G. Kim, S.H. Cho, J.H. Boo, Plasma-polymerized toluene films for corrosion inhibition in microelectronic devices, Surf. Coat. Technol. 162 (2003) 161–166, https://doi.org/10.1016/S0257-8972(02)00582-0.

[45] G. Francz, A. Schroeder, R. Hauert, Surface analysis and bioreactions of Ti- and V-

containing a-C:H, Surf. Interface Anal. 28 (1999) 3–7, https://doi.org/10.1002/(SICI)1096-9918(199908)28:1<3::AID-SIA609>3.0.CO;2-U.

[46] A.C. Ferrari, J. Robertson, Resonant Raman spectroscopy of disordered, amorphous, and diamond like carbon, 075414-1-075414-13, Phys. Rev. B 64 (2001), https://doi.org/10.1103/PhysRevB.64.075414.

[47] A.C. Ferrari, J. Robertson, Interpretation of Raman spectra of disordered and amorphous carbon, Phys. Rev. B 61 (2000) 14095–14107, https://doi.org/10.1103/PhysRevB.61.14095.

[48] P.K. Chu, L. Li, Characterization of amorphous and nanocrystalline carbon films, Mater. Chem. Phys. 96 (2006) 253–277, https://doi.org/10.1016/j.matchemphys.2005.07.048.

[49] L. Qiang, B. Zhang, Y. Zhou, J. Zhang, Improving the internal stress and wear resistance of DLC film by low content Ti doping, Solid State Sci. 20 (2013) 17–20, https://doi.org/10.1016/j.solidstatesciences.2013.03.003.

[50] Y. Lifshitz, S.R. Kasi, J.W. Rabalais, Subplantation model for film growth from hyperthermal species: Application to diamond, Phys. Rev. Lett. 62 (1989) 1290–1293, https://doi.org/10.1103/PhysRevLett.62.1290.

[51] Y. Lifshitz, S.R. Kasi, J.W. Rabalais, W. Eckstein, Subplantation model for film growth from hyperthermal species, Phys. Rev. B 41 (1990) 10468–10480, https://doi.org/10.1103/PhysRevB.41.10468.

[52] K. Kanda, K. Fukuda, K. Kidena, R. Imai, M. Niibe, S. Fujimoto, K. Yokota, M. Tagawa, Hyperthermal atomic oxygen beam irradiation effect on the Ti-containing DLC film, Diam. Relat. Mater. 41 (2014) 49–52, https://doi.org/10.1016/j.diamond.2013.10.006.

[53] K.N. Pandiyaraj, J. Heeg, A. Lampka, F. Junge, T. Barfels, M. Wienecke, Y.H. Rhee, H.W. Kim, In vitro cyto and blood compatibility of titanium containing diamond-like carbon prepared by hybrid sputtering method, Plasma Sci. Technol. 14 (2012) 829–836, https://doi.org/10.1088/1009-0630/14/9/11.

[54] Q.Z. Wang, F. Zhou, Z.F. Zhou, Y. Yang, C. Yan, C.D. Wang, W.J. Zhang, L.K.Y. Li, I. Bello, S.T. Lee, Influence of Ti content on the structure and tribological properties of Ti-DLC coatings in water lubrication, Diam. Relat. Mater. 25 (2012) 163–175, https://doi.org/10.1016/j.diamond.2012.03.005.

[55] P.V. Bharathy, D. Nataraja, P.K. Chu, H.V. Wang, Q. Yang, M.S.R.N. Kiran, J.S. Albero, D. Mangalarai, Effect of titanium incorporation on the structural, mechanical and biocompatible properties of DLC thin films prepared by reactive-biased target ion beam deposition method, Appl. Surf. Sci. 257 (2010) 143–150, https://doi.org/10.1016/j.apsusc.2010.06.052.

[56] Y.J. Jo, T.F. Zhangb, M.J. Sona, K.H. Kim, Synthesis and electrochemical properties of Ti-doped DLC films by a hybrid PVD/PECVD process, Appl. Surf. Sci 433 (2018) 1184–1191, https://doi.org/10.1016/j.apsusc.2017.10.151.

[57] D. Martinez-Martinez, C. Lopez-Cartes, R. Gago, A. Fernandez, J. Carlos Sanchez-Lopez, Thermal stability and oxidation resistance of nanocomposite TiC/a-C protective coatings, Plasma Process. Polym. 6 (2009) 462467, https://doi.org/10.1002/ppap.200931002.

[58] A. Lippitz, I. Koprinarov, J.F. Friedrich, W.E.S. Unger, K. Weiss, Ch. Woll, Surface analysis of metallized poly (bisphenol A carbonate) films by X-ray absorption spectroscopy (NEXAFS), Polymer 37 (1996) 3157–3160, https://doi.org/10.1016/0032-3861(96)89419-5.

[59] E. Stoyanov, F. Langenhorst, G. Steinle-Neumann, The effect of valence state and site geometry on Ti $L_{3,2}$ and O K electron energy-loss spectra of Ti$_x$O$_y$ phases, Am. Mineral. 92 (2007) 577–586, https://doi.org/10.2138/am.2007.2344.

[60] T. Hiratoko, A. Yoshiasa, T. Nakatani, M. Okube, A. Nakatsuka, K. Sugiyama, Temperature dependence of pre-edge features in Ti K-edge XANES spectra for ATiO3 (A = Ca and Sr), A2TiO4 (A = Mg and Fe), TiO2 rutile and TiO2 anatase, J. Synchrotron Radiat. 20 (2013) 641–643, https://doi.org/10.1107/S0909049513009175.

[61] J.J. Velasco-Velez, B. Davaasuren, M. Scherzer, S. Cap, M. Willinger, J.H. Guo, R. Schlögl, A. Knop-Gericke, Exploring the incorporation of nitrogen in titanium and its influence on the electrochemical corrosion resistance in acidic media, Surf. Sci. 650 (2016) 272–278, https://doi.org/10.1016/j.susc.2016.01.007.

[62] I. Jimenez, R. Gago, J.M. Albella, L.J. Terminello, X-Ray absorption studies of bonding environments in graphitic carbon nitride, Diam. Relat. Mater. 10 (2001) 1170–1174, https://doi.org/10.1016/S0925-9635(00)00383-6.

[63] S.C. Ray, H.M. Tsai, J.W. Chiou, B. Bose, J.C. Jan, K. Kumar, W.F. Pong, D. Dasgupta, M.H. Tsai, X-ray absorption spectroscopy (XAS) study of dip deposited a-C:H(OH) thin films, J. Phys.: Condens. Matter. 16 (2004) 5713–5719, https://doi.org/10.1088/0953-8984/16/32/008.

[64] N. Soin, S.S. Roy, S.C. Ray, P. Lemoine, M.A. Rahman, P.D. Maguire, S.K. Mitra, J.A. McLaughlin, Thickness dependent electronic structure of ultra-thin tetrahedral amorphous carbon (ta-C) films, Thin Solid Films 520 (2012) 2909–2915, https://doi.org/10.1016/j.tsf.2011.12.039.

[65] C. Lenardi, P. Piseri, V. Briois, C.E. Bottani, A. Li Bassi, P. Milani, Near-edge X-ray absorption fine structure and Raman characterization of amorphous and nanostructured carbon films, J. Appl. Phys. 85 (1999) 7159–7167, https://doi.org/10.1063/1.370527.

[66] D.A. Oulka, J. Stöhr, Curve fitting analysis of near edge core excitation spectra of free, adsorbed, and polymeric molecules, J. Chem. Phys. 88 (1988) 3539–3554, https://doi.org/10.1063/1.453902.

[67] F. Mangolini, J.B. McClimon, F. Rose, R.W. Carpick, Accounting for nanometer-thick adventitious carbon contamination in X-ray absorption spectra of carbon-based materials, Anal. Chem. 86 (2014) 12258–21265, https://doi.org/10.1021/ac503409c.

[68] K.H. Er, M.G. So, Thermal annealing behavior of Si-doped diamond like-carbon films deposited by reactive sputtering, J. Ceram. Process. Res. 11 (2010) 760–764.

[69] G. Ma, S. Gong, G. Lin, L. Zhang, G. Sun, A study of structure and properties of Ti-doped DLC film by reactive magnetron sputtering with ion implantation, Appl. Surf. Sci. 258 (2012) 3045–3050, https://doi.org/10.1016/j.apsusc.2011.11.034.

[70] P.B. Mirkarimi, D.L. Medlin, K.F. McCarty, D.C. Dibble, W.M. Clift, J.A. Knapp, J.C. Barbour, The synthesis, characterization, and mechanical properties of thick, ultrahard cubic boron nitride films deposited by ion-assisted sputtering, J. Appl. Phys. 82 (1997) 1617–1625, https://doi.org/10.1063/1.365961.

[71] K. Ankit, A. Varade, K. Niranjan Reddy, S. Dhan, M. Chellamalai, N. Balashanmugam, P. Krishna, Synthesis of high hardness IR optical coating using diamond-like carbon by PECVD at room temperature, Diam. Relat. Mater. 78 (2017) 39–43, https://doi.org/10.1016/j.diamond.2017.07.008.

[72] B.F. Coll, M. Chhowalla, Amorphous diamond film by enhanced arc deposition, Surf. Coat. Technol. 79 (1996) 76–86, https://doi.org/10.1016/0257-8972(95)02444-1.

[73] J. Robertson, Diamond-like amorphous carbon, Mater. Sci. Eng. R 37 (2002) 129–281, https://doi.org/10.1016/S0927-796X(02)00005-0.

[74] J.K. Luo, Y.Q. Fu, H.R. Le, J.A. Williams, S.M. Spearing, W.I. Milne, Diamond and diamond-like carbon MEMS, J. Micromech. Microeng. 17 (2007) 147–163, https://doi.org/10.1088/0960-1317/17/7/S12.

[75] X.Z. Ding, B.K. Taya, S.P. Lau, P. Zhang, X.T. Zeng, Structural and mechanical properties of Ti-containing diamond-like carbon films deposited by filtered cathodic vacuum arc, Thin Solid Films 408 (2002) 183–187, https://doi.org/10.1016/S0040-6090(02)00145-1.

[76] C. Donnet, Recent progress on the tribology of doped diamond-like and carbon alloy coatings: a review, Surf. Coat. Technol. 100–101 (1998) 180–186, https://doi.org/10.1016/S0257-8972(97)00611-7.

[77] J. Zhang, X. Yu, X. Zhao, L. Zhang, Influence of interfacial carbonization on the structure and mechanical properties of Cr-containing diamond-like carbon films, J. Phys. Chem. C 121 (2007) 6781–6787, https://doi.org/10.1021/acs.jpcc.7b00436.

[78] D. Bootkul, B. Supsermpol, N. Saenphinit, C. Aramwit, S. Intarasiri, Nitrogen doping for adhesion improvement of DLC film deposited on Si substrate by filtered cathodic vacuum arc (FCVA) technique, Appl. Surf. Sci. 310 (2014) 284–292, https://doi.org/10.1016/j.apsusc.2014.03.059.

[79] B. Beverskog, I. Puigdomenech, Revised Pourbaix diagrams for iron at 25–300°C, Corros. Sci. 38 (1996) 2121–2135, https://doi.org/10.1016/S0010-938X(96)00067-4.

[80] B. Beverskog, I. Puigdomenech, Revised Pourbaix diagrams for chromium at 25–300°C, Corros. Sci. 39 (1997) 43–57, https://doi.org/10.1016/S0010-938X(97)89244-X.

[81] B. Beverskog, I. Puigdomenech, Revised Pourbaix diagrams for nickel at 25–300°C, Corros. Sci. 38 (1997) 969–980, https://doi.org/10.1016/S0010-938X(97)00002-4.

[82] M.M. Najafpour, N.J. Moghaddam, S.M. Hosseini, S. Madadkhani, M. Hotynska, S. Mehrabani, R. Bagheri, Z.L. Song, Nanolayered manganese oxide: insights from inorganic electrochemistry, Roy. Soc. Chem. 1–3 (2017) 1–13, https://doi.org/10.1039/C7CY00215G.

[83] V.M.C.A. Oliveira, C. Aguiar, A.M. Vazquez, A.L.M. Robin, M.J.R. Barboza, Corrosion behavior analysis of plasma-assisted PVD coated Ti-6Al-4V alloy in 2 M NaOH Solution, Mater. Res. 20 (2017) 436–444, https://doi.org/10.1590/1980-5373-mr-2015-0737.

[84] J. Robertson, Classification of diamond-like carbons, in: C. Donnet, A. Erdemir (Eds.), Tribology of Diamond-Like Carbon Films: Fundamentals and Applications, Springer, Boston, 2008, pp. 13–24, , https://doi.org/10.1007/978-0-387-49891-1_1.

[85] L.R. De Jesus, R.V. Dennis, S.W. Depner, C. Jaye, D.A. Fischer, S. Banerjee, Inside and outside: X-ray absorption spectroscopy mapping of chemical domains in graphene oxide, J. Phys. Chem. Lett. 4 (2013) 3144–3151, https://doi.org/10.1021/jz401717j.

[86] R.P. Gandhiraman, D. Nordlund, C. Javier, J.E. Koehne, B. Chen, M. Meyyappan, X-ray absorption study of graphene oxide and transition metal oxide nanocomposites, J. Phys. Chem. C 118 (2014) 18706–18712, https://doi.org/10.1021/jp5039411.

[87] S. Viswanathan, M.M. Reddy, L. Mohan, P. Bera, H.C. Barshilia, C. Anandan, Corrosion and wear properties of Ti/tetrahedral amorphous carbon multilayered coating, J. Bio. Tribo. Corros. 3 (2017) 1–10, https://doi.org/10.1007/s40735-017-0100-5.

[88] J.M. Bastidas, M.F. Lopez, A. Gutierrez, C.L. Torres, Chemical analysis of passive films on type AISI 304 stainless steel using soft X-ray absorption spectroscopy, Corros. Sci. 40 (1998) 431–438, https://doi.org/10.1016/S0010-938X(97)00149-2.

[89] L. Soriano, M. Abbate, F.M.F. de Groot, D. Alders, J.C. Fuggle, S. Hofmann, H. Petersen, W. Braun, Chemical analysis of passivated and oxidized layers on FeCr and FeTi alloys by soft X-ray absorption spectroscopy, Surf. Interface. Anal. 20 (1993) 21–26, https://doi.org/10.1002/sia.740200105.

BIOGRAPHY

Natthaphong Konkhunthot was born on June 3, 1988 in Nakhon Ratchasima, Thailand. He graduated with second-class honors in 2009 with a Bachelor's Degree in Metallurgical Engineering, Institute of Engineering at Suranaree University of Technology (SUT). During studying at final year, he received the scholarship from the Thai Tohken Thermo Co., Ltd. for the cooperative education program and participated in Department of Research and Development as an assistant engineer where he worked with the other engineers on continuous improvement and development of heat treatment processes. After finishing such program, he was awarded the School of Metallurgical Engineering prize for an excellent cooperative education student and joined a group of students to perform a special project at the Daisin Co., Ltd, Nakhon Ratchasima, Thailand. After completing his graduation, he enrolled in the Institute of Engineering, SUT and graduated in School of Metallurgical Engineering with a Master's Degree in 2013. He received the scholarship from the Royal Thai Government under the Office of the Ministry of Science and Technology sponsored by Synchrotron Light Research Institute (SLRI), Nakhon Ratchasima, Thailand. During his studying, he worked as a teaching assistant in the School's course and also as a research assistant at the BL3.2Ub: PEEM at the SLRI where he learned and developed his experiences and skills in a vacuum system and synchrotron-based analytical technique. During his Masters, he has participated in the 6th Thailand Metallurgy Conference (TMETC), Chiang Mai, Thailand, which resulted in a conference presentation and published a paper in the Journal of Metals, Materials and Mineral. In 2013, he started his Ph.D. program in Metallurgical

Engineering, Institute of Engineering at SUT. During his studying, he was financially supported by the Thailand Research Fund under the Office of the Prime Minister, the Royal Thai Government through The Royal Golden Jubilee (RGJ) Ph.D. Programme, Bangkok, Thailand and the SLRI. In 2015, he attended the International Symposium on Engineering and Applied Science held on Kuala Lumpur, Malaysia for a conference presentation. His research was focused on characterizing and improving the desired properties of diamond-like carbon (DLC) film deposited using simultaneous filtered cathodic vacuum arc (FCVA) technique by Ti incorporation. During his Ph.D. program, he spent 10 months as an exchange research student for research in the Opto-Electronic Ceramics Laboratory at the Nagaoka University of Technology, Niigata, in Japan. After that, he had come back to SUT and published the first paper in which some experiments had been done during his exchange in the Journal of Thin Solid Films and conference presentation in the RGJ-Ph.D. Congress 18 on Global Sustainability: Lesson Learned from The Royal Projects, Nonthaburi, Thailand. He continued for research on the incorporation of Ti atoms into DLC structure and published a paper in the Journal of Applied Surface Science. Both Thin Solid Films and Applied Surface Science are the Journal indexed in the ISI Web of Science database. He completed his Doctoral Degree in 2019. His expertise includes the design and develops the pulsed two-FCVA system, and the deposition and characterization of the carbon-based materials, particularly amorphous DLC films. In his current project, he will apply the DLC film as protective coatings in tribological and engineered applications and is interested for study and for synthesis the properties of the metal-doped DLC films.